ABSTRACT

Title of dissertation: ANALYSIS, VALIDATION, PREDICTION AND FUNDAMENTAL UNDERSTANDING OF ROTOR BLADE LOADS IN AN UNSTEADY MANEUVER

Abhishek Abhishek, Doctor of Philosophy, 2010

Dissertation directed by: Professor Inderjit Chopra
Department of Aerospace Engineering

This study predicts, analyzes, and isolates the mechanisms of main rotor airloads, structural loads, and swashplate servo loads in a severe unsteady maneuver. The objective is, to develop a comprehensive transient rotor analysis for predicting maneuver loads. The main rotor structural loads encountered during unsteady maneuvers are important to size different critical components of the rotor system, particularly for advanced combat helicopters. These include the blade structural loads, control/pitch-link loads, and swashplate servo loads. Accurate and consistent prediction of maneuver loads is necessary to reduce the risks and costs associated with use of prior flight test data as a basis for design. The mechanism of rotor loads in different level flight regimes is well understood – transonic shock in high speed flight, inter-twinning of blade tip vortices below the rotor disk at low speed transonic flight, and two dynamic stall cycles on retreating blade during high altitude dynamic stall flight. All these physical phenomena can occur simultaneously during a maneuver.

The goal is to understand the key mechanisms involved in maneuver and model them accurately. To achieve this, the aerodynamics and structural dynamics of UH-60A rotor in unsteady maneuvering flight is studied separately. For identification of prediction deficiencies in each, first, the measured lift, drag, pitching moment and damper force from the UH-60A Flight Test Program for UTTAS pull-up maneuver (C11029: 2.16g pull-up maneuver) are used to obtain an accurate set of deformations. A multibody finite element blade model, developed for this purpose, is used to perform measured airloads analysis. Next, the resultant blade deformations are used to predict the airloads using lifting-line and RANS CFD aerodynamic models. Both lifting-line as well as CFD analyses predict all three stall cycles with prescribed deformations. From the airloads predicted using prescribed deformations, it is established that the advancing blade transonic stall, observed from revolution 12 onwards, is a twist stall triggered by 5/rev elastic twist deformation resulting in shock induced flow separation. The 5/rev elastic twist is triggered by the two retreating blade stalls from previous revolution, which are separated by $1/5^{th}$ rev. The accurate prediction of both stall cycles on retreating blade holds the key to prediction of advancing blade stall. In analysis, advancing blade stall is triggered by a correct combination of control angles and 5/rev elastic twist. Some discrepancies are observed in higher harmonics of predicted torsion moment, which are not resolved by using measured airloads.

The structural model and the aerodynamic models are coupled together to predict blade loads for the maneuver. The structural model is refined to include a three degrees of freedom swashplate model to calculate servo loads and to study the

effect of swashplate dynamics on rotor loads. Lifting-line coupled analysis, though of low fidelity, is ideally suited to isolate the effects of free wake and dynamic stall. It is concluded that the UTTAS maneuver is almost entirely dominated by stall with little or no wake induced effect on blade loads, even though the wake cuts through the disk twice during the maneuver. At the peak of the maneuver, almost 75% of the operating envelope of a typical airfoil lies beyond stall. The peak-to-peak structural loads prediction from the lifting-line analysis show an under-prediction of 10%–20% in flap and chord bending moments and 50% in torsion loads. The errors stem from the prediction of 4 and 5/rev stall loads. Swashplate dynamics appears to have a significant impact on the servo loads - unlike in level flight – with more than 50% variation in peak loads.

The coupled analysis using CFD/CSD tight coupling shows considerable improvements in the predicted results by using a CFD model over a traditional lifting-line approach. In particular, the coupled CFD/CSD simulation is able to correctly predict the magnitude and phasing of the two dynamic stall cycles on the retreating side of the rotor disk during the maneuver. Further it shows significant improvement in the predicted peak-to-peak structural loads. The advancing blade stall is not predicted by either of the analyses. CFD/CSD analysis is not able to predict the advancing blade stall due to less satisfactory prediction of retreating blade dynamics stall cycles which are sensitive to the grid refinements and turbulence modeling.

Analysis, Validation, Prediction And Fundamental Understanding Of Rotor Blade Loads In An Unsteady Maneuver

by

Abhishek Abhishek

Dissertation submitted to the Faculty of the Graduate School of the
University of Maryland, College Park in partial fulfillment
of the requirements for the degree of
Doctor of Philosophy
2010

Advisory Committee:

Professor Inderjit Chopra, Chair/Advisor
Dr. Anubhav Datta
Professor James Baeder
Professor Roberto Celi
Professor Sung Lee
Professor Howard Elman, Dean's Representative

Acknowledgments

Acknowledging everyone who has contributed in accomplisment of this reasearch work would be very difficult, as this work has been completed with the participation, help, and guidance that I received from my colleagues and teachers at the Alfred Gessow Rotorcraft Center and the participants of the UH-60A Airloads workshop.

First and foremost I'd like to thank my advisor, Dr. Chopra for allowing me to work on one of the most challenging problems in the area of rotorcraft dynamics. He showed the greatest amount of patience and faith in me and encouraged me to give my best, without this I would have been overwhelmed by the complexity and enormity of this research work. His keenness to learn and fascination for unsolved problems is remarkable, a trait I want to inculcate in myself. Every time I got stuck with my research he was always the one to show me the correct way, for this I would forever be grateful to him.

If I have to name one person apart from my advisor who had the biggest influence on this research then that person would be Dr. Anubhav Datta, my co-advisor and my mentor. It was he who inspired me to take up this challenging problem, although I was initially inclined to work in the area of micro air vehicles. He remained the biggest source of motivation, encouragement and guidance during the course of this research. His expertise on rotorcraft aeromechanics is phenomenal, and he has always been forthcoming in sharing his vast knowledge with me. Nearly everything that I learnt and achieved during my PhD research, can be attributed to him.

I would like to thank Dr. Baeder for all the help in resolving issues related to CFD/CSD coupling, the numerous discussions we had helped me understand the advancing blade stall mechanism better.

I would also like to thank Dr. Celi for his constructive criticism which helped in improving the quality of this work. I express my gratitude to Dr. Lee and Dr. Elman for accepting to be on my committee and over-viewing the progress of my research.

During my PhD work I had the privilege of working and interacting with eminent researchers like Prof. Marat Tishchenko of the Russian Academy of Sciences, and Robert Ormiston and Bill Bousman of the Army AFDD – whose dedication for rotorcraft research have been a great source of inspiration and encouragement for me. I would also like to thank Hyeonsoo Yeo, Alan Egolf, and Mahendra Bhagwat for useful comments and discussions regarding the analysis of maneuver. Dr. Nagaraj taught me the basics of helicopter design and has always supported my research with insightful feedback and encouragement.

I cannot thank Dr. Ananthan enough for all the help I received in using UMTURNS CFD code for my research. His participation in my research acted as a catalyst in identification and resolution of several issues in my analysis work. The success of the CFD/CSD coupling must be attributed solely to him and to Benjamin Silbaugh. This research was funded in part by NASA NRA and I would like to thank the Dr. Guru Guruswamy for various useful discussions and guidance.

My colleagues, Arun, Nitin, Jaye, Asitav, Moble, Vikram, Smita, Anand, Sachit, Anne and Monica, to name a few, have been a great source of support and

happiness during the ups and downs that I encountered in course of this research. My housemates at my place of residence at different times, Satheesh, Sonam, Amardip, Abhishek Padma, Milind, Sachin and Siddharth have provided a relaxed "home" like atmosphere which has been a crucial factor in my finishing smoothly.

Acknowledging the sacrifice and dedication of my parents, especially my mother, at making me who I am would amount to showing *a candle to the Sun* (an Indian aphorism). I learnt from my father to never give up and to do my duties with utmost sincerity without ever worrying about the outcomes. This teaching from *Bhagavad Gita* has been the biggest inspiration of my life.

My wife Preeti's love, care and support has made my journey through life a pleasurable one. She sacrificed her own career as a Bio-technologist to come and support me in the completion of my work, which she did by taking away all my worries, allowing me to focus completely on my work.

It is impossible to remember all, and I apologize to those I've inadvertently left out.

Table of Contents

List of Figures

List of Tables

Chapter 1

Introduction

The main rotor structural loads encountered during unsteady maneuvers are important to size different critical components of the rotor system, particularly for advanced combat helicopters. These include the blade structural loads, control/pitch-link loads, and swashplate servo loads. Therefore, the knowledge of the source or sources of these vibratory loads and accurate methods for their prediction can help in the expansion of the flight envelope for the helicopter.

The current state-of-the-art for rotor loads prediction is becoming satisfactory for steady level flight. Level flight conditions with the key aerodynamic mechanisms of intertwinning rotor wake, transonic pitching moments, and dynamic stall have all been studied in isolation and understood. Maneuvers have been only studied using lower order models for study of handling qualities, trajectory optimization, and wake modeling. Detailed prediction of rotor loads during maneuver using high fidelity tools has received only limited attention so far.

Accurate analysis and prediction of loads mechanisms in an unsteady maneuver is a critical challenge in the field of rotor aeromechanics, primarily due to the following two reasons: (1) several complex aerodynamic phenomena can occur simultaneously in a maneuver, (2) an inverse solution procedure to determine the trim variables (pitch control angles, vehicle attitude angles, and yaw control) in order to

fly a prescribed trajectory is quite involved and not yet available to a satisfactory level. In steady level flight, the trajectory is simple, and the aircraft Euler equations reduce to six equilibrium equations from which the trim variables are determined successfully, such is not the case in a maneuvering flight. The complexity of the solution procedure has been the primary hurdle for a first principles prediction of maneuver loads. Today, extensive flight test data from the U. S. Army/NASA Airloads Program (Refs. [1,2]) has opened opportunity to bypass this complexity. The measured values of rotor controls, aircraft attitudes, and flight trajectory can now all be prescribed from flight test data in order to focus solely on the loads mechanisms.

This chapter introduces the requirements for analyzing helicopter main rotor loads and swashplate loads during an unsteady maneuver to reduce the empiricism involved in current design practices. First, the role of maneuver loads in helicopter design is addressed, and the current approaches used for helicopter design is discussed. Next, the source of high loads in a helicopter undergoing maneuver is discussed, followed by the analysis requirements for development of comprehensive analysis for maneuver. Next, the state-of-art of loads prediction is discussed, and the description of the goals of the present research, with the challenges associated with it is described. Finally, the approach taken to address those challenges is explained and the contributions of the present research is highlighted. The focus of this work is on the development of methodology for prediction and fundamental understanding of rotor and swashplate-servo loads for an unsteady maneuver.

1.1 Importance of Maneuver Loads in Design

Helicopters experience a complex dynamic loading environment due to interaction of aerodynamic, structural, centrifugal, and inertial forces. This is the case for most flight conditions for a helicopter, except for the vertical flight and hover conditions, where the loads are closest to being static. The dynamic loads experienced by the rotor blades get transmitted to the airframe via hub and are important in the design of sub-components to safeguard them from fatigue failure.

Typically a helicopter spends the largest time of its operational life in steady level flight. During steady flight, the loads encountered in the rotor blade constitute of harmonics that are integer multiples of the rotational frequency. For a N_b-bladed rotor with identical blades, pN_b/rev harmonics of the loads, where p is an integer, get transmitted from the rotor to the hub during steady flight. These harmonics in the fixed frame are generated by pN_b and $pN_b \pm 1$/rev harmonics in the rotating frame. The accurate prediction of rotor vibrations in the airframe requires a good understanding of coupling of aerodynamic and dynamic characteristics of airframe and rotor.

An accurate estimation of maneuver loads is essential for sizing the critical components of rotor and control system. In general, only the peak-to-peak magnitude of the structural loads are needed for selecting the material properties for designing a rotor, but the magnitude and phase of higher harmonics of the structural loads, especially the torsion moment and pitch-link load are critical for sizing the control system and the swashplate servo actuators, which are located in the fixed

frame.

1.2 Current Design Practice

Main rotor and other critical components (pitch-links, swashplate, servos etc.) have traditionally been designed using previous experience and experimental data. The quote from Bob M. Kee (Ref. [3]) highlighted the state of loads prediction back in 1959 when the helicopter loads prediction was in its infancy, *"Analytical calculations are carried out on blades. However, experience has shown that theoretical calculations are a guide to the structural integrity of a metal blade, but that extensive testing must follow"*. Crichlow [4] reaffirmed the situation in 1967. More than twenty years later (1986), prediction methodology had not improved significantly, *"... rotor blade loadings are difficult to accurately predict: all current airworthiness requirements specify that fatigue analyses must be based on measured loads."*, de Jonge [5].

Accurate and consistent prediction of maneuver loads is necessary to reduce the risks and costs associated with use of prior flight test data as a basis for design. At present, the data from the loads survey is used as the basis for the design of helicopters. Currently, the design process for flight qualification of modern helicopters involves the following four phases: (1) design analysis, (2) ground qualification tests, (3) aircraft flight tests, and (4) service and evaluation tests [6]. The design analysis involves the analytical load predictions and static and dynamic structural analyses, which form the basis for the initial structural substantiation. However, due to the

inherent assumptions and limitations of the analyses tools, test verification has been essential. The ground qualification tests involves, model and/or full scale wind tunnel testing of the helicopter. In addition, static failure or limit load testing is carried out to minimize risk during flight testing. Finally, a comprehensive flight test loads survey is undertaken to evaluate the influence of variables like gross weight, altitude, air speed, rotor speed and center of gravity. The flight testing must also include effects due to the changes in mission or configuration requirements. This involves lot of expenditure in testing, as the flight loads survey: (1) establishes the flight envelope, (2) provides load and stress data for fatigue substantiation, (3) provides data to support and/or update predicted loads, (4) provides verification of critical load distributions and (5) provides a library of test data to be used to support future helicopter development. Often, due to the restrictions imposed by the flight data acquisition systems, along with time and cost associated with flight testing, conservatism has to be introduced in data reduction, analysis and application. This results in a conservative design to ensure highest levels of safety, as the prediction of maneuver loads using the high fidelity prediction tools is seldom attempted due to inadequacy of tools. With the development of accurate and reliable tools for loads prediction in maneuvers, such conservatism can be overcome, leading to the development of a more efficient and agile helicopter.

1.3 Flight Test Data

The analysis tools developed for the rotor loads prediction can be considered reliable for design purposes only when they are validated against comprehensive experimental data. Wind tunnel tests provide a controlled environment for studying specific sets of phenomenon and provide detailed data, which can be used for validating numerical models for rotor loads. But, unsteady maneuvers, cannot be simulated in wind tunnels, and only a full scale flight test can provide the desired detailed information (such as pressure distribution, strain gage data, pitch-link loads, control angles, vehicle attitudes and rates time history) to rigorously validate a comprehensive analysis for maneuver loads prediction.

The earliest documentation of rotor airloads and structural loads measurements in flight for a maneuver was by Beno in 1973 [7]. The flight tests were conducted using NH-3A compound helicopter and the CH-53A conventional helicopter. Measurements were made for the blade pressures (which were integrated to obtain sectional airloads) and for root torsion moment, only the banked right turn flight was considered.

The U.S.Army/NASA UH-60A Black Hawk Airloads Program [1] is the first detailed flight test program which provided an extensive set of repeatable flight test data covering steady level flight regimes (high speed, low speed transition, high thrust and low thrust), steady turns and severe unsteady maneuvers. One of the blades was instrumented with pressure gages at 9 stations. The pressure measurements were integrated to obtain airloads (normal force, chord force and

pitching moment). Another blade was instrumented with 9 flap bending gages, 8 chord bending gages and 4 torsion gages. All four pitch-links were instrumented along with the three servos under the non-rotating swashplate.

Kufeld and Bousman [8] investigated some of the key flights with high load factors. Based on the criteria of six structural measurements: pitch-link load, torsion moment (30% R), and flap and chord bending moments (11.3% R and 60% R), they identified and ranked the maneuvers from the most to the least severe. The severest maneuvers noted in this study are listed in Table 1.1. As expected, the highest loads in different categories are exhibited in a wide range of flight conditions and no single flight condition has the highest loads in every category of load. For example, a diving right turn at 140 knots (Counter 11680), which is one of the severest maneuvers, has the highest torsion moment at $30\%R$, highest pitch-link load, and highest chord bending moment at the root, but only 15^{th} most severe in terms of the root flap bending moment and 14^{th} most severe for chord bending moment at $60\%R$. This highlights the importance of studying a wide range of maneuvers, to separately identify the physical mechanisms involved. Some of the maneuvers flown during the airloads program lie close to the boundary of the operational envelope of the UH-60A helicopter. Figure 1.1 shows the plot of rotor thrust against advance ratio for several key flight conditions flown during the UH-60A flight tests. Each steady flight condition is depicted by a solid dot joined using lines, while the maneuvers have been shown using symbols connected using solid line. Two of the severest maneuvers shown in the Fig. 1.1 achieve the rotor thrust well in excess of the aerodynamic rotor lift boundary, obtained in wind tunnel testing using a model rotor (known as

McHugh's lift boundary [9]). A survey of loads for all flight tests revealed that the highest loads were seen for the high load factor or high speed conditions or some combination of both [8]. The examination of aerodynamics loads from UTTAS pull-up, maneuver which is a 2.1g pull-up with third largest pitch-link loads revealed that the high loads were a result of dynamic stall occurring in the outboard portion of the blade. C11029 2.1g pull-up maneuver is based on an Utility Tactical Transport Aerial System (UTTAS) maneuver of the original UH-60A design specification and discussed in detail in the coming section.

Multiple dynamic stall cycles (up to three) were common feature of several high load conditions for both steady and maneuvering flights, for example, UTTAS pull-up (C11029) and high speed diving right turn (C11679) [10]. The two maneuvers mentioned above are characterized by highest control loads (second highest pitch-link loads for C11679, third highest pitch-link load for C11029), arising from multiple dynamic stall events as shown in Fig. 1.2.

1.3.1 UTTAS Pull-up Maneuver

The second most severe maneuver, designated by Counter 11029, is studied in this thesis. This maneuver is carried out in a period of 9 seconds and covers 40 rotor revolutions. The reasons for the selection of this flight are: (1) it is one of the severest maneuvers, and (2) at the time of this study the test data was made available for this maneuver only. It is a dynamic pull-up that reaches 2.12g at 139 knots and produces the highest root flap bending moment and the third highest

oscillatory pitch-link load of all the UH-60A maneuvers. Even though the pitch-link load is only third highest of all the maneuvers, it still exceeds the loads encountered in operational use (see Fig. 1.3). For example, the peak-to-peak pitch link loads at this flight are 20% higher than those encountered during free engagement air-to-air combat test (AACT) flights of similar kind, Ref. [11]. These high loads are possibly the result of advancing blade transonic effects, three dynamic stall cycles (Fig. 1.2) and wake interactions. The wake is expected to pass through the rotor disk around rotor revolution number 10 and 24 – first from below to above and then from above to below as shown in Fig. 1.4.

The measured load factor and velocity ratio are shown in Figs. 1.5 and 1.6, which show the critical requirements for this maneuver to maintain a load factor of 1.75g for 3 seconds with less than 30 kts loss in airspeed. The aircraft attitude angles and angular rates are shown in Figs. 1.7(a) and 1.7(b), with negative representing the nose down attitude. Due to a discrepancy in the angle of attack measurement for this maneuver, the aircraft shaft angle has to be derived from the pitch angle. The aircraft pitch angle when reduced using the measured flight path angle (not shown), and after accounting for 3° forward built-in shaft angle produces the effective shaft tilt with respect to the on-coming flow which is shown in Fig. 1.4. The shaft and sidelip angles (Fig. 1.4) angle dictate the evolution of rotor wake.

1.4 Challenges for Maneuver Loads Prediction

To understand the challenges associated with the development of high fidelity tools for prediction of maneuver loads, the mechanism of maneuver loads must be understood. The complex unsteady aerodynamic forces in an unsteady maneuver may occur due to some or all of the following factors

1. Cyclic variation of blade pitch angle and its rate, resulting in asymmetric flow on advancing and retreating sides.

2. Reverse flow on the retreating side due to low effective air speeds and large angles of attack required to counter the lift asymmetry.

3. Multiple dynamic stall cycles. Stall response under high subsonic to transonic flow excited by controls, elastic twist and inflow.

4. Compressibility and 3D transonic effects on the advancing side.

5. Rotor wake interaction with following blades.

The maneuvers that a helicopter can perform can be broadly classified into steady turns and unsteady maneuvers. Steady turns (e.g. constant altitude banked turn, where pitch rate and yaw rate are non zero constants and the roll rate is zero) in general possesses similar levels of complexity as level flight, from simulation point of view, but unsteady maneuvers (e.g. a rolling pullout or a high load-factor pull-up), are far more complicated due to transient nature of blade dynamics, compressibility and dynamic stall. Some of the key aerodynamic events observed during

an unsteady maneuver have been observed in steady flight conditions – high speed, low speed transition, and moderate speed high altitude dynamic stall flights [12]. The high speed high vibration flight is dominated by 3D transonic pitching moments on the advancing side. The moderate speed high altitude flight is dominated by two dynamic stall cycles on the retreating side. The low speed high vibration transition flight is dominated by vortex loadings on the advancing and retreating sides. All of these three mechanisms can occur simultaneously in an unsteady maneuver.

As mentioned earlier, accurate prediction of rotor loads during unsteady maneuver holds the key to advanced rotorcraft design. A well validated reliable analysis tool can allow quick evaluation and comparison of performance capabilities of different designs and configurations without having to resort to wind tunnel or flight testing which can be time consuming and economically less viable. Such an analysis tool when developed would be a valuable asset to the helicopter design community, making the design process streamlined, and may result in the design of more agile, low vibration, low noise, and efficient vertical flight vehicles, which may have enormous impact on the civilian short haul flights. To realize this goal, it is important to understand the physical mechanisms that need to be modeled for prediction of the loads.

1.5 Requirements for Comprehensive Analysis for Maneuver Loads

The complicated aerodynamics environment encountered during the maneuvers result in high aerodynamic and inertial loads. These high loads acting on

rotor blades cause moderate to large deformations in flap, lag and torsion. Due to the transient nature of the maneuver, these deformations are no longer similar from blade to blade, as is the case during steady flight with identical blades (deformations have same magnitude and only differ in phase). Each blade experiences different inflow, angle of attack, airloads and deformation. This implies that all the blades need to be modeled individually. The effect of large deformation and its rate gets fed back to the aerodynamics and results in a highly non-linear aeroelastic behavior. This makes the modeling of large blade deformation critical for analysis of a rotor undergoing maneuver. The simulation modeling requirements for prediction of maneuver loads are listed below.

1. A helicopter rotor undergoing severe unsteady maneuver is expected to undergo large blade deformations. Therefore, structural model capable of modeling large blade deformations is necessary for accurate representation of blade response. Large deformations can be typically modeled using exact beam formulations or using second order moderate deformation beam model in conjunction with multibody formulation. The non-linear inertial coupling, multiple load paths at root end boundary conditions should be included.

2. High control loads experience during the maneuver are of primary interest to the designers. The servos, rotating and stationary swashplates are sized based on the servo loads. Therefore, a model for swashplate, servo and full control system (pitch-links, pitch bearings etc.) is important for accurate control loads prediction.

3. Transient aerodynamic model for the analysis of maneuver can comprise of either: (1) lifting-line based analysis should have quasi-steady aerodynamics based on airfoil table look-up, near wake and unsteady aerodynamics modeling for dynamic stall, and time accurate far wake evolution, or (2) 3D Computational Fluid Dynamic formulations, which have become more feasible with the advances in parallel computational capabilities of modern computers.

4. Control angles time history is required to simulate the maneuver. These can be either obtained from the flight test or obtained using a flight dynamic inverse simulation. The inverse simulation can be performed to either target the time history of loads and moments encountered by the vehicle or the exact trajectory itself. In addition, a vehicle trim model may be used for the steady flight regime. The trim angles thus obtained are applied as steady correction to the flight test control angle history to make it more suitable for use with analysis.

5. Modeling of rotor-fuselage interactions. The analysis should incorporate appropriate aerodynamic as well as structural dynamic model of fuselage.

A detailed modeling to account for each and every requirement of the simulation of the maneuver is prohibitive, primarily due to the enormity of computational time required. Therefore, depending on the desired level of solution accuracy (loads, control angle estimation, stability, flight dynamics) and the computational resource availability, the models mentioned above are combined to setup the simulation of the maneuver. For example, an analysis comprising of finite element structural model,

lifting-line aerodynamics, free wake and prescribed history of control angles may not be adequate for an accurate prediction of blade loads, but these can be used for initial sizing. It also serves as a good means for physics based studies to isolate different load mechanisms. Multibody dynamics model combined with RANS CFD model and prescribed control angles is expected to provide significantly accurate loads when compare to the lifting-line analysis, and can be used to refine the estimates made using lifting-line analysis, especially at the limit of stall envelope. But such a detailed analysis cannot be used routinely due to the associated computational time. However, none of the above combinations may be appropriate for an estimation of control angles required to simulate a maneuver or provide estimates of handling qualities. Such estimations can be obtained using a simple FEM structural model with modal reduction combined with dynamic inflow based lifting-line analysis.

A survey of development of various elements of the analysis strategy for accurate prediction of loads is necessary to understand the modeling requirements, and is discussed in following sections.

1.5.1 Structural Model

1.5.1.1 Blade Modeling

The first ever helicopter blades used on Sikorsky's VS-300 in 1940, were constructed using tubular steel spar, plywood ribs with fabric / plywood covering and were considered essentially rigid for analysis [13]. Flax [14] was first to include the effects of bending flexibility in the study of blade response in 1947. The analysis

was still simple as he did not include the effect of blade bending on the inertial and aerodynamic loads. Around same time, Johnson and Mayne [15] recognized the role of out-of-plane blade bending on the blade inertial loads and bending moments.

The equations for flap and lag motions for the analysis of rotating blades were first developed independently by Prima and Handelman [16] and Shulman [17]. While the analysis acknowledged the coupling between flap and lag due to Coriolis terms, it was neglected to keep the equations linear.

The first successful attempt at deriving linear coupled equations of flap, lag, and torsion was made by Houbolt and Brooks [18]. The development of hingeless rotors led to increased interest in blade structural modeling. The Hodges and Dowell [19] came up with coupled non-linear flap-lag-torsion equations for moderately large deformations in which the non-linear terms were retained through an ordering scheme. This beam model underwent several refinements with contributions from several researchers. Hodges, Ormiston, and Peters [20] extended the formulation by treating the elastic torsion variable as a quasi-coordinate. Also, Kvaternik *et al.* [21], Rosen and Friedmann [22] and Johnson [23] led to the development of moderate deformation second-order nonlinear beam theories.

Crespo da Silva [24] showed that the third-order terms, neglected in earlier models, have some effect on the rotor aeroelastic stability. But retaining third order terms via ordering schemes greatly increases the complexity of the resulting equations. This lead to development of large deflection theories which did not rely upon an ordering scheme. Hodges [25] first derived an implicit set of equations using compact notations for a beam undergoing large rotations. Simo [26] (and later

Hodges [27]) derived an explicit non-linear beam equations using a mixed formulation. Within the assumptions imposed on the physical model, the kinematics of the equations are exact. The models conforming to this definition are called exact beam formulations. Hodges derivation, a mixed variational formulation, extended the analysis of Simo and Vu-Quoc [28] for study of beams undergoing large motions in space. In this formulation, Hodges prescribed the rigid-body (frame) motions of the beam as kinematical variables (floating frame), separate from the beam elastic deformations. These developments led to the emergence of use of multibody dynamics in beam modeling. Simo and Vu-Quoc, on the other hand implicitly included the frame motion in the beam kinematics. The use of floating frame of reference allows to treat the elastic deformations and rigid body motions separately, but the coupling between the rigid-body and elastic motion tends to be complex. The extension of the floating frame approach is the corotational frame approach. While the floating frame follows an average rigid body motion of the entire flexible component or substructure, the corotational frame follows an average rigid body motion of an individual finite element within the flexible component. The goal of these "new" beam modeling approaches was to derive beam models which are robust enough to handle large deformations. This can be achieved in two ways: (1) by using the "geometrically exact" beam theories [27–30], or (2) by using multibody formulations [31–33], that allow both rigid and elastic motion of its components using floating frame approach as mentioned above. In addition to the floating frame approach mentioned above, another way of incorporating large deformations using moderate deformation beam elements is the corotational frame approach, which was initially developed as

a part of the natural mode method proposed by Argyris *et al.* [34]. In this approach, the motion of a finite element is divided into a rigid body motion and natural deformation modes. It was developed for the static analysis. The dynamic modeling of planar continuum and beam type elements using rigid convected frames or corotational frames was developed by Belytschko and Hsieh [35]. The definition of the corotational frame depends on the type of elements used for modeling the flexible components. For two-node beam elements, the corotational frame is usually defined by the vector connecting the two nodes [35, 36].

A third approach commonly used in flexible multibody dynamics is inertial frame approach, which finds its origin in non-linear finite element methods. This approach has been used for dynamic analysis of bodies undergoing large rotations and large deformations since early 1970s [37,38]. Work of Simo and Vu-Quoc [26,28] and Downer *et al.* [39] can be classified in to this category. Efforts have been made recently to integrate large deformation finite element formulations with flexible multibody system algorithms to develop capabilities for the analysis of engineering models with significant details [40].

1.5.1.2 Rotor Dynamics Formulations

Complex boundary conditions can be modeled in a generalized manner using a multibody formulation [41, 42]. Flexible multibody formulations were originally developed for applications in spacecraft dynamics, to model large, slender space structures with its components undergoing arbitrary rotations and translations rel-

ative to one another. The multibody formulations started to find applications in rotorcraft dynamics due to its ability to increase the scope of analysis, without having to re-derive and re-validate the equations with each additional feature. This has been the shortcoming of the conventional rotor formulations which usually exploits the topology of rotor system to simplify the derivation of the governing equations, at the cost of loss of expandability. For example, for an existing rotor model, extending it to incorporate a fully coupled rotor-fuselage or a rotor-swashplate model would require a re-derivation and re-validation of the equations.

First rotor aeromechanical analysis to incorporate multibody formulation was GRASP by Hodges *et al.* [43], which could model arbitrary configurations of modern rotors. Apart from the capability to model arbitrary topology, multibody formulations enable modeling of large deformation problems using second-order nonlinear beam theory by breaking the rotor blade into multiple bodies undergoing only moderate deformations within its local frame. The net deformation is obtained by adding the local deformations for each body to the net deformation of its parent body. This approach is used in comprehensive analysis codes like CAMRAD II [32] and RCAS [33] and is also used for the present study as this methodology helps to extend the existing finite element formulations for modeling large deformation problems without the need of using algebraic constraints. For RCAS, the model is constructed in such a way that the element connectivity and constraints are built into the element equations. Elements are connected directly to one another without relative motion between the elements at the connection nodes, except for the hinges and slides which provides relative motion between the elements. In the present study

constraints are applied by manually removing the redundant degrees of freedom.

DYMORE [31] and MBDyn [44] are examples of modern flexible multibody codes which have been developed as multibody codes to begin with and are capable of modeling arbitrary configurations by using algebraic constraint equations. A popular method for modeling algebraic constraints, is the Lagrange multiplier technique which is used in the above mentioned codes. This method finds its root in the rigid multibody system dynamics. It was first applied to flexible multibody system using floating frame approach by Thompson and Barr [45], Song and Haug [46]. The main advantage of the Lagrange multiplier method is that the constraints are satisfied accurately (within the accuracy of the numerical iterations). However, the modeling flexibility comes at a price. The use of Lagrange multipliers results in a system of DAEs (Differential Algebraic Equations) with zero terms introduced at the diagonal of the nonlinear stiffness matrix, which increases the stiffness considerably thereby making the solution procedure more difficult. In addition, the use of algebraic equations prevents the use of state space stability analysis. The procedures used for solving DAEs are an active area of research. A survey of classical and contemporary approaches of constraint modeling for multibody systems can be found in Refs. [47, 48].

If algebraic equations are not present, full non-linear finite element equations present in most modern rotorcraft codes can be solved using time-marching schemes (such as Newmark algorithm), which are ideally suited for transient analysis (such as studying maneuver), but are not suitable for calculation of rotor trim in level flight. Time marching procedures require artificial damping to damp out the initial

condition response of lightly damped modes, such as the rotor lag mode, which would otherwise take several rotor revolutions to converge. This damping has to be progressively removed as the solutions approaches the correct periodic steady state response.

However, the expansion of scope of structural modeling using multibody formulation has not shown any significant improvement, so far, in the accuracy of blade loads prediction, resulting in the investigation of novel approaches of modeling the rotor blades. Ref. [49] discusses the ongoing development of a unified formulation for a 3-dimensional finite element based non-linear multibody analysis for helicopter rotors. In this approach, rotor blades are modeled using special multibody brick elements, which are developed with the capability to embed arbitrary joint rotations within a 3-dimensional structure. The goal of this work was to develop scalable Computational Structural Dynamics (CSD) solver for high fidelity rotorcraft analysis. The multibody brick formulation is used to study the impact of non-linear 3-dimensional hub end effects in rotors that are not modeled by current generation beam based models. This facilitates the capability to capture fundamental physics of 3-D stress fields on rotary wing structures which is not possible with beam based formulations.

1.5.2 Lifting-line Aerodynamic Model

The analytical modeling of rotor aerodynamics is quite involved due to the complicated nature of the aerodynamics environment encountered by a rotor. For

example, for a helicopter flying at its nominal cruise speed, at typical Mach numbers of operation, the flow near the blade is compressible while the flow in the wake of the rotor is incompressible as the rotor wake diffuses with the rapid reduction in velocity. During high speed flight conditions, the flow may be transonic or locally supersonic on the advancing blade side, where the relative velocity past the blade is in the direction of the relative free stream, thereby increasing the possibility of formation of shock waves near the tip of the blade. At the same time, the retreating blade side where the relative velocity past the blade is in the direction opposite to the relative free stream, the angle of attack can be greater than that on the advancing side to encounter lift imbalance, which may cause the blade to stall, making the viscous effects more important in this region. Due to the sudden drop in pressure at the blade tip, strong tip vortex may be shed from the blade tips, which due to the rotation of the blade may interact with following blades, resulting in the blade vortex interactions (BVI), which is a major source of noise for helicopters. Flow interactions between a number of individual components of the helicopter also occur, two important interactions are main rotor–fuselage interaction, and main-rotor–tail-rotor interactions. All of these aerodynamic mechanisms occur simultaneously with the evolution and convection of a complex three-dimensional and, in general, unsteady wake flow.

The aerodynamic modeling typically involves two main components: (1) blade solution, and (2) wake solution. The blade solution comprises of the airloads (pressure and skin friction) calculated based on the excitation from the blade deformations and air velocities. The wake solution in itself is composed of near wake and

far wake components. The classical lifting-line aerodynamic models are inviscid in nature and therefore, are incapable of calculating the wake directly as part of the response solution. Therefore, for this case wake has to be modeled seperately as a system of trailed and shed vortices. The trailed wake is generally partitioned as the near wake and far wake systems. The near wake accounts for the trailers immediately behind each blade and is coupled to the lifting-line or a lifting-surface blade model. The far wake accounts for the rolled up vortices from all the blades, and essentially calculates the non-uniform rotor inflow. The shed wake is modeled separately using the unsteady aerodynamic modeling.

1.5.2.1 Rotor Wake Modeling

The calculation of accurate airloads depends on the proper modeling of the inflow and the wake, which is true for all flight conditions, including hover. This statement by Prof. Gessow [50], made in 1986 Nikolsky lecture, highlights this fact: "Perhaps the key element in understanding and predicting helicopter characteristics is knowing the behavior of rotor inflow and wakes."

The earliest efforts attempting the rotor inflow calculation date from the 1940s and 1950s, these studies assumed a sweptback, rigid undistorted cylindrical wake for their inflow calculations for hover and low speed forward flight [51, 52]. Prescribed wake models were popular during the early 1960s as several researchers contributed towards their development [53–56], until Scully [57] and Crimi [58] came up with "distorted wake" or free wake models. Their models were based on experimental

observations, such as smoke visualization of the wake. The initial efforts were not very successful due to numerical stability issues associated with the time marching algorithm. Scully [59] overcame these issues with his relaxation free wake model by enforcing the periodicity for steady level flight conditions. These wake models were now "circulation-coupled", in that the shed and trailing vortex strengths used for inflow calculations included the radial and azimuthal variations in blade circulation and the wake structure was more realistic, as it showed distortions and tip vortex effects in the wake structure. Egolf and Landgrebe [60], and Beddoes [61] extended the prescribed wake models to forward flight.

Generally, the wake calculations methods are divided into two categories: (1) time marching, (2) relaxation methods. While, the time-marching methods are usually very accurate if the time step is small enough, the slowness of the numerically expensive wake calculations often used to limit the time steps to be as large as 15° to 30°. At such large time steps, time-marching methods are susceptible to numerical error. The alternative approach was to use an iterative procedure in which spatial periodicity is enforced as a boundary condition to "relax" the steady free wake solution, provided such a solution exists [62–65]. Most modern free wake analyses incorporate modeling of multiple rotors with a generalized set of trailers. Even though Landgrebe [55], Clark and Leiper [66], and Sadler [67] used time marching for studying the wake evolution in the late 1960s to early 1970s, the time marching free wake analysis started to gain popularity only in 1990s, with the advent of fast computers, which made time marching wake analysis practical.

Typically, the rotor wake is composed of high-strength tip vortices which roll

up downstream of each blade tip, an inboard vortex sheet and a weaker root vortex [68]. The vorticity in the inboard sheet and the tip vortex is confined to very thin regions which are surrounded by substantially irrotational fluid. Under the assumption that the region outside the vortex sheet and the tip vortex is potential (irrotational and incompressible), the vortex system in the rotor wake can be represented by the incompressible Biot-Savart law. This means that the wake evolutions is based on the velocity felt at each point on the tip-vortex and the vortex sheet. Once the velocity distribution is determined at each point, the wake is advanced forward in time using an initial-value problem solver. Typical methods used include first-order explicit Euler [69], Euler predictor-corrector, and a second-order time marching Adams-Bashforth [70] to name a few. It should be noted that the Biot-Savart law is only valid for incompressible flow, therefore rotor codes generally employ the Prandtl-Glauert compressibility correction to model compressible flow conditions. In these methods, the tip vortex is discretized as a series of line vortex filaments and is tracked using a Lagrangian technique, which implies that the time derivative of position equals velocity. These free wake methods accounted for self induced distortions of a rotor wake, such as roll up, in forward flight.

Bhagwat and Leishman [71, 72] contributed to the development of the comprehensive time accurate vortex wake methods. Ref. [71] exhibited second-order accuracy and grid independent nature for the wake geometry solution for hover and forward flight. Ref. [72] demonstrated that the relaxation wake was not adequate and time accurate wake was necessary for modeling maneuvers with significant angular rates. The wake study of maneuvers was later extended by Ananthan and

Leishman [73, 74].

1.5.2.2 Blade Unsteady Aerodynamics Modeling

Unlike fixed wing, the sectional angle of attack across the rotor blade does not remain constant during steady flight or maneuver as the blade pitch angle varies with azimuth. The application of cyclic introduces a rate of change in pitch angle leading to unsteadiness, in effect causing the blade to pitch and plunge as it goes through different azimuthal positions. This makes the modeling of unsteady aerodynamics very involved. It should be noted that the term "unsteady aerodynamics" doesn't necessarily implies "dynamic stall" and that the significant unsteady effects may be present even in the absence of dynamic stall.

Two-dimensional, unsteady aerodynamic theories describing unsteady airfoil behavior in fully attached flow typically forms the basis for rotor analysis. Most of the tools necessary for the analysis of incompressible as well as compressible unsteady aerodynamic problems were developed in 1950s [75]. Incompressible, unsteady airfoil problems have been formulated by various researchers in both the frequency domain and the time-domain, primarily by Wagner, Theodorsen, and Küssner. A good reference documenting the work of these researchers is the classic text by Bisplinghoff, Ashley and Halfman [76].

For a fully attached flow at low angles of attack, typically the contribution from the unsteady effects to the magnitude and phase of the net aerodynamic load is less significant. But as the unsteadiness increases with the increase in reduced frequency,

k, these contributions start to become more and more significant. The velocity at the blade element does not remain constant and therefore the definition of k remains ambiguous, rendering the frequency domain based calculations (Theodorsen) less useful. This makes the time domain calculations due to Wagner (gives a solution for the indicial lift on a thin-airfoil undergoing a step change in angle of attack) and Küssner (solution for a sharp change in vertical upwash velocity) become important for the rotorcraft aerodynamic modeling. But these models are valid for thin airfoils in incompressible flows and do not account for phenomenon like separation and dynamic stall, which is of great importance for the study of a rotor undergoing unsteady maneuver.

An airfoil undergoing dynamic motion can witness dynamic stall if its angle of attack goes beyond its static stall limit [77]. The most distinguishing feature of the dynamic stall phenomenon is the shedding of a concentrated vortical disturbance from the leading-edge region of the blade section, which gets swept over the chord. This phenomenon results in significant change in sectional airloads by increasing the lift at the cost of significantly large nose-down pitching moments, which finally impacts the blade loads significantly. Accurate modeling of this nonlinear phenomenon is only achievable by first principles through numerical solution of Navier-Stokes equations. But with the availability of large amount of experimental data for oscillating two-dimensional airfoils in wind tunnels, it became possible to model dynamic stall using semi-empirical procedures. A number of different approaches have been developed for modeling of dynamic stall for helicopters. While, these models are not strictly predictive tools, and can really only be used confidently

for conditions that are bounded by their validation with experimental or CFD data.

A number of dynamic stall methods can be found in the literature. UTRC α, A, B method is a pure re-synthesis (empirical) method which reconstructs the contributions to the dynamic stall airloads using large data tables generated for the airfoil [78,79]. In this approach, the lift and moment data are correlated as functions of angle of attack α, $A = \dot{\alpha}c/2V$ and $B = \ddot{\alpha}(c/2V)^2$, which assumes that the loads are independent of the past history of the airfoil motion. This approach was not widely accepted for its assumptions.

Boeing-Vertol dynamic stall method developed by Gross and Harris [80] and then later extended by Gormont [81] uses oscillating airfoil data to obtain an empirical expression for the dynamic stall angle

$$\alpha_{ds} = \alpha_{ss} + C_1\sqrt{\dot{\alpha}c/V} \tag{1.1}$$

where C_1 is a function of Mach number, determined from the oscillating airfoil data. The unsteady effects are first accounted for using Theodorsen's theory, the "corrected" angle of attack shown above is then used to obtain values of the airloads from the static force and moment curves. This has the effect of delaying the onset of stall to higher angles of attack with increasing pitch rate, a result observed experimentally. However, the predictions obtained for rotor blades were not very accurate near the stall regions.

Since the initial efforts, largely empirical in nature, at the development of the dynamic stall model were not very successful, Beddoes [82, 83] developed a time-domain dynamic stall model by focusing on the physics of the phenomenon. The

time domain based unsteady models are well suited for rotor applications. After accounting for the unsteadiness using the Wagner indicial response function, two time delays are used to separate the different dynamic stall flow states. The first delay represents the nondimensional time period in the onset of separation after the static stall angle has been exceeded, and the second time delay represents the time taken by the leading edge vortex to travel along the chord till it is shed in the wake. These time delays were obtained from a statistical analysis of many airfoil tests over a relatively wide range of Mach numbers. Gangwani [84] developed a similar model as Beddoes with the difference in the representation of forces and moments produced by the dynamic stall events. He used a set of equations with empirical coefficients which were derived from the steady and unsteady airfoil data.

Johnson [85] developed a dynamic stall model using the experimental data from Ham and Garelick [86]. The assumption that the dynamic stall occurs 3° above the static stall limit gave good correlation with the experimental data. It was assumed that the leading-edge vortex shedding produced a large increase in lift and moment with a short rise time. This large increase was considered proportional to the rate of change of angle of attack, $\dot{\alpha}$.

The ONERA model [87,88], later version known as ONERA Edlin (*Equations Differentielles Linearires*) model [89] described the unsteady airfoil behavior (delayed angle of attack, lift, drag, and moment increments) using a set of second-order differential equations. Like various other models, the coefficients in the equations are determined using the experimental data for oscillating airfoils. The later model known as ONERA BH (*Bifurcation de Hopf*) was developed by Truong [90].

Leishnam and Beddoes [91, 92] developed a dynamic stall model capable of predicting the 2D unsteady airfoil behavior for use in rotor analysis. The model, that was initially developed by Beddoes [93], consists of the following components: (1) an attached flow model for linear unsteady airloads, (2) a separated flow model for the nonlinear airloads, (3) a dynamic stall model for onset of stall and vortex induced inflow. It is valid for high subsonic Mach numbers (up to 0.8) and uses first-order differential equations for the delayed angle of attach and leading-edge vortex lift calculations. The nonlinear aerodynamic effects associated with flow separation on the airfoil are derived from Kirchhoff/Helmholtz theory, which is used to relate the airfoil lift to the angle of attack and an effective trailing-edge separation point. Most of these models did not account for the 3D effects and the effect of blade sweep on the dynamic stall model.

The 3-D effects encountered in rotor aerodynamic modeling can be incorporated using lifting-line, nonlinear lifting-line and lifting-surface models [94]. Dwyer and McCroskey [95] studied the effect of the spanwise development of the boundary layer on a rotating blade and reported its effect on delaying the onset of flow separation to a higher angle of attack. Effect of sweep on the oscillating wing was studied experimentally by St. Hillaire *et al.* [96, 97]. These studies identified blade sweep as a source for delay in the dynamic lift stall. The 3D effects of transonic flow on the advanced geometry rotor was subsequently studied by several researchers, both experimentally and analytically [98–101] and incorporated in the dynamic stall modeling [102].

1.5.3 CFD based Aerodynamics

The term computational fluid dynamics (CFD) generally refers to conservation law based solutions of the Navier-Stokes equations or some simplification of these equations (such as the Euler equations for inviscid flow) or the full potential equation for potential flow.

As discussed earlier, the main aspects of rotor airloads calculation involves the modeling of trailed and shed wake, which are modeled separately for conventional lifting-line analysis, but can be part of the same solution in fully viscous CFD analysis. However, CFD does provide the option of extraction of the wake from the airloads calculation for consistent comparison with lifting-line airloads calculations. Datta *et al.* [12] provides a detailed survey of the state-of-art of rotorcraft CFD research.

Early efforts to model rotorcraft aerodynamics using CFD involved inviscid, irrotational, single equation flow solvers which were incapable of predicting vortical flows. The objective was to improve the predictions of lifting-line models by capturing transonic shocks. Caradonna and Isom [103] first used potential flow equations to analyze steady rotor flows, first in hover and then in forward flight [104]. Several researchers contributed to the development of full potential rotor (FPR) formulations [105–112]. Some of these analyses were adaptations of fixed wing analysis to rotary wing problem, for example, Egolf and Sparks [110] extended the fixed wing code by Jameson and Caughey [113] and Shankar and Prichard [111] refined the analysis by Bridgeman *et al.* [114] for rotorcraft applications. Full potential meth-

ods, because of their grid-dependence, suffer from faster vorticity diffusion in the regions where the vorticity is nonzero. This affects blade loads and moments, leading to errors in the estimation of various design parameters such as payload capability. To remedy these deficiencies, Steinhoff and Ramachandran [115] used the idea of embedding the vortex structure into the flow and calculate the effect of the vorticity on the surrounding flow without having to calculate the vortical flow itself.

The late 1980s and early 1990s started to witness the development of Euler and Navier-Stokes formulations for rotorcraft applications. It started with the development of Euler solvers which could easily be modified to incorporate viscous terms as and when the computational resources started to become available. The vorticity gradients can be easily modeled by Euler solves resulting in accurate prediction of 3D unsteady shocks and wave drag. Some of the earliest efforts at modeling rotorcraft aerodynamics using CFD are due to Pulliam and Steger [116], Wake and Sankar [117], Srinivasan and McCroskey [118], Agarwal and Deese [119], and Wake and Baeder [120]. The Navier-Stokes methods have been under constant development and have had most significant impact on the rotor loads prediction.

CFD analysis coupled to a computational structural dynamics (CSD) model forms the basis of modern rotorcraft aeromechanics. This coupling can be achieved in two ways: (1) loose or weak coupling, in which the structural solver and CFD solver exchange information after every one or more rotor revolutions, (2) tight coupling or strong coupling where information exchange takes place at every rotor revolution and time accuracy can be enforced by using Newton like sub-iterations at each time step. Although a third approach of true aeroelastic coupling is pos-

sible, in theory, in which the combined fluid-structure problem may be formulated simultaneously and integrated simultaneously. While this approach has been used in the fixed wing community [121], rotorcraft researchers have chosen to stay with the partitioned approaches mentioned above, possibly due to the following reasons: (1) the frequencies of interest are expected to be adequately resolved using the domain partitioning approach, (2) the complexity of the aeroelastic rotor problem renders a full continuum dynamics solution impractical.

Johnson *et al.* [122] were first to propose the method of loose coupling (also know as *delta* method) for coupling the CFD and CSD (Computational Structural Dynamics) solvers. In this approach, initial loads and deformations are calculated using conventional lifting-line based comprehensive analysis, the calculated deformations are then used by CFD to obtain new estimate for airloads which are then applied as delta corrections over the lifting-line airloads. This approach continues to be the most efficient way of analyzing steady flight conditions and for obtaining trim angles. If the initial trim angles are known, the tight coupling method involves marching in time with the structural and fluid solvers exchanging information at each time step or each sub-iteration level. In tight coupling, it takes significantly longer to obtain a converged solution than loose coupling, up to 2.5 times as shown by Altmikus [123], due to the weakly damped lag mode, making the convergence to trim a challenge. The convergence can be accelerated by using artificial damping to damp out the initial transient response, which is then removed progressively. Prediction of control angles using tight coupling approach is computationally expensive and identification of efficient approaches is an active area of research. However,

if the control angle is known beforehand, tight coupling approach can be used by avoiding the problematic trim issue [124, 125]. Recent research using CFD/CSD coupled analysis has focused on the study of high loads and high vibration level flight conditions using the loose coupling methodology [126–130].

1.5.4 Flight Dynamics

For rotorcraft aeroelastic analysis, in addition to the structural and aerodynamic models, a procedure for estimation of the control angles is also required. In the steady flight, this is carried out by trimming the helicopter. The trimming is done to maintain the equilibrium condition, which is achieved by evaluating the rotor pitch control angles, tail rotor collective and shaft orientation angles to match a desired helicopter steady state. Johnson [131] provides a good discussion on various trim options.

But for unsteady maneuvers, a time history of control angles, tail rotor collective and shaft angle orientations are needed to achieve a specific trajectory. This process of calculation of pilot inputs required to achieve a particular trajectory or maneuver is referred to as inverse simulation. Thomson and Bradley [132] provided a good discussion of various inverse simulation procedures currently in use in the rotorcraft flight dynamics community.

Etkin [133] was possibly the first person to discuss simple inverse simulation methods applied to a problems such as prescribed roll response using simple linearized models. Wood *et al.* [134] used a simple energy based method to analyze

helicopter maneuver. Haverdings [135, 136] simulated a desired trajectory for a simplified mathematical model of a helicopter using a "pseudo pilot".

Towards late 1980s and early 1990s, more general and practical inverse flight simulation algorithms start to make their appearance, starting with Thomson and Bradley [137, 138] and then with Hess *et al.* [139, 140]. The method developed by Thomson and Bradley resembles a "trim" like calculation carried out at every time step. The approach used by Hess *et al.* involves numerical integration, in which, first the entire trajectory for the maneuver is divided into small steps. Then at each instance of time, an estimate of the change in the amplitude of control displacement required to move the aircraft to the next point is carried out. The error in the resulting position is then estimated and an iterative procedure using a Newton-Raphson is used to minimize the error by a series of control displacements. This approach is named "integration inverse method" as apposed to the approach described in Ref. [137], which is called "differentiation inverse method", as it involves a step requiring the differentiation of the trajectory. While the two show comparable accuracy [141], the integration method is an order of magnitude slower than the differentiation method, but has become the most widely adopted method, due to its flexibility and the fact that it is not model-specific.

Both the approaches are susceptible to numerical issues as discussed by Rutherford and Thomson [141], and Lin [142]. Some of these numerical instabilities disappeared when the Newton-Raphson step was replaced by a local optimization problem as demonstrated first by de Matteis *et al.* [143] and then by Celi [144]. A "two timescale" method of inverse simulation was proposed by Avanzini and de Mat-

teis [145], which takes advantage of the fact that the rotor dynamics is significantly faster than the translational dynamics of the helicopter allowing the use of a coarser time step for the vehicle dynamics equations. It is very important to note that with the exception of the Ref. [141, 144], all the methods discussed above excluded the rotor dynamics. Bottasso *et al.* [146] proposed a methodology by blending aeroelasticity, flight mechanics, trajectory optimization and optimal control to bridge the gap between helicopter dynamics and flight mechanics, which till then had mostly been pursued independently.

It should be noted that the dynamic stall phenomenon is the key mechanism responsible for the high loads during the unsteady maneuvers that size the rotor blades. Although adequate for studying handling qualities, none of the methods discussed above can be expected to work in this regime primarily due to the following two reasons: (1) inability of lower order aerodynamic models to predict dynamic stall, and (2) current flight dynamics algorithms are computationally expensive to be coupled with high-fidelity CFD analysis. Therefore, the high fidelity coupled flight dynamics simulation remains beyond the state-of-art, and coupled CFD/CSD simulation have to rely on the flight test data for the control angles.

1.6 Prediction of Rotor Loads - State of Art

The prediction of rotor airloads during maneuver is extremely challening due to the complex aerodynamic environment that the blade encounters during the maneuver. It is very important to survey the state of rotor loads prediction to fully

understand the lessons learnt so far and to identify the key challenges that lie ahead.

1.6.1 Level Flight

The study of level flight is critical for vibration sizing of the helicopter and serves as the stepping stone towards the ultimate goal of development of reliable loads prediction tools for maneuvers. This is because, conditions during level flights are often characterized by unique dominant aerodynamic mechanisms, which allows it to be studied in isolation and address the challenges associated with its accurate analysis.

Traditionally, the lifting-line based comprehensive rotorcraft analysis tools have been used to predict rotor loads in level flight and have been found to be plagued by two key discrepancies, identified by Bousman in 1999 [147]: (1) negative lift phase error in high speed flight, and (2) underprediction of blade pitching moments resulting in significant underprediction of control loads. It is now understood that the two problems are inter-connected. But, for a long time, it remained unsolved, with the negative lift peak observed consistently across different rotors and configurations [148, 149], including full scale and model rotors [150]. The similarity of airloads for model rotors effectively ruled out the possibility of fuselage effects. The effort by Torok and Goodman [151], and then Torok and Berezin [152] to isolate the physics of structural dynamics and aerodynamics, by using measured airloads to predict flap bending moment and then, use derived torsional deformations (using a modal approach) from measurements to accurately predict the negative lift phase.

It indicated that the problem was probably in the calculation of the torsional response, which is again related to the accuracy of predicted pitching moment. This is expected, as the lifting-line based analysis fails to predict the complex yet fundamental aerodynamic events occurring over the rotor disk such as the advancing blade transonic shock observed in the pitching moment, retreating blade stall, and the vortex wake evolution, roll-up, and interaction with the rotor blades [127, 147]. In addition, the predictions using lifting-line analysis become less accurate close to the blade tip due to the limited capability of lifting-line based analysis at modeling 3D effects. Due to the coupled nature of the problem, it is always difficult to conclusively identify the source of discrepancy, whether it is structural or aerodynamic, in the prediction. The solution lies in decoupling these two effects, as demonstrated by Datta *et al.* [126, 127]. In this work the problem of structural dynamics and aerodynamics is decoupled by using measured airloads to calculate an accurate deformation set, and then using this deformation set to calculate airloads. It was established that the two problems of advancing blade negative lift phase and pitching moment prediction are related to each other via the calculation of accurate structural response.

Recently, with the advances in computing power, researchers have been able to couple comprehensive CFD solvers with CSD to model steady flight conditions, without incurring serious computational penalties. Refs. [126, 128–130] analyzed the three critical steady flight conditions: (1) high speed, $\mu = 0.37$, with advancing blade negative lift, (2) low speed, $\mu = 0.15$, with blade–vortex interaction, and 3) high thrust with dynamic stall, $\mu = 0.24$ using "loose" aerodynamic/structural cou-

pling with Refs. [126, 128, 129] using UMARC in conjunction with TURNS, and in Ref. [130] using CAMRAD II and RCAS coupled with OVERFLOW-D. It was identified that the negative lift impulse can be captured accurately only in the presence of correct torsion response (1 and 2/rev), which is the primary mechanism of vibratory lift for the high speed flight. The 3D unsteady transonic pitching moments were accurately predicted by CFD, which excites correct torsion response from the blade, resolving the long standing negative lift phase discrepancy observed with lifting-line predictions. The CFD calculations for wake appeared to be adequate for vibratory airloads calculations and the analysis was able to capture the vortex inter-twinning phenomenon. However, the level of grid refinement necessary for resolving the tip vortex core structure and BVI loads still posed significant computational challenge. The dynamic stall cycles observed during the high altitude stall flight condition are known to be similar to the to the dynamic stall cycles observed in some of the severest maneuvers, as discussed earlier. The "loose coupled" CFD/CSD analysis was able to predict the retreating blade stall cycles encoutered at the high thrust flight with good accuracy. The accuracy of this prediction was observed to be dependent on rotor trim, elastic torsion, and turbulence model, in that order. The first dynamic stall event was determined by the correct trim angles, which then triggers the higher harmonics (4, 5/rev) of the torsion dynamics, which in turn results in the prediction of second stall due to the change in angle of attack in the fourth quadrant. Second stall prediction is also related to the turbulent re-attachment after the first stall, which is governed by the turbulence modeling with the CFD model and inflow. This establishes the multidisciplinary nature of the problem of rotor

loads prediction, with the flight dynamics, CSD and CFD all combining together in determining the accuracy of predicted blade loads.

A review of the state-of-the-art in main rotor loads in steady level flight – critical for vibratory loads – using Computational Fluid Dynamics (CFD)/Structural Dynamics (CSD) coupled analysis can be found in Ref. [12]. The work done using CFD / CSD analysis paved the way for taking up the challenge of maneuver loads prediction, where the aerodynamic mechanisms mentioned above, observed to occur in different flight regimes, occur simultaneously.

1.6.2 Maneuver

The existing tools available for the analysis of the steady-level flight could not be easily extended for the analysis of the maneuver, as the condition encountered during maneuvers introduce additional challenges that need to be addressed by the computational tools: (1) aperiodic rotor airloads and structural response, and (2) dependence of rotor response on vehicle dynamics. The rotor response in maneuvering flight conditions is aperiodic and often occurs over several rotor revolutions (> 10 revs). This requires a robust and accurate time-marching algorithm. While the computational tools have matured to the point where they can be reliably used to model the aperiodic maneuvering rotor response, determining the control settings necessary to fly a certain vehicle trajectory requires an inverse solution procedure, as well as the aerodynamic environment surrounding the helicopter fuselage, empennage, and the tail rotor surfaces, and is not attempted at this time. Analysis

of maneuvering flight, therefore, requires *a priori* knowledge of the instantaneous control pitch settings, the freestream velocities, vehicle attitudes, and the pitch, roll, and yaw rates and accelerations as a function of time. The comprehensive flight test database obtained from the US Army/NASA Airloads Program [153, 154] contains the aforementioned data for several maneuvers, which can now be prescribed in the simulation tools allowing the researchers to focus primarily on the rotor vibratory loads.

For a long time, maneuvers were only analyzed from the flight dynamics perspective using simplified aerodynamic and structural models, primarily due to the complexity and the challenges associated with such a study. Beno in 1973 [7] tried to predict air loads for a right turn flight using a normal mode based blade aeroelastic analysis. The primary focus of this study was on the flight testing. Schillings *et al.* [155] presented the measurement and prediction of maneuver performance and correlation of rotor maneuvering loads for the XV-15 tiltrotor. The blade predictions were compared only qualitatively against the flight test data and the focus of the study was on performance study.

Sopher and Duh [156] made a systematic attempt to predict the critical design loads for maneuvers for a SH-60B, Sea-Hawk. In addition, some steady flight cases for MH-60K and UH-60A were also analyzed. The motivation was to reduce the part played by empiricism in the design of the flight control systems. For this work, GENHEL flight dynamics simulation code was coupled to the RDYNE rotor dynamics code to study level flight as well as maneuvers (a 45° angle-of-bank turn and a symmetric pull-up maneuver) for prediction of pitch-link loads and servo

loads. RDYNE used elastic blades in conjunction with lifting-line analysis, which featured Beddoes and Leishman dynamic stall model, and a free wake analysis. The simulation for maneuver was started from the level flight trim condition, and the maneuver was simulated by prescribing the change in control angles predicted by GENHEL to RDYNE. During this, no attempt was made to correct RDYNE thrust prediction to match the calculated thrust from GENHEL. Predictions for pitch-link showed good correlation for the magnitude of some of the critical loads, but the inaccurate phase of the predictions indicated a deficiency in the modeling of the physics. Especially, the magnitude of aft stationary servo of MH-60K showed error in magnitude and phase.

A high fidelity simulation of the prescribed UTTAS pull-up was carried out by Bhagwat *et al.*, Refs. [157, 158], using a multibody finite element structural model (RCAS) coupled with a Reynolds Averaged Navier-Stokes model (OVERFLOW-2). This study used a coarse grid with 4.4 million grid points which was first used by Potsdam *et al.* [130] for the study of level flight conditions. Baldwin-Barth turbulenc model was used for the RANS closure. This work demonstrated RANS capability in predicting two rotor dynamic stall cycles for the first time for a maneuver, and showed that the oscillatory blade structural loads could be predicted with increased accuracy using isolated rotor calculations. Refs. [157, 158] also compared the predictions from CFD/CSD analysis to those obtained using standalone RCAS's lifting-line model, and observed that the lifting-line model failed to predict the dynamic stall events. Neither of the two analyses was able to resolve the mechanism of advancing blade stall. Reference [159] carried out a simpler lifting-line

analysis, as part of the present research work, also applied to an isolated rotor, with an attempt to calculate the rotor pitch control angles. However, it was unsuccessful due to large errors stemming from the unknown horizontal tail lift during the maneuver, and inability to predict the maneuver trajectories in absence of detailed aircraft data. Subsequently, with availability of flight test control angles, several researchers have predicted loads for this prescribed maneuver. Ref. [160] focused on lower fidelity lifting-line predictions using CAMRAD II comprehensive analysis code and observed that the analysis was not able to capture any of the negative pitching moment peaks, and the use of semi-empirical ONERA EDLIN dynamic stall model did not improve the correlation of pitching moment prediction when compared with the static airfoil table look-up based calculations. Ref. [161], as part of current research used lifting-line analysis for fundamental understanding of maneuver loads and reported significant improvements (up to 50%) in peak-to-peak pitching moment prediction with the use of Leishman Beddoes dynamic stall model. Refs. [162] compared the lifting-line model's capabilities used in Ref. [161] with CFD/CSD analysis. The predictions using lifting line analyses in general showed significant underprediction of peak maneuver loads when compared to the CFD/CSD analysis. Ref. [163] coupled DYMORE, a multibody CSD solver with UMTURNS CFD solver to study maneuver using wake-coupling approach. Later Sebastian *et al.* [164] used the same approach for analyzing maneuver by coupling UMARC2 with UMTURNS CFD solver. Pitching moment predictions using wake coupling approach in Refs. [163, 164] failed to resolve the transonic shock in the advancing blade pitching moment which is a common feature in all wake capturing solutions mentioned above.

Ref. [165] concentrated on isolating the differences between the time accurate and serial-staggered coupling approaches and performed simulations only for the first 15 revolutions of the maneuver.

1.7 Objective of Present Research

The objective of this research is the prediction, validation and fundamental understanding of blade loads and servo loads in an unsteady maneuver. The loads encountered during severe maneuvers size the critical components of a helicopter and their accurate prediction and the understanding of the loads mechanism is key to improved helicopter design. The goal is to: (1) isolate the effects of structural dynamics, free wake inflow, dynamic stall, swashplate dynamics and rotor pitch control angles, separately, on the prediction of maneuver loads, and (2) examine the prediction accuracy of airloads, blade loads, and swashplate servo loads using an unsteady lifting-line aerodynamic model, and (3) use CFD/CSD coupled analysis for accurate prediction of blade loads.

These goals are realized in a systematic step-by-step manner, which involves: (1) methodology development for consistent and accurate prediction capability, (2) validation of loads with test data for specific flight conditions, and (3) fundamental understanding. The details are discussed in the following section.

1.8 Technical Approach

The focus of the present research is on the fundamental understanding of the mechanisms of high blade loads observed during the pull-up maneuver. Therefore, a progressively incremental approach is taken, in which, the structural and aerodynamic models are refined systematically in steps and the improvement from each refinement is carefully noted and understood. This allows for the isolation and identification of loads mechanisms.

In the first step, the physics of structural dynamics and aerodynamics is decoupled using the flight test data. This is achieved by using the measured airloads from the flight test. The measured airloads, damper force and control angles from the flight test are used to simulate the measured airloads problem (also termed as the mechanical airloads problem), by applying the measured forced on the multibody structural dynamics model. This serves two purposes: (1) the accuracy of structural model can be studied by itself, and (2) the validated blade response can be used to predict airloads in isolation, first with lifting-line analysis and then with Reynolds Averaged Navier-Stokes (RANS) CFD model, thereby decoupling the structural dynamics and aerodynamics. The use of same deformations for calculations of airloads with the two aerodynamic models ensures their consistent comparison. This approach helps to identify and understand the mechanism of the multiple pitching moment stalls, which are the dominant feature of most severe maneuvers.

In the second step, comprehensive analysis is carried out using structural model coupled to the lifting-line aerodynamic model to isolate the effects of free wake

inflow, dynamic stall, swashplate dynamics and rotor pitch control angles, on the prediction of maneuver loads. It should be noted that the lifting-line analysis, although a low fidelity model, facilitates the separation of the effects of dynamic stall and wake. It provides direct airfoil angle of attack estimation, which is critical for better understanding of the airloads mechanism.

Finally, the RANS CFD model is coupled to the structural model for accurate prediction of stall loads during the maneuver, and the airloads predicted using the coupled CFD/CSD analysis is systematically compared to those obtained using coupled lifting-line/CSD analysis.

1.9 Contribution of Present Research

The contributions of this research can be broadly summarized in the following categories

1. Methodology development: This involved the development of multibody blade structural model, and swashplate dynamics model. These are essential for modeling large blade deformations and prediction of servo loads. A transient lifting-line aerodynamic model was also developed and finally CFD/CSD coupling framework was established resulting in accurate blade loads prediction.

2. Prediction, analysis and validation: Both steady (high speed and stall flights) and unsteady pull-up maneuver was analyzed and results obtained for airloads and structural loads were validated with the flight test data from UH-60A airloads program. The study using steady flight was necessary for identification

of swashplate and servo properties which were not available in the public domain.

3. Fundamental understanding of physics: The role played by large blade deformations, cyclic variation of control system stiffness and swashplate dynamics on rotor dynamics was studied and understood. The effects of wake and dynamic stall on maneuver loads was isolated. The mechanism of advancing blade stall was identified and understood.

Based on this work, the specific conclusions can be summarized as follows.

1. The pull-up maneuver appears almost entirely to be a stall dominated maneuver. The high structural loads observed during this maneuver are the outcome of multiple stall cycles observed across the rotor disk. The dynamic stall model, provides the most significant improvement to predicted rotor loads, and the free wake is less important. Almost up to 75% of a typical airfoil operating envelope (outboard of 67.5% R) during the 10-25 revolutions occur beyond the static stall boundary. Thus, the sectional airload properties are governed predominantly by stall phenomenon.

2. The two dynamic stall cycles observed on the retreating side of the blade, are known to be trim and elastic stalls. The third stall event observed on the advancing side of the blade, during the peak load factor regime of the UTTAS pull-up maneuver (revolutions $12 - 20$), is identified to be transonic twist stall of steady nature, resulting from a shock induced flow separation. It is excited by the 5/rev component of blade elastic twist which in turn

is triggered by two retreating stalls from the previous revolution, which are spaced by approximately $1/5th$ rotor revolution. In addition to 5/rev elastic twist, the magnitude and extent of the advancing blade stall is also dictated by the collective angle. For example, a 10% error in collective angle can result in under-prediction of first stall peak by up to 30%. Both elastic torsion and rotor collective, together, are key to accurate prediction of advancing blade stall. Either of the two factors alone may not be sufficient for accurate prediction of this phenomenon.

3. Use of CFD significantly improves the prediction of pitching moment characterized by the three distinct stall events as the rotor experiences load factors greater than $1.75g$ during the maneuver. The two dynamic stall events on the retreating side are predicted by the CFD/CSD analysis. The lifting-line analysis is unable to predict the high-frequency stall loads during the maneuver, especially the peak magnitude of pitching moment is under-predicted significantly.

4. The cyclic variation of control system stiffness, which is a result of the presence of the servos underneath, and swashplate dynamics does not have any significant influence on the blade dynamics and structural loads. However, swashplate dynamics is very important for the prediction of servo loads.

1.10 Organization of Thesis

Chapter 1 describes the need and requirements for analysis and prediction of rotor loads and vibration in a severe unsteady maneuver and its importance in the evolution of future rotor designs. It reviews the development of the helicopter aeromechanics and the state-of-art in the loads prediction, and discusses the objective of this research and highlights the key contributions.

Chapters 2 to 5 describe the steps taken for the attainment of the objectives set for this research. Chapters 2 describe the details of development and validation of the structural model using the flight test measured airloads. The aerodynamic models used in this study are described in detail int chapter 3. The deformations obtained during the validation of the structural model with the measured airloads analysis in chapter 2 is used in chapter 3 to validate and compare the predictions from aerodynamic models followed by the discussion on the mechanism of the advancing blade stall and the physics governing it. Chapter 4 details the use of lifting-line based comprehensive analysis for fundamental understanding by isolating the effects of dynamic stall, wake and swashplate dynamics. Chapter 5 describes the CFD/CSD tight coupling methodology for improved prediction of airloads and blade loads.

Chapter 6 summarizes the key conclusions of this research work and recommends the directions for future work.

Table 1.1: **UH-60A flight test most severe maneuvers and their rank orders [8]**

Maneuver	Counter	Pitch -link Load	Torsion Moment r/R = 0.30	Flap Bending r/R=0.113	Flap Bending r/R=0.6	Chord Bending r/R=0.113	Chord Bending r/R=0.6
RT Turn, 140 KIAS, 60°	11680	1	1	15	4	1	14
UTTAS Pull-up, 130 KIAS, 2.1g	11029	3	8	1	15	8	4
RT Turn, 140 KIAS, 55°	11679	2	2	23	7	23	15
Dive Roll Pull-out, 120 KIAS	11028	6	5	8	23	3	22
Pull-up, 120 KIAS, 2.25g	11023	10	7	2	26	4	25
LT Turn, 130 KIAS, 60°	11686	9	3	7	17	12	5
Descent, 186 KIAS	11682	24	24	28	1	21	2
LT Turn, 120 KIAS, 60°	11660	8	4	13	14	7	6
RT Turn, 130 KIAS, 60°	11672	13	6	10	18	5	8
UTTAS Pull-up, 130 KIAS, 1.8g	11031	4	14	5	13	11	9

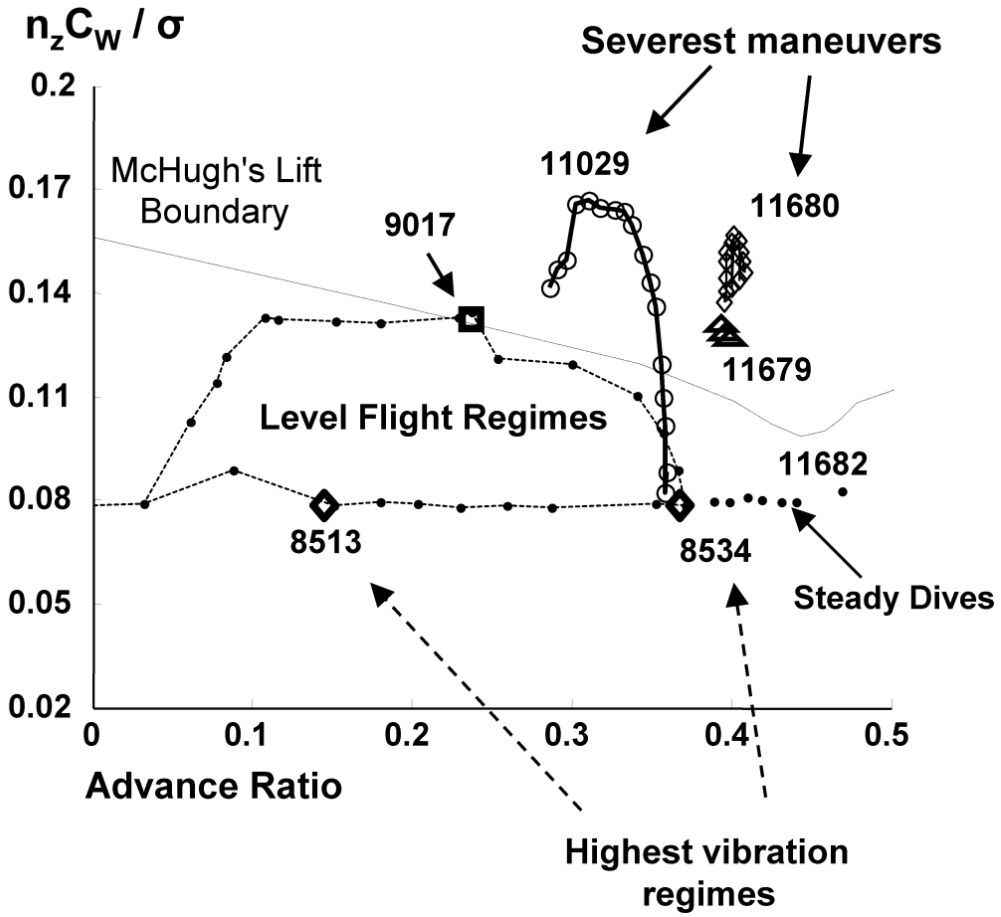

Figure 1.1: **UH-60A Airloads Program thrust speed envelope; comparison of rotor thrust and advance ratio for maneuvers and level flight conditions**

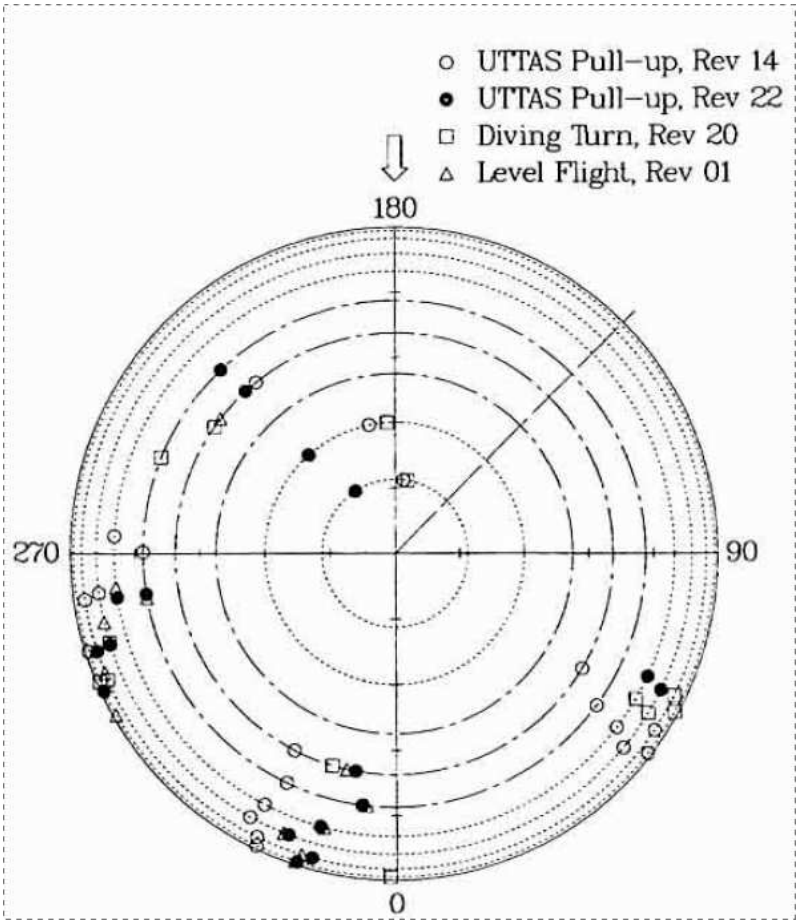

Figure 1.2: **Rotor map of dynamic stall locations for three flight conditions (C11029, C11679, C9017) [10]**

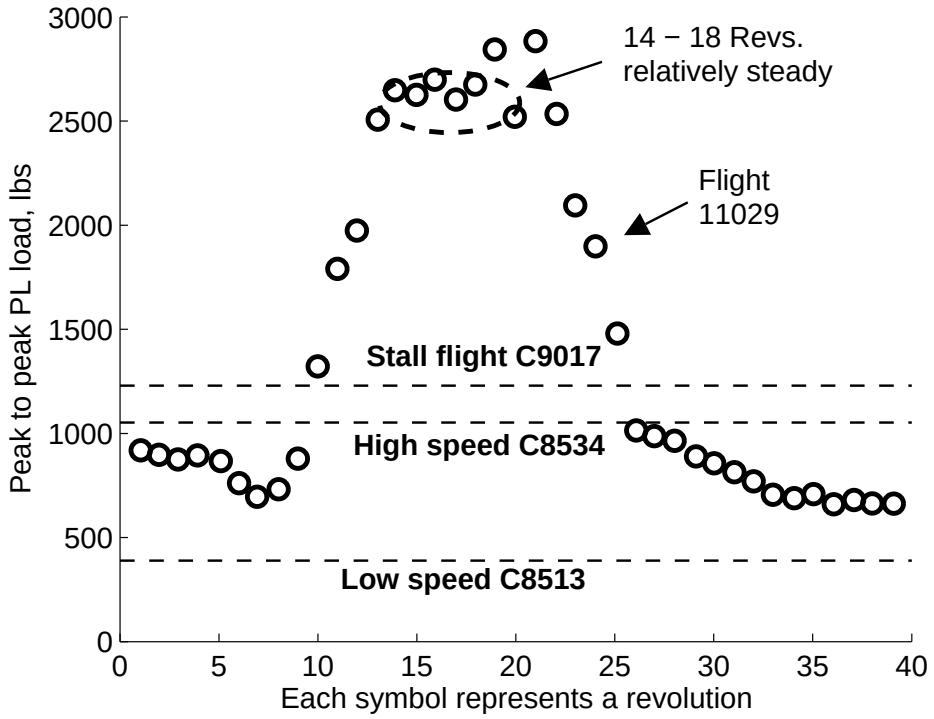

Figure 1.3: **Oscillatory pitch link loads encountered during a 2.12g UTTAS pull-up maneuver compared with level flights 8534 (high speed, high vibration), 8513 (low speed, high vibration), and 9017 (moderate speed, dynamic stall)**

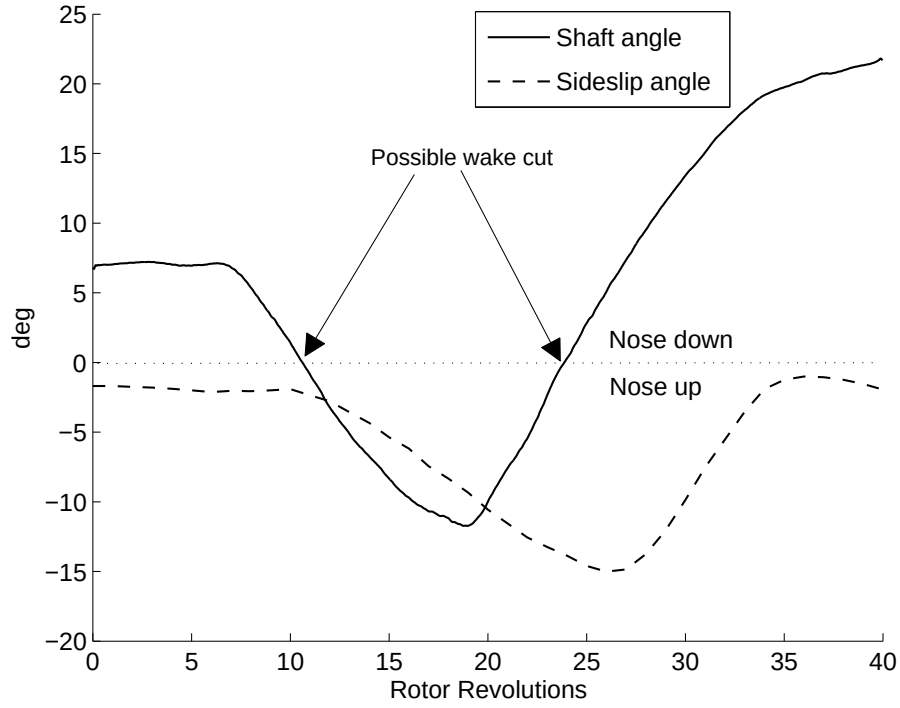

Figure 1.4: **Aircraft shaft angle with respect to oncoming flow and side-slip angle**

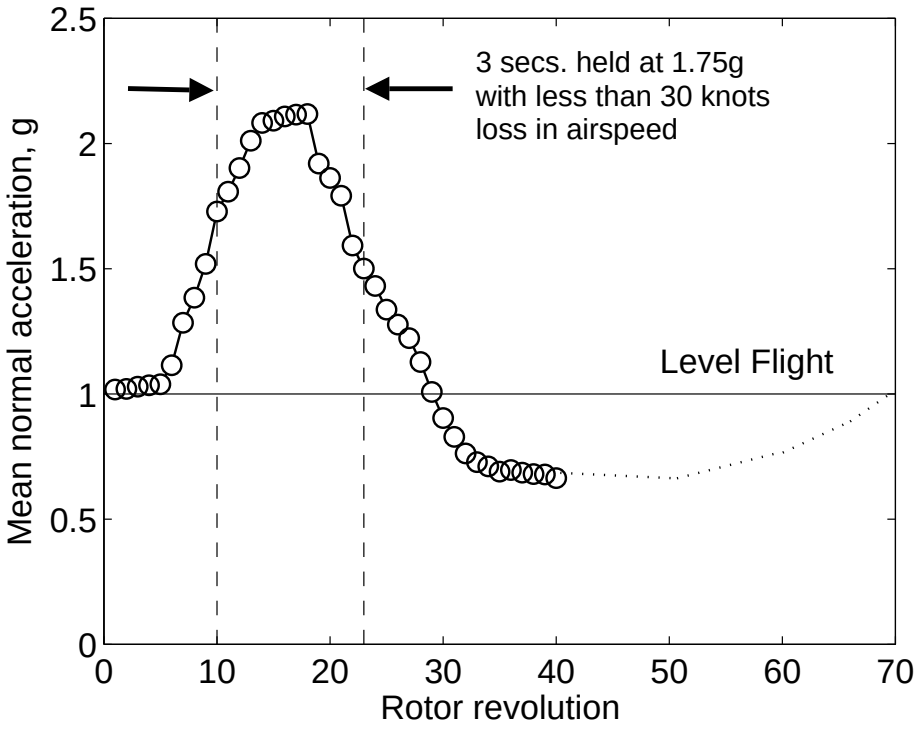

Figure 1.5: **Measured mean load factor**

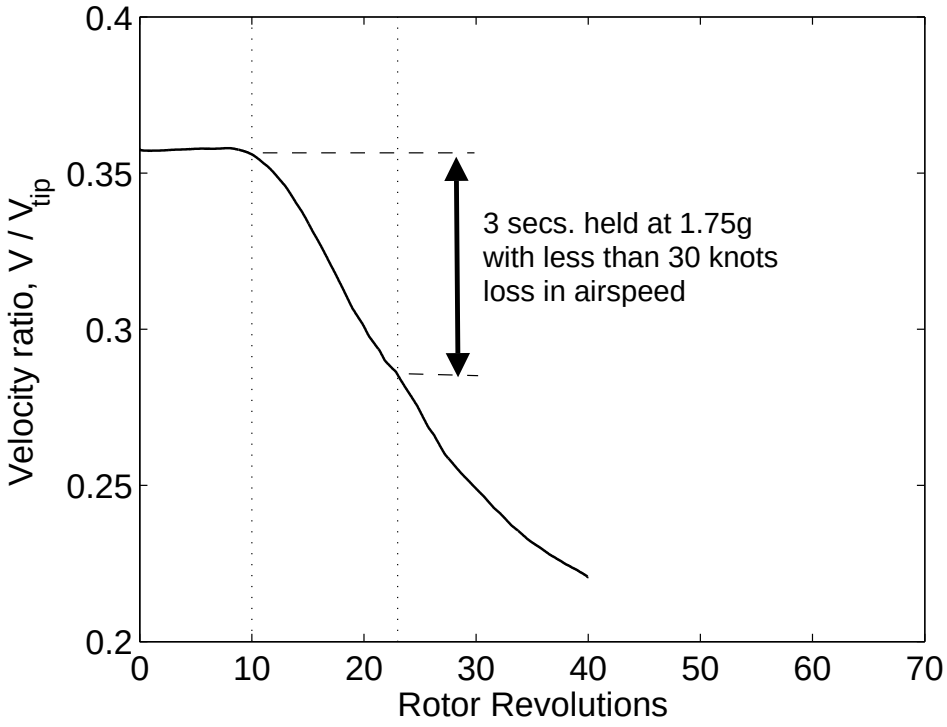

Figure 1.6: **Measured aircraft velocity ratio**

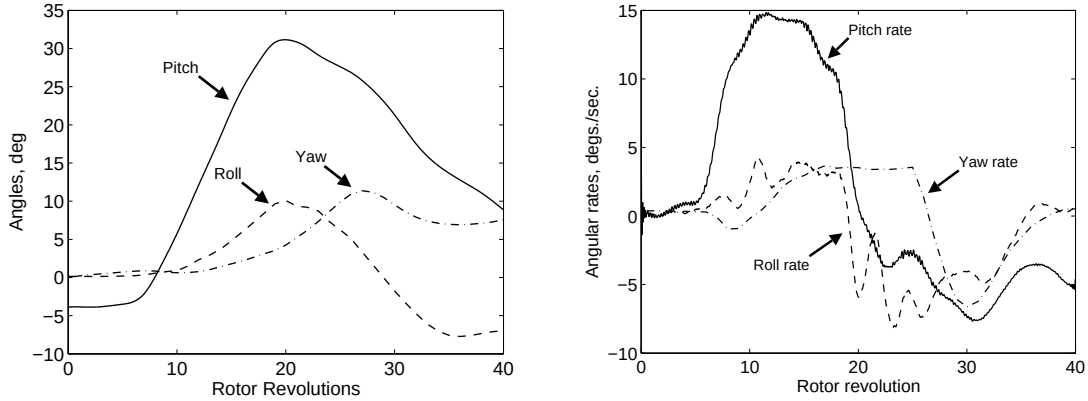

(a) Attitude

(b) Rate

Figure 1.7: **Measured aircraft attitude and rates**

Chapter 2

Structural Modeling

2.1 Introduction

The analysis of maneuver requires a structural model capable of modeling large blade deformations. This chapter describes and validates such a structural model for UH-60A rotor. A swashplate model is also developed, to fulfill two objectives: (1) prediction of servo-loads and (2) study of effect of periodic variation of control system stiffness and swashplate dynamics on blade loads. Once the structural model is developed, it is used to study level flight conditions to: (1) compare three progressively refined rotor blade structural dynamics formulations for the prediction of structural loads for a given set of aerodynamic forcing, (2) estimate swashplate-servo properties, which are not available in public domain, and, (3) study the effect of coupled rotor-swashplate dynamics on the prediction of servo loads and rotor blade structural loads. The goal is to isolate the physics of structural dynamics from the aeroelastic response problem to understand the mechanisms behind high structural loads encountered during unsteady maneuvers.

Arbitrary large deformations of a flexible beam can be modeled in two ways: (1) using a geometrically exact beam theory (Ref. [30, 31]), and (2) using a second order nonlinear beam theory (Ref. [32, 33, 167]) within a multibody formulation.

The latter uses additional frames attached locally to a set of individual beam finite elements, within which the elements undergo only moderate (second order) elastic deformations. Since the multibody formulation is chosen for the current work, the use of second order beam model is adequate for modeling large deformations and therefore, the second approach is chosen for this work. The second order non-linear beam model used is same as the one used in Reference [168]. The structural formulation developed for this study is first verified with analytical solutions for elastica, after that it is validated with non-linear experimental data for Princeton beam test. Next, UH-60A rotor structural model is validated for two level flight conditions: a high-speed level flight (counter 8534: 158 kts, $\mu = 0.368$, $C_W/\sigma = 0.0783$), and a high altitude dynamic stall flight (counter 9017: 101 kts, $\mu = 0.237$, $C_W/\sigma = 0.135$). The level flight data is used to compare three structural formulations using measured airloads analysis: (1) a second order nonlinear beam Finite Element Method (FEM) with modal reduction, (2) a second order nonlinear beam FEM without modal reduction, and (3) a second order nonlinear beam FEM within a multibody formulation. These are referred to as FEM with modal, full FEM, and the multibody method, which is used as the baseline structural model throughout this thesis. The goal of this study is to identify whether any improvements are provided by large deformation modeling, and the modeling of exact kinematics of the root end lag-damper and pitch link on the blade loads. Conceptually, the measured airloads problem (also termed as the mechanical airloads problem) allows one to assess the accuracy of the structural model separately from the airloads model. The technique was first applied by Sweers in 1968 for the XH-51A compound helicopter (Ref. [169]). Subse-

quently it was applied by Esculier and Bousman (Ref. [170]) on the CH-34 rotor and by Torok and Goodman on the model UH-60A rotor (Ref. [171]). In practice, the measured airloads problem can pose significant difficulties. The natural frequencies of the blades often lie close to the forcing harmonics and because the imposed airloads do not change with the calculated response there is zero aerodynamic damping in the system. Thus, even though uncontaminated with errors associated with predicted airloads, the measured airloads solution can be extremely sensitive to small differences in modeling, input parameters, and unavoidable errors in measured airloads and their interpolation, factors which are either non-existent or insignificant for fully coupled solutions.

The second part of this chapter describes a swashplate model, and studies the effect of swashplate dynamics on servo loads and blade loads. The multibody model is coupled to the swashplate model in this part of the study. In all cases, measured airloads, damper forces, and control angles from the US Army/NASA UH-60A flight test program (Refs. [**?**, 172]) are used for the validation of the analyses. Finally, the rotor model is used to analyze the UTTAS pull-up maneuver using the measured flight test data. Once the structural model has been validated, the resulting blade deformations provide with an accurate set of inputs to test aerodynamic models, because, the flight test measurement of blade deformations is not available. The blade deformations obtained using measured airloads analysis, termed as *prescribed or calculated blade deformation*, serve as basis for consistently comparing airloads predicted using different aerodynamic models with flight test and provide an opportunity to separate the physics of aerodynamics from the aeroelastic response

problem. This forms the basis for Chapter 3, where results for lifting-line analysis are compared to those obtained using a CFD model using prescribed blade deformations.

2.2 Multibody Formulation with Full FEM

The rotor blades and supporting structures are first divided into several bodies, rigid and flexible. Each flexible body is discretized into several finite elements. The rotor is modeled as a second order nonlinear Euler-Bernoulli beam with axial elongation and elastic twist modeled as quasi coordinates (Refs. [19–21]). The current formulation incorporates additional frames of reference at the individual beam element level. Arbitrary large deformations of the beam can be accommodated by the finite motion of the frames attached to individual elements while the elastic deformations within each element remain moderate. The rigid body motion of the frames involves large rotations and translations in space. The rotor pitch control angles are imposed as linear displacements at the bottom of the pitch links and are adjusted iteratively to generate the measured root pitch angles. The measured damper force is imposed in a direction based on the exact kinematics of the damper as determined by its configuration and the instantaneous location of blade attachment point. The equations of motion are formulated using Kane's method.

2.2.1 Blade Coordinate Systems

There are five important coordinate systems, as shown in Fig. 2.1, required for formulating the blade equations, the hub-fixed system, (X_H,Y_H,Z_H) with unit vectors $\hat{I}_H,\hat{J}_H,\hat{K}_H$, the hub-rotating system, (X,Y,Z) with unit vectors $\hat{I},\hat{J},\hat{K}$, the undeformed blade coordinate system, (x,y,z) with unit vectors $\hat{i},\hat{j},\hat{k}$, unit vectors, the element coordinate system (x_E,y_E,z_E) denoted by unit vectors $\hat{i}_E,\hat{j}_E,\hat{k}_E$, and the deformed element coordinate system, (ξ,η,ς) represented with unit vectors $\hat{i}_\xi,\hat{j}_\eta,\hat{k}_\varsigma$. These reference frames would be referred to as H, R, U, E, and D respectively. The transformation between hub-fixed and hub-rotating system is defined as

$$\begin{Bmatrix} \hat{I} \\ \hat{J} \\ \hat{K} \end{Bmatrix} = T_{RH} \begin{Bmatrix} \hat{I}_H \\ \hat{J}_H \\ \hat{K}_H \end{Bmatrix} = \begin{bmatrix} \cos\psi & \sin\psi & 0 \\ -\sin\psi & \cos\psi & 0 \\ 0 & 0 & 1 \end{bmatrix} \begin{Bmatrix} \hat{I}_H \\ \hat{J}_H \\ \hat{K}_H \end{Bmatrix} \tag{2.1}$$

where ψ is the azimuth angle which is equal to Ωt. The transformation from the rotating frame to blade undeformed coordinate which is at an angle β_p is expressed by

$$\begin{Bmatrix} \hat{i} \\ \hat{j} \\ \hat{k} \end{Bmatrix} = T_{UR} \begin{Bmatrix} \hat{I} \\ \hat{J} \\ \hat{K} \end{Bmatrix} = \begin{bmatrix} \cos\beta_p & 0 & \sin\beta_p \\ 0 & 0 & 1 \\ -\sin\beta_p & 0 & \cos\beta_p \end{bmatrix} \begin{Bmatrix} \hat{I} \\ \hat{J} \\ \hat{K} \end{Bmatrix} \tag{2.2}$$

The transformations from the blade undeformed frame to element local frame and the element frame to the deformed blade reference frame would be discussed later in the text.

2.2.2 Element Frame Motion

The motion of the beam element frame E is specified relative to the blade undeformed frame, U. The origin of the element frame is located at the first node of the beam element, and is rigidly attached to the element, the position of which is denoted by the vector $\vec{r}^E$ which is defined in the element undeformed frame

$$\vec{r}^E = \begin{Bmatrix} r_x & r_y & r_z \end{Bmatrix}^T \begin{Bmatrix} i_E \\ j_E \\ k_E \end{Bmatrix} \tag{2.3}$$

Similarly, velocity and acceleration of the origin of E are defined by the vectors $\vec{v}^E$, and $\vec{a}^E$. The orientation of the frame E can be specified in terms of transformation matrix, which is discussed later in text. If $\vec{\omega}^E$ represents the angular velocity of E with respect to the inertial frame, then the expressions for velocity and acceleration can be specified in terms of position and angular velocity as

$$\vec{v}^E = \dot{\vec{r}}^E + \vec{\omega}^E \times \vec{r}^E \tag{2.4}$$

$$\vec{a}^E = \ddot{\vec{r}}^E + \dot{\vec{\omega}}^E \times \vec{r}^E + \vec{\omega}^E \times \dot{\vec{r}}^E + \vec{\omega}^E \times (\vec{\omega}^E \times \vec{r}^E) \tag{2.5}$$

where $\dot{\vec{\omega}}^E$ is the angular acceleration, and $\dot{()}$ is time derivative relative to the local frame.

2.2.3 Deformed Blade Geometry

The location of an arbitrary point, P, on the beam is defined in the element reference frame (x_E,y_E,z_E) attached to the root of the element. The element reference frame remains rigidly attached to the element and translates and rotates

as the beam deforms remaining normal to and along the principle axes at the element root. In the undeformed state element reference frame remains parallel to the blade's undeformed frame except for the elements that are swept which are at and angle defined by the angle of sweep. In the deformed state, orientation of the element frame E is defined relative to the undeformed frame U using a series of three successive rotations which are determined by the deformed position of the tip of the previous element. Let the deformed position of the point P on the blade be denoted by P' (Figure to be attached). A frame attached to point P and deforming with it to reach the deformed position P' defines the deformed coordinate system (ξ,η,ς) which is the orientation of the principal axis of the cross section at that location. The deformation of a point P is defined relative to the element reference frame and has to be transformed to the blade reference frame to obtain the net deformation for the blade. Deformation of the point P in the frame E combined with the translational motion of the origin of E (x_E,y_E,z_E) and its orientation and any out of plane warping accurately determines the deformed location P' in the inertial frame. The rotor blades are slender structures and hence can be idealized as beams. Here cross sectional out of plane warping and shear are neglected, such that the cross section remains rigid and perpendicular to the elastic axis after deformation. This implies that two of the angles are functions of the derivatives of the deflection variables, while the third angle, the angle of elastic twist – remains the only rotational variable. This approximation is exact up to moderate deformations.

Modified Euler angles are used to denote rotations needed to align the element reference frame (x_E,y_E,z_E) with the deformed frame (ξ,η,ς). The successive rotations

used are ξ_1 about z_E resulting in an intermediate system (x_{E1},y_{E1},z_{E1}), β_1 about $-y_{E1}$ resulting in (x_{E2},y_{E2},z_{E2}) and finally θ_1 about x_{E2} respectively. The resulting transformation matrix is given by

$$\begin{Bmatrix} \hat{i}_\xi \\ \hat{j}_\eta \\ \hat{k}_\varsigma \end{Bmatrix} = T_{DE} \begin{Bmatrix} \hat{i}_E \\ \hat{j}_E \\ \hat{k}_E \end{Bmatrix} \tag{2.6}$$

where $T_{DE} =$

$$\begin{bmatrix} \cos\beta_1 \cos\xi_1 & \cos\beta_1 \sin\xi_1 & \sin\beta_1 \\ -\cos\xi_1 \sin\beta_1 \sin\theta_1 - \cos\theta_1 \sin\xi_1 & \cos\xi_1 \cos\theta_1 - \sin\xi_1 \sin\beta_1 \sin\theta_1 & \cos\beta_1 \sin\theta_1 \\ -\cos\xi_1 \sin\beta_1 \cos\theta_1 + \sin\theta_1 \sin\xi_1 & -\cos\xi_1 \sin\theta_1 - \sin\xi_1 \sin\beta_1 \cos\theta_1 & \cos\beta_1 \cos\theta_1 \end{bmatrix} \tag{2.7}$$

The T_{DE} matrix is same as the classical T_{DU} matrix [19], with the difference that the deformations are now relative to the element reference frame.

The position of any generic point on the deformed-blade elastic axis relative to the origin of the element reference frame measured along the element frame is given as

$$\vec{\mathbf{r}}_E = (x+u)\hat{i}_E + v\hat{j}_E + w\hat{k}_E \tag{2.8}$$

where, x is the radial distance measured from the root of the element frame along axis x_E. The derivative of $\vec{\mathbf{r}}$ with respect to the curvilinear distance coordinate of the deformed beam reference line is a unit vector tangent to the deformed beam reference line at that location, thus

$$\frac{\partial \vec{\mathbf{r}}_E}{\partial r} = (x+u)^+\hat{i}_E + v^+\hat{j}_E + w^+\hat{k}_E \tag{2.9}$$

$$\frac{\partial \vec{\mathbf{r}}_E}{\partial r} = \hat{i}_\xi = T_{11}\hat{i}_E + T_{12}\hat{j}_E + T_{13}\hat{k}_E \tag{2.10}$$

where $()^+ = \partial/\partial()$ and T_{ij} is the element on the i^{th} row and j^{th} column of T_{DE}. The elastic axial elongation, u_e is subtracted from total elongation to calculate the unit vector tangent to the elastic axis.

$$\hat{i}_\xi = (x + u - u_e)^+ \hat{i}_E + v^+ \hat{j}_E + w^+ \hat{k}_E \tag{2.11}$$

By comparing Eqs. 2.10 and 2.11 we get

$$\left.\begin{aligned} T_{11} &= (x + u - u_e)^+ \\ T_{12} &= v^+ \\ T_{13} &= w^+ \end{aligned}\right\} \tag{2.12}$$

Invoking the condition for orthonormality of the T_{DE} we get

$$T_{11}^2 + T_{12}^2 + T_{13}^2 = 1 \tag{2.13}$$

which gives

$$(x + u - u_e)^+ = \sqrt{1 - v^{+2} - w^{+2}} \tag{2.14}$$

Using the two expressions for T_{DE} from equations 2.7 and 2.12

$$\left.\begin{aligned} \sin\beta_1 &= w^+ \\ \cos\beta_1 &= \sqrt{1 - w^{+2}} \\ \sin\xi_1 &= \frac{v^+}{\sqrt{1 - w^{+2}}} \\ \cos\xi_1 &= \frac{\sqrt{1 - v^{+2} - w^{+2}}}{\sqrt{1 - w^{+2}}} \end{aligned}\right\} \tag{2.15}$$

Using the expressions above in Eq. 2.7 results in

$$T_{DE} = \begin{bmatrix} \sqrt{1 - v^{+2} - w^{+2}} & v^+ & w^+ \\ \frac{-v^+\cos\theta_1 - w^+\sin\theta_1\sqrt{1-v^{+2}-w^{+2}}}{\sqrt{1-w^{+2}}} & \frac{-v^+w^+\sin\theta_1 + \cos\theta_1\sqrt{1-v^{+2}-w^{+2}}}{\sqrt{1-w^{+2}}} & \sin\theta_1\sqrt{1-w^{+2}} \\ \frac{v^+\sin\theta_1 - w^+\cos\theta_1\sqrt{1-v^{+2}-w^{+2}}}{\sqrt{1-w^{+2}}} & \frac{-v^+w^+\cos\theta_1 - \sin\theta_1\sqrt{1-v^{+2}-w^{+2}}}{\sqrt{1-w^{+2}}} & \cos\theta_1\sqrt{1-w^{+2}} \end{bmatrix} \tag{2.16}$$

where

$$\theta_1 = \theta_t + \hat{\phi} \tag{2.17}$$

with

$$\left.\begin{aligned} \theta_t =& \theta_0 + \theta_{1c}\cos\psi + \theta_{1s}\sin\psi + \theta_{tw} \\ \hat{\phi} =& \phi - \int_0^{r_l} \frac{w^+}{\sqrt{1-v^{+2}-w^{+2}}}\left(v^{++} + \frac{v^+ w^+ w^{++}}{1-w^{+2}}\right) \end{aligned}\right\} \tag{2.18}$$

where, r_l is the distance measured from the root of the element to the point P. Making the second order assumptions and applying the ordering scheme described in Ref. [19] we get

$$T_{DE} = \begin{bmatrix} 1-\frac{v'^2}{2}-\frac{w'^2}{2} & v' & w' \\ -v'\cos\theta_1 - w'\sin\theta_1 & (1-\frac{v'^2}{2})\cos\theta_1 - v'w - \sin\theta_1 & \sin\theta_1(1-\frac{w'^2}{2}) \\ v'\sin\theta_1 - w'\cos\theta_1 & -(1-\frac{v'^2}{2})\sin\theta_1 - v'w - \cos\theta_1 & \cos\theta_1(1-\frac{w'^2}{2}) \end{bmatrix} \tag{2.19}$$

Also,

$$\hat{\phi} = \phi - \int_0^{r_l} w'v''dr \tag{2.20}$$

2.2.4 Formulation Using Kane's Method

Kane's method is used for deriving the equations of motion (Ref. [173]), which states that

$$\{f^*\} + \{f\} = 0 \tag{2.21}$$

where $\{f^*\}$ denotes the generalized inertia forces and $\{f\}$ denotes all other generalized forces including the generalized external forces $\{f_e\}$, the generalized structural forces $\{f_s\}$ and the generalized damping forces $\{f_d\}$

$$\{f^*\} + \{f_e\} + \{f_s\} + \{f_d\} = 0 \tag{2.22}$$

The derivation of the various components of the Eq. 2.22 is described in the following subsections.

2.2.5 Derivation of Inertial Forces

Using Eq. 2.8, the position of the point P' on the deformed beam cross section with respect to the undeformed blade reference can be defined as

$$\vec{\mathbf{r}} = \vec{\mathbf{r}}_{EO} + (x+u)\hat{i}_E + v\hat{j}_E + w\hat{k}_E + \xi\hat{i}_\xi + \eta\hat{i}_\eta + \varsigma\hat{i}_\varsigma \tag{2.23}$$

where $\vec{\mathbf{r}}_{EO}$ is the position of element reference frame origin with respect to the blade reference frame. The equation above can be written in the basis U

$$\mathbf{r} = \mathbf{r}_{EO} + T_{UE}\begin{Bmatrix} x+u \\ v \\ w \end{Bmatrix} + T_{UE}T_{ED}\begin{Bmatrix} -\lambda\phi' \\ \eta \\ \varsigma \end{Bmatrix} \tag{2.24}$$

The deformations u, v, w are the displacements of the beam elastic axis due to elastic deformations in the element frame, and η and ς are the cross-sectional position coordinates. The deformations at any location can be defined using the shape function and the nodal degrees of freedom of the beam in the blade undeformed reference frame as

$$\begin{aligned} \mathbf{r} =& \mathbf{r}_{EO} + T_{UE}(\mathbf{r} + H\mathbf{q}) + T_{UE}T_{ED}\mathbf{r}_{gc} \\ =& \mathbf{r}_{EO} + T_{UE}\mathbf{u} \end{aligned} \tag{2.25}$$

where $\mathbf{r} = [x,\ 0,\ 0]^T$, $\mathbf{r}_{gc} = [-\lambda\phi',\ \eta,\ \varsigma]^T$ and $\mathbf{q}$ is the vector of generalized elastic coordinates and $[H]$ is the shape function used to discretize the blade deformations.

As per the definition above $\mathbf{u} = \mathbf{r} + H\mathbf{q} + T_{ED}\mathbf{r}_{gc}$. The velocity for the point defined above in the basis of blade reference frame is given by

$$\mathbf{v} = \dot{\vec{\mathbf{r}}}_{EO} + T_{UE}\tilde{\omega}\{\bar{\mathbf{u}}\} + T_{UE}\dot{\mathbf{u}} \tag{2.26}$$

where, $\bar{\omega}$ is the angular velocity defined in the local coordinate system. Further, we have

$$\vec{\omega} \times \vec{\mathbf{u}} = \tilde{\omega}\mathbf{u} = -\tilde{\mathbf{u}}\omega \tag{2.27}$$

where $\tilde{\mathbf{u}}$ is the skew symmetric matrix defined as

$$\tilde{\mathbf{u}} = \begin{bmatrix} 0 & -u_3 & u_2 \\ u_3 & 0 & -u_1 \\ -u_2 & u_1 & 0 \end{bmatrix} \tag{2.28}$$

with u_1, u_2, and u_3 are components of vector $\mathbf{u}$. The angular velocity vector ω can be written in terms of the derivatives of the reference rotational coordinates of body as

$$\omega = \mathbf{G}\dot{\boldsymbol{\theta}} \tag{2.29}$$

allowing us to rewrite Eq. 2.27 as

$$\omega\mathbf{u} = -\tilde{\mathbf{u}}\mathbf{G}\dot{\boldsymbol{\theta}} \tag{2.30}$$

where, $\mathbf{G}$ can be specified analytically for Euler angles (ϕ_E, θ_E, and ψ_E) as

$$\mathbf{G} = \begin{bmatrix} 0 & \cos\phi_E & \sin\theta_E \sin\phi_E \\ 0 & \sin\phi_E & -\sin\theta_E \cos\phi_E \\ 1 & 0 & \cos\theta_E \end{bmatrix} \tag{2.31}$$

Further,

$$\dot{\mathbf{u}} = H\dot{q} + \dot{T}_{ED}\mathbf{r}_{gc} + T_{ED}\dot{\mathbf{r}}_{gc} \tag{2.32}$$

Using, Eqs. 2.30, and 2.32 in Eq. 2.26 and the fact that $\{\dot{r}_{gc}\}$ is equal to zero (because sectional deformation is neglected), we get

$$\mathbf{v} = \mathbf{v}_{EO} - T_{UE}\tilde{\mathbf{u}}\mathbf{G}\dot{\boldsymbol{\theta}} + T_{UE}H\dot{\mathbf{q}} + T_{UE}\dot{T}_{ED}\mathbf{r}_{gc} \tag{2.33}$$

The equation above can be rewritten as

$$\mathbf{v} = \begin{bmatrix} I & -T_{UE}\tilde{\mathbf{u}}\mathbf{G} & T_{UE}H \end{bmatrix} \begin{bmatrix} \dot{\mathbf{r}}_{EO} \\ \dot{\boldsymbol{\theta}} \\ \dot{\mathbf{q}} \end{bmatrix} + T_{UE}\dot{T}_{ED}\mathbf{r}_{gc} \tag{2.34}$$

where $\begin{bmatrix} \mathbf{v}_{EO} & \boldsymbol{\theta} & \mathbf{q} \end{bmatrix}^T$ is the set of generalized coordinates to be denoted by $\mathbf{p}$. The acceleration of the point defined in the basis of blade reference can be expressed by

$$\mathbf{a} = \dot{\mathbf{v}} = \mathbf{a}_{EO} + 2T_{UE}\tilde{\omega}\dot{\mathbf{u}} + T_{UE}\dot{\tilde{\omega}}\mathbf{u} + T_{UE}\tilde{\omega}\tilde{\omega}\mathbf{u} + T_{UE}\ddot{\mathbf{u}} \tag{2.35}$$

The substitution of expressions for $\mathbf{u}$ and it's derivatives yields

$$\begin{aligned} \mathbf{a} =& \ddot{\mathbf{r}}_{EO} + 2T_{UE}\tilde{\omega}(H\dot{\mathbf{q}} + \dot{T}_{ED}\mathbf{r}_{gc}) - T_{UE}\tilde{\mathbf{u}}\dot{\tilde{\omega}} \\ & + T_{UE}\tilde{\omega}\tilde{\omega}(\mathbf{r} + H\mathbf{q} + T_{ED}\mathbf{r}_{gc}) + T_{UE}(H\ddot{\mathbf{q}} + \ddot{T}_{ED}\mathbf{r}_{gc}) \end{aligned} \tag{2.36}$$

which can be written in the form similar to Eq. 2.34 as shown below

$$\begin{aligned} \mathbf{a} =& \begin{bmatrix} I & -T_{UE}\tilde{\mathbf{u}}\mathbf{G} & T_{UE}H \end{bmatrix} \begin{bmatrix} \ddot{\mathbf{r}}_{EO} \\ \ddot{\boldsymbol{\theta}} \\ \ddot{\mathbf{q}} \end{bmatrix} + \begin{bmatrix} 0 & -T_{UE}\tilde{\omega}\tilde{\mathbf{u}}\mathbf{G} & 2T_{UE}\tilde{\omega}H \end{bmatrix} \begin{bmatrix} \dot{\mathbf{r}}_{EO} \\ \dot{\boldsymbol{\theta}} \\ \dot{\mathbf{q}} \end{bmatrix} \\ & + (2T_{UE}\tilde{\omega}\dot{T}_{ED} + T_{UE}\ddot{T}_{ED})\mathbf{r}_{gc} - T_{UE}\tilde{\mathbf{u}}\dot{\mathbf{G}} \end{aligned} \tag{2.37}$$

According to Kane's method the generalized inertial forces for a system is given by

$$\{f^*\} = -\sum \int m\{\mathbf{a}\}\frac{\partial\{\mathbf{v}\}}{\partial \dot{p}_i} dl \tag{2.38}$$

where, m is the mass per unit length and $\dot{p}_i$ is the time derivative of the i^{th} generalized coordinate. The expressions for $\{\mathbf{a}\}$ and $\partial\{\mathbf{v}\}/\partial\dot{p}_i$ can be substituted in the Eq. 2.38 to obtain net inertial forces from which mass matrix can be extracted

$$\begin{aligned}
\{f^*\} = -\int_0^l m(& \begin{bmatrix} I & T_{UE}\tilde{\mathbf{u}}^T\mathbf{G} & T_{UE}H \\ \mathbf{G}^T\tilde{\mathbf{u}}T_{UE}^T & -\mathbf{G}^T\tilde{\mathbf{u}}\tilde{\mathbf{u}}\mathbf{G} & \mathbf{G}^T\tilde{\mathbf{u}}H \\ H^TT_{UE}^T & H^T\tilde{\mathbf{u}}\mathbf{G} & H^TH \end{bmatrix} \begin{Bmatrix} \ddot{\mathbf{r}}_{EO} \\ \ddot{\theta} \\ \ddot{\mathbf{q}}_f \end{Bmatrix} \\
& + \begin{bmatrix} 0 & -T_{UE}\tilde{\omega}\tilde{\mathbf{u}}^T\mathbf{G} & 2T_{UE}\tilde{\omega}H \\ 0 & -\mathbf{G}^T\tilde{\mathbf{u}}\tilde{\omega}\tilde{\mathbf{u}}\mathbf{G} & 2\mathbf{G}^T\tilde{\mathbf{u}}\tilde{\omega}H \\ 0 & -H^T\tilde{\omega}\tilde{\mathbf{u}}\mathbf{G} & 2H^T\tilde{\omega}H \end{bmatrix} \begin{Bmatrix} \dot{\mathbf{r}}_{EO} \\ \dot{\theta} \\ \dot{\mathbf{q}}_f \end{Bmatrix} \\
& + (\mathbf{I} + \mathbf{G}^T\tilde{\mathbf{u}}T_{UE}^T + H^TT_{UE}^T)\{(2T_{UE}\tilde{\omega}\dot{T}_{ED} + T_{UE}\ddot{T}_{ED})\mathbf{r}_{gc} \\
& - T_{UE}\tilde{\mathbf{u}}\dot{\mathbf{G}}\})dl
\end{aligned} \tag{2.39}$$

The first term in the equation above represents the symmetric mass matrix. It can be noted that the mass matrix is highly non-linear.

$$M = -\int_0^l m \begin{bmatrix} I & T_{UE}\tilde{\mathbf{u}}^T\mathbf{G} & T_{UE}H \\ \mathbf{G}^T\tilde{\mathbf{u}}T_{UE}^T & -\mathbf{G}^T\tilde{\mathbf{u}}\tilde{\mathbf{u}}\mathbf{G} & \mathbf{G}^T\tilde{\mathbf{u}}H \\ H^TT_{UE}^T & H^T\tilde{\mathbf{u}}\mathbf{G} & H^TH \end{bmatrix} dl \tag{2.40}$$

2.2.6 Derivation of Generalized Elastic Forces

The generalized elastic forces are obtained by differentiating the strain energy with respect to the generalized coordinates. The rotor blades being modeled have

very large aspect ratio allowing them to be treated as slender beams, allowing for the application of uniaxial stress assumption, i.e. $\sigma_{yy} = \sigma_{yz} = \sigma_{zz} = 0$. For isotropic beam operating within elastic limits, the stress-strain relation can be expressed as

$$\sigma_{xx} = E\epsilon_{xx} \tag{2.41}$$

$$\sigma_{x\eta} = G\epsilon_{x\eta} \tag{2.42}$$

$$\sigma_{x\varsigma} = G\epsilon_{x\varsigma} \tag{2.43}$$

where ϵ_{xx} is axial strain, and $\epsilon_{x\eta}$ and $\epsilon_{x\varsigma}$ are the engineering shear strains defined by the strain-displacement relations given below

$$\epsilon_{xx} = \frac{1}{2}\left(2\frac{\partial r_x}{\partial x} + \left(\frac{\partial r_x}{\partial x}\right)^2 + \left(\frac{\partial r_y}{\partial x}\right)^2 + \left(\frac{\partial r_z}{\partial x}\right)^2\right) \tag{2.44}$$

$$\epsilon_{x\eta} = \frac{1}{2}\left(\frac{\partial r_x}{\partial \eta} + \frac{\partial r_y}{\partial \eta} + \frac{\partial r_x}{\partial x}\frac{\partial r_x}{\partial \eta} + \frac{\partial r_y}{\partial x}\frac{\partial r_y}{\partial \eta} + \frac{\partial r_z}{\partial x}\frac{\partial r_z}{\partial \eta}\right) \tag{2.45}$$

$$\epsilon_{x\varsigma} = \frac{1}{2}\left(\frac{\partial r_x}{\partial \varsigma} + \frac{\partial r_y}{\partial \varsigma} + \frac{\partial r_x}{\partial x}\frac{\partial r_x}{\partial \varsigma} + \frac{\partial r_y}{\partial x}\frac{\partial r_y}{\partial \varsigma} + \frac{\partial r_z}{\partial x}\frac{\partial r_z}{\partial \varsigma}\right) \tag{2.46}$$

After making the assumptions for moderately large deflections, the non-linear strain displacement relations for a pre-twisted beam, accurate up to second order, are given by (from Ref. [19])

$$\left.\begin{aligned} \epsilon_{xx} = & u' + \frac{v'^2}{2} + \frac{w'^2}{2} - \lambda_T\phi'' + (\eta^2 + \varsigma^2)\left(\theta'\phi' + \frac{\phi'^2}{2}\right) \\ & -v''[\eta\cos(\theta+\phi) - \varsigma\sin(\theta+\phi)] \\ & -w''[\eta\sin(\theta+\phi) + \varsigma\cos(\theta+\phi)] \\ \epsilon_{x\eta} = & -\left(\varsigma + \tfrac{\partial\lambda_T}{\partial\eta}\right)\phi' = -\hat{\varsigma}\phi' \\ \epsilon_{x\varsigma} = & -\left(\eta - \tfrac{\partial\lambda_T}{\partial\varsigma}\right)\phi' = -\hat{\eta}\phi' \end{aligned}\right\} \tag{2.47}$$

where λ_T is the cross-sectional warping function. Using the expressions for ϕ and u from Eqs. 2.14 and 2.18 respectively in Eq. 2.47 above results in

$$\left.\begin{aligned}
\epsilon_{xx} =& u_e' - \lambda_T(\hat{\phi}'' + w'v''' + v''w'') \\
&+(\eta^2+\varsigma^2)(\theta'\hat{\phi}' + \theta'w'v'' + \frac{\hat{\phi}'^2}{2} + \frac{w'^2v''^2}{2} + \hat{\phi}'w'v'') \\
&-v''[\eta\cos(\theta+\phi) - \varsigma\sin(\theta+\phi)] \\
&-w''[\eta\sin(\theta+\phi) + \varsigma\cos(\theta+\phi)] \\
&\epsilon_{x\eta} = -\hat{\varsigma}(\hat{\phi}' + w'v'') \\
&\epsilon_{x\varsigma} = -\hat{\eta}(\hat{\phi}' + w'v'')
\end{aligned}\right\} \tag{2.48}$$

The expression for the strain energy of the beam element is given by

$$U = \frac{1}{2}\int_0^R \left[\int\int_A (E\epsilon_{xx}^2 + G\epsilon_{x\eta}^2 + G\epsilon_{x\varsigma}^2)d\eta d\varsigma\right]dx \tag{2.49}$$

The elastic deflections u_e, v, w, and ϕ are defined by using interpolating polynomial shape functions as shown below

$$\left.\begin{aligned}
u(s) &= \sum_{i=1}^{4} H_{u_i}(s)u_i \\
v(s) &= \sum_{i=1}^{2}(H_i(s)v_i + H_{i+2}(s)v_i') \\
w(s) &= \sum_{i=1}^{2}(H_i(s)w_i + H_{i+2}(s)w_i') \\
\hat{\phi}(s) &= \sum_{i=1}^{3} H_{\phi_i}(s)\hat{\phi}_i
\end{aligned}\right\} \tag{2.50}$$

where $s = \frac{x}{l}$ is the non-dimensional length with l being length of the element and the shape functions are give by

$$\left.\begin{aligned} H_{u_1} &= -4.5s^3 + 9s^2 - 5.5s + 1 \\ H_{u_2} &= 13.5s^3 - 22.5s^2 + 9s \\ H_{u_3} &= -13.5s^3 + 18s^2 - 4.5s \\ H_{u_4} &= 4.5s^3 - 4.5s^2 + s \end{aligned}\right\} \tag{2.51}$$

$$\left.\begin{aligned} H_1 &= 2s^3 - 3s^2 + 1 \\ H_2 &= l(s^3 - 2s^2 + s) \\ H_3 &= -2s^3 + 3s^2 \\ H_4 &= l(s^3 - s^2) \end{aligned}\right\} \tag{2.52}$$

$$\left.\begin{aligned} H_{\phi_1} &= 2s^3 - 3s + 1 \\ H_{\phi_2} &= -4s^2 + 4s) \\ H_{\phi_3} &= 2s^2 - s \end{aligned}\right\} \tag{2.53}$$

The generalized structural forces for the generalized coordinates $\begin{bmatrix} \mathbf{r}_{EO} & \boldsymbol{\theta} & \mathbf{q} \end{bmatrix}$ can be evaluated by differentiating the strain energy U given by Eq. 2.49 with respect to the generalized coordinates

$$\frac{\partial U}{\partial p_i} = \int_0^R \left[\int\int_A \left(E\epsilon_{xx}\frac{\partial \epsilon_{xx}}{\partial p_i} + G\epsilon_{x\eta}\frac{\partial \epsilon_{x\eta}}{\partial p_i} + G\epsilon_{x\varsigma}\frac{\partial \epsilon_{x\varsigma}}{\partial p_i} \right) d\eta d\varsigma \right] dx \tag{2.54}$$

to obtain the stiffness matrices. The generalized structural force vector can then be given by

$$f_s = \begin{bmatrix} 0 & 0 & 0 & 0 & 0 & 0 & \frac{\partial U}{\partial q_i} \cdots \end{bmatrix}^T \tag{2.55}$$

which can be written in a matrix form in terms of the generalized coordinates as

$$f_s = \begin{bmatrix} 0 & 0 & 0 \\ 0 & 0 & 0 \\ 0 & 0 & \mathbf{K} \end{bmatrix} \begin{Bmatrix} \bar{\mathbf{r}}_{EO} \\ \theta \\ \mathbf{q} \end{Bmatrix} \tag{2.56}$$

It should be noted that all the derivatives of U with respect to the rigid body translation and rotation would be zero, as the rigid body motions do not result in any strain. The procedure to derive an expression for $\mathbf{K}$ in equation above is discussed in Ref. [168]. Finally the equations of motion can be obtained using Eq. 2.22 by substituting the expressions for different components.

2.2.7 Numerical Solution Procedure

The equation of motion is setup for a fixed topology to begin with, by explicitly constraining the system at the problem definition stage. This obviates the need for handling algebraic constraints separately, thereby sacrificing topology independence for simplicity, as there are no algebraic constraint equations with associated Lagrange multipliers. Thus, the resulting formulation can be treated using linearized system analysis tools. Only the displacement constraints are used (holonomic constraints) and as they have been found to be adequate for modeling rotorcraft configurations.

The governing ordinary differential equation obtained using the approach above is of the form

$$\mathbf{M}\ddot{\mathbf{x}} + \mathbf{C}\dot{\mathbf{x}} + \mathbf{K}\mathbf{x} = F(t, \mathbf{x}, \dot{\mathbf{x}}, \ddot{\mathbf{x}}) \tag{2.57}$$

and is solved by marching in time using Newmark family of method with Hilber-Hughes-Taylor (HHT) correction (Ref. [174]). The advantage of Newmark family of methods is that it requires the storage of information for only one time step and can be second order accurate with appropriate selection of parameters. In the Newmark method (Ref. [175]), an integration formula that depends on two parameters β and γ is defined

$$x_{n+1} = x_n + \Delta t \dot{x}_n + \frac{\Delta t^2}{2}[(1-2\beta)\ddot{x}_n + 2\beta \ddot{x}_{n+1}] \tag{2.58}$$

$$\dot{x}_{n+1} = \dot{x}_n + \Delta t[(1-\gamma)\ddot{x}_n + \gamma \ddot{x}_{n+1}] \tag{2.59}$$

where, Δt is the time step size and the x_i, $\dot{x}_i$ and $\ddot{x}_i$ represents the generalized coordinates, velocity and acceleration respectively at the i^{th} time step. The Newmark's method in itself is implicit and unconditionally stable for $\gamma \geq \frac{1}{2}$ and $\beta \geq \frac{(\gamma+0.5)^2}{4}$. The only combination of β and γ that leads to second-order accuracy is $\gamma = \frac{1}{2}$ and $\beta = \frac{1}{4}$. This choice of parameters produces the trapezoidal method, which is unconditionally-stable and second order, but it does not include any numerical damping in the solution, which is necessary to dissipate non physical high-frequency oscillations exhibited at very small time steps ($\leq 1^\circ$ azimuth). The HHT method is used as an integrator in this analysis as it is unconditionally stable and offers desirable level of numerical damping.

The HHT method makes use of the same expressions for the integration formula described above, but uses a modified discretized equation of motion as shown below

$$\mathbf{M}\ddot{\mathbf{x}}_{n+1} + (1+\alpha)\mathbf{C}\dot{\mathbf{x}}_{n+1} - \alpha\mathbf{C}\dot{\mathbf{x}}_n + (1+\alpha)\mathbf{K}\mathbf{x}_{n+1} - \alpha\mathbf{K}\mathbf{x}_n = \mathbf{F}(\tilde{t}_{n+1}, \mathbf{x}_n, \dot{\mathbf{x}}_n, \ddot{\mathbf{x}}_n) \tag{2.60}$$

where

$$\tilde{t}_{n+1} = t_n + (1+\alpha)\Delta t \tag{2.61}$$

Substituting the expressions for $\mathbf{x}_{n+1}$ and $\dot{\mathbf{x}}_{n+1}$ from Eqs. 5.3 and 5.4 in Eq. 2.60 results in the following

$$\begin{aligned}\left[\mathbf{M} + (1+\alpha)\gamma\Delta t\mathbf{C} + (1+\alpha)\beta\Delta t^2\mathbf{K}\right]\ddot{\mathbf{x}}_{n+1} &= (1+\alpha)\mathbf{F}(\tilde{t}_{n+1}) - \alpha\mathbf{F}(t_n) + \alpha\mathbf{K}\mathbf{x}_n \\ -(1+\alpha)\mathbf{C}\left[\dot{\mathbf{x}}_n + \Delta t(1-\gamma)\ddot{\mathbf{x}}_n\right] - (1+\alpha)\mathbf{K}&\left[h\dot{\mathbf{x}_n} + \frac{\Delta t^2}{2}(1-2\beta)\ddot{\mathbf{x}_n}\right] + \alpha\mathbf{C}\dot{\mathbf{x}}_n\end{aligned} \tag{2.62}$$

which is a set of linear equations of the form

$$\mathbf{A}\ddot{\mathbf{x}}_{n+1} = \mathbf{B} \tag{2.63}$$

to be solved at every time step. Only the states at the current time step are needed for evaluating the elements of $[A]$ and $[B]$. Once $\ddot{\mathbf{x}}_{n+1}$ is calculated, $\mathbf{x}_{n+1}$ and $\dot{\mathbf{x}}_{n+1}$ can be calculated using Newmark formulas. The solution procedure is started by assuming zero initial deformation (i.e. $\mathbf{x}_1 = \dot{\mathbf{x}}_1 = \ddot{\mathbf{x}}_1 = 0$).

HHT method is second order accurate and has the desired stability for $-\frac{1}{3} \leq \alpha \leq 0$ and

$$\gamma = \frac{1-2\alpha}{2} \qquad\qquad \beta = \frac{(1-\alpha)^2}{4} \tag{2.64}$$

The smaller the value of α, the more damping it introduces in the numerical solution. A value of $\alpha = -\frac{1}{3}$ was used throughout the analysis.

2.3 Verification and Validation

The analysis methodology is first validated against analytical and experimental large deformation data. Two static elasticity problems are considered: (1) the problem of a cantilever elastica with tip moment and tip forcing, and (2) the Princeton beam static test problem involving deflection of a cantilever beam data.

2.3.1 Elastica with tip moment and tip force

The shape of the elastic deflection curve of a cantilever beam undergoing large deflection is called elastica. Assuming that the material of the beam remains linearly elastic, the exact governing differential equation is given by:

$$\kappa = \frac{d\theta}{ds} = -\frac{M}{EI} \tag{2.65}$$

where κ is the curvature of the beam at a given section, θ is the angle of rotation of the deflection curve, M is the sectional bending moment, E is the modulus of elasticity, and I is the area moment of inertia of the beam section (Fig. 2.2). For a beam undergoing large deflections, the differential equation governing the curve takes the following form:

$$\frac{\frac{d^2w}{dx^2}}{\left[1 + \left(\frac{dw}{dx}\right)^2\right]^{\frac{3}{2}}} = -\frac{M}{EI} \tag{2.66}$$

where w is the transverse deflection of a point on the beam. The exact analytical solution of the elastica with tip moment has been described in Ref. [176].

A multibody model of a uniform cantilever beam of length L of 20 ft is developed using 20 elements. The bending stiffness, EI is taken to be 9000 lb-ft^2 and a moment of 2500 ft-lb is imposed on the beam tip. The resultant radius of curvature, ρ $(= 1/\kappa)$ is then 3.6 ft. Figure 2.3(a) verifies the predicted solution with the analytical solution. For a tip force, the analytical solution takes the form of a transcendental equation involving elliptic integrals, which can be evaluated using numerical integration. The solutions are tabulated in Ref. [176], and are used in Figs. 2.3(b)–(d) to verify the current calculations. The tip force is applied such that $PL^2/EI = 5.0$. The vertical tip deflection δ_w, the axial foreshortening δ_u, and angle of rotation θ_b are verified in Figs. 2.3(b)–(d).

2.3.2 Princeton beam test

The Princeton beam test, carried out by Dowell and Traybar (Refs. [177,178]), provides bending and torsional deformation data for an aluminum cantilever beam with rectangular cross-section. The beam was rotated to various pitch angles introducing strong flap-lag-torsion coupling (Fig. 2.4). A multibody model is constructed to simulate the Princeton beam test setup. The geometric and sectional properties used for the simulation were obtained from reference [177] and are listed in Table 2.1. Static deformation data from reference [178] is used to validate the predicted results. Figure 2.5 compares the predicted flap bending (w/L), lag bending (v/L), and torsion deflections with measured data for a range of tip loading. The deflection in the softer bending direction called flap showed very good correlation with the test data

for all loading conditions and for all root pitch angle settings. Predicted torsion deflection is also predicted satisfactorily. However, the same is not observed in the stiffer bending direction, and the results are less accurate for the higher loading conditions (3 and 4 lb cases). This is possibly due to ideal treatment of the support fixture at the root end of the beam. The beam was held using specially fabricated fixtures, which were inserted into a milling machine type precision indexing-chuck, which under higher loading conditions might not be providing ideal cantilever conditions (Ref. [179]).

2.3.3 Classical Formulation with Full FEM and FEM with Modal Reduction

The classical FEM formulation typically uses a single body coordinate frame and all deformations and loads are calculated in that particular frame, which are then transformed to an inertial frame. Within a single body coordinate frame, the second order (almost-exact) beam model is accurate up to moderate bending deflections of 15% (Ref. [32]). The model described above has been used to model the rotor blade as a fully articulated beam with flap and lag hinges coincident at 4.66% span, and is referred to as Classical formulation with Full FEM. Sweep is incorporated as a center of gravity offset from the straight undeformed elastic axis. The multibody formulation with full FEM can be reduced to classical FEM formulation in several steps. First, the additional frames attached at the element level are removed and all the element to element and element to body transformation matrices are replaced

by identity matrices. All the deformations and forces are now evaluated in a single global reference frame located at the blade hub. Second, the pitch link spring-damper element undergoing exact kinematics is replaced by an equivalent torsional spring-damper system at the pitch link attachment point, based on the undeformed geometry. The control angles are now imposed directly. Finally, the lag damper force is imposed as a set of concentrated forces and moments based on the undeformed geometry of the damper attachment. To reduce the classical full FEM formulation further, an eigen analysis is performed on the linearized stiffness and mass matrices. The first ten linearized modes are then chosen to transform the governing equations into the modal coordinate system. This is referred to as FEM with modal reduction.

2.3.4 UH-60A Rotor Model for Structural Loads

A multibody model of an isolated UH-60A rotor blade is shown in Fig. 2.6. The measured airloads, damper force and root pitch angles from the two UH-60A flight test data points are then used to calculate the structural response. Results obtained using the classical formulations are compared with those obtained using the multibody approach.

The multibody model consists of the flexible blade and rigid root end damper and control linkages. The blade is modeled as a fully articulated beam with flap and lag hinges coincident at 4.66% span using 20 nonlinear beam elements, with each element having an individual frame of reference attached to it. The blade property data are obtained from the NASA (Ames) master database. The swept portion of

the blade has been modeled using 3 elements with swept elastic axis. The pitch horn and the hub is modeled using rigid bodies, and the pitch link is modeled as a linear spring-damper element. The pitch link stiffness is obtained from the measured equivalent root torsion spring stiffness of 1090 ft-lbs/deg (Ref. [180]), evaluated using the undeformed pitch-horn length. The control angles are imposed via translational displacements at the base of the pitch link, which are then iteratively adjusted to provide the measured root pitch angles. The measured damper force is applied as a follower force. The direction of the damper force is determined by a vector, one end of which is attached to the location where the damper is physically connected to the hub and the other end is attached to the blade at 7.6% of span. The elastomeric bearing stiffness and damping are modeled as linear springs and dampers.

Table 2.1: **Beam geometric and sectional properties used for the analysis of Princeton beam test**

Length, R	20 in
Width, b	0.5 in
Height, h	0.125 in
Density, ρ	0.1014 lb/in^3
Poisson's ratio, ν	0.31
Shear Modulus, G	4.0383×10^6 lb/in^2
Young's Modulus, E	10.576×10^6 lb/in^2
Polar Moment of Inertia, J	0.2807 bh^3

Table 2.2: **UH-60A rotor blade operating frequencies; collective angle 14.5 degrees; effective root spring stiffness 1090 ft-lbs/degree**

	Frequencies /rev
First Chord	0.27
First Flap	1.04
Second Flap	2.87
First Torsion	4.38
Second Chord/Third Flap	4.76
Third Flap/Second Chord	5.22
Fourth Flap	7.81
Fifth Flap	11.44
Third Chord	12.52
Second Torsion	12.93

2.3.5 Validation of UH-60 Structural Response and Loads

The multibody formulation is now used to predict the UH-60A structural response and loads at the two flight conditions. The first ten natural frequencies of the rotor blade at the operating rotational speed are given in Table 2.2.

2.3.5.1 High Speed Flight (8534: $C_W/\sigma = 0.0783$, $\mu = 0.368$)

Figure 2.7(a) shows the oscillatory flap angle at the blade root. A damping value of 4% critical in flap is required for good agreement in magnitude and phase.

Without this damping, the 1/rev magnitude is over-predicted by 20% (Fig. 2.7(b)) and the 1/rev phase shows an error of 40°. Note that the effect of damping is primarily on 1/rev rigid motion, the structural loads due to bending remain unaffected. Under the trim condition, the 1/rev aerodynamic flap hinge moment is a small number generated by large but 180° out of phase inboard and outboard lift forces. Unavoidable errors in airloads measurements and the issues related to spanwise and chordwise resolution of data throws this balance off and results in error in the magnitude of 1/rev response, as the flap frequency is close to 1/rev. More detailed studies on this issues can be found in Refs. [181] and [182]. The root lag angle (Fig. 2.7(c)) is affected by the 4% structural damping in flap due to the coupling between flap and lag via the built-in twist angle (9.31°) near the root. Figure 2.7(d) shows the root pitch angle. It is determined by the flight test control inputs and the pitch link flexibility.

The predicted flap bending moments are shown in Fig. 2.8. The peak-to-peak magnitude of the moments are satisfactorily predicted. The peak moment on the retreating side at the root station (11.3%R) is caused by the lag damper force. The flap moment at the root station is affected by the damper force via the built-in twist angle (9.31°) near the root. The moments at all other stations are mostly dependent on the airloads. Figure 2.9 shows the dominant vibratory harmonics (3-5/rev), both magnitude and phase, varying over span. These harmonics are the primary source of 4/rev vibration in the fuselage. The radial trends are similar, although the magnitudes are over-predicted. The 3/rev is predicted within 5%–10% of the flight test value except at 70%R.

The predicted lag bending moments are shown in Fig. 2.10. The measured damper force waveform is shown in Fig. 2.10(a). The bending moment waveform at the root, is almost entirely determined by the damper force. The sharp gradient in the moment waveform at all blade locations near 180°–250° azimuths is a direct effect of the damper force. Figure 2.11 shows the harmonics for the lag bending moments (1-5/rev). The magnitude of all the harmonics except 3/rev shows similar trends as test data, and generally follows the predictions in Refs. [181] and [182]. The 2 and 4/rev harmonics are under-predicted and the 5/rev is over predicted. It is important to note that the chord force data from the flight test is obtained from the pressure data alone, and hence does not include the effect of viscous drag. However reference [183], studied the effect of viscous drag from CFD predictions and showed negligible effect in rectifying this discrepancy.

The torsion moment is shown in Fig. 2.12(a). The torsion moment is important for the prediction of the pitch link load (Fig. 2.12(b)), which in turn drives the 4/rev servo loads. Even though the peak-to-peak magnitude is satisfactory, there is significant discrepancy in all harmonics of the waveform, particularly in 3, 4, and 5/rev. The waveform also shows a 15° phase discrepancy on the advancing side. Figure. 2.12(c) shows the harmonic break-up of the pitch link load, and clearly demonstrates the error in 3, 4, and 5/rev. The pitch link load is the integrated effect of the span-wise torsion moments, and hence show trend similar to the torsion moment. The discrepancy in waveform on the retreating side stems from the errors in higher harmonics (4/rev and higher).

Figure 2.13 compares the predictions from the multibody, full FEM and FEM

with modal reduction. The comparisons are similar at all radial stations, including near the root, hence predictions at only one radial station are shown. There is no phenomenological difference between any of the predictions. This can be attributed to the fact that the magnitudes of maximum flap and lag deformations at the blade tip is less than 15%R, and therefore within the limits of moderate deformation assumptions made in the second order beam element. The root causes of the discrepancies in higher harmonics of the predictions, are clearly unrelated to large deformations or root end kinematics, and therefore remain unclear at the present time.

2.3.5.2 High Altitude Stall Flight (9017: $C_W/\sigma = 0.135$, $\mu = 0.237$)

The oscillatory flap angle at the blade root is shown in Fig. 2.14(a). As in the high speed case, here a damping value of 5% critical in flap produces good agreement in magnitude and phase (Fig. 2.14(b)). Again, note that this additional damping primarily affects the first flap mode and is required only when accurate 1/rev flap deformations are desired. They do not affect the bending moment predictions, which are primarily determined by second and higher modes.

Figure 2.15 shows the predicted flap bending moments. The phase and the higher harmonic content of the waveforms are satisfactory at all locations. For this flight, the lag bending moment data is available only at the root location (11.3%R). Similar to high speed flight, it is dominated by the damper force (Figs. 2.16(a) and (b)). The torsion moments at 11.3%R and 50%R, and the pitch link load are shown

in Figs. 2.17(a), (b) and (c) respectively. The 4/rev and 5/rev harmonics are the source of the torsion oscillations on the retreating blade, which are important for stall prediction at these azimuths (Ref. [183]). Even though the waveforms appear satisfactory, closer examination of the harmonics (Fig. 2.17(d)) reveal a similar 3, 4, and 5/rev discrepancy as high speed. There is a significant 6/rev component in this flight. The analysis fails to predict any of these higher harmonic trends accurately.

A comparison of predictions from the three different formulations, again reveal no phenomenological difference. Even though for a stall flight, the effect of large deformations in this flight is expected to be even less pronounced. The rotor is trimmed to near zero hub moment in this flight and as a result the 1/rev tip flap displacements are close to zero. The higher frequencies of twist are more pronounced in this flight, but, their variation is still limited compared to the low frequency dominated twist in high speed.

2.4 Swash-Plate Dynamics

In this section, a three degree of freedom swashplate model is formulated and coupled with the blade model. First, a static load analysis is carried out. The purpose is to estimate the unknown servo stiffnesses. The stiffnesses are estimated by comparing predictions with test data from Ref. [180]. Second, a dynamic analysis is carried out using three different swashplate masses: 50 kg, 75 kg, and 85 kg. The actual swashplate mass is unknown, but it is expected to lie in this range, as discussed later in the paper. The measured pitch link loads are used for this

analysis. The purpose is to study the effect of swashplate mass on the servo loads. Note that a zero mass case, with zero damping, reduces to a geometric force transfer problem between the four pitch links and the three servos. Third, a coupled blade swashplate dynamic analysis is carried out using a simple 7 degrees of freedom model. The measured pitch link loads are no longer used. Instead the measured airloads are used on the blade, and each blade is now idealized as a single torsion degree of freedom system. The span-wise integrated pitching moments are imposed at the blade root as aerodynamic twisting moments. The purpose is to identify the servo steady displacements necessary to obtain the measured blade root pitch angles. Finally, the idealized blade model is replaced with the full finite element based multibody model. This is referred to as the detailed blade-swashplate model.

2.4.1 Swashplate Model

The swashplate is modeled as a thin disk with 3 degrees of freedom: vertical heave, pitch, and roll. It is attached to the four pitch links on the top, and three servo actuators at the bottom. The forward stationary link is placed at an azimuthal location of $123°56'$, the other two servos are arranged with $90°$ between each of them as shown in Fig. 2.18(a). The rotating and the non-rotating swashplates are not modeled as separate structures, but idealized together as a single functional element. It has three functions: (1) transfer loads between the servos at the bottom and the pitch links on the top, (2) transfer displacements from servos at the bottom to the pitch links on the top, and (3) apply rotating to fixed frame transformation from

top to bottom. The four pitch links, and the three servos are modeled as linear spring-damper systems.

Consider Fig. 2.18(b). P_1, P_2, P_3, and P_4 are the rotating frame pitch link loads from the blades 1 through 4. The net force and moments in the fixed frame are then

$$\frac{P_x}{r} = P_1 \sin(\psi+\phi) + P_2 \cos(\psi+\phi) - P_3 \sin(\psi+\phi) - P_4 \cos(\psi+\phi) \quad (2.67)$$

$$\frac{P_y}{r} = -P_1 \cos(\psi+\phi) + P_2 \sin(\psi+\phi) + P_3 \cos(\psi+\phi) - P_4 \sin(\psi+\phi) \quad (2.68)$$

$$P_z = P_1 + P_2 + P_3 + P_4 \quad (2.69)$$

where r (= 17.4 in) is the radius of the rotating swashplate where the pitch links are attached, P_x, P_y denote the lateral and longitudinal moments respectively acting on the swashplate, P_z is the force in the vertical direction. ψ is the blade 1 azimuth angle, and ϕ is the difference in azimuthal location of a blade and its pitch link. The UH-60A rotor has leading edge pitch links and when a pitch link is aligned with the forward servo (at azimuth 123°56′) the corresponding blade is at 90° azimuth, and thus $\phi = 33°56'$. That is, when a blade is at 0 azimuth, its pitch link is at ϕ.

The three servos must be such that they provide the following net reaction loads on the swashplate

$$F_z = -m\ddot{z} + P_z \quad (2.70)$$

$$M_x = -I_{xx}\dot{\omega}_x - (I_{zz} - I_{yy})\omega_y\omega_z + P_x \quad (2.71)$$

$$M_y = -I_{yy}\dot{\omega}_y - (I_{xx} - I_{zz})\omega_z\omega_x + P_y \quad (2.72)$$

where, ω_x, ω_y, and ω_z are the angular velocities of the swashplate about the x, y,

and z axes respectively of a reference frame attached to the vehicle (Fig. 2.18(b)). These can be related to the swashplate motions as

$$\omega_x = \dot{\alpha}_x - \alpha_y \Omega \tag{2.73}$$

$$\omega_x = \dot{\alpha}_y + \alpha_x \Omega \tag{2.74}$$

$$\omega_z = \alpha_y \dot{\alpha}_x - \alpha_x \dot{\alpha}_y + \Omega \approx \Omega \tag{2.75}$$

Substituting equations (2.73–2.75) in equations (2.70–2.72) and using $I_{zz} = I_{xx} + I_{yy}$, results in

$$F_z = -m\ddot{z} + P_z \tag{2.76}$$

$$M_x = -I_{xx}\ddot{\alpha}_x - I_{xx}\Omega^2\alpha_x + P_x \tag{2.77}$$

$$M_y = -I_{yy}\ddot{\alpha}_y - I_{yy}\Omega^2\alpha_y + P_y \tag{2.78}$$

where I_{xx}, I_{yy}, I_{zz} and m are respectively the moments of inertia about x (lateral), y (longitudinal), and z (normal) axes and the mass of the swashplate. The servo loads causing the above net reaction loads are given by

$$R_f = \frac{F_z}{2} + \frac{M_x + M_y}{2r_s}\sin\phi + \frac{M_x - M_y}{2r_s}\cos\phi \tag{2.79}$$

$$R_l = \frac{M_y \cos\phi - M_x \sin\phi}{r_s} \tag{2.80}$$

$$R_a = \frac{F_z}{2} + \frac{M_x - M_y}{2r_s}\sin\phi - \frac{M_x + M_y}{2r_s}\cos\phi \tag{2.81}$$

where r_s (= 10.75 in) is the radius of the stationary part of the swashplate where the servos are attached, and, R_f, R_l, and R_a are the servo loads for forward, lateral, and aft servos respectively. It should be noted that the lateral servo load R_l is independent of F_z, because of the asymmetric positioning of the three servos

across the swashplate. The forward and aft servos are arranged at diametrically opposite azimuths at approximately 123°56′ and 303°56′ while the lateral servo is half-way at 213°56′ azimuth. Note that, when all the pitch link loads are same, i.e. P_1=P_2=P_3=P_4, then M_x=M_y=0 and $R_l = 0$. The servo deflections needed to produce the desired swashplate motions z, α_x, and α_y, are

$$v_f = z + \alpha_x r_s \cos\phi + \alpha_y r_s \sin\phi \tag{2.82}$$

$$v_l = z - \alpha_x r_s \sin\phi + \alpha_y r_s \cos\phi \tag{2.83}$$

$$v_a = z - \alpha_x r_s \cos\phi - \alpha_y r_s \sin\phi \tag{2.84}$$

where v_f, v_l, and v_a denote the forward, lateral and aft servo deflections. Modeling the servos as linear spring-damper systems, we have

$$R_f = K_{s_f}(v_f - y_f) + C_{s_f}(\dot{v}_f - \dot{y}_f) \tag{2.85}$$

$$R_l = K_{s_l}(v_l - y_l) + C_{s_l}(\dot{v}_l - \dot{y}_l) \tag{2.86}$$

$$R_a = K_{s_a}(v_a - y_a) + C_{s_a}(\dot{v}_a - \dot{y}_a) \tag{2.87}$$

where y_f, y_l, and y_a are a prescribed set of static servo deflections necessary to tilt the swashplate to generate the desired control angles at the blade root.

To obtain the final set of governing equations for the swashplate dynamics, we substitute expressions 2.67–2.69 in equations 2.76–2.78, and then use them in equations 2.79–2.81. The resulting expressions are then equated with equations 2.85–2.87. The final form of the swashplate equations are expressed as below

$$\begin{bmatrix} m & A_1 I_{xx} & B_1 I_{yy} \\ 0 & A_2 I_{xx} & B_2 I_{yy} \\ m & A_3 I_{xx} & B_3 I_{yy} \end{bmatrix} \begin{pmatrix} \ddot{z} \\ \ddot{\alpha}_x \\ \ddot{\alpha}_y \end{pmatrix} + \begin{bmatrix} 2C_{s_f} & 2C_{s_f} r_s \cos(\phi) & 2C_{s_f} r_s \sin(\phi) \\ C_{s_l} & -C_{s_l} r_s \sin(\phi) & C_{s_l} r_s \cos(\phi) \\ 2C_{s_a} & -2C_{s_a} r_s \cos(\phi) & -2C_{s_a} r_s \sin(\phi) \end{bmatrix} \begin{pmatrix} \dot{z} \\ \dot{\alpha}_x \\ \dot{\alpha}_y \end{pmatrix}$$
$$+ \begin{bmatrix} 2K_{s_f} & 2K_{s_f} r_s \cos(\phi) + A_1 I_{xx} \Omega^2 & 2K_{s_f} r_s \sin(\phi) + B_1 I_{yy} \Omega^2 \\ K_{s_l} & -K_{s_l} r_s \sin(\phi) + A_2 I_{xx} \Omega^2 & K_{s_l} r_s \cos(\phi) + B_2 I_{yy} \Omega^2 \\ 2K_{s_a} & -2K_{s_a} r_s \cos(\phi) + A_3 I_{xx} \Omega^2 & -2K_{s_a} r_s \sin(\phi) + B_3 I_{yy} \Omega^2 \end{bmatrix} \begin{pmatrix} z \\ \alpha_x \\ \alpha_y \end{pmatrix}$$
$$= \begin{pmatrix} A_1 P_x + B_1 P_y + F_z + 2(K_{s_f} y_f + C_{s_f} \dot{y}_f) \\ A_2 P_x + B_2 P_y + K_{s_l} y_l + C_{s_l} \dot{y}_l \\ A_3 P_x + B_3 P_y + F_z + 2(K_{s_a} y_a + C_{s_a} \dot{y}_a) \end{pmatrix} \tag{2.88}$$

where,

$$A_1 = \frac{\sin\phi + \cos\phi}{r_s} \quad A_2 = -\frac{\sin\phi}{r_s} \quad A_3 = \frac{\sin\phi - \cos\phi}{r_s} \tag{2.89}$$

$$B_1 = \frac{\sin\phi - \cos\phi}{r_s} \quad B_2 = \frac{\cos\phi}{r_s} \quad B_3 = -\frac{\sin\phi + \cos\phi}{r_s} \tag{2.90}$$

The position of the servos and the pitch links are obtained from Ref. [180]. The servo stiffnesses are unknown. They are now identified using the static part of equation 2.88 in the following manner.

2.4.2 Static Loading

The servo stiffnesses are identified by comparing detailed control system stiffness measurements given in Ref. [180] with predictions from the above formulation. An approximate stiffness value, from Ref. [184], is also quoted. Three types of static loading were applied in Ref. [180]: (1) collective, (2) reactionless, and (3) cyclic.

The same loading conditions are simulated using the above analytical model. In the case of collective loading, identical leading-edge-down root pitching moments are imposed in the same direction on all the four blades at each azimuth station (+1824 ft-lbs). The moments are transmitted to the swashplate via the pitch links and then to the servos. In the case of reactionless loading, identical root pitching moments are imposed in opposite directions on alternate blades (+1824, -1824, +1824, and -1824 ft-lbs). In the case of cyclic loading, the root pitching moments are imposed in cyclical manner.

Figure 2.19(a) shows that the maximum collective stiffness (imposed moment divided by root twist) occurs near 180° but is not symmetric. The model predicts the same behavior. This is caused by the placement of the servos. The stiffness is high in the regions immediately above the servos, and low farther away. The magnitude of prediction depends on the forward and aft servo stiffnesses. The stiffness values of 1.5×10^7 and 0.58×10^7 N/m for forward and aft servos respectively provide a good magnitude agreement with test data.

In the case of reactionless loading, the net force and moments on the servos are zero (Fig. 2.19(b)). Thus this configuration isolates the pitch link stiffness, as none of the servos are deflected. The test data shows a higher frequency variation (higher than 1/rev) which is not expected to be predicted by the analysis. This appears to stem from swashplate elastic deformations which were not included in the model.

In Ref. [180], cyclic loading is applied in two steps. In the first step, all blades start with equal loading (1063 ft-lbs), and then the loading on only one set of

opposite blades is changed, e.g. for blades at 0° and 180°. Loading on one blade is increased to 1824 ft-lbs while the loading on the opposite blade is decreased to 303 lbs. The loading on the blades at 90° and 270° remain constant. The net loading on the blades are then 1824, 1063, 303, and 1063 ft-lbs. This loading condition is called Cyclic Loading 1. In the second step, the load change is performed on the other two blades at 90° and 270°. The loads on blades at 0° and 180° now remain constant. The experimental stiffness values differ marginally, the predictions, of course, are identical. Note that the predictions do not depend on the exact magnitudes of the loading but depend on their variation, however the test data does, because of the nonlinearities associated with loading hysteresis. The lateral servo stiffness is determined as 0.45x10^7 N/m to provide a good magnitude agreement with the cyclic loading data (Fig. 2.19(c)).

2.4.3 Dynamic loading

The mass of the swashplate is not known, hence the Tischenko equation for swashplate mass is used to get an estimate. Tischenko (Ref. [185]) considers that the weight of the swashplate is proportional to the moment of forces coming from the rotor blades. The forces coming from the rotor blades are in turn proportional to $N_b C_b^2 R$. Thus, the mass of swashplate is given by:

$$m = W_{sp} N_b C_b^2 R \tag{2.91}$$

where N_b is the number of blades, C_b is the average blade chord, and R is the blade radius. The coefficient of mass for the swashplate W_{sp} is approximately equal to 8

kg/m^3 for most modern helicopters in UH-60A weight category. Using the UH-60A blade data in the expression above, the mass of the swashplate is estimated to be around 75 kg (73 kg, 160.94 lbs).

The measured pitch link load from blade 2 is now phase shifted for four blades and imposed on the swashplate. The swashplate mass is varied about the estimated value to study its effect on the servo loads prediction. Figures 2.20(a) and (b) compares the predicted servo loads for the two flight conditions with the test data without swashplate dynamics, i.e. with swashplate mass set to 0 kg. The servo loads in the high altitude stall flight are two to three times greater than those occurring in the high speed flight. Therefore, the loads in the high altitude stall flight is studied further in Fig. 2.20(c). Here, the harmonics of the three servo loads are shown, and they are compared with predictions corresponding to swashplate masses of 0, 50, 75, and 85 kg. Note that, unlike the test data, only integer harmonics of the blade number are expected from the analysis as the imposed pitch link loads are kept the same for all blades (only phase shifted) and therefore no blade-to-blade dissimilarity is modeled. It appears that the dynamics of swashplate can have a significant effect on the servo loads. The frequencies (at 0° azimuth) of a 50 kg swashplate are 11.6, 22.4, and 33.4/rev. The frequencies corresponding to 75 and 85 kg masses are 9.48, 18.3, and 27.24/rev, and 8.9, 17.2, and 25.6/rev. Figure 2.20(c) shows that the 4/rev servo loads increase in general with an increase in swashplate mass – this is simply because the swashplate motions, that are primarily 4/rev, increase with swashplate inertia as the first natural frequency decreases. The 8 and 12/rev servo loads are more significantly affected by swashplate dynamics. As expected from the

frequencies, 8/rev is most sensitive for a 50 kg mass and 12/rev for 85 kg.

The servo loads are predominantly 4/rev and as noted earlier the stall flight shows a significantly higher 4/rev content than high speed flight. The 4/rev pitch link load, on the other hand, is higher in high speed flight than in the stall flight, as shown in figure 2.21. The 4/rev servo loads are the result of 3, 4, and 5/rev pitch link forcing. The 3/rev forcing is similar in both flight conditions. Thus, it appears that the 4/rev servo loads are dominated by 5/rev pitch link forcing. The 5/rev pitch link forcing is significantly higher in the stalled flight than in high speed, and is consistent with the servo loads. The analysis appears to show this trend of the test data. The magnitude of the servo loads are satisfactorily predicted in both flights. Thus, even though the 4/rev forcing on the swashplate is twice as high in high speed, the servo loads are still only half of those in stall flight. This is possibly because the servo loads for this rotor are dominated by 5/rev forcing.

2.4.4 Seven Degree of Freedom blade-swashplate coupled model

This simple blade-swashplate coupled model is used only to estimate the unknown servo displacements for the two flights that will be studied with the detailed blade model in the next section. Here, each one of the four blades is idealized as a single degree of freedom system having only rigid torsion degree of freedom. The first torsion frequency of the UH-60A blades is 4.38/rev, corresponding to a pitch link stiffness of 2.745×10^6 N/m, or equivalently a root spring stiffness of 1090 ft-lbs/deg. The blades are assumed identical. The measured airloads are imposed

on the rigid blades as integrated root aerodynamic pitching moment at the pitch bearing.

The steady servo displacements that are required to generate the measured control angles at the bearing can now be calculated. For the high speed flight, they are 0.3, 0.07, and 0.3% R (1, 0.23, 1 inches) for the forward, lateral and aft servos respectively. Figure 2.22(a) shows that the above values produce a good agreement with the measured blade root pitch angle. Similarly, for the stalled flight, servo displacements of 0.3, 0.045, and 0.25% R (1, 0.14, 0.8 inches) produce the flight test measured angles. This is shown in figure 2.22(b).

In the next section, the detailed blade model is coupled to the swashplate model. The input servo deflections for control angles are those obtained using the simple model in this section.

2.4.5 Detailed finite element blade-swashplate coupled model

The swashplate model is coupled to the multibody blade model in this section. The pitch link load obtained at every time step using the blade model is imposed on the swashplate model and the swashplate motions are calculated. The steady servo deflections below the swashplate are held fixed at values calculated in the previous section. The total swashplate motions are then used for the next time step for the calculation of the blade response. Note that the total motion includes the steady tilt that is necessary to generate the pitch control angles. The blade-swashplate coupled analysis is then carried out until periodicity. The inclusion of swashplate

model in the analysis facilitates the study of effect of cyclic variation of control system stiffness and the swashplate mass on the rotor dynamics. It is observed that the swashplate dynamics has an insignificant effect on the overall dynamics of the rotor (Fig. 2.23). This is attributed to the fact that the swashplate motions do not have any significant effect on the blade root pitch angle which governs the blade dynamics (Fig. 2.24).

Figure 2.25(a) shows the predicted servo loads for flight 9017 for a swashplate mass of 75 kg. The peak-to-peak forward link load is under-predicted by 40% stemming from a 4/rev error. Figure 2.25(b) shows the harmonic break-up of the servo loads. Because 4/rev and 5/rev pitch link loads are over-predicted for flight 9017 (Fig. 2.17(d)), the under-prediction of the forward servo load stems from an under-prediction of 3/rev pitch link load. The peak-to-peak lateral link load is well predicted, but it shows a 10°–20° error in 4/rev phase. The aft servo load is predicted well in both magnitude and phase. It can be observed from Figs. 2.23 and 2.25 that swashplate dynamics do not have any effect on the blade loads for this rotor, but affects the servo loads prediction significantly. Figure 2.25(b) shows that a deviation of 25% can occur in the magnitude of 4/rev servo loads and an over-prediction of 100–200% in the magnitude of the 4, 8 and 12/rev servo loads depending on the dynamics of the swashplate.

2.5 Prediction of Structural Loads During Maneuver

After validating the blade swashplate model in steady flight, the measured airloads analysis is carried out using the flight test data for the pull-up maneuver. The solution procedure for the analysis with measured airloads, damper loads, and control angles, starts with a periodic solution for the first revolution which corresponds to steady flight condition. The steady periodic solution is obtained by using the periodic airloads taken from rev. 1 of the maneuver by letting the analysis run for 50 revolutions. Once the dynamic response settles into periodicity, then, the maneuver is initiated. Note that, unlike in level flight, it is not possible to iteratively correct the root pitch control angles based on the calculated pitch-link deflection. However, this error, as shown later, is insignificant. The main source of error is the absence of airloads data (gage out) at the 55% R station. A small amount of damping, 0.02% of critical, has to be used to decay initial transients during the course of analysis. This necessitates about 50 revs of initiation run before the imposition of transient airloads.

2.5.1 Blade Root Deflections

The predicted blade pitch angle is compared with the measured values at the root (blade #3) in Fig. 2.26. Root pitch angle is the net result of applied rotor pitch control and elastic pitch-link deflection. The latter being small, the two sets are expected to match closely.

Figure 2.27 shows the predicted and measured flap angle (blade #1). Investi-

gation of the time history reveals that for the initial part of the maneuver (revolution number 0-6) the blade flap angle is predominantly 1/rev, with significant 2/rev only in the later part of the maneuver. The analysis showed good prediction of root flap angle at the beginning of the maneuver. The flap angle is over-predicted from revolution 12 onwards.

2.5.2 Flap and Lag Bending Loads

The time history of predicted flap bending moments (mean removed) at 11.3%R is shown in Figs. 2.28 and 2.29, and at 50%R is shown in Figs. 2.30 and 2.31. It is important to note that the sectional airloads at 55% radial station are not available because of failed instrumentation, Ref. [10]. Therefore the airloads has to be linearly interpolated between 40% to 67.5% radial stations. This lack of information seems to have impacted the peak-to-peak magnitude of structural loads in general, and flap bending moment in particular, throughout the maneuver, especially at 50%R station (Fig. 2.38(a)), resulting in under-prediction.

The prediction for lag bending moment at 11.3%R is shown in Figs. 2.32 and 2.33. As noted earlier, the bending moment waveform near the blade root is completely dominated by the damper force and is well predicted throughout the maneuver. Figures 2.34 and 2.35 show the predicted lag bending moment at 50%R. The sharp gradient in the moment waveform at all radial locations and all revolutions near 180°–250° azimuths is a direct effect of the damper force (Ref. [181]). Predictions only show fair correlation with the test data at 50% radial station, particularly

revolution 12 onwards.

2.5.3 Torsion Loads

The torsion moment at 30%R is shown in Figs. 2.36 and 2.37. At the beginning of the maneuver, it is over-predicted, and there is a discrepancy in the waveform on the restreating side. This discrepancy is less pronounced in the later part of the maneuver, due to significant natural response between 4 and 5/rev (the first torsion frequency is 4.4/rev) and the the predicted magnitude shows good correlation with the test data (Fig. 2.38(c)). The effect of stall is clearly visible. The peak-to-peak structural loads are summarized in Fig. 2.38. The pitch-link load (Figs. 2.39 and 2.40) shows a similar trend.

To gain in-depth understanding of the sources of high torsional loads, harmonic analysis of structural loads and aerodynamic pitching moment is carried out. The revolutions 14–18 are known to be steady, thereby justifying harmonic analysis. Figures 2.41 and 2.42 show the predicted 1–10 harmonics for torsion moment at 70% radial station and pitch-link load respectively for the revolution 1. Predictions for torsion moment as well as pitch-link load show trends similar to flight-test data, however, 3/rev torsion moment and 4/rev pitch-link load show significant under-prediction. The predicted pitch-link load harmonics for revolution 14, corresponding to high load-factor regime, shows only fair correlation with flight-test data as 3/rev is under-predicted and 5/rev is over-predicted by 60% (Fig. 2.43). It should be noted that both the flight test data and predictions show significant 5/rev pitch-

link load during revolution 14, which is consistent with significant 5/rev observed in flight test pitching-moment (Fig. 2.44). Unlike blade pitching-moment and pitch-link load, flight test torsion moment for revolution 14, as shown in Fig. 2.45, lacks significant 5/rev component, consequently, analysis is over-predicting it significantly. The reason for this observation is not clear, and possibly related to the uncertainties associated with flight test measurements.

2.6 Conclusions

A detailed finite element multibody structural dynamic analysis is developed for a rotor-swashplate system. The model is first verified with analytical solutions for large deformation problems. Next, it is validated with static Princeton beam large deformation data. Finally, the full scale measured airloads from the full-scale UH-60A flight tests are used to calculate the structural loads under two flight conditions – a high speed high vibration flight and a high altitude dynamic stall flight. Selected predictions were systematically compared between three formulations: full finite element with multibody dynamics, full finite element, and finite element with modal reduction. A swashplate model was coupled to the rotor model to study the effect of swashplate dynamics on structural loads. Based on this study the following key conclusions are drawn.

1. All three of the structural dynamic formulations: multibody, full finite element, and finite element with modal reduction showed identical prediction of structural loads for the UH-60A rotor at the two flight conditions – a high

speed high vibration flight (counter 8534: 158 kts, $\mu = 0.368$, $C_W/\sigma = 0.0783$), and a high altitude dynamic stall flight (counter 9017: 101 kts, $\mu = 0.237$, $C_W/\sigma = 0.135$). The flap bending moment is satisfactory across all harmonics. The chord bending moment is under-predicted in 4/rev and over-predicted in 5/rev. Torsion moment prediction is least satisfactory for harmonics 3/rev and higher. The peak-to-peak magnitudes are however correct for all loads.

2. The dynamics of the swashplate do not appear to have a significant effect on the prediction of torsion loads on the blade and pitch link. The blade loads, predicted with or without coupled swashplate dynamics, show the same peak-to-peak and higher harmonic content. The cyclic variation of control system stiffness is substantial due to the presence of the servos underneath, but it does not affect the predicted torsion loads.

3. The magnitude of servo loads is affected not only by the pitch link load magnitudes but also by swashplate inertia. Variation of 25% can occur in the magnitude of predicted 4/rev servo loads depending on the swashplate dynamics. Swashplate dynamics is particularly important for the prediction of higher frequencies of servo loads – 8 and 12/rev servo loads. Over-prediction of 100-200% can occur in the magnitude of prediction depending on the swashplate dynamics. The 4/rev servo load, however, is affected primarily by the pitch link loads. For the UH-60A rotor, it appears that the 5/rev component of pitch link load dominates the 4/rev servo harmonic. This conclusion is consistent across the two flight conditions investigated in the present study.

4. In the maneuvering flight, predicted structural loads using measured airloads data show correct trends as flight test. Flap bending moment prediction shows best correlation among all structural loads predicted. The over-prediction of root flap angle in the later part of the maneuver might be related to uncertainities associated with the flight test data, as this over-prediction is consistent with all analysis as noted in Chapters 3 and 4.

5. Unlike pitch-link load, flight test torsion moment in the stalled region (revolutions 12–20), lack significant 5/rev component predicted by measured airloads analysis. The blade pitching-moment data from flight test for outboard stations (77.5%R–92%R) show significant 5/rev. A similar trend is expected for the torsion loads, which are reactions to the pitching-moment. While, the flight test pitch-link load is in harmony with this observation, the torsion moment doesn't conform. The reason for this discrepancy may be related to the errors associated with the flight test measurements.

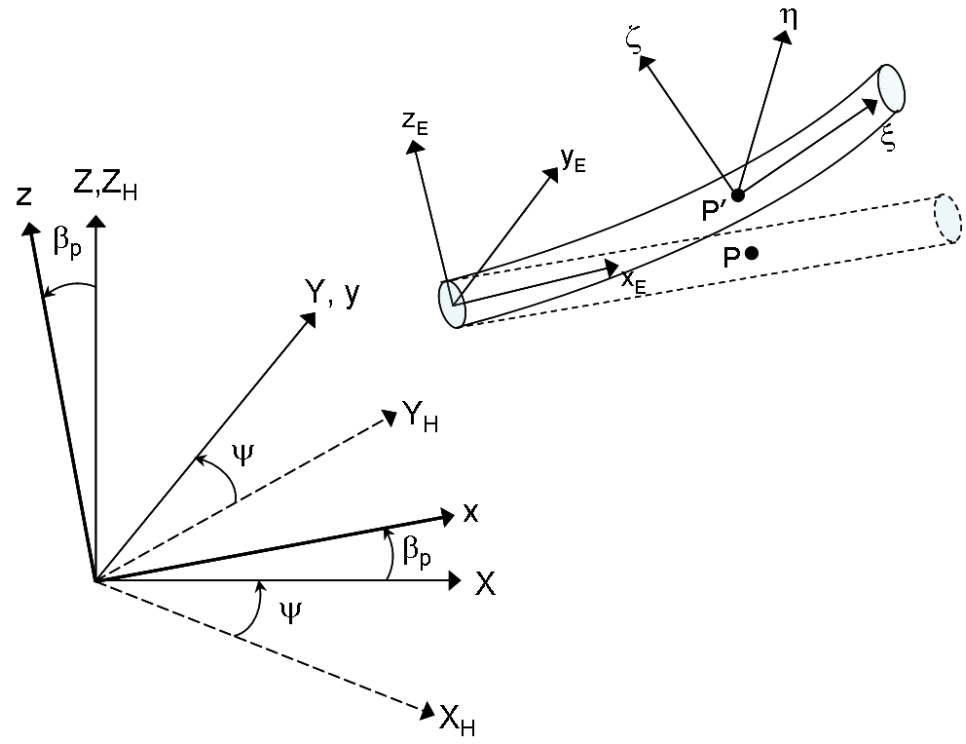

Figure 2.1: **Coordinate systems used in modeling of rotor blade**

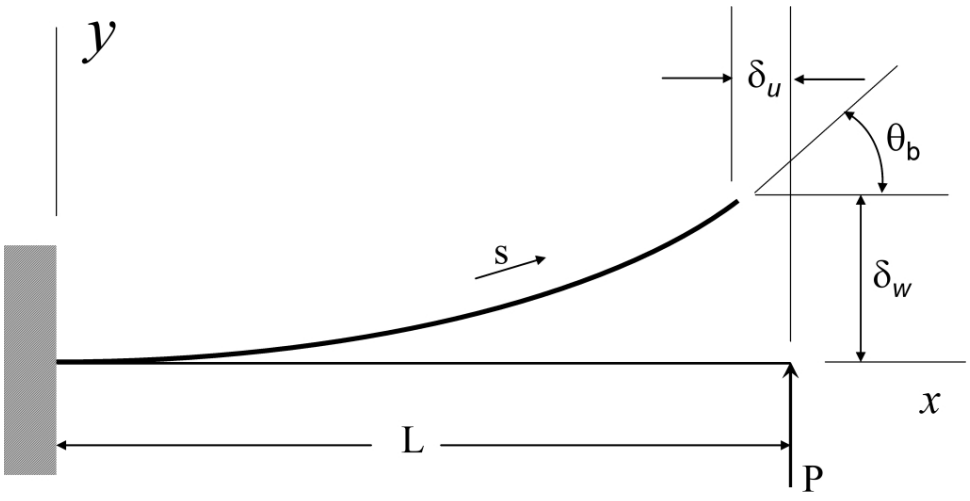

Figure 2.2: **Large deflections of a cantilever beam due to a tip load**

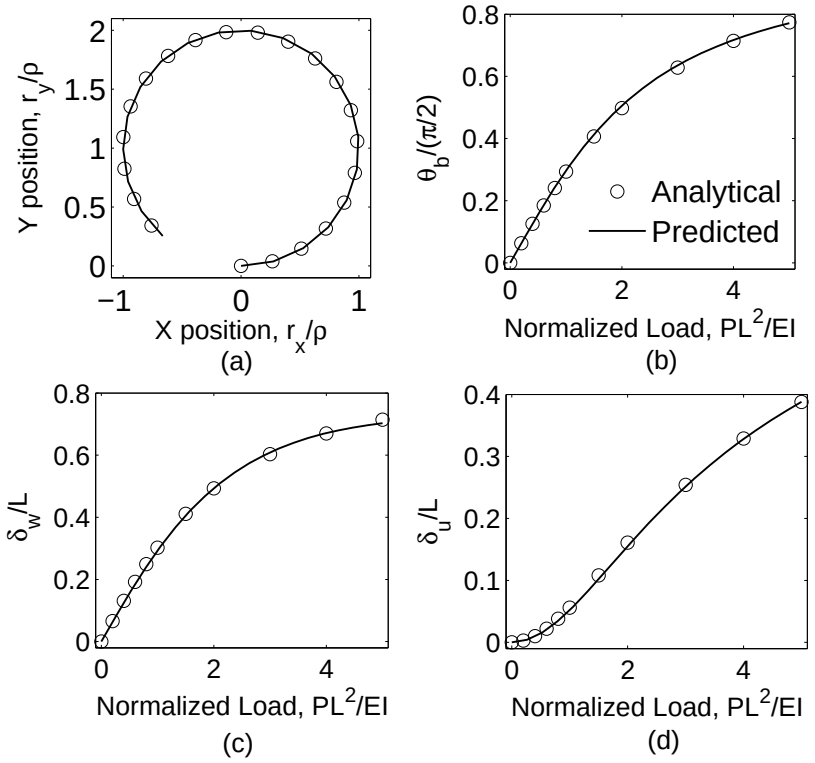

Figure 2.3: **(a) Elastica analytical vs. predicted for an Aluminum beam of length L = 20 ft under tip moment M = 2500 ft-lb, EI = 9000 lb-ft^2, $\rho = 3.6$ ft, (b)–(d) Elastica under tip force – rotation angle (θ_b), vertical deflection (δ_w), and axial foreshortening (δ_u) vs. normalized tip force**

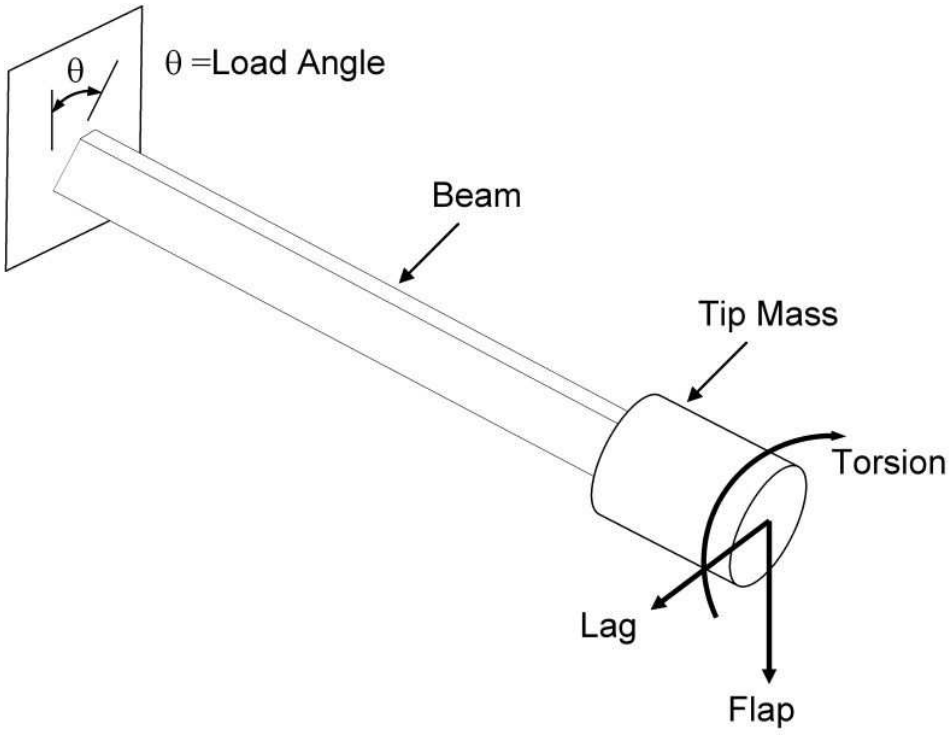

Figure 2.4: **Schematic representing the Princeton beam test carried by Dowell and Traybar to study flap-lag-torsion coupling.**

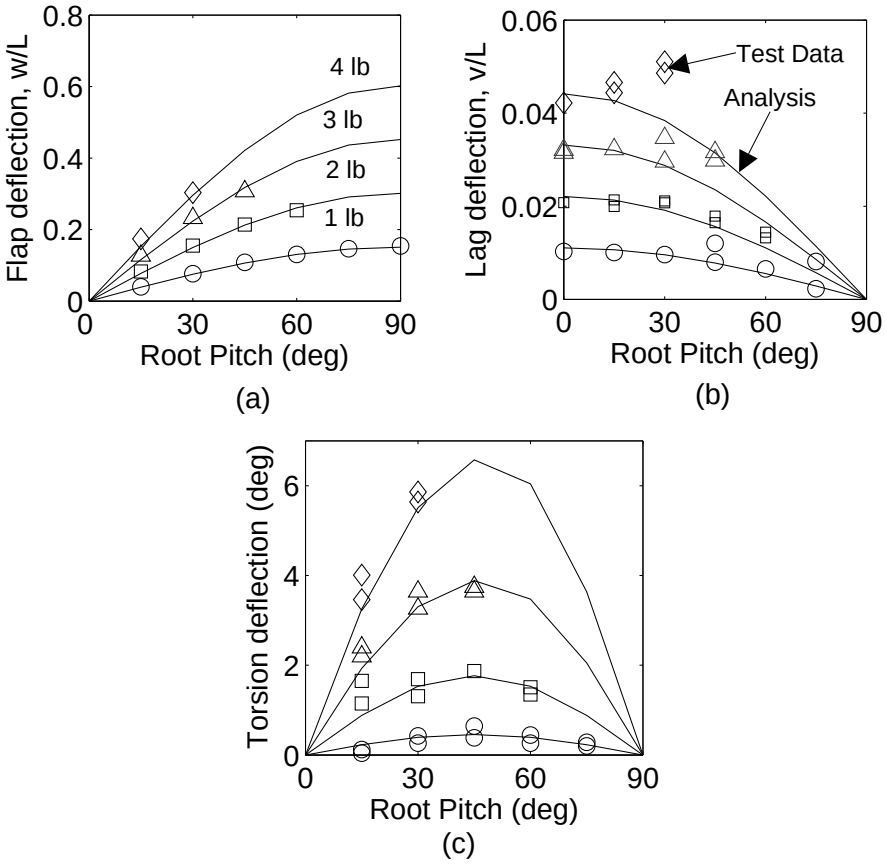

Figure 2.5: **Princeton beam test - (a) flap bending deflection, (b) lag bending deflection, (c) torsion deflection**

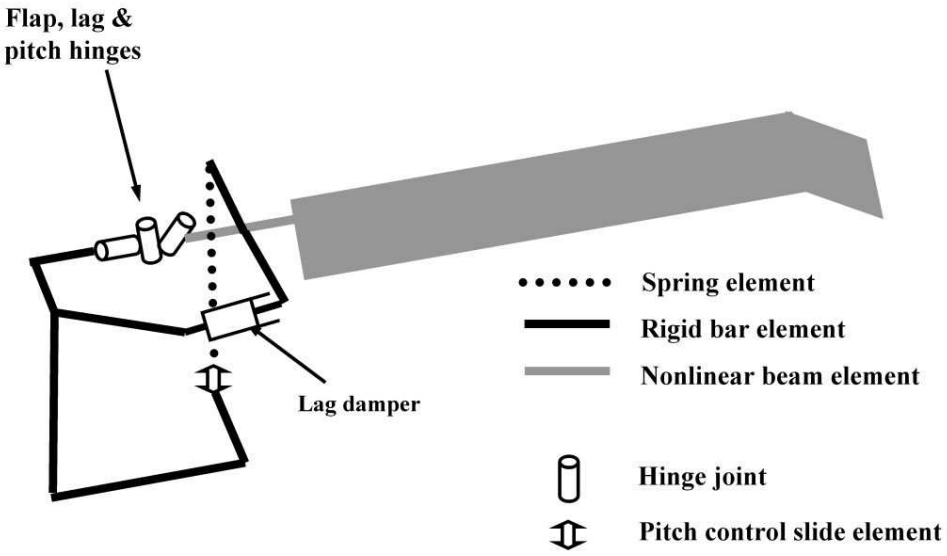

Figure 2.6: **Schematic of an UH-60A blade structural model**

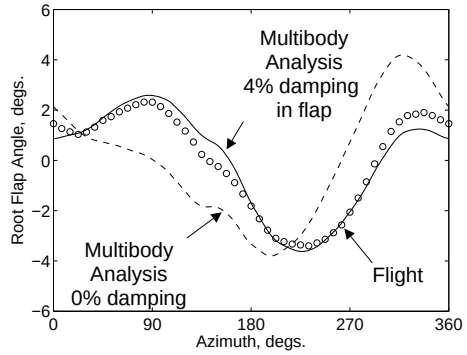

(a) Root flap angle, steady removed

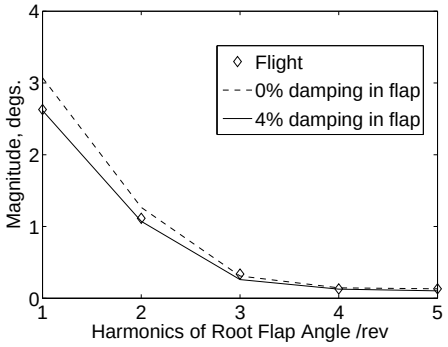

(b) Magnitude of root flap angle

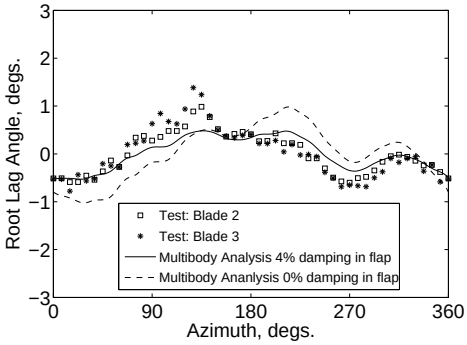

(c) Root lag angle, steady removed

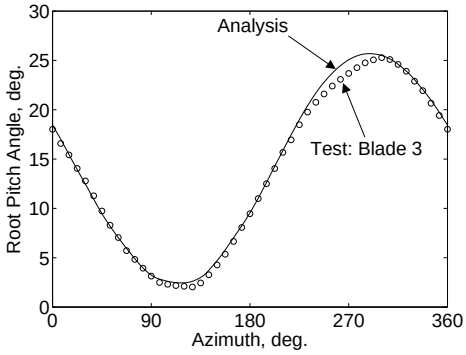

(d) Root pitch angle

Figure 2.7: **Predicted root flap, lag and torsion angles using measured airloads; effect of damping on the root flap and lag angles; high speed flight C8534 ($C_W/\sigma = 0.0783$, $\mu = 0.368$)**

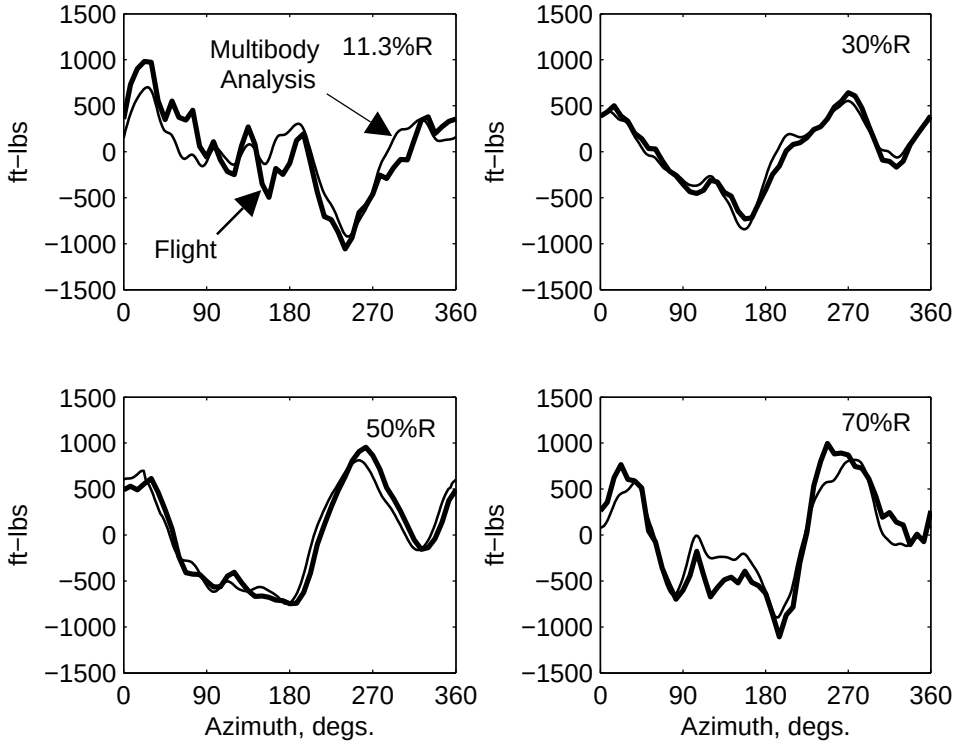

Figure 2.8: **Predicted and measured flap bending moments using measured air loads from high speed flight C8534 ($C_W/\sigma = 0.0783$, $\mu = 0.368$), steady loads removed**

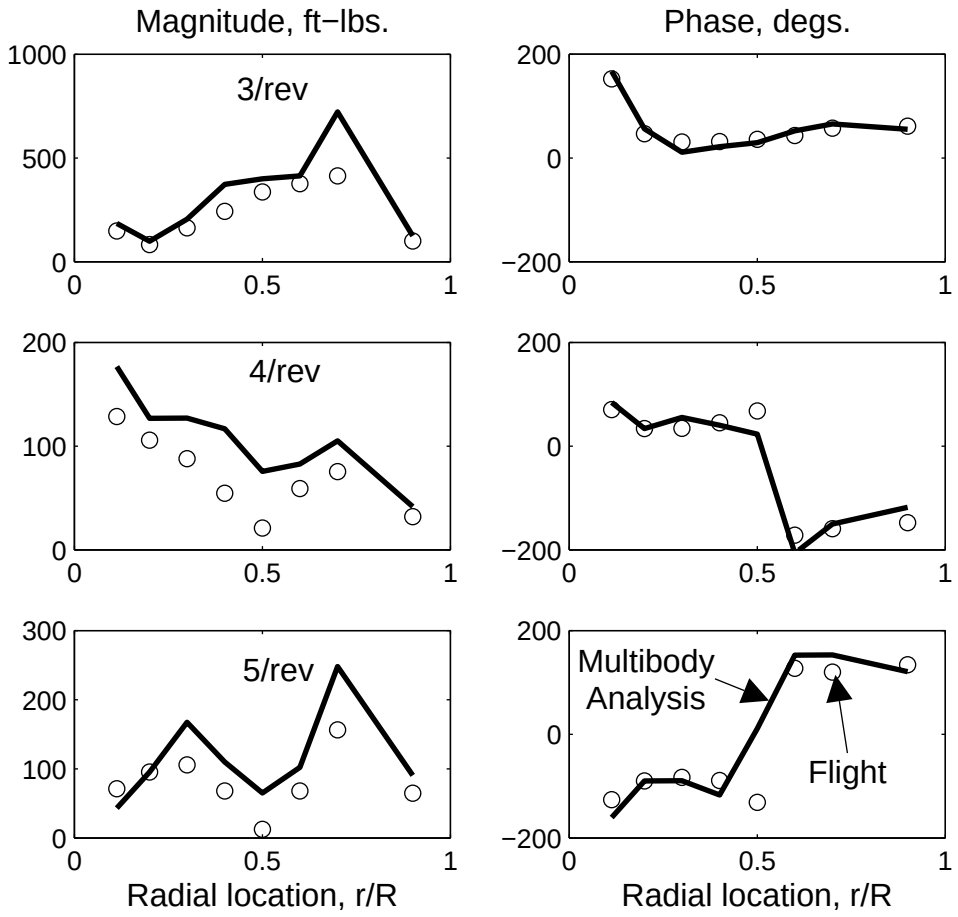

Figure 2.9: **Predicted and measured harmonics of flap bending moment for high speed flight C8534 ($C_W/\sigma = 0.0783$, $\mu = 0.368$)**

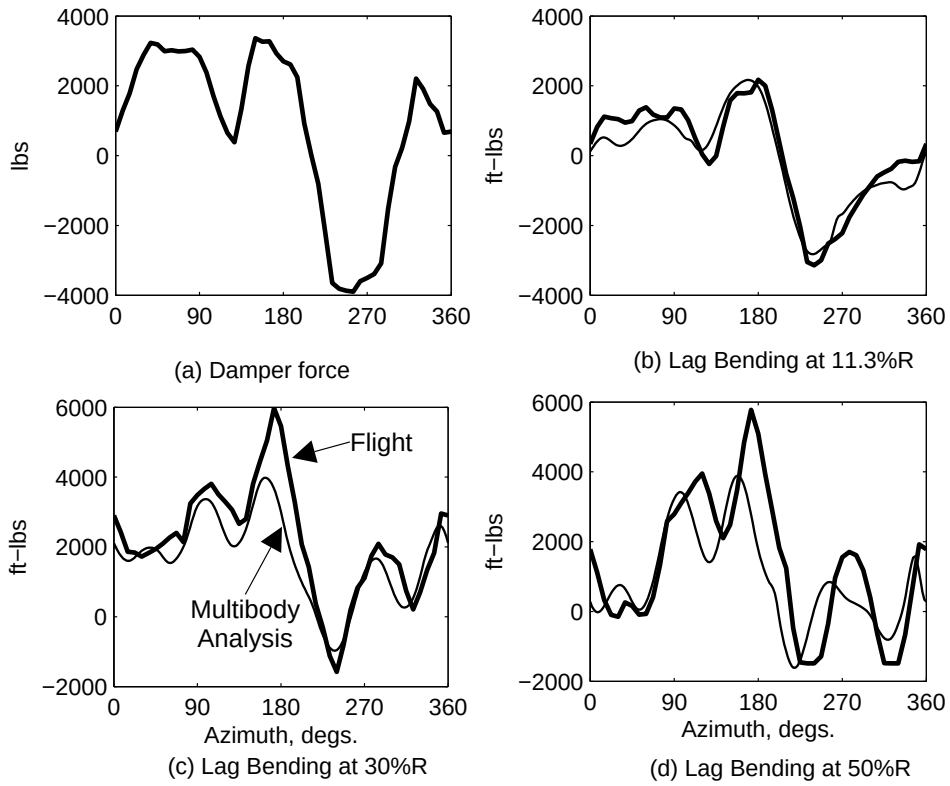

Figure 2.10: **Predicted and measured lag bending moments using measured air loads and damper force from high speed flight C8534 ($C_W/\sigma = 0.0783$, $\mu = 0.368$), steady loads removed**

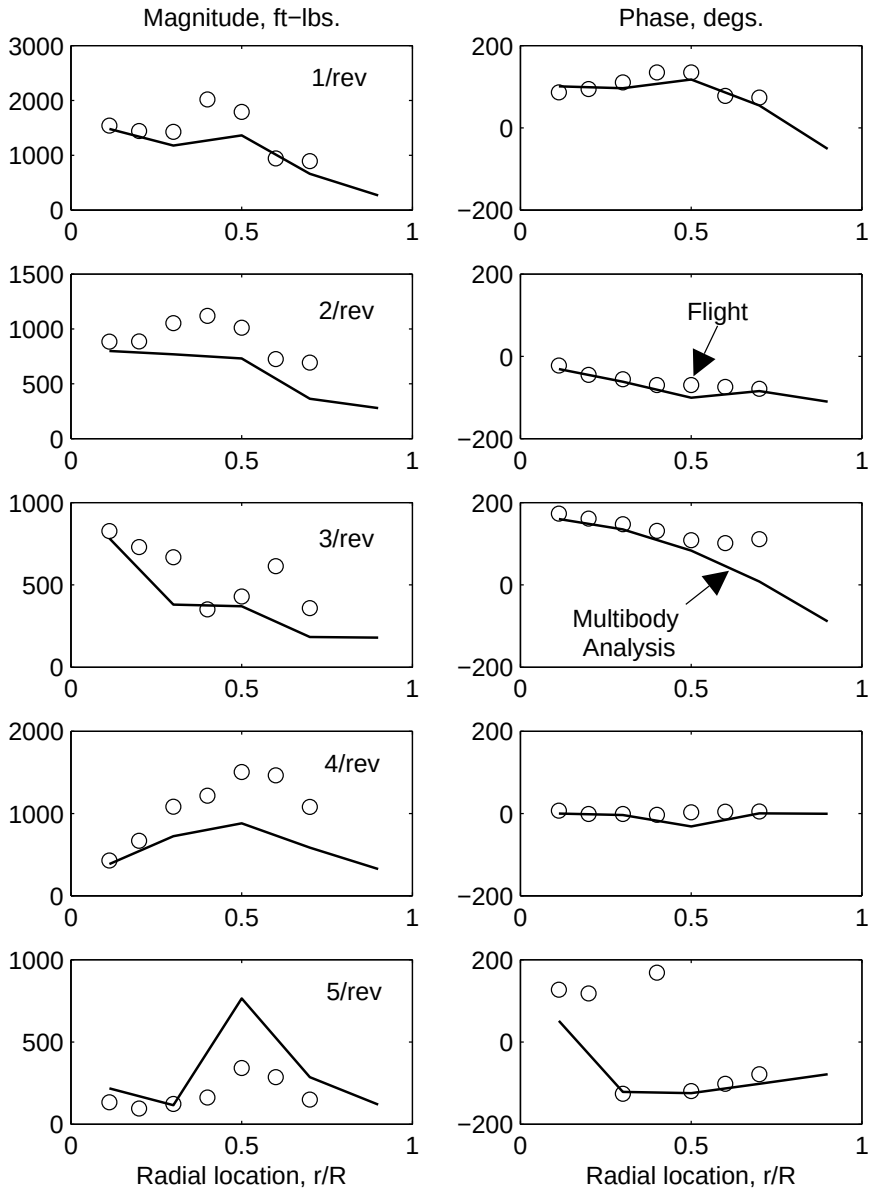

Figure 2.11: **Predicted and measured harmonics of lag bending moment for high speed flight C8534, ($C_W/\sigma = 0.0783$, $\mu = 0.368$)**

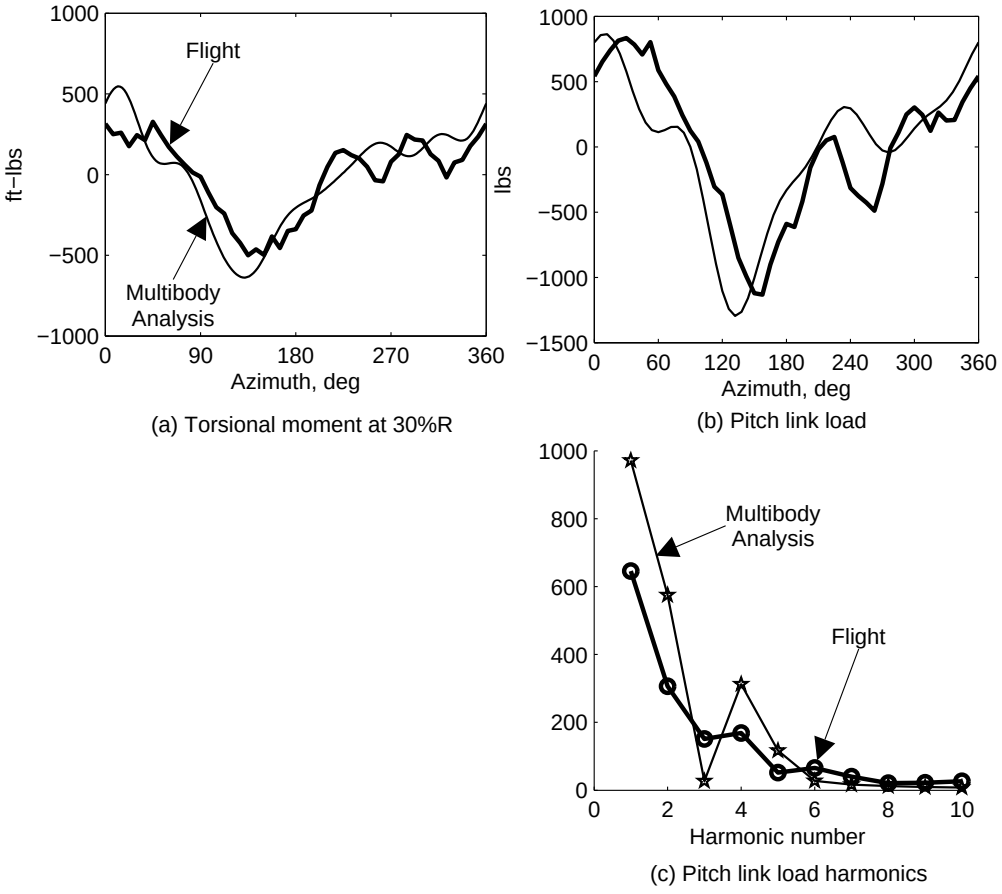

Figure 2.12: **Predicted and measured torsional moment, pitch link load and pitch link load harmonics using measured air loads from high speed flight C8534 ($C_W/\sigma = 0.0783$, $\mu = 0.368$), steady loads removed**

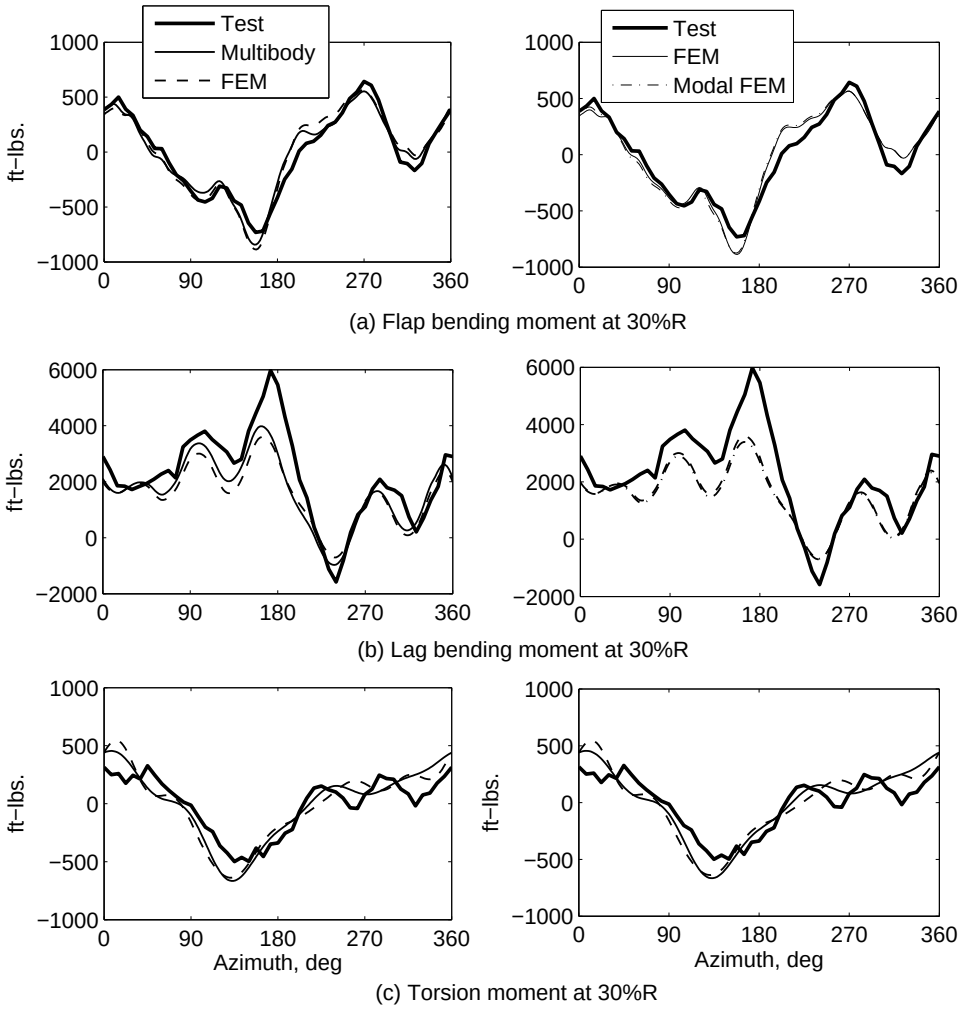

Figure 2.13: **Comparison between multibody, full FEM and Modal FEM predictions for high speed flight C8534, ($C_W/\sigma = 0.0783$, $\mu = 0.368$)**

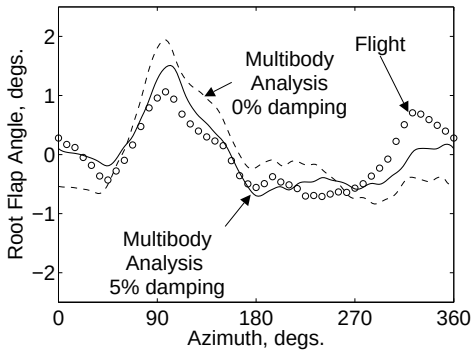

(a) Root flap angle, steady removed

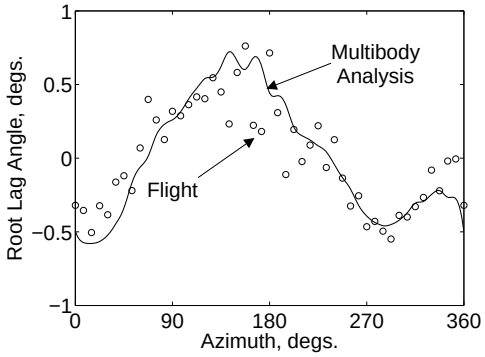

(b) Root lag angle, steady removed

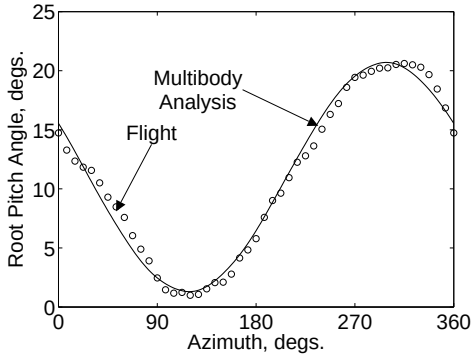

(c) Root pitch angle

Figure 2.14: **Predicted root flap, lag and torsion angle using measured airloads; effect of damping on the root flap angle; high altitude stall flight C9017 ($C_W/\sigma = 0.135$, $\mu = 0.237$)**

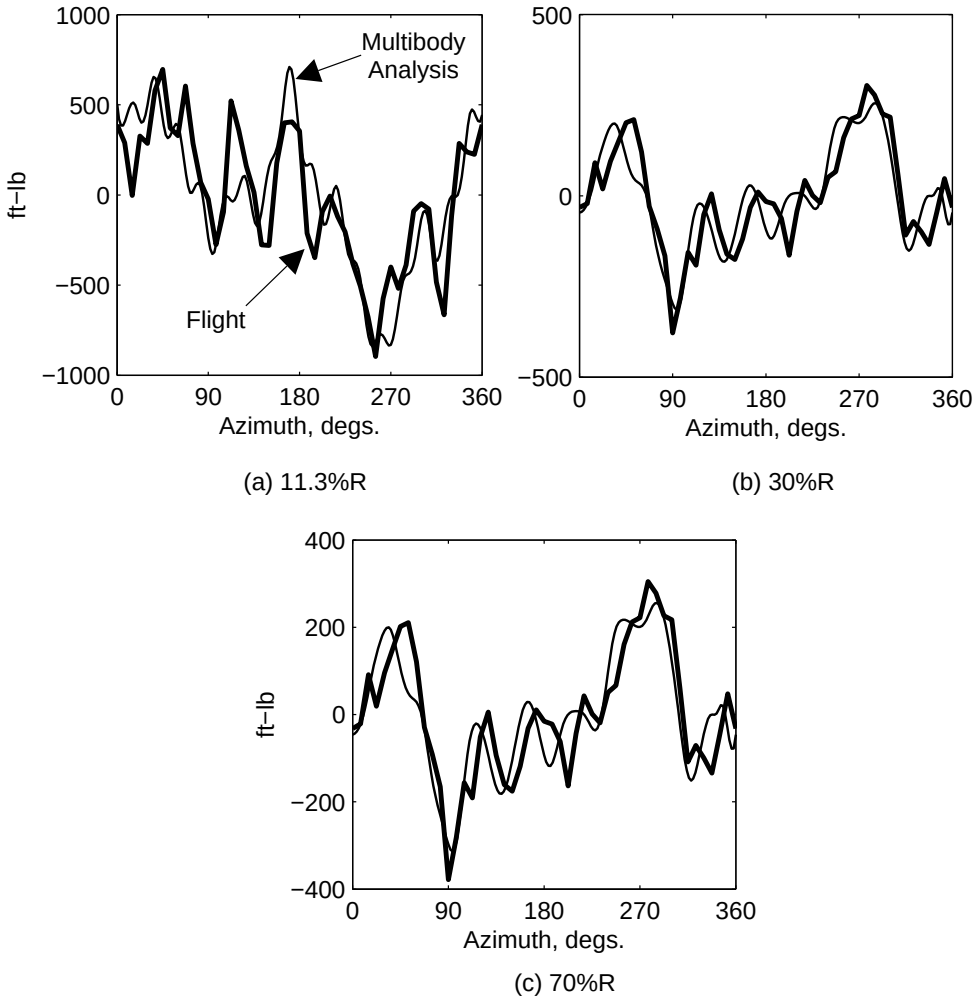

Figure 2.15: **Predicted and measured flap bending moment using measured air loads from high altitude stall flight C9017 ($C_W/\sigma = 0.135$, $\mu = 0.237$), steady loads removed**

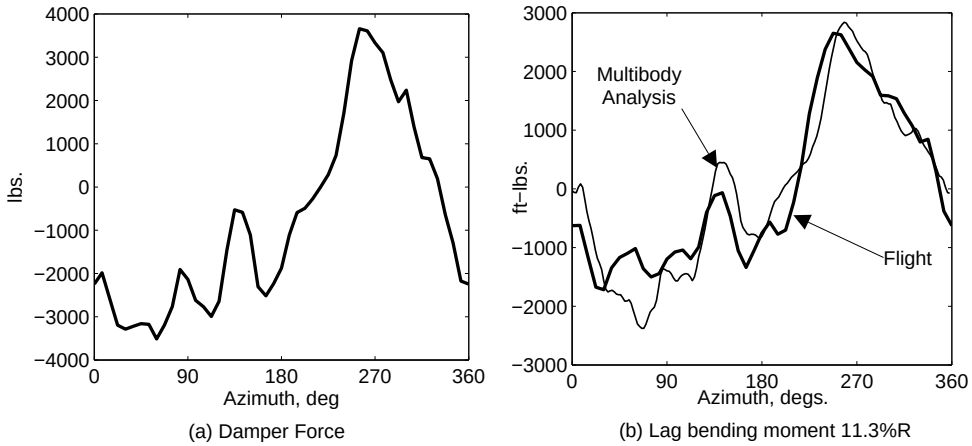

Figure 2.16: **Predicted and measured lag bending moment using measured air loads from high altitude stall flight C9017 ($C_W/\sigma = 0.135$, $\mu = 0.237$), steady loads removed**

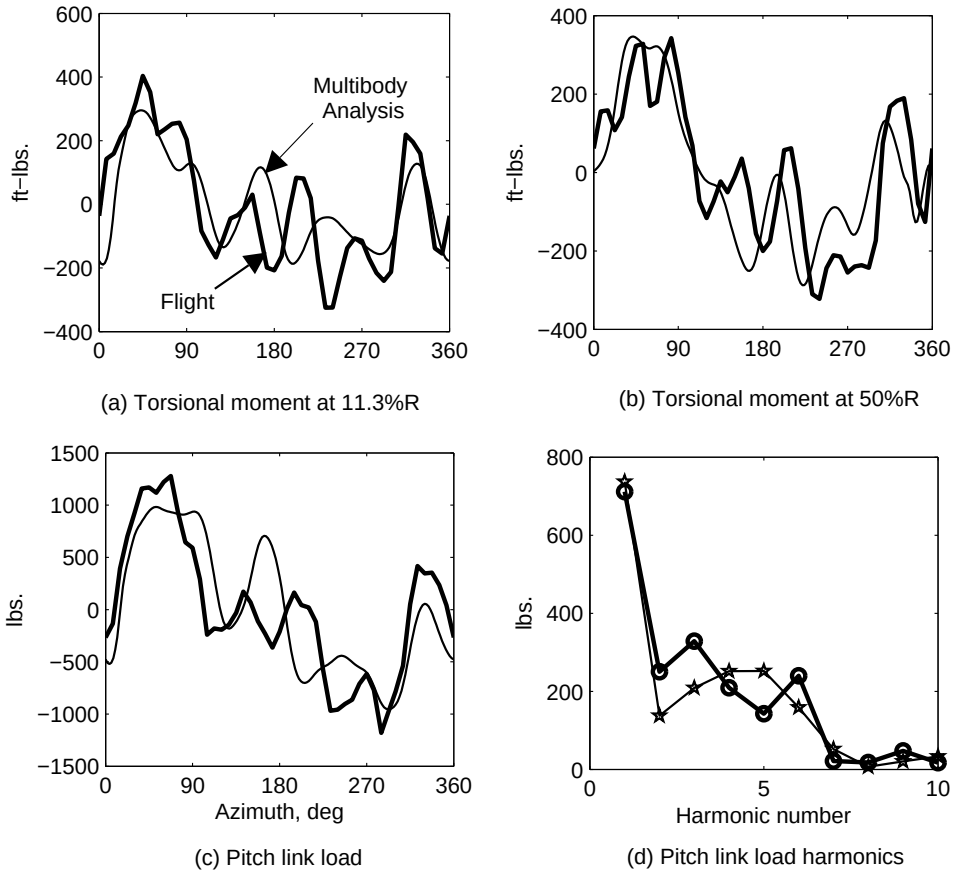

Figure 2.17: **Predicted and measured torsional moment, pitch link load and pitch link load harmonics using measured air loads from high altitude stall flight C9017 ($C_W/\sigma = 0.135$, $\mu = 0.237$), steady loads removed**

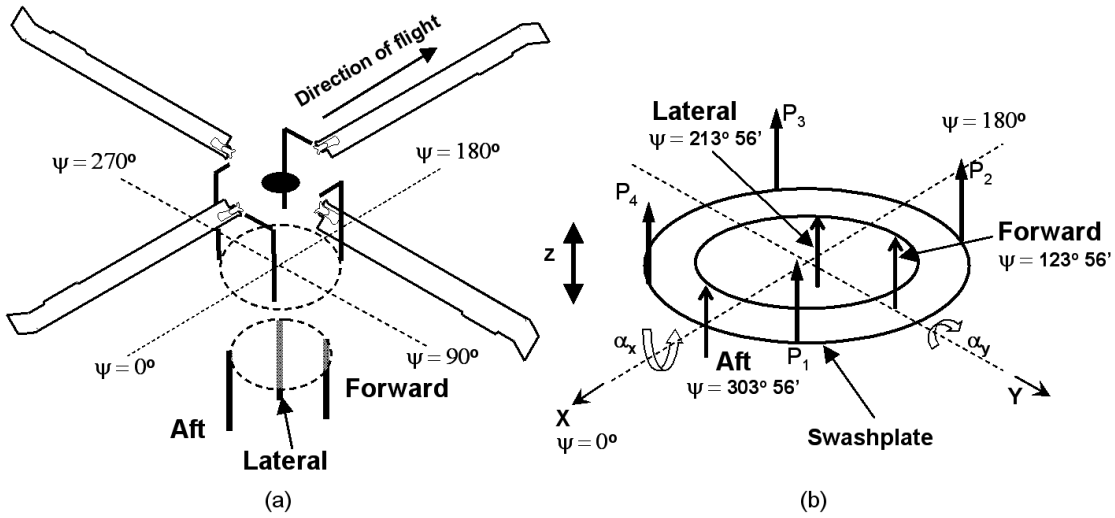

Figure 2.18: **(a) Schematic of UH-60A Blade-Swashplate model; (b) Detailed Swashplate model with 3 servo actuators (forward, aft and lateral) and four pitch links (P_1, P_2, P_3 and P_4); both the rotating and stationary swashplates are of the same size but have been shown to have different sizes for clarity**

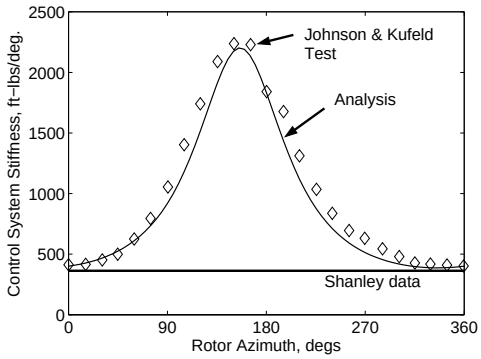

(a) collective

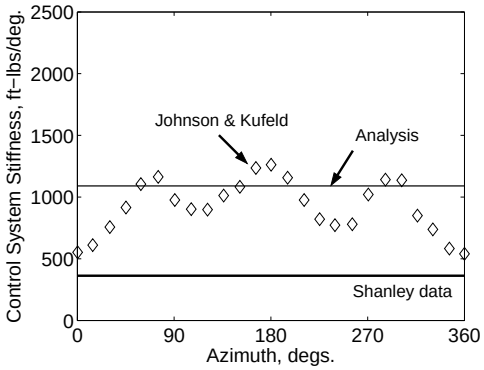

(b) reactionless

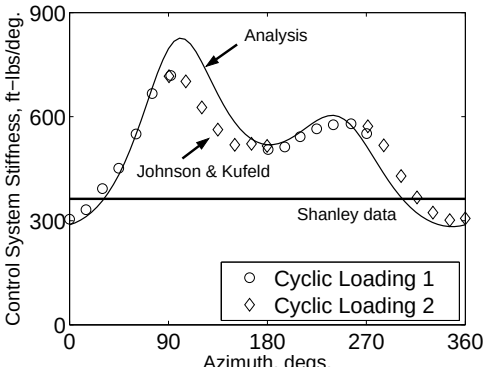

(c) cyclic

Figure 2.19: **Predicted individual blade stiffness as a function of rotor azimuth for (a) collective, (b) reactionless, (c) cyclic loading compared with Johnson and Kufeld (Ref. [180]) and Shanley data (Ref. [184])**

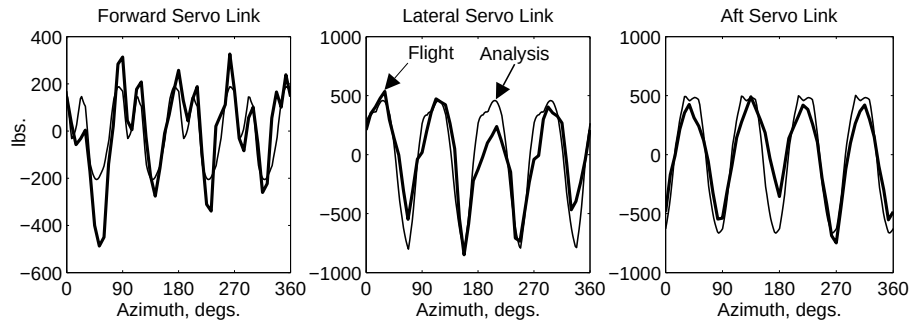

(a) Flight 8534

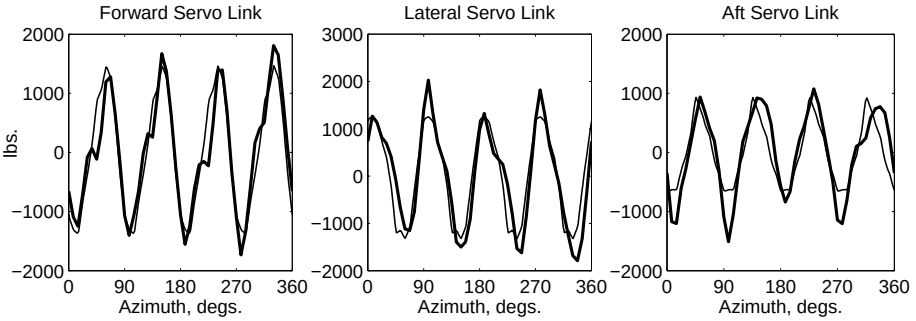

(b) Flight 9017

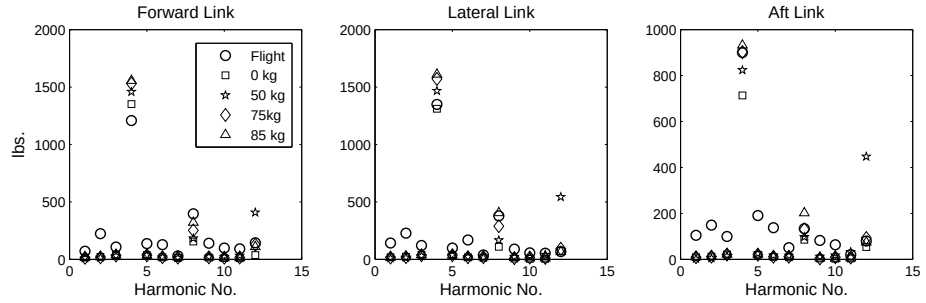

(c) Servo link load harmonics for flight 9017

Figure 2.20: **Predicted swashplate servo loads using measured pitch link load and with 0 kg swashplate mass for (a) high speed flight 8534, and (b) dynamic stall flight 9017, and (c) servo load harmonics for 9017 with swashplate mass of 0, 50, 75, and 85 kg swashplate mass**

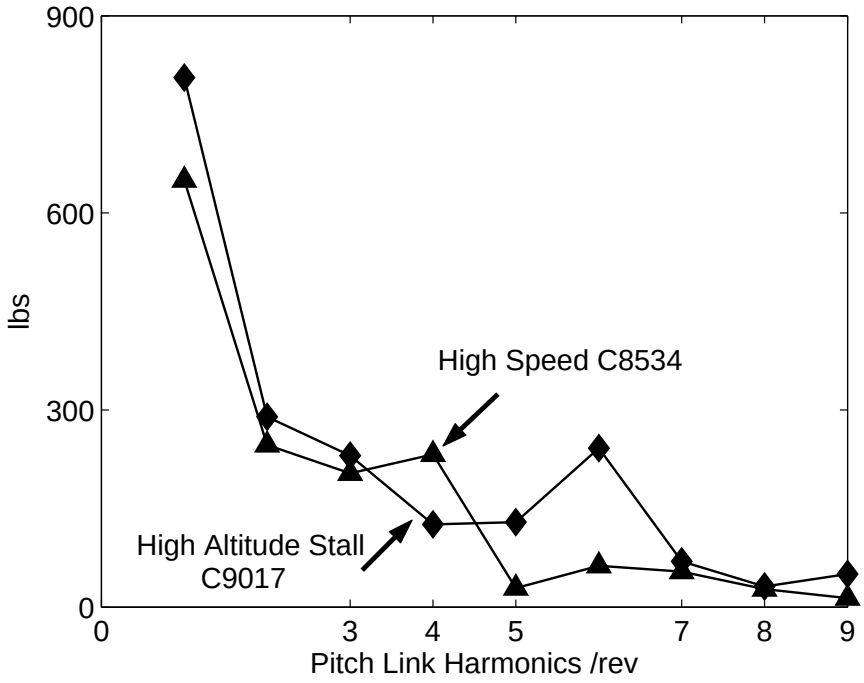

Figure 2.21: **Flight test results: pitch link load harmonics compared for high speed UH-60A flight 8534; $C_W/\sigma = 0.0783$, $\mu = 0.368$; and high altitude dynamic stall flight 9017; $C_W/\sigma = 0.135$, $\mu = 0.237$**

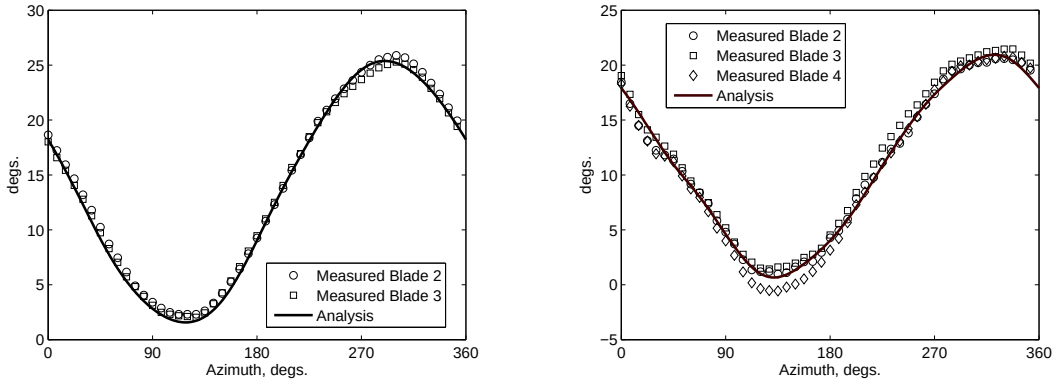

(a) flight 8534 (b) flight 9017

Figure 2.22: **Predicted blade root pitch angle using steady servo inputs for flight 8534 and 9017; using airloads measured in flight; simple 7 degree of freedom, coupled blade swashplate dynamic model**

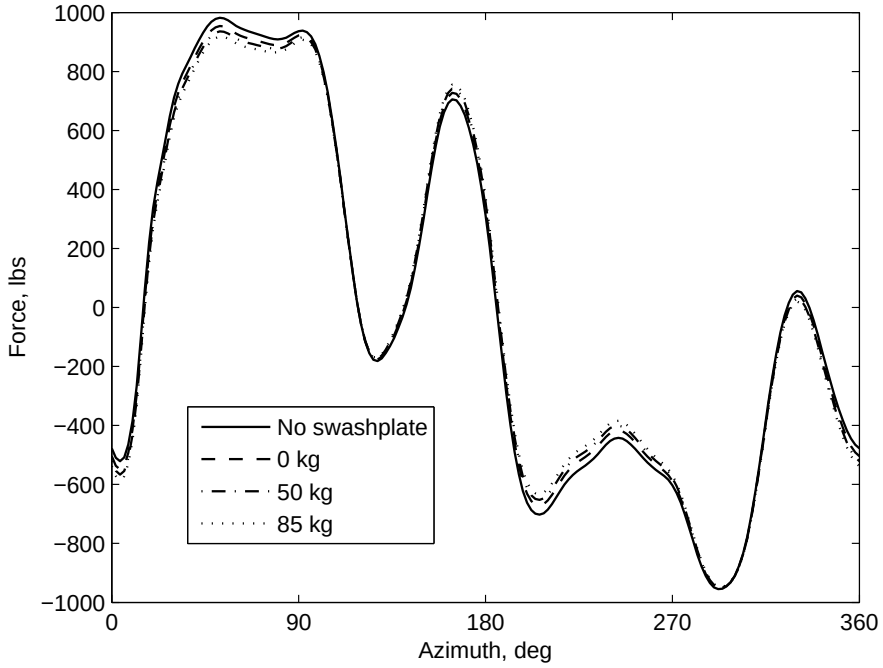

Figure 2.23: **Effect of swashplate dynamics on the pitch link load variation for coupled blade swashplate model for flight 9017**

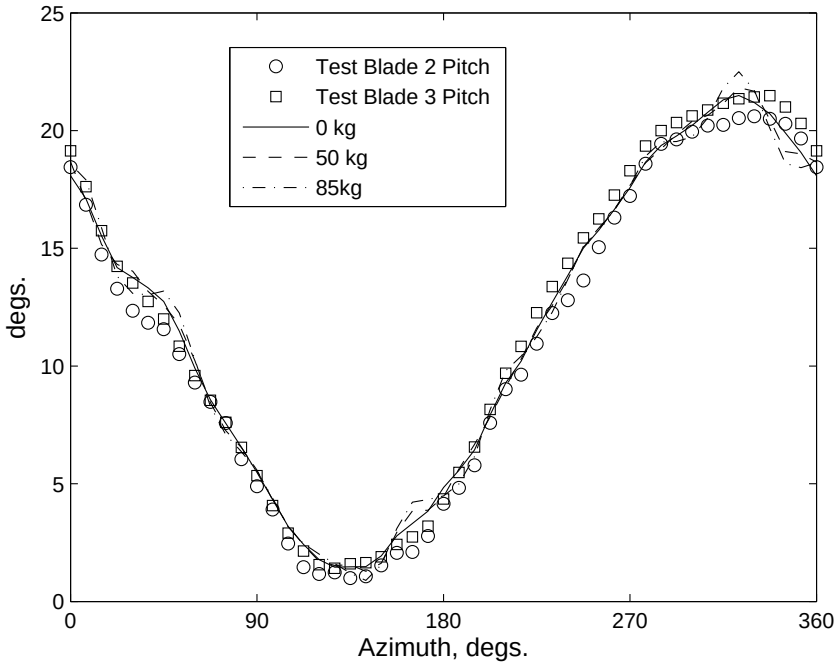

Figure 2.24: **Effect of swashplate dynamics on the blade root pitch angle for coupled blade swashplate system for flight 9017**

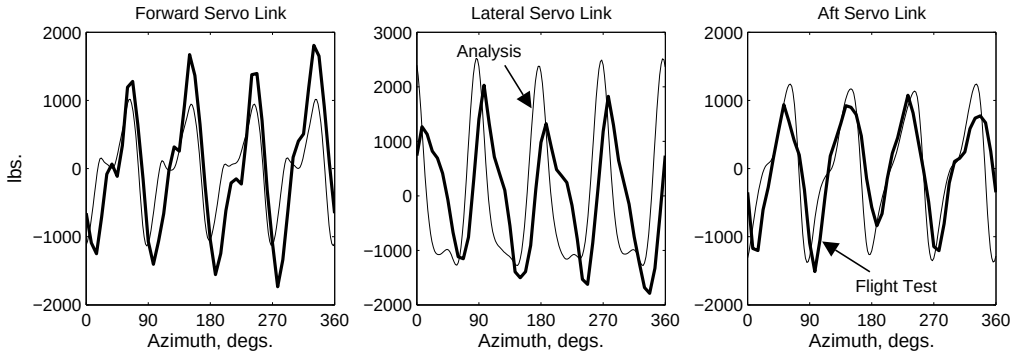

(a) servo loads using swashplate mass of 75 kg

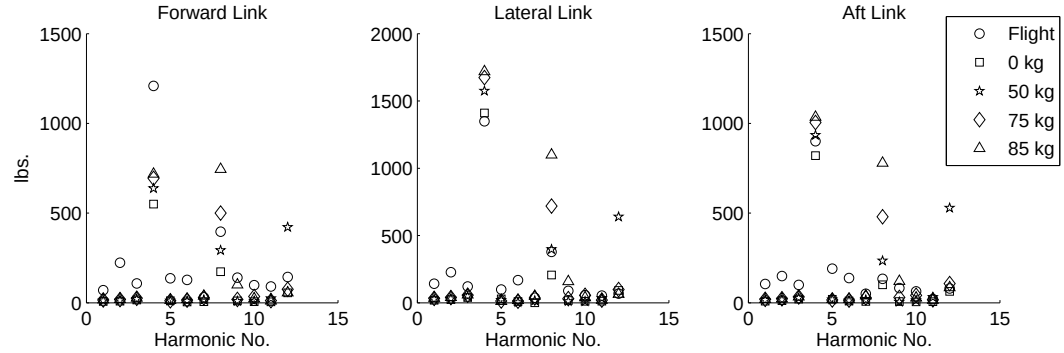

(b) servo loads harmonics

Figure 2.25: **Predicted and measured servo loads for coupled blade swashplate system for flight 9017 (C_W/σ = 0.135, μ = 0.237) (a) waveform, using a swashplate mass of 75 kg, and (b) harmonics using swashplate masses of 0, 50, and 85 kg**

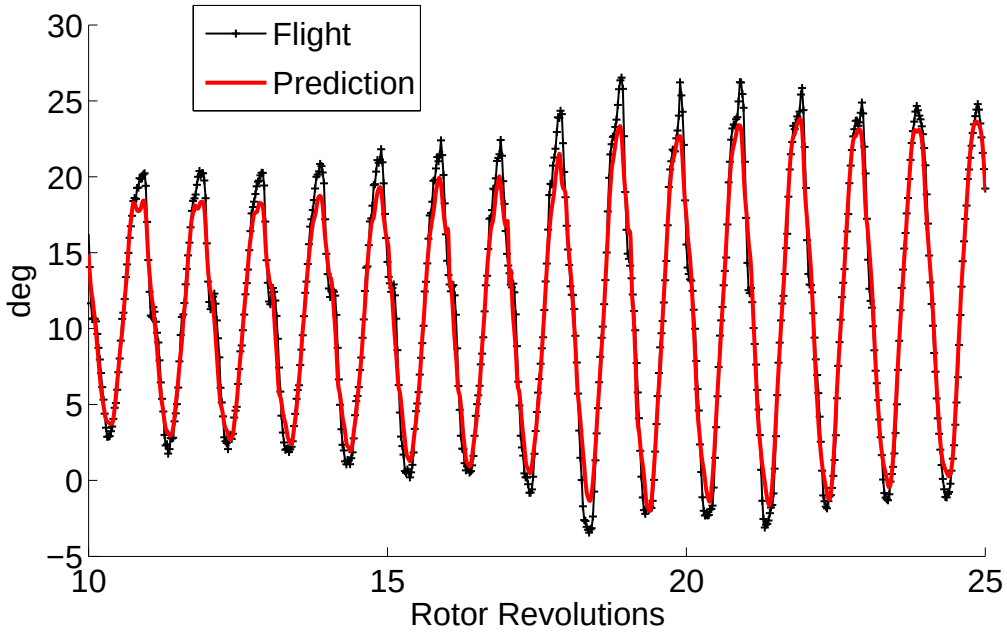

(a) Time history

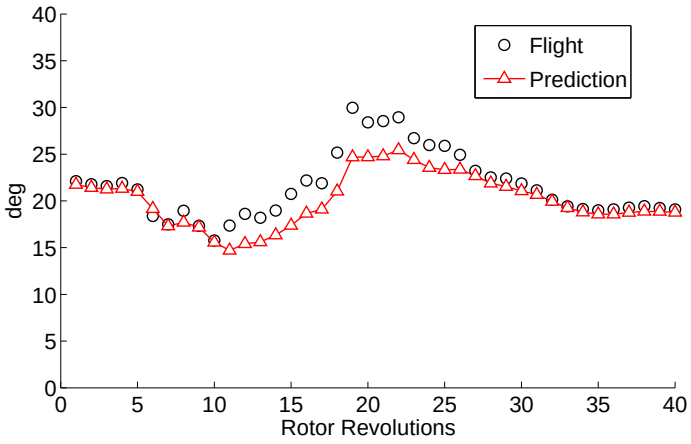

(b) Peak-to-peak

Figure 2.26: **Measured (blade #3) and predicted pitch angle at root; predictions using flight test airloads; time history shown for only 20 revolutions for clarity**

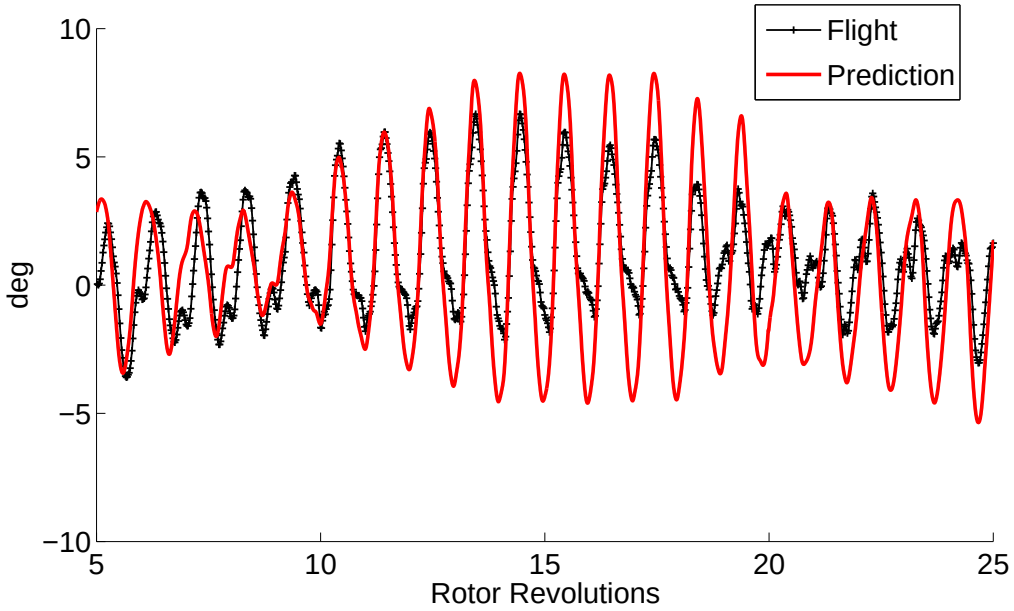

(a) Time history

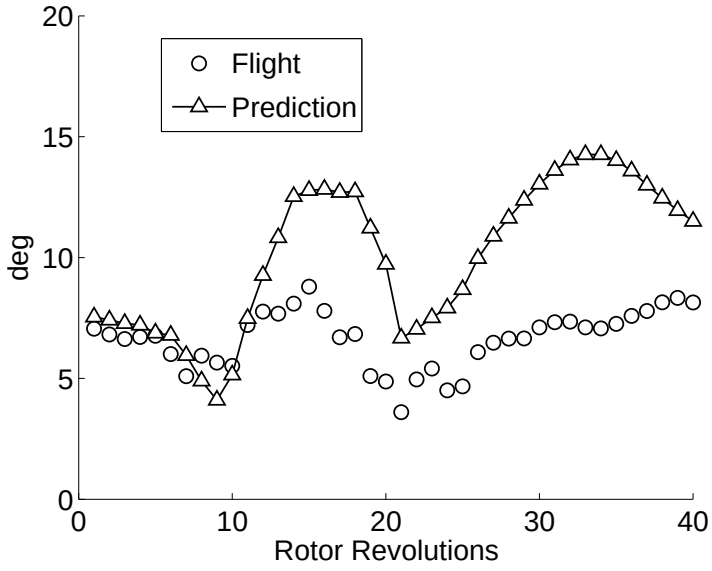

(b) Peak-to-peak

Figure 2.27: **Measured (blade #1) and predicted flap angle at root; predictions using flight test airloads; time history shown for only 20 revolutions for clarity**

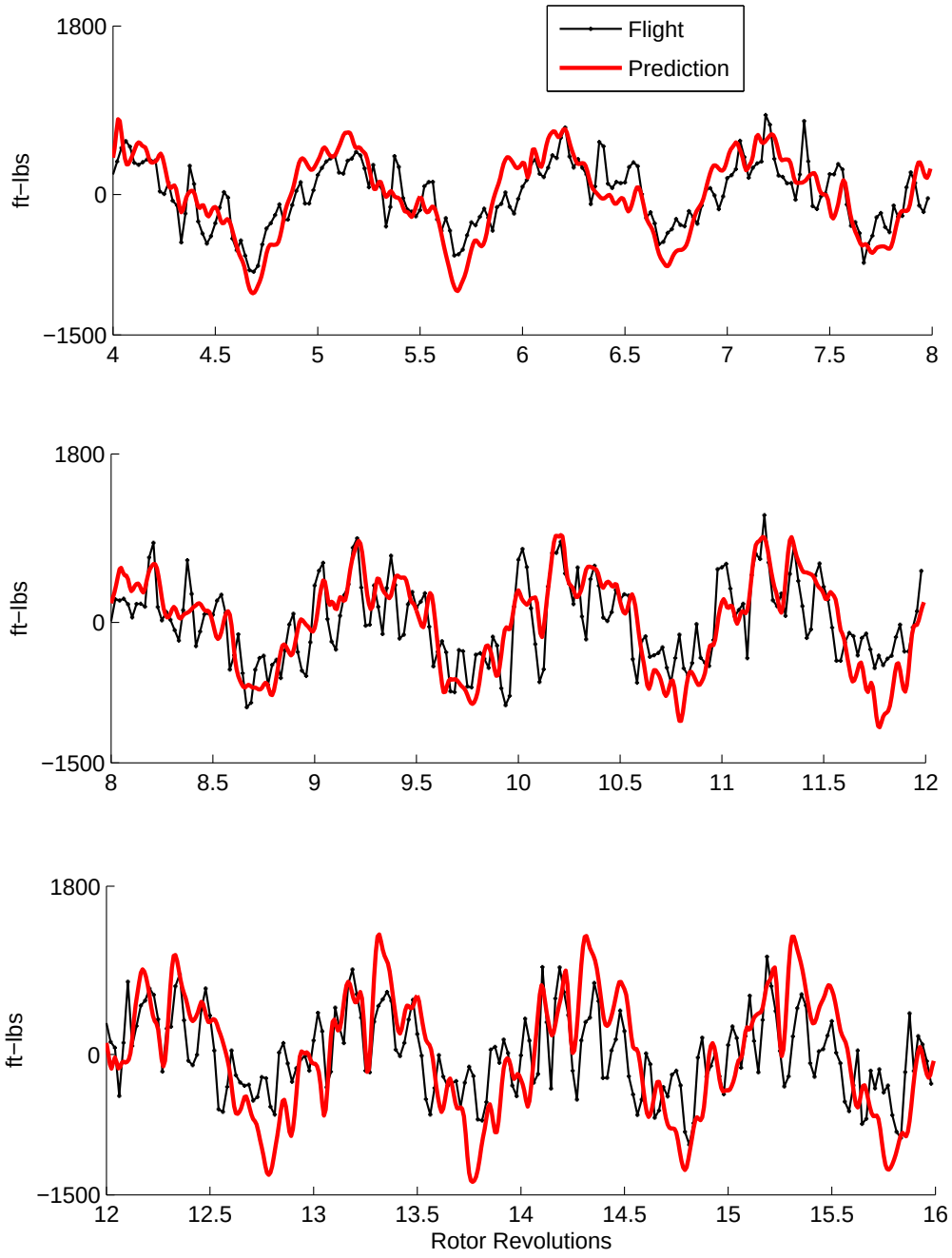

Figure 2.28: **Measured and predicted flap bending moment at 11.3%R; predictions using flight test airloads; mean removed**

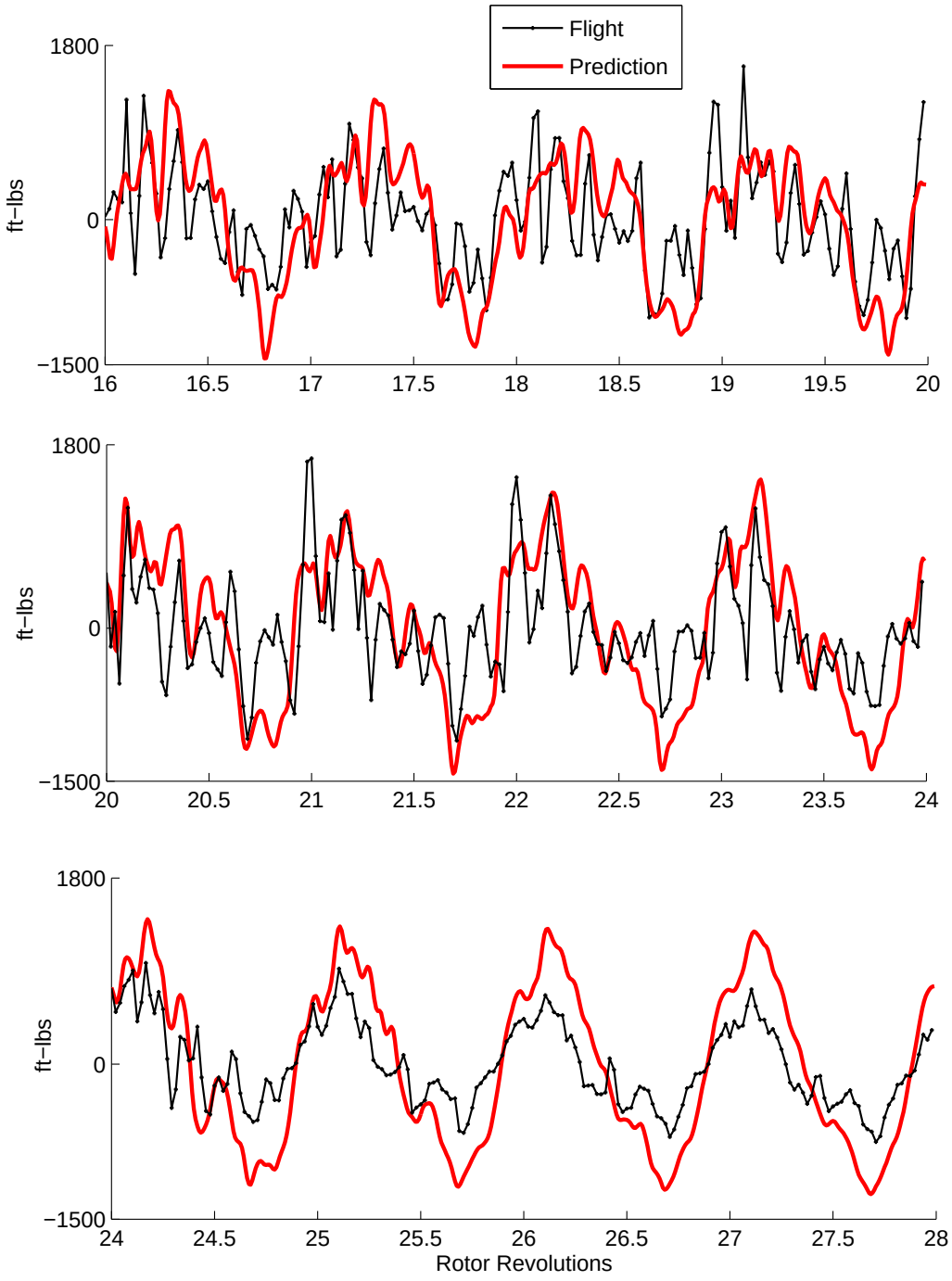

Figure 2.29: **Measured and predicted flap bending moment at 11.3%R; predictions using flight test airloads; mean removed**

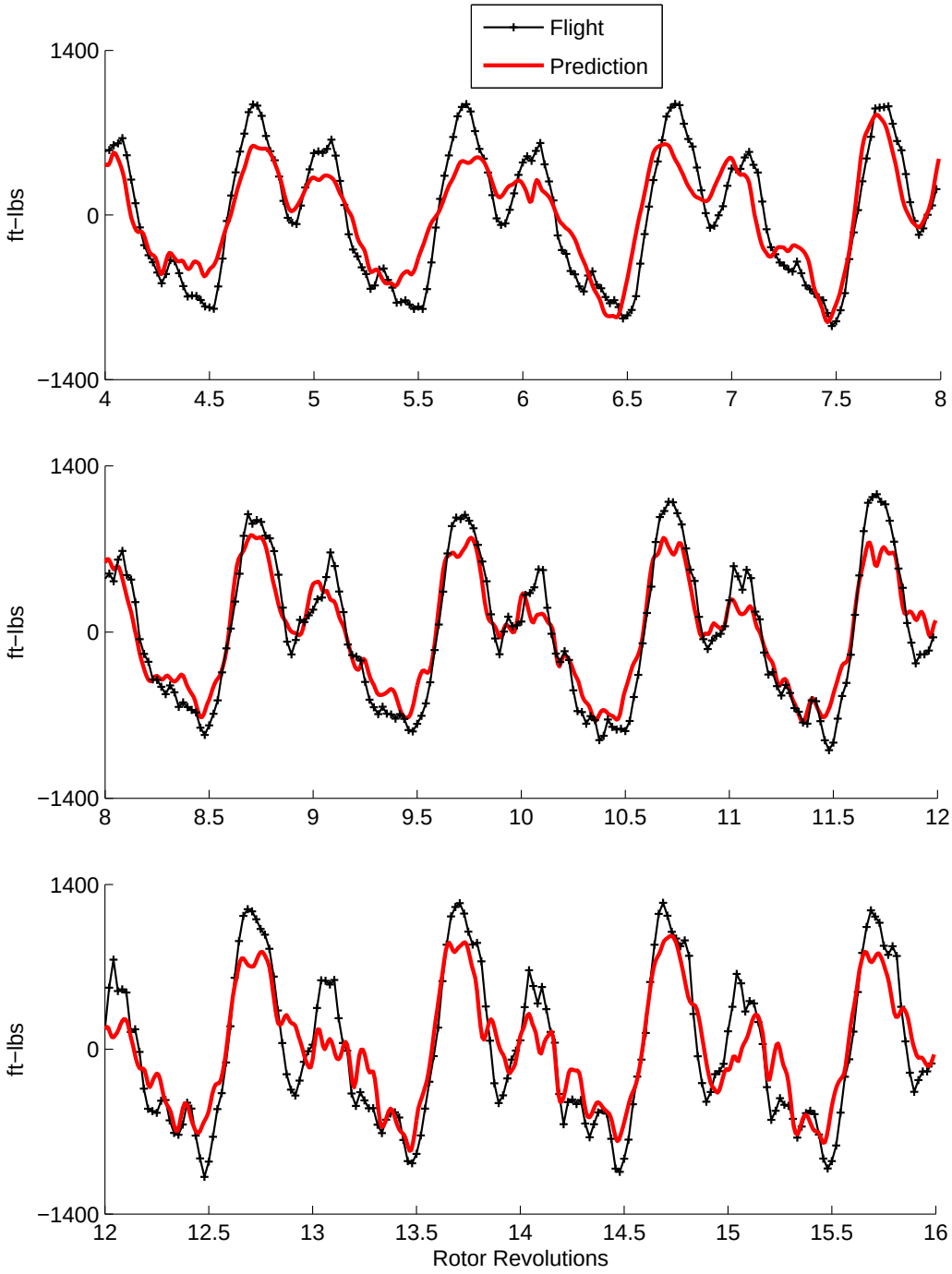

Figure 2.30: **Measured and predicted flap bending moment at 50%R; revs 4–16; predictions using flight test airloads; mean removed**

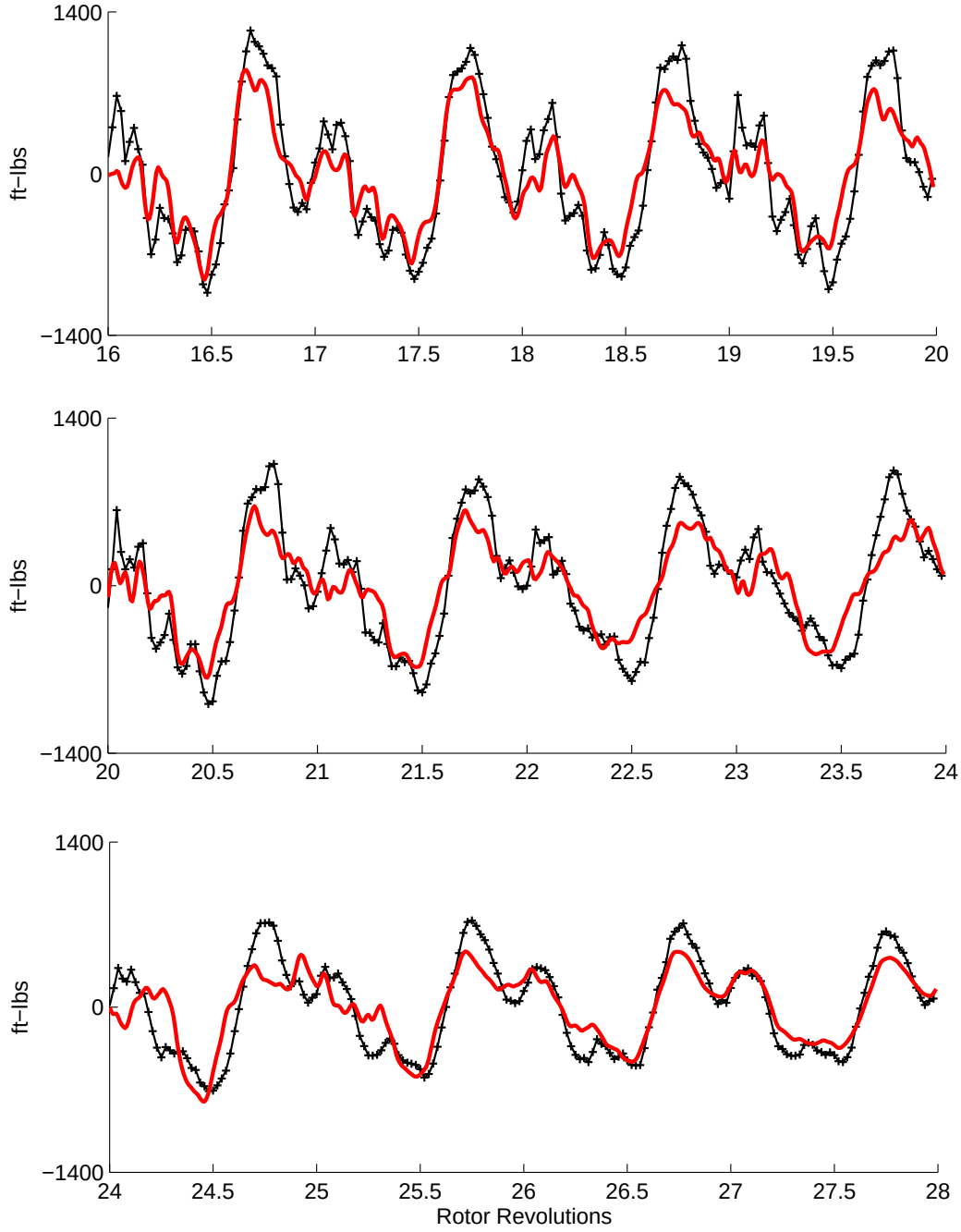

Figure 2.31: **Measured and predicted flap bending moment at 50%R; revs 16–28; predictions using flight test airloads; mean removed**

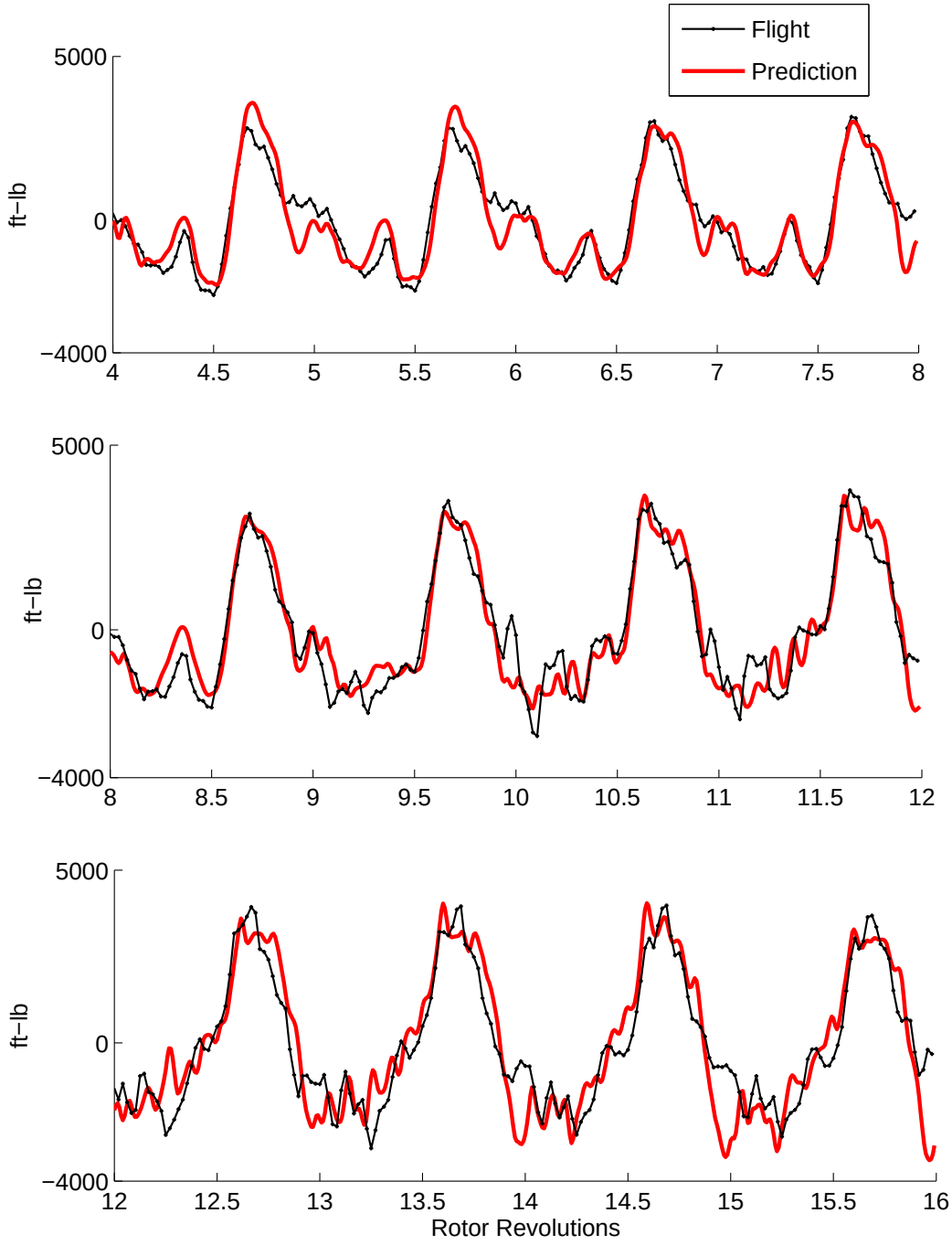

Figure 2.32: **Measured and predicted lag bending moment at 11.3%R; revs 4–16; predictions using flight test airloads; mean removed**

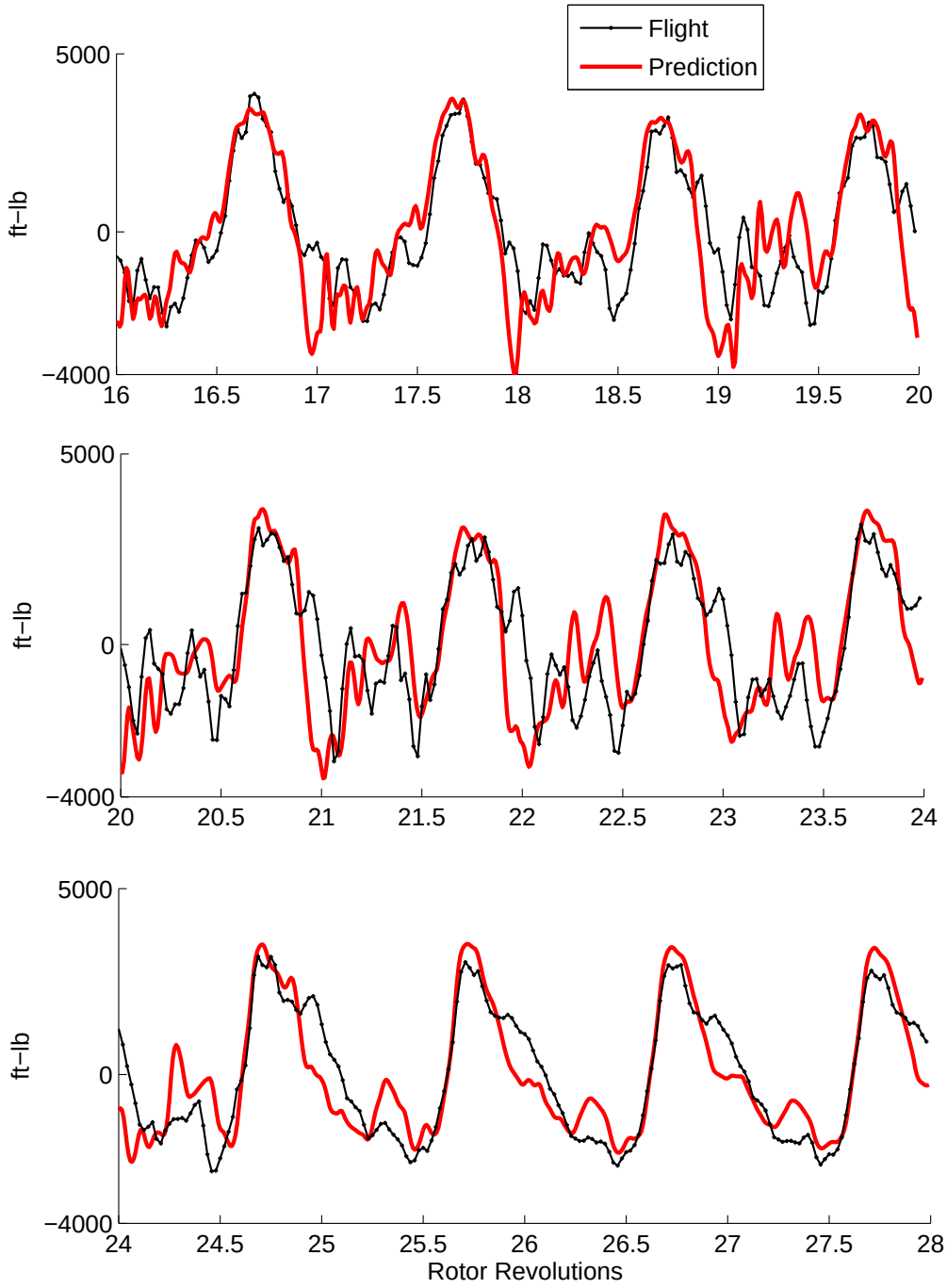

Figure 2.33: **Measured and predicted lag bending moment at 11.3%R; revs 16–28; predictions using flight test airloads; mean removed**

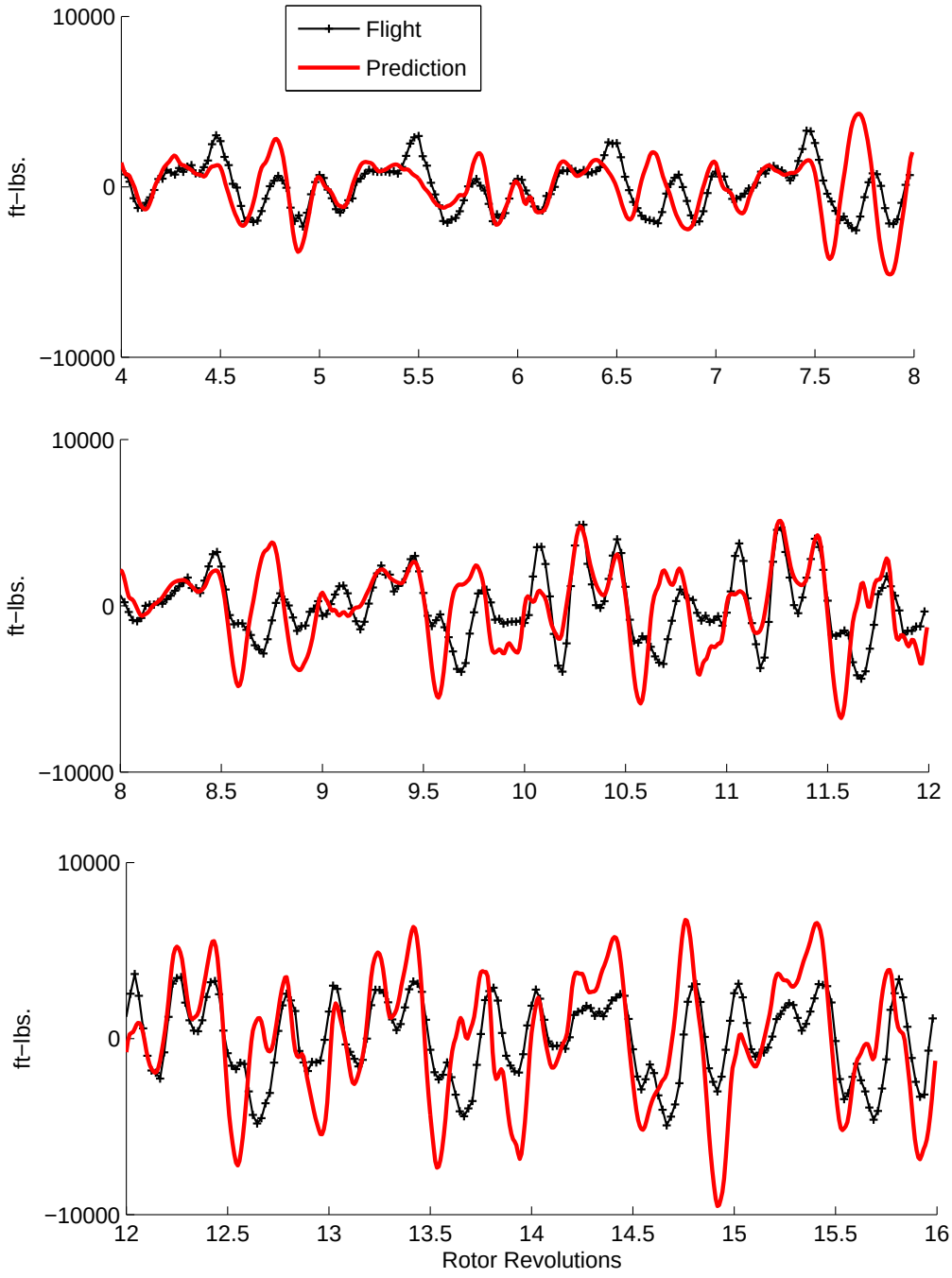

Figure 2.34: **Measured and predicted lag bending moment at 50%R; revs 4–16; predictions using flight test airloads; mean removed**

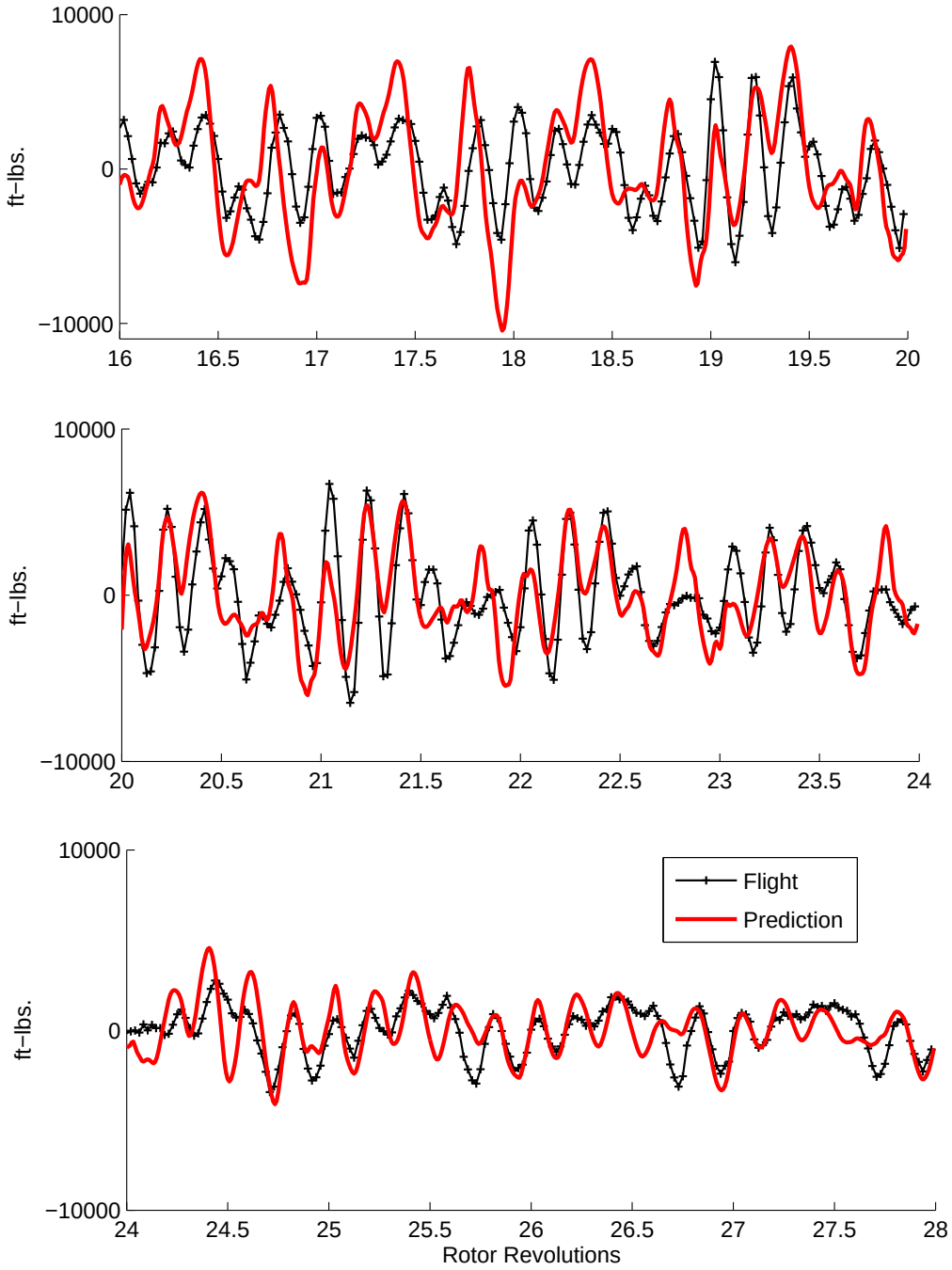

Figure 2.35: **Measured and predicted lag bending moment at 50%R; revs 16–28; predictions using flight test airloads; mean removed**

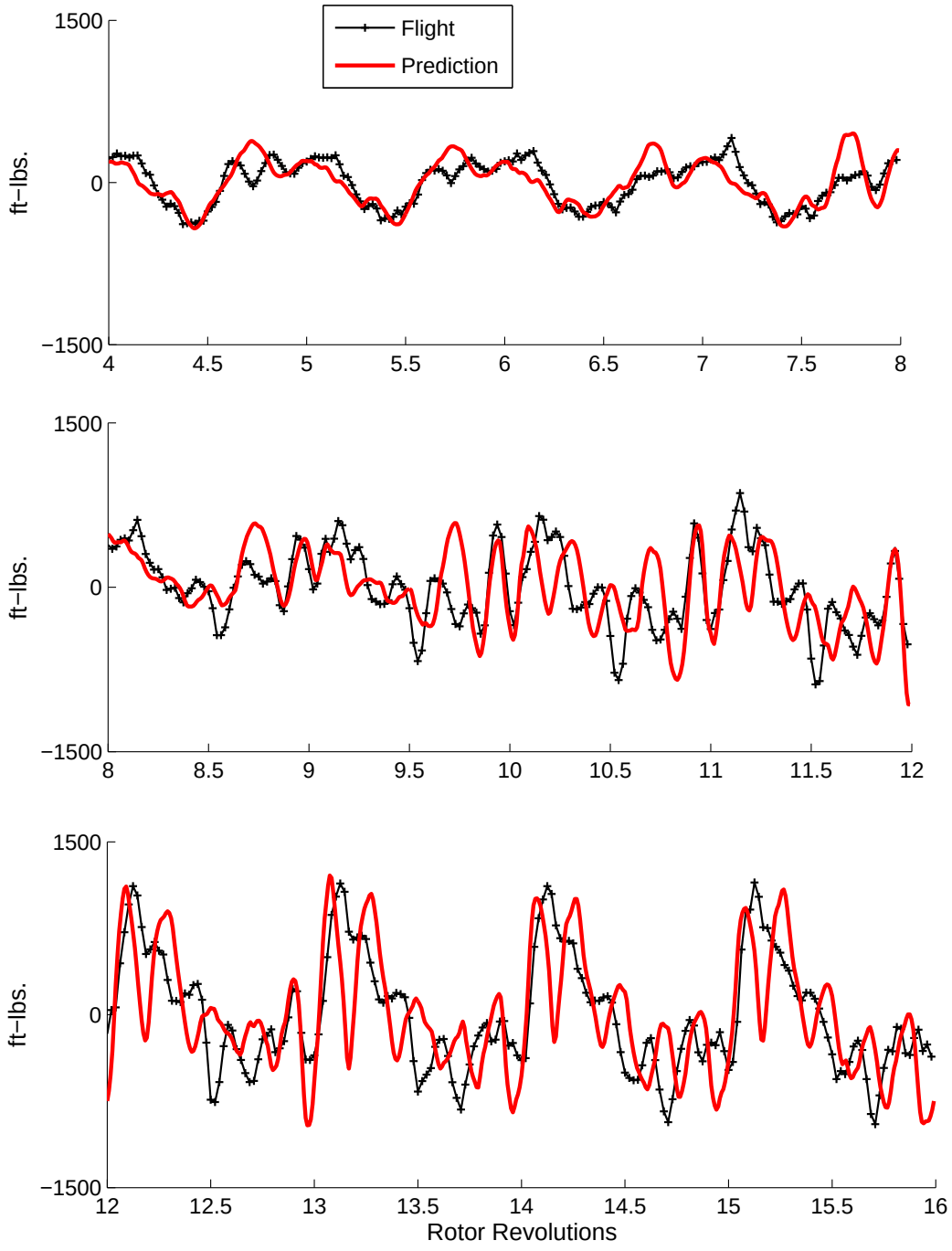

Figure 2.36: **Measured and predicted torsion moment at 30%R; revs 4–16; predictions using flight test airloads; mean removed**

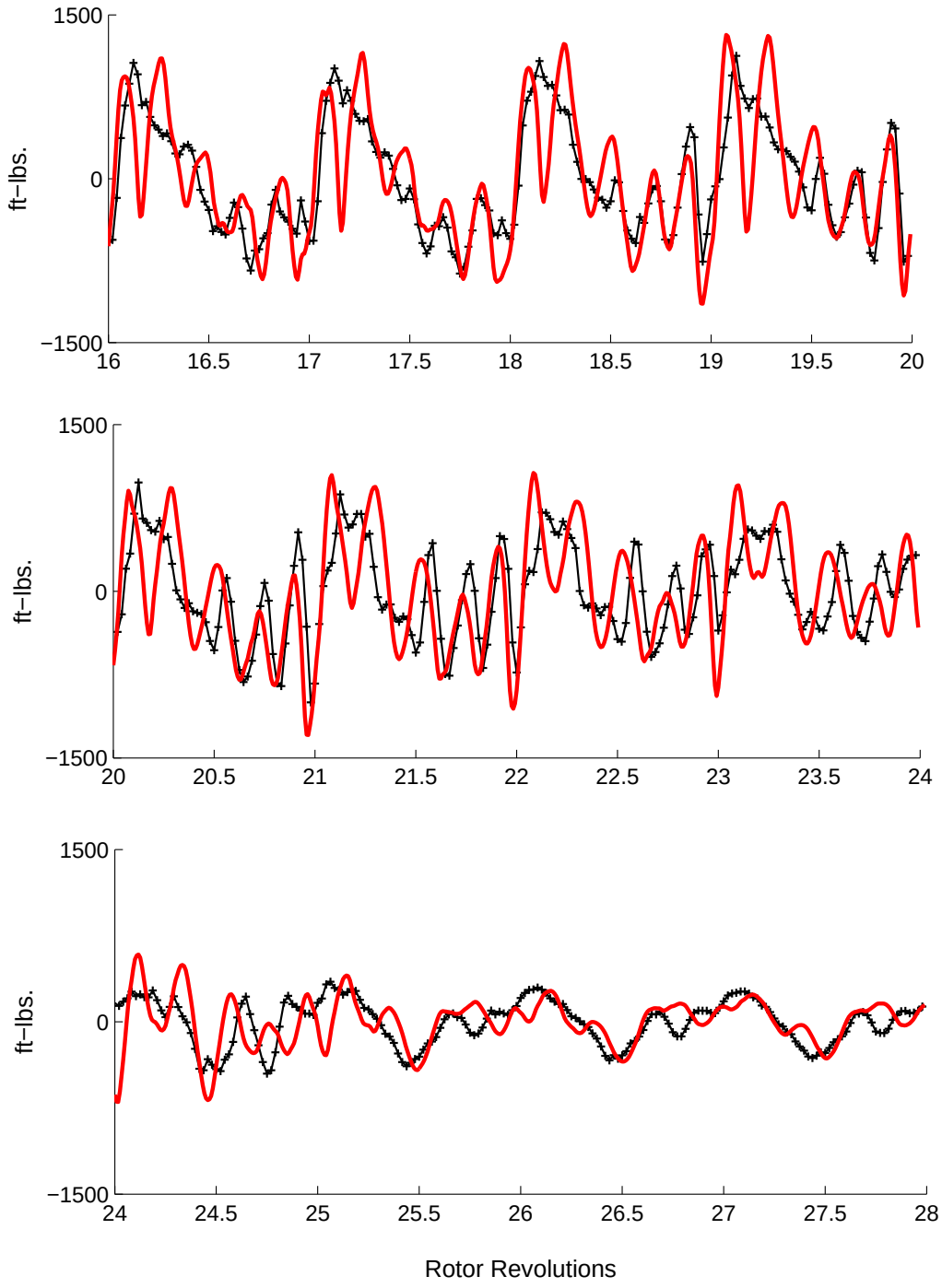

Figure 2.37: **Measured and predicted torsion moment at 30%R; revs 16–28; predictions using flight test airloads; mean removed**

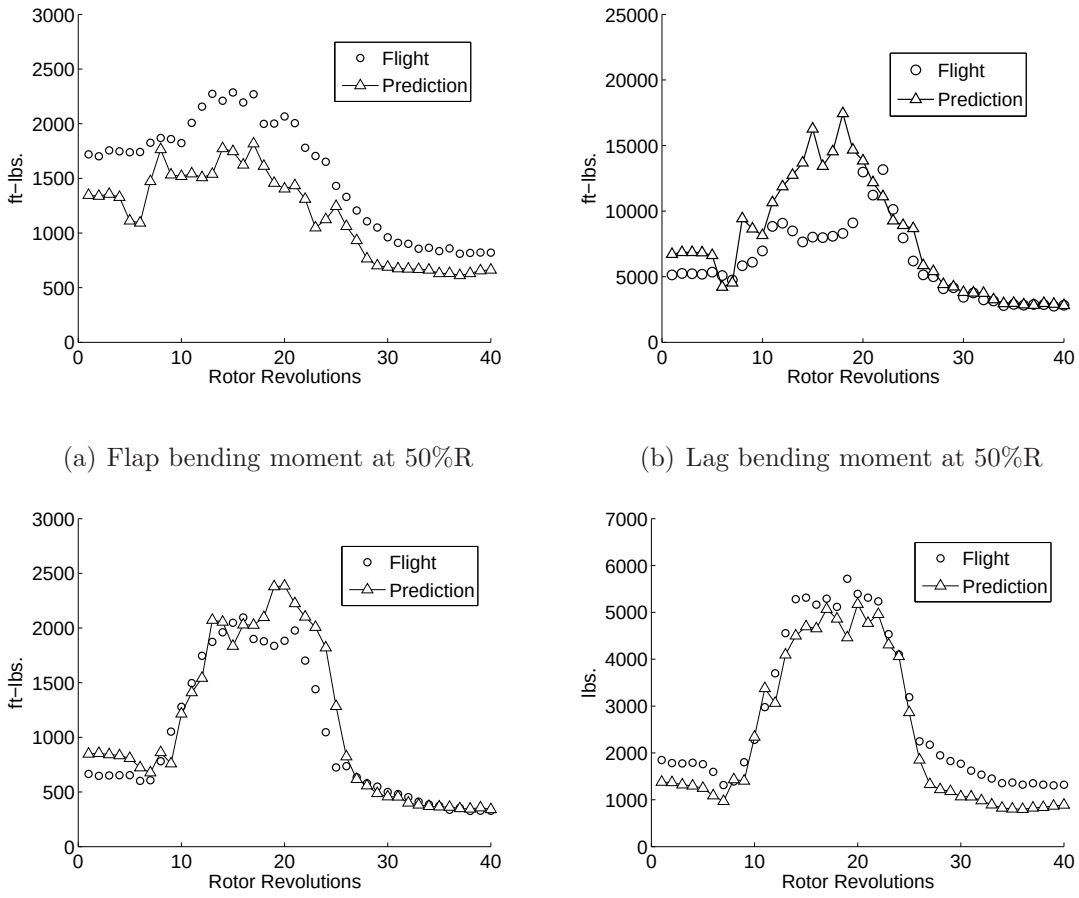

(a) Flap bending moment at 50%R

(b) Lag bending moment at 50%R

(c) Torsion moment at 30%R

(d) Pitch-link load

Figure 2.38: **Measured and predicted peak-to-peak structural loads; predictions using flight test airloads**

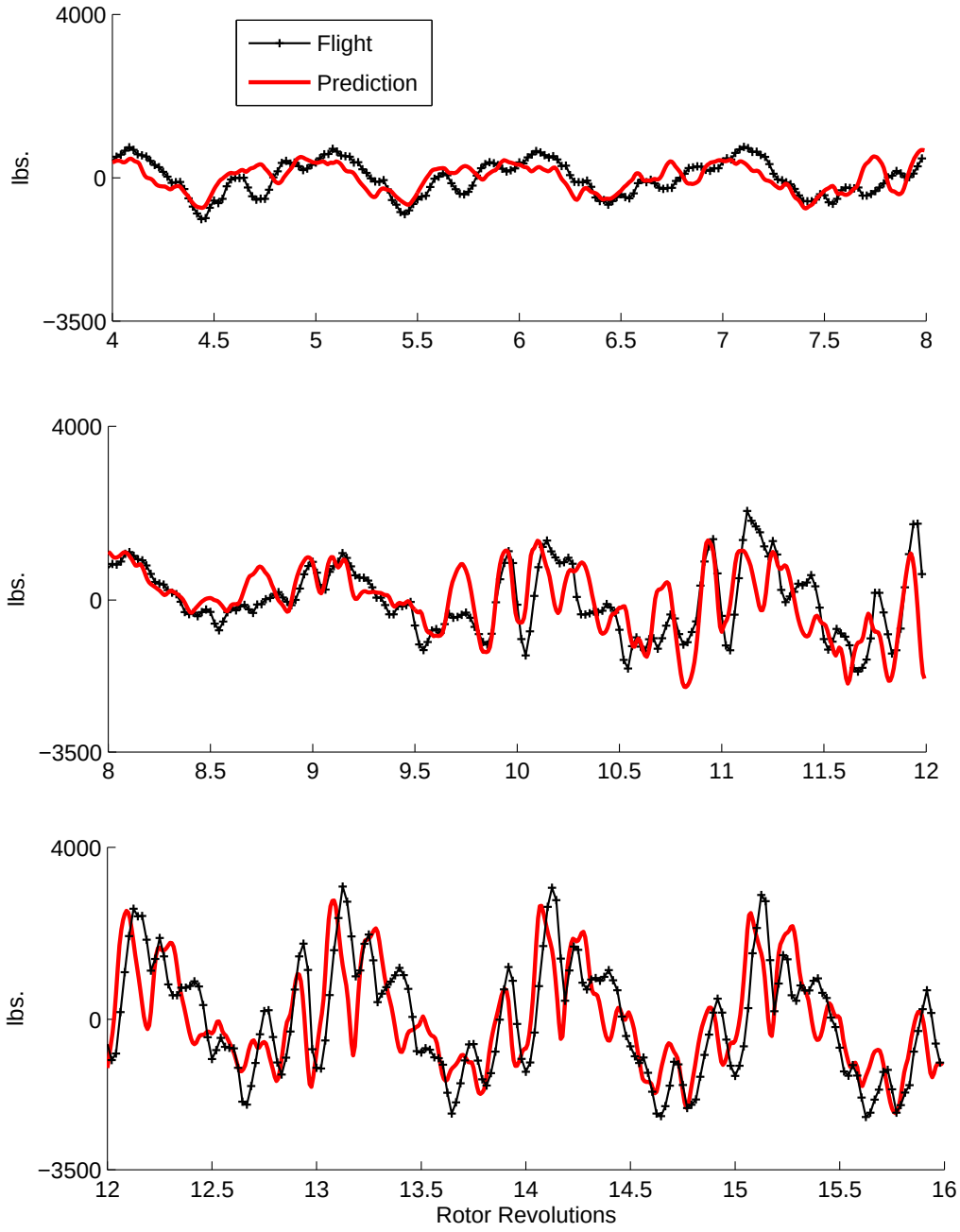

Figure 2.39: **Measured and predicted pitch-link load; revs 4–16; predictions using flight test airloads; mean removed**

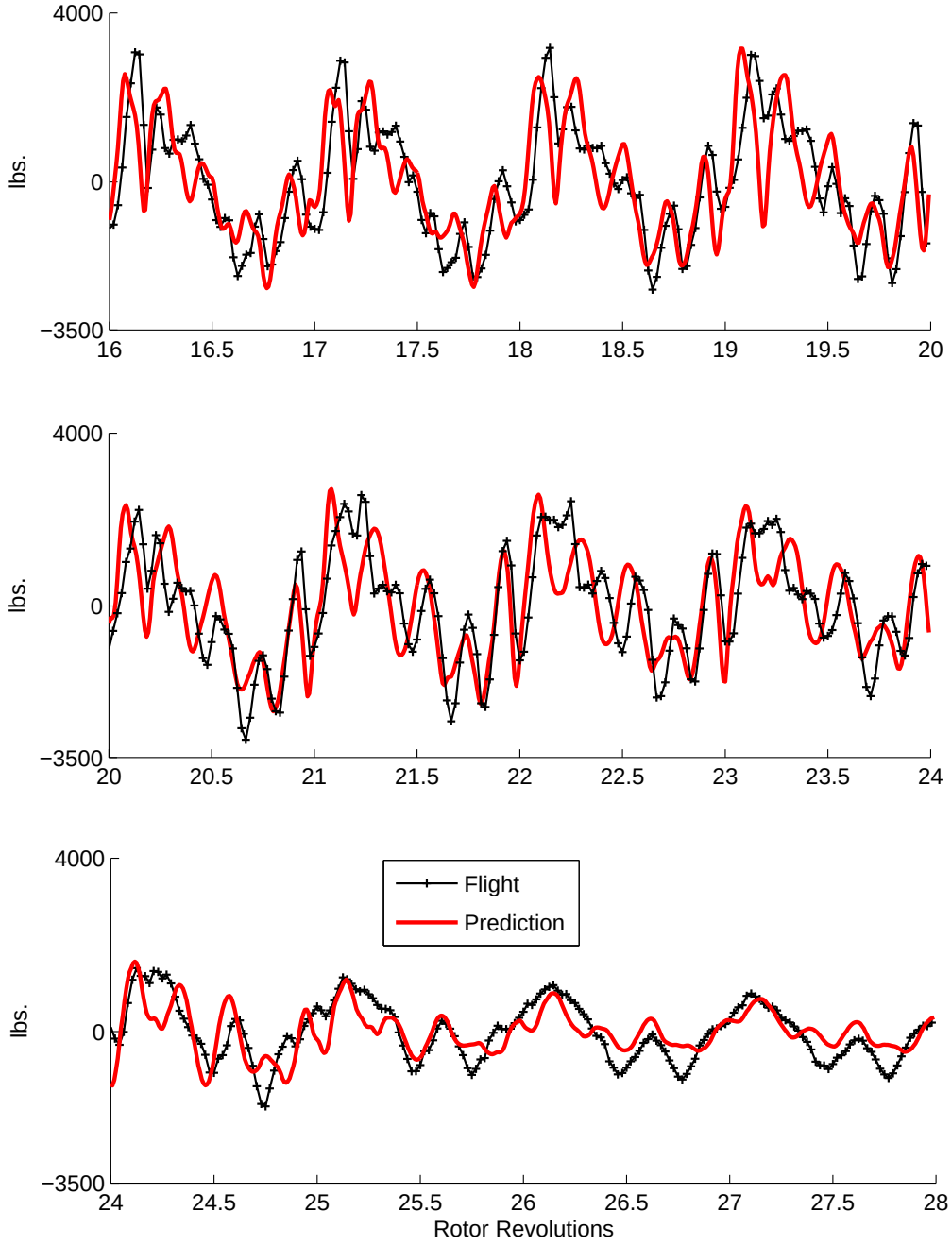

Figure 2.40: **Measured and predicted pitch-link load; revs 16–28; predictions using flight test airloads; mean removed**

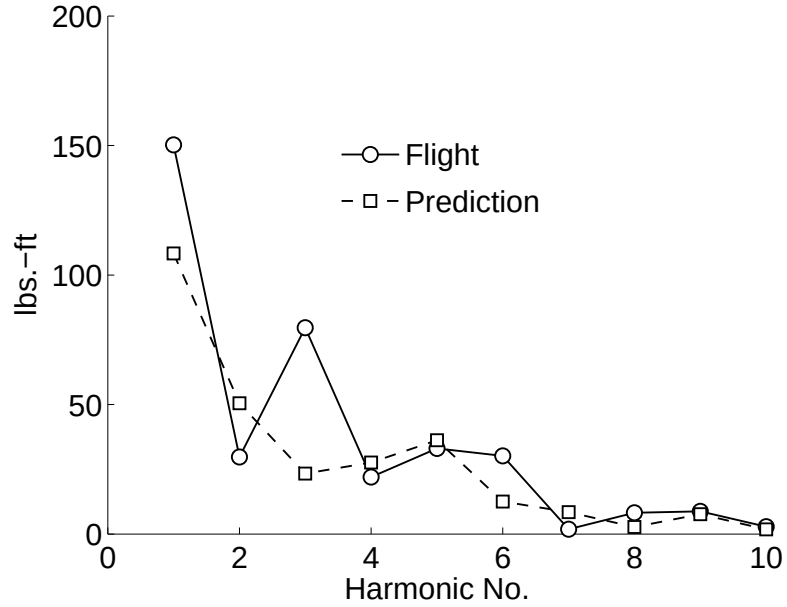

Figure 2.41: **Measured and predicted torsion moment harmonics at 70%R for rev 1 (steady flight conditions); predictions using flight test airloads.**

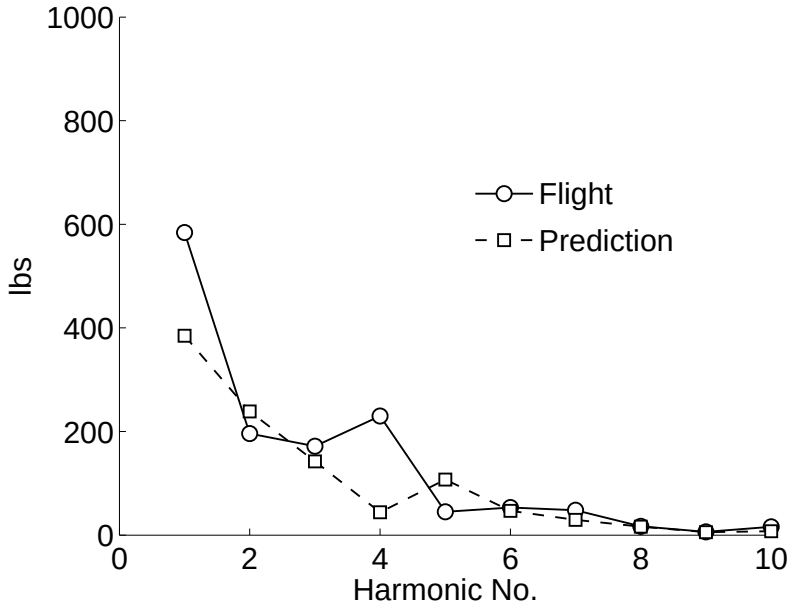

Figure 2.42: **Measured and predicted pitch-link load harmonics for rev 1; predictions using flight test airloads.**

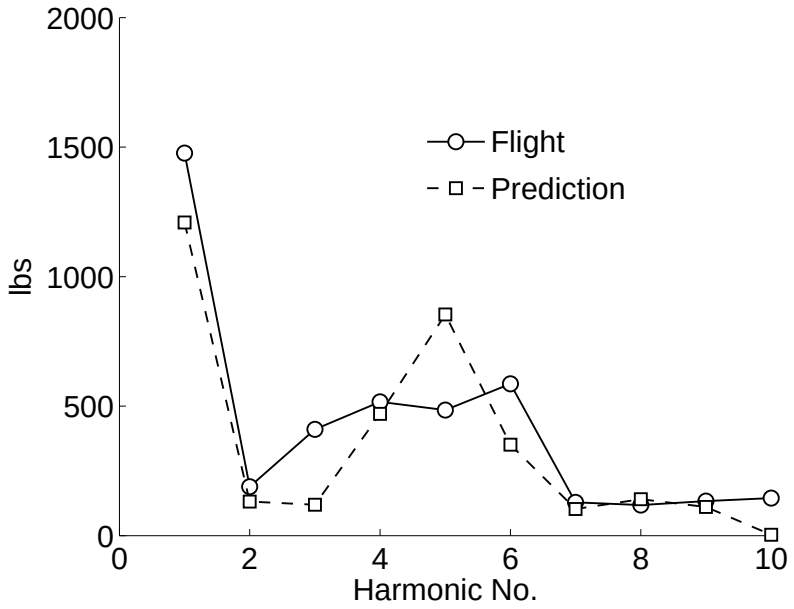

Figure 2.43: **Measured and predicted pitch-link load harmonics for rev 14 (highest load factor); predictions using flight test airloads.**

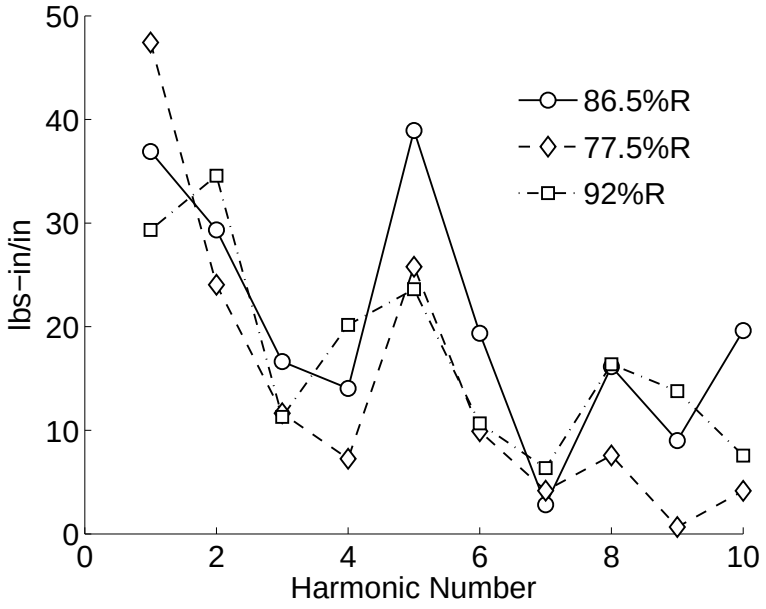

Figure 2.44: **Measured pitching moment harmonics for rev 14 at different radial stations.**

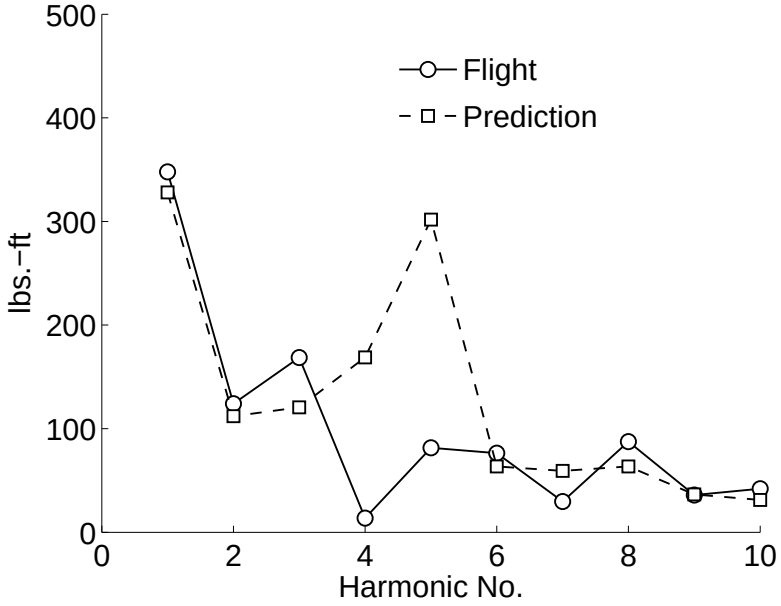

Figure 2.45: **Measured and predicted torsion moment harmonics for rev 14.**

Chapter 3

Aerodynamic Modeling

3.1 Introduction

This chapter describes and validates the aerodynamic modeling of rotor blades. The objective is prediction and fundamental understanding of airloads during an unsteady maneuver. Two aerodynamics analyses are used: (1) a lifting-line analysis, and (2) a 3-D Reynolds Averaged Navier Stokes (RANS) CFD analysis. These two methodologies in that order define the state-of-art in low and high-fidelity airloads calculation.

The lifting-line model, although a low fidelity model, facilitates the separation of the effects of control angles, dynamic stall and wake. In addition, it provides direct airfoil angle of attack calculation, which is critical for better understanding of the airloads mechanism. Comparisons of the airloads predicted using lifting-line analysis to those obtained using CFD helps in the identification of its limitations in comprehensive rotor analysis for maneuver. The deformations obtained from measured airloads analysis carried out in chapter 2 is used to predict the airloads. The use of identical deformations for both the aerodynamic models allows for their consistent comparison. Further, this isolates the physics of structural dynamics and aerodynamics and allows them to be studied separately. The prescribed deforma-

tions serve as an accurate set of input to the aerodynamic models and would be used in the identification of the physical mechanism of the advancing blade stall which was never attempted before.

This chapter first discusses the development of a lifting-line based comprehensive analysis with focus on the refinements made for maneuver. Next, the CFD model used in the present study, University of Maryland Transient Unsteady Reynolds Navier Stokes (UMTURNS), is described briefly. Rotor structural model described in the chapter 2 is coupled to each aerodynamic model separately to simulate the UTTAS pull-up maneuver (chapters 4 and 5).

3.2 Lifting-line Analysis

The lifting line aerodynamic model described later in this chapter consistently combines 2D airfoil table look-up, based on angle of attack calculated using blade deformation, with Leishman-Beddoes 2D unsteady aerodynamics for attached and separated flows [91]. The wake modeling includes a Weissinger-L (W-L) type lifting-surface model for near wake modeling and a time accurate free wake model based on Ananthan and Leishman [73] for modeling the far wake. The original free wake model is modified to include flexible blade deformations and a generalized set of vortex trailers. The blade angle of attack calculation includes the effect of helicopter roll and pitch motions.

At each azimuth (i.e. time), the inputs into the lifting-line analysis are the blade deformations for all blades, the instantaneous advance ratio, shaft tilt angles,

the rotor pitch and roll angles and angular rates, and the control angles. The outputs from the model are the airloads occurring on all blades, and the inflow velocities at the blade control points (swept 3/4 chord line) on all blades, at that instant. Within the model, the airloads are calculated using the inflow velocities obtained in the previous time step. The current blade deformations are used along with inflow velocities stored from the previous time step to calculate the airloads, bound circulation distribution, near wake trailer strengths, and near wake induced velocities at the blade control points. The near wake induced velocities are then used to re-calculate the airloads. The bound circulation distribution and the current blade deformations are then used to advance the free wake solution to the present time step. This free wake solution is then used in the calculation of airloads in the next time step. The airloads at the present time step are re-calculated including the near wake induced velocities. The effect of shed wake is incorporated using an unsteady aerodynamic model. At each time step, the unsteady model is updated based on the change in airloads from the previous time step. The Leishman- Beddoes unsteady model (for attached and separated flows) is used in the present analysis. The numerical solution procedure of the free wake is same as that of the Ananthan-Leishman model, validated in Ref. [73]. However, the present formulation incorporates flexible blade deformations in flap, lag, and torsion, and the vortex strengths and boundary conditions are prescribed. The objective is to formulate a N_b bladed transient lifting line analysis that can be interfaced with a CSD model for a time-marching aeroelastic solution. In this chapter, the aerodynamic model is validated in isolation.

3.2.1 Angle of Attack Calculation

The sectional angle of attack for a rotor is the net result of two velocity components; the wind velocity and the blade velocity. The blade velocity is determined by rotor motion relative to the hub, and the motion of hub relative to the helicopter center of gravity (c.g.). The general expression for which, at a radial station x in the rotating undeformed frame is

$$\vec{V} = -\vec{V}_w + \vec{V}_b + \vec{V}_f \tag{3.1}$$

where $\vec{V}_w$ is the wind velocity relative to hub fixed frame, due to the vehicle speed and inflow, $\vec{V}_b$ is the blade velocity relative to the hub fixed frame resulting from blade motion, and $\vec{V}_f$ is the blade velocity caused by hub motion relative to the c.g. It should be noted that the $\vec{V}_f$ only includes the effect of fuselage angular speed for a rigid shaft, the effect of translational speed is already included in $\vec{V}_w$.

The wind velocity in the non-rotating hub frame can be expressed as:

$$\vec{V}_w = (\mu\Omega R)\hat{I}_H - (\lambda\Omega R)\hat{K}_H \tag{3.2}$$

where $\mu = V\cos\alpha_s/\Omega R$ is the rotor advance ratio; V is the vehicle forward speed, α_s is the rotor longitudinal shaft tilt (positive nose down); λ is the rotor non-dimensional inflow; and ΩR is the rotor tip speed.

The wind velocity can be transformed to the rotating deformed frame using two transformations, first from the hub fixed non-rotating frame to the rotating frame (Eq. 3.3) and then to the rotating system with the precone angle β_p (Eq. 3.5).

$$\begin{Bmatrix} \hat{I} \\ \hat{J} \\ \hat{K} \end{Bmatrix} = T_{RH} \begin{Bmatrix} \hat{I}_H \\ \hat{J}_H \\ \hat{K}_H \end{Bmatrix} \tag{3.3}$$

where

$$T_{RH} = \begin{bmatrix} \cos\psi & \sin\psi & 0 \\ -\sin\psi & \cos\psi & 0 \\ 0 & 0 & 1 \end{bmatrix} \tag{3.4}$$

The second transformation from the rotating frame with no precone to that at a precone angle is expressed by

$$\begin{Bmatrix} \hat{i} \\ \hat{j} \\ \hat{k} \end{Bmatrix} = T_{UR} \begin{Bmatrix} \hat{I} \\ \hat{J} \\ \hat{K} \end{Bmatrix} \tag{3.5}$$

where

$$T_{UR} = \begin{bmatrix} \cos\beta_p & 0 & \sin\beta_p \\ 0 & 0 & 1 \\ -\sin\beta_p & 0 & \cos\beta_p \end{bmatrix} \tag{3.6}$$

The final expression of the wind velocity in the undeformed frame can be obtained by substituting Eqs. 3.3 and 3.5 in Eq. 3.2

$$\left.\begin{aligned} V_{w_x} &= \mu\Omega R\cos\psi - \lambda\Omega R\beta_p \\ V_{w_y} &= -\mu\Omega R\sin\psi \\ V_{w_z} &= -\mu\Omega R\cos\psi\beta_p - \lambda\Omega R \end{aligned}\right\} \tag{3.7}$$

and making the small angle assumption for β_p.

The blade velocity relative to the hub, in the rotating undeformed frame can be written as

$$\vec{V_b} = \dot{\vec{r}} + \vec{\Omega} \times \vec{r} \tag{3.8}$$

where,

$$\vec{r} = x_1\hat{i} + y_1\hat{j} + z_1\hat{k} \tag{3.9}$$

$$\dot{\vec{r}} = \dot{x_1}\hat{i} + \dot{y_1}\hat{j} + \dot{z_1}\hat{k} \tag{3.10}$$

$$\vec{\Omega} = \Omega\hat{K} \tag{3.11}$$

The expressions for $x_1, y_1, z_1, \dot{x_1}, \dot{y_1}, \dot{z_1}$ are given by (Ref. [168])

$$\left.\begin{aligned} x_1 &= x + u - \lambda_T\phi' - v'(y_1 - v) - w'(z_1 - w) \\ y_1 &= v + (y_1 - v) \\ z_1 &= w + (z_1 - v) \end{aligned}\right\} \tag{3.12}$$

where,

$$\left.\begin{aligned} (y_1 - v) &= \eta\cos(\theta + \hat{\phi}) - \eta\sin(\theta + \hat{\phi}) \\ (z_1 - v) &= \eta\sin(\theta + \hat{\phi}) + \eta\cos(\theta + \hat{\phi}) \end{aligned}\right\} \tag{3.13}$$

and

$$\left.\begin{aligned} \dot{x}_1 &= \dot{u} - \lambda_T\dot{\phi}' - (\dot{v}' + w'\dot{\theta}_1 - (w' - v'\dot{\theta}_1(z_1 - w) \\ \dot{y}_1 &= \dot{v} + (y_1 - v)\dot{\theta}_1 \\ \dot{z}_1 &= \dot{w} + (z_1 - v)\dot{\theta}_1 \end{aligned}\right\} \tag{3.14}$$

It should be noted that the deformations (u, v, w, ϕ) used in the above expressions are no longer defined in the local element frame, which was the case in chapter 2. The deformations used in the derivation of aerodynamic loads are the deformations in the undeformed blade reference frame obtained after transforming deformations

from the respective element frames as described in chapter 2. This facilitates the derivation of airloads. The blade velocities V_{b_x}, V_{b_y}, and V_{b_z} can be expressed in terms of the expressions shown in Eqs. 3.13 and 3.14 as

$$\left.\begin{aligned} V_{b_x} &= \dot{x}_1 - y_1 \cos\beta_p \\ V_{b_y} &= x_1 \cos\beta_p + \dot{y}_1 - z_1 \sin\beta_p \\ V_{b_z} &= y_1 \sin\beta_p + \dot{z}_1 \end{aligned}\right\} \tag{3.15}$$

The angle of attack is calculated at $\frac{3}{4}^{th}$ chord location corresponding to $\eta = \eta_r$ and $\zeta = 0$. The final expressions for V_{b_x}, V_{b_y}, and V_{b_z} are given by

$$\left.\begin{aligned} V_{b_x} &= \dot{u} - \lambda_T \dot{\bar{\phi}}' - (\dot{v}' + w'\dot{\theta}_1)\eta_r \cos\theta_1 - (\dot{w}' - v'\dot{\theta}_1)\eta_r \sin\theta_1 - (v + \eta_r \cos\theta_1) \\ V_{b_y} &= \dot{v} - \dot{\theta}_1 \eta_r \sin\theta_1 + x + u - v'\eta_r \sin\theta_1 - \beta_p(w + \eta_r \sin\theta_1) \\ V_{b_z} &= \dot{w} + \dot{\theta}_1 \eta_r \cos\theta_1 + \beta_p(v + \eta_r \cos\theta_1) \end{aligned}\right\} \tag{3.16}$$

Since the rotor shaft has been considered rigid the shaft motion is the representative of the vehicle motion for all practical purposes. The rigid body fuselage motion results in blade velocity (at a point at three quarter chord on the rotating deformed blade) given by

$$\vec{V_f} = \vec{V_F} + \vec{\omega}_f \times \vec{r_F} \tag{3.17}$$

where, $\vec{r_F}$ is the position vector of this point relative to the vehicle's center of gravity, $\vec{V_F}$ is the velocity with which the fuselage center of gravity is moving in the inertial frame and $\vec{\omega}_f$ is the angular velocity relative to the inertial frame. The components

of Eq. 3.17 are written as:

$$\vec{r_F} = (x_{CG}\hat{I_F} + y_{CG}\hat{J_F} + h\hat{K_F} + ((x+u)\hat{i} + v\hat{j} + w\hat{k} + \eta_r\hat{j_\eta}) \quad (3.18)$$

$$\vec{V_F} = \dot{x_F}\hat{I_I} + \dot{y_F}\hat{J_I} + \dot{z_F}\hat{K_I} \quad (3.19)$$

$$\omega_f = -\dot{\phi_s}\hat{I_I} - \dot{\alpha_s}\hat{J_I} \quad (3.20)$$

where ϕ_s is the lateral shaft tilt angle (positive advancing side-down). Substituting Eqs. 3.18, 3.19 and 3.20 in Eq. 3.17 and then transforming the resulting vector to the undeformed rotating axis ($\hat{i},\ \hat{j},\ \hat{k}$) and dropping all terms higher than ϵ^2 in accordance with ordering scheme, yields

$$\vec{V_f} = V_{f_x}\hat{i} + V_{f_y}\hat{j} + V_{f_z}\hat{k} \quad (3.21)$$

where,

$$V_{f_x} = (\dot{x_F} - h\dot{\alpha_s})\cos\psi + (\dot{y_F} + h\dot{\phi_s})\sin\psi$$

$$V_{f_y} = -(\dot{x_F} - h\dot{\alpha_s})\sin\psi + (\dot{y_F} + h\dot{\phi_s})\cos\psi$$

$$V_{f_y} = \dot{z_F} - \dot{\phi_s}x\sin\psi + \dot{\alpha_s}x\cos\psi + x_{cg}\dot{\alpha_s} - y_{cg}\dot{\phi_s}$$

The corresponding transformations involved are give below.

$$\begin{Bmatrix} \hat{i} \\ \hat{j} \\ \hat{k} \end{Bmatrix} = T_{UR}T_{RH}T_{HI} \begin{Bmatrix} \hat{I_I} \\ \hat{J_I} \\ \hat{K_I} \end{Bmatrix} \quad (3.22)$$

$$\begin{Bmatrix} \hat{i} \\ \hat{j} \\ \hat{k} \end{Bmatrix} = T_{UR}T_{RH} \begin{Bmatrix} \hat{I}_F \\ \hat{J}_F \\ \hat{K}_F \end{Bmatrix} \tag{3.23}$$

$$\begin{Bmatrix} \hat{i} \\ \hat{j} \\ \hat{k} \end{Bmatrix} = T_{DU} \begin{Bmatrix} \hat{i}_\xi \\ \hat{j}_\eta \\ \hat{k}_\varsigma \end{Bmatrix} \tag{3.24}$$

The resultant blade velocity at a radial station x expressed in rotating undeformed coordinate system is given by

$$\begin{aligned} \widehat{V} &= U_x\hat{i} + U_y\hat{j} + U_z\hat{k} \\ &= (V_{b_x} - V_{w_x} + V_{f_x})\hat{i} + (V_{b_y} - V_{w_y} + V_{f_y})\hat{j} + (V_{b_z} - V_{w_z} + V_{f_z})\hat{k} \end{aligned} \tag{3.25}$$

The sectional airloads are calculated in the deformed blade reference frame using the resultant velocity and aerodynamic angle of attack. The velocity calculated above needs to be transformed to the deformed frame

$$\begin{Bmatrix} U_R \\ U_T \\ U_P \end{Bmatrix} = T_{DU} \begin{Bmatrix} U_x \\ U_y \\ U_z \end{Bmatrix} \tag{3.26}$$

Finally, we have

$$\widehat{V} = U_R\hat{i_\xi} + U_y\hat{j_\eta} + U_z\hat{k_\varsigma} \tag{3.27}$$

where,

$$\begin{aligned} \frac{U_R}{\Omega R} &= \dot{u} - v + v'(x + \mu\sin\psi) - \mu\cos\psi(1 - \beta_p w') + \lambda(\beta_p + w') \\ &\quad - \eta_r\cos\theta_0(1 + \dot{v}') + \eta_r\sin\theta_0(\hat{\phi} - \dot{w}' + v'\dot{v} + w'\dot{w} \\ &\quad + \frac{1}{2}\mu\cos\psi(v'^2 + w'^2)\underline{+(\dot{x_F} - \dot{\alpha_s}h)\cos\psi + (\dot{y_F} + \dot{\phi_s}h)\sin\psi} \end{aligned} \tag{3.28}$$

$$\begin{aligned}
\frac{U_T}{\Omega R} &= [\dot{v} + u - w\beta_p + \hat{\phi}(\lambda + \dot{w}) + v'v + (x + \mu\sin\psi)(1 - \frac{v'^2}{2}) \\
&\quad + \mu\cos\psi(v' + \hat{\phi}(\beta_p + w')]\cos\theta_0 + [\dot{w} + \lambda + v(\beta_p + w') - \hat{\phi}\dot{v} \\
&\quad - (x + \mu\sin\psi)(v'w' + \hat{\phi}) + \mu\cos\psi(w' + \beta_p - \hat{\phi}v')]\sin\theta_0 \\
&\quad \underline{-[(\dot{x_F} - \dot{\alpha_s}h)\sin\psi - (\dot{y_F} + \dot{\phi_s}h)\cos\psi]\cos\theta_0} \\
&\quad \underline{+[\dot{z_F} - \dot{\phi_s}x\sin\psi + \dot{\alpha_s}x\cos\psi + x_{cg}\dot{\alpha_s} - y_{cg}\dot{\phi_s}]\sin\theta_0}
\end{aligned} \tag{3.29}$$

$$\begin{aligned}
\frac{U_P}{\Omega R} &= [\dot{w} + \lambda + v\beta_p + vw' + \mu\cos\psi(\beta_p + w' - \hat{\phi}v') \\
&\quad - (x + \mu\sin\psi)(v'w' + \hat{\phi})]\cos\theta_0 + [-(\dot{v} + u) - vv' + w\beta_p \\
&\quad - \hat{\phi}(\dot{w} + \lambda) - \mu\cos\psi(v' + \hat{\phi}(\beta_p + w')) \\
&\quad - (x + \mu\sin\psi)(1 - \frac{v'^2}{2})]\sin\theta_0 + \eta_r(\dot{\theta_0} + \dot{\hat{\phi}} + w' + \beta_p)) \\
&\quad \underline{-[(\dot{x_F} - \dot{\alpha_s}h)\sin\psi - (\dot{y_F} + \dot{\phi_s}h)\cos\psi]\sin\theta_0} \\
&\quad \underline{+[\dot{z_F} - \dot{\phi_s}x\sin\psi + \dot{\alpha_s}x\cos\psi + x_{cg}\dot{\alpha_s} - y_{cg}\dot{\phi_s}]\cos\theta_0}
\end{aligned} \tag{3.30}$$

The angle of attack α, yaw angle Γ, and the incident Mach number M are given by

$$\left.\begin{aligned}
\alpha &\approx -\frac{U_P}{U_T} \\
\Gamma &\approx \frac{U_R}{U_T} \\
M &= M_{tip}\sqrt{U_P^2 + U_T^2}
\end{aligned}\right\} \tag{3.31}$$

The underlined terms above are contributions from the helicopter maneuver and go to zero during steady flight. For a pull-up maneuver the contribution from vehicle pitch rate tends to increase the angle of attack by increasing both U_P and U_T. Although the denominator also increases, the net change is more significant for the numerator resulting in an increase in angle of attack.

Once the angle of attack and Mach number is calculated, the airfoil properties

can be found using table look-up. The sectional normal force, chord force, and quarter chord pitching moment and the axial force in the deformed rotating frame can be given in their non-dimensional form as

$$\left.\begin{aligned} \bar{L_w} &= \frac{\gamma \widehat{V}^2}{6a}(C_l \cos\alpha + C_d \sin\alpha) \\ \bar{L_v} &= \frac{\gamma \widehat{V}^2}{6a}(C_l \sin\alpha - C_d \cos\alpha) \\ \bar{M_\phi} &= \frac{\gamma \widehat{V}^2}{6a}\frac{c}{R}C_m \\ \bar{L_u} &= -\frac{\gamma \widehat{V}^2}{6a}C_d \sin\Gamma \end{aligned}\right\} \tag{3.32}$$

where, $\bar{L_w}, \bar{L_v}, \bar{L_u}$ are non-dimensionalized with respect to $m_0\Omega^2 R$ and $\bar{M_\phi}$ with respect to $m_0\Omega^2 R^2$. All the velocities are non-dimensionalized with respect to ΩR. γ is the Lock Number, $\gamma = \frac{\rho a c R^4}{I_b}$, where, flap inertia, $I_b = \frac{m_0 R^3}{3}$. The expressions for airloads are further manipulated for convenience, and the aerodynamic constants are replaced with their following expanded forms

$$C_l = c_0 + c_1\alpha \tag{3.33}$$

$$C_d = d_0 + d_1\alpha + d_2\alpha^2 \tag{3.34}$$

$$C_m = f_0 + f_1\alpha = c_{m_{ac}} + f_1\alpha \tag{3.35}$$

Using the expressions above in Eqs. 3.31 and 3.32, we obtain the following expressions

$$\bar{L_w} = \frac{\gamma}{6a}(c_0 U_T^2 - (c_1 + d_0)U_T U_P + d_1|U_P|U_P) \tag{3.36}$$

$$\bar{L_v} = \frac{\gamma}{6a}(-d_0 U_T^2 - (c_0 U_P - d_1|U_P|)U_T + (c_1 - d_2)U_P^2) \tag{3.37}$$

$$\bar{M_\phi} = \frac{\gamma}{6a}\frac{c}{R}(C_{m_{ac}}(U_T^2 + U_P^2) - f_1 U_T U_P) \tag{3.38}$$

$$\bar{L_u} = -\frac{\gamma}{6a}(-d_0 U_R U_T) \tag{3.39}$$

It should be noted that the airloads thus calculated are in deformed frame and need to be transformed to undeformed frame before applying to the structural model for which the following transformation is used

$$\begin{Bmatrix} L_U^A \\ L_V^A \\ L_W^A \end{Bmatrix} = T_{DU}^T \begin{Bmatrix} \bar{L_U} \\ \bar{L_V} \\ \bar{L_W} \end{Bmatrix} \tag{3.40}$$

$$M_\phi^A \approx \bar{M}_\phi \tag{3.41}$$

The airloads obtained above only represent the circulatory component. The non-circulatory component (also called apparent or virtual forces) must be added to the non-circulatory lift and pitching moment to get total airload. The non-circulatory lift and pitching moment in their non-dimensionalized form are given respectively by

$$\frac{(L_w^A)_{NC}}{m_0\Omega^2 R} = \frac{\gamma\pi\frac{c}{R}}{12a}\left(-\frac{\ddot{w}}{R} + \frac{\frac{c}{4}+e_d}{R}\ddot{\theta}_1 + (x+\mu\sin\psi)\dot{\theta}_1\right) \tag{3.42}$$

$$\frac{(M_{\hat{\phi}}^A)_{NC}}{m_0\Omega^2 R} = \frac{\gamma\pi\frac{c}{R}}{12a}\left(\frac{\frac{c}{4}+e_d}{R}\frac{\ddot{w}}{R} - (\frac{\frac{c}{4}+e_d}{R})^2\ddot{\theta}_1 - \frac{\frac{c}{2}+e_d}{R}(x+\mu\sin\psi)\dot{\theta}_1 - \frac{c^2}{R^2}\frac{1}{32}\ddot{\theta}_1\right) \tag{3.43}$$

where c is the length of the chord, $\ddot{w}$ is the plunge acceleration (positive up), $\ddot{\theta}_1 (= \ddot{\theta}_0 + \ddot{\hat{\phi}})$ is the pitch acceleration (positive nose up), and $\dot{\theta}_1$ is pitch angular velocity.

3.2.2 Weissinger-L model (Near trailed wake)

The Weissinger-L (W-L) model [186] is essentially a lifting-surface model with a single chord-wise element. The W-L model represents blade lift using a series of spanwise horseshoe vortex elements. For a given angle of attack as input the W-L

model calculates the bound circulation strengths at quarter-chord locations, taken as the location for lifting-line. The flow tangency condition is imposed at three-quarter chords where the vertical component of the induced velocity due to bound vortex system is equal and opposite to the corresponding component of the incident flow. The bound circulation strengths are used to determine circulation strengths of near wake trailers, which are used to calculate the induced angle of attack at three-quarter chord locations. This induced angle of attack is subtracted from the input angle of attack to obtain the net angle of attack to be used for sectional airloads calculations.

3.2.3 2D Unsteady Model (Near shed wake and stall vortices)

The Leishman-Beddoes unsteady model [91] (for attached flow and dynamic stall) is used in the present analysis. The formulation for both attached as well as separated flow is needed because the maneuver starts with high speed flight condition where there is no evidence of stall, but as the helicopter starts to pull-up, two to three stall cycles are observed per rotor revolution. The Leishman Beddoes dynamic stall model acts on the effective section angles of attack after including free wake and near wake trailed vorticity. The effect of shed vorticity is then provided by the unsteady model. This is because, unlike trailed wake, the effect of shed wake is local and the use of unsteady model allows the effects of compressibility, viscosity, and dynamic stall to be incorporated. As discussed later in the Chapter 4 on comprehensive analysis, the dynamic stall model seems to be the single most

important tool needed to analyze the UTTAS pull-up maneuver.

3.2.4 Far Wake Model (Far trailed wake)

The transient far wake model used in the present study is the Maryland Free wake model which has been validated in Ref. [73]. The original free wake analysis uses rigid blade model and hence is modified to incorporate flexible blade deformations in flap, lag, and torsion. In addition the vortex strengths and boundary conditions are prescribed as inputs to the free wake model, which in turn results in the non-linear inflow distribution as output.

A wake discretization of 2 degree and 2 wake turns is used for all wake calculations. Increasing the wake turns to 4 does not make any significant change in the predicted inflow during the pull-up maneuver. A single peak free tip vortex model is used for all the calculations involving free wake model. The strength of the tip vortex is equal to the maximum bound circulation occurring outboard of 50% blade span. To understand the role played by the inflow prediction on airloads, the predictions using free wake model are also compared to those obtained using uniform inflow calculated using rotor thrust and shaft angles. The expression for quasi-steady inflow in forward flight is given by

$$\lambda = \mu \tan \alpha_s + \frac{C_T}{2\sqrt{\mu^2 + \lambda^2}} \tag{3.44}$$

for $\mu > 0.1$ it simplifies to

$$\lambda = \mu \tan \alpha_s + \frac{C_T}{2\mu} \tag{3.45}$$

where μ is the advance ratio, α_s is the rotor shaft angle and C_T is rotor thrust.

3.3 Reynolds Averaged Navier-Stokes CFD Model

The baseline CFD solver used in the present work is the in-house developed parallelized version of overset, structured mesh, unsteady RANS solver OVERTURNS (OVERset Transonic Unsteady Rotor Navier-Stokes) developed by *Sitaraman and Baeder* [187] and *Duraisamy and Baeder* [188] and recently implemented with large scale parallelism by *Ananthan and Baeder* [162]. Time integration is performed using a second-order backward difference method using Lower-Upper Symmetric Gauss Seidel (LUSGS) [189]. Newton sub-iterations (typically 8) are used to remove factorization errors and recover time accuracy for unsteady computations [190]. The inviscid fluxes are computed using an upwind scheme that uses Roe's flux differencing with MUSCL type limiting. The viscous fluxes are computed using second-order central differencing. The Baldwin-Lomax turbulence model is utilized for RANS closure for all baseline results. OVERTURNS uses the arbitrary LagrangianEulerian (ALE) formulation for modeling unsteady flows with motion of the solid surfaces, as in the case of helicopter flows.

Since the motions of the vehicle undergoing the maneuver are known in terms of translational and angular rates, and position and attitude are not strictly known. Use of pseudo material frame requires the grid velocity field to be directly prescribed, which may result in violation of the geometric conservation law. Therefore, an alternative approach involving analytical mapping of the Navier-Stokes equations to a vehicle fixed frame is used. This allows the deformation of vehicle components to be described relative to the vehicle fixed frame. This alternative mapping is realized

via two successive transformations. The first transformation is from an inertial reference frame, to a body fixed non-rotating frame and the second transformation involves the projection of the velocity field in the body fixed non-rotating frame to a body fixed rotating frame. The solver uses a non-inertial vehicle fixed frame of reference, and the effects of maneuver (attitudes and rates) are incorporated using source terms in the Navier-Stokes equation [165].

The solver uses an overset mesh system for efficient wake capturing. In this arrangement, the body-fitted blade meshes are embedded inside a cylindrical off-body mesh to capture the entire rotor blade-wake aerodynamics – see Fig. 3.1. The body conforming C-O meshes ensures a better definition of the blade tips, and consists of 129 points in the wraparound direction (of which 97 points are on the blade surface), 129 points in the spanwise direction, and 65 points in the normal direction. The spacing of grids near the blade surface in the normal direction is approximately 10^{-5} chord which is required for the viscous calculations. The background mesh is composed of four overlapping cylindrical quadrants with $49 \times 99 \times 110$ in the azimuthal, spanwise, and normal direction respectively. The off-body mesh uses grid stretching to maintain clustering in regions of high vorticity, i.e., the root and tip vortex regions in the wake.

The coupling between the different solvers (structural and CFD) is achieved using Python scripts. Each solver provides a Python class interface which interacts with the FORTRAN modules using FORTRAN to Python Interface generator (F2PY). Parallelized execution of the code is achieved using pyMPI. The Python NumPy library is used for general array manipulation and data exchange between

the solvers. The interpolation of the deformation for grid motion at each time step is done using the structural solver for the specified grid locations. This ensures the consistency between grid deformation and beam deformation kinematics. To minimize grid movement near the outer boundary of the body fitted grids, a decaying radial function is applied to the beam kinematic parameters.

3.4 Airloads Using Prescribed Deformations

The deformations obtained using measured airloads analysis are first used to validate the lifting-line model for the steady flight regime of the maneuver. It is then used to predict the airloads for the maneuver. It should be noted that the lifting-line analysis, although a low fidelity model, facilitates the separation of the effects of dynamic stall and wake, which is important for the identification of stall physics. It further provides direct airfoil angle of attack estimation, which is critical for better understanding of the airloads mechanism. Recall, that by prescribed or calculated deformation we imply the deformations obtained by the application of the flight test airloads on the structural model.

The procedure for simulation of maneuver using prescribed deformations is straightforward. The maneuver is initiated from the level flight condition and then the adjusted control angles (described later) are smoothly applied in an incremental manner. The vehicle advance ratio, shaft angles, attitudes, and rates from the flight test are subsequently prescribed. For prediction of airloads, the structural dynamics model is replaced with pre-calculated structural response from measured airloads

analysis. The steady, periodic flight condition is used as the initial solution from which the maneuver is started. It is important to note that, unlike coupled analysis, the prescribed deformation analysis does not start from a trimmed flight condition. A conventional trim analysis cannot be carried out in this situation as the blade response is already frozen. This calls for an estimate of the initial control angles. The control angles corresponding to trimmed CFD/CSD loose coupling analysis give good correlation for the predicted airloads at the beginning (rev 1) of the maneuver (Fig. 3.2). This is because, the deformations obtained using measured airloads analysis are similar in magnitude and phase to those obtained from CFD/CSD coupled analysis during the steady part of the maneuver. Therefore, the control angle used at any time instance for this simulation can be represented by

$$\theta = \theta_{CFD/CSD_{steady}} + (\theta_{Flight_{maneuver}} - \theta_{Flight_{steady}}) \tag{3.46}$$

where, $\theta_{CFD/CSD_{steady}}$ corresponds to the control angle used for the CFD/CSD trimmed analysis, $\theta_{Flight_{maneuver}}$ is the control angle measured during the flight test at any instance of time, and $\theta_{Flight_{steady}}$ is the measured angle at time $t = 0$. Before discussing the results from the analysis it is important to understand how the control angle time history from the flight test is estimated.

3.4.1 Control Angle Time History

The flight test control angles are used for the prediction of airloads using the calculated deformations. There was no direct measurement of the control angles $(\theta_0, \theta 1s, \theta_{1c})$ during the UH-60A flight testing. However, the root pitch angle data,

which is the net effect of the applied control angle and the blade elastic twist deformation at the root, can be used to extract the three control angles by doing FFT (Fast Fourier Transformations). In order to achieve this the 40 revolutions of the pull-up maneuver are considered quasi-periodic and the control angles are estimated for all forty revolutions by doing a windowed FFT. The data then can either be linearly interpolated or pre-interpolated using splines to obtain the entire control angle time history. The pre-interpolated spline fit to the data allows smoother control angle variation and is used throughout the analysis.

3.4.2 Results

The predicted normal force using lifting-line analysis, as shown in Fig. 3.2(a), exhibits correct negative-lift phase and correlates very well with flight test data at most stations due to the accurate elastic twist obtained from the measured airloads analysis. Pitching moment (Fig. 3.2(b)), however shows only fair correlation, due to inherent limitations of lifting-line analysis in predicting transonic shock observed in outboard blade pitching moment during high advance ratio ($\mu = 0.375$).

After having validated the aerodynamic model for steady high speed flight condition at the beginning of the maneuver, maneuver is finally simulated by prescribing the calculated deformations along with the flight test control angles and vehicle motions history data. The predicted and measured pitching moment for revolutions 13–15 and 16–18 are shown in Fig. 3.3(a). The lifting-line model is able to predict all three stall events. Reference [191] identified the mechanisms of the two retreating

blade stalls for the high altitude dynamic stall flight ($C_W/\sigma = 0.135, \mu = 0.237$), which are known to be similar (Ref. [8]) to the dynamic stall cycles observed in the UTTAS maneuver. The study showed that first retreating stall cycle was caused by high trim angles in the retreating blade, and the second stall cycle was triggered by 4 and 5/rev elastic twist deformation that produced a local angle of attack perturbation in the fourth quadrant. The mechanism of advancing blade stall is not known, hence the focus is on its systematic understanding. To isolate the nature of the advancing blade stall, dynamic stall model in the lifting-line aerodynamic analysis is turned off and instead static airfoil table look-up is used to predict the pitching-moments. Figure 3.3(a) shows that while the retreating blade stalls are no longer predicted, the advancing blade stall is still well predicted, even with the static airfoil table look-up. This implies that the stall observed in first quadrant is a transonic stall phenomenon in a static sense and not a dynamic stall vortex induced event. To identify the contribution of the wake in prediction of this stall, analysis is carried out without the free wake model. A quasi-steady uniform inflow calculated using flight test thrust and the effective shaft angle with respect to on-coming flow is used and all three stall cycles are still present in the predicted pitching moment (Fig. 3.3(b)), implying that the effect of wake interactions are less significant for prediction of stall for this flight. The quasi-steady inflow is shown in Fig. 3.4. The reason for this observation – the high airfoil operating angle of attack that renders inflow induced contributions to angle of attack as less significant – is discussed in the chapter 4 during the discussion of comprehensive analysis. Further, no wake bundling phenomenon is observed by the analysis as the wake gets blown down-

stream due to high advance ratio. Figure 3.5 shows the mesh plot for flight test and predicted pitching moment across the disk and the prediction has three distinct stall cycles, similar to the flight test, thereby validating the lifting-line aerodynamic model during the maneuver regime.

The calculation above is repeated using the RANS CFD model, described earlier, to reconfirm the observations made using lifting-line analysis and to compare the airloads predicted using the two approaches. The blade deformations, blade velocities and accelerations used for the lifting-line calculations are interpolated using splines to 0.25 degree resolution to match the CFD time step. Figure 3.6 shows the pitching moment at 86.5% span with predicted using CFD with prescribed deformations. CFD predictions with prescribed deformations show all three stalls like the predictions from lifting-line model. However, it should be noted that the lifting-line analysis under-predicts the magnitude of retreating blade stalls significantly and the predicted phase is less satisfactory. In addition it is also observed that the CFD prediction of the third stall observed in fourth quadrant, though significantly better than predictions using lifting-line analysis, are not accurate enough to trigger adequate 5/rev harmonic. The third stall seems to be holding the key to the prediction of first stall in the following revolution, as discussed in chapter 5.

3.4.3 Mechanism of the Advancing Blade Stall

The advancing blade stall, unlike the first retreating stall, is a very localized event, occurring over a small region on the outboard side. The mechanism of the

advancing blade stall, which appears to be a transonic stall is analyzed carefully, and the effect of torsion, control angles and transonic flow is studied.

Effect of Torsion

The blade elastic twist directly affects angle of attack on the blade and has been known to influence retreating side stall prediction as concluded during the study of dynamic stall flight [191]. Therefore, blade elastic twist deformation is analyzed in detail to investigate its possible impact on the advancing side. Figure 3.7 shows the waveform and harmonics of blade tip elastic twist obtained using measured airloads analysis for revolution 14 of the maneuver. It is observed that elastic twist deformation has a significant 5/rev harmonic. The role of 5/rev elastic twist is to increase the angle of attack on advancing side of the blade, via positive (nose-up) elastic twist, as seen in Fig. 3.7(a). Figure 3.8 shows the airfoil operating envelope, i.e. variation of angle of attack vs. Mach number for deformations obtained using measured airloads analysis. It can be observed that, with contribution from 5/rev elastic twist airfoil is operating at high angle of attack in the first quadrant, whereupon entering deeper stall and remaining beyond static stall limit for longer duration. This results in the prediction of first stall by the lifting-line analysis.

To understand the source of 5/rev component present in elastic twist obtained from measured airloads analysis, the flight test pitching moment data for revolutions 11–12 is analyzed – those that precede revolution 14. For example, the flight test pitching moments for rev 11 and 12 show two retreating stall events separated by 70° or approximately 1/5-th of a rev – see Fig. 3.9(a), in addition revolution 12

has an additional stall in first quadrant. This stall is again separated from the second stall from revolution 12 by another $1/5^{th}$ rev. This temporal separation of stall events implies that, pitching moment with at least two such stalls would have significant 5/rev component, which is confirmed by harmonic analysis of pitching moment shown in Fig. 3.9(b). This further entails that 5/rev elastic twist needed to trigger advancing blade stall is a result of excitation by stalls on the retreating blade from previous revolution.

Effect of Transonic Flow

Further understanding of stall physics is obtained by studying the pressure variation across the blade chord at the 86.5% spanwise location on the blade. Since, the advancing blade stall is observed between the azimuthal locations of 25° to 50°, the coefficient of pressure (C_P) is studied at several azimuth locations for the above mentioned regions. The C_P plot at 25° azimuth (Fig. 3.10(a)) shows a strong leading edge suction and development of a weak oblique shock sitting near $25-30\%$ of chord as depicted by the sharp gradient in the pressure. This shock triggers flow separation and creation of the vortex at approximately 30% chord length from the leading edge. and is responsible for the advancing blade stall as this vortex travels downstream. By the time blade reaches the 35° azimuth, the shock gains in strength, diminishing the leading edge suction peak as seen in Fig. 3.10(b). Further, the upper surface of the airfoil now shows a small vortex associated with a small *b*ump near the 40% of chord which got created between the 25° and 35° azimuths. Figure 3.10(c) shows that at 40° azimuth it has travelled further downstream and reached 70% of chord

and then finally it has left the blade by 45° azimuth (Fig. 3.10(d)). The shock in the meanwhile has also travelled upstream towards the leading edge and has gotten stronger and has destroyed the leading edge suction as seen in Fig. 3.10(d). Based on the discussion above, it can be concluded that the triggering mechanism for the flow separation during advancing blade stall is a weak oblique shock, which sets it apart from the conventional dynamic stall phenomenon.

Effect of Control Angle Perturbation

However, the 5/rev elastic twist cannot be solely responsible for the prediction of advancing blade stall, which is first observed in the flight test data during revolution 12, but is not predicted by the lifting-line analysis (Fig. 3.11(a)). The deformation for rev 12 clearly has a significant 5/rev elastic twist component as seen in Fig. 3.11(b), yet the advancing blade stall is not predicted. A look at the airfoil operating envelope (Fig. 3.11(c)) reveals that the starting angle of attack is smaller than the static stall limit and hence the contribution from 5/rev elastic twist is not adequate to predict a stall. Therefore, the effect of control angles on the prediction of the stall is also studied by perturbing the control angles from their baseline values. The collective (15.4°) and longitudinal cyclic (−9.1°) angles are perturbed by 10% and lateral cyclic (4.3°) is perturbed by 20% from their baseline values at the beginning of the maneuver.

The predictions for revolution 18 correlates very well with the flight test data for the advancing blade stall magnitude, and is therefore chosen to study the influence of control angle perturbation. The effect of collective angle perturbation on

pitching moment prediction for revolution 18 using prescribed deformation is shown in Fig. 3.12(a). The collective angle directly determines the angle of attack in the first quadrant (Fig 3.12(b)) and thus determines how deep the stall is, thereby directly influencing the advancing blade stall magnitude. A 10% increase in collective results in 10% improvement of advancing blade stall peak from its baseline value, while a 10% decrease in collective amounts to as much as 30% reduction in the advancing blade stall peak. Collective angle also has a significant impact on the stall observed in the third quadrant (second stall), which reconfirms the fact that it is a trim stall, caused due to high trim angles.

A 10% perturbation in longitudinal cyclic doesn't influence the angle of attack at 0°–45° azimuth (Fig. 3.13(b)), unlike collective, and hence its impact on advancing blade stall prediction is not significant, as seen in Fig. 3.13. Similar to the effect of longitudinal cyclic, the change in lateral cyclic also doesn't significantly impact the advancing blade stall, but it does affect the magnitude and phasing of the retreating stalls, as observed in Fig. 3.14. The effect of control angle perturbation on stall prediction establishes the fact that in addition to accurate 5/rev elastic twist, control angles are also important for accurate prediction of stalls observed during the C11029 maneuver.

3.5 Concluding Observations

The development of lifting-line model for prediction of airloads in an unsteady maneuver is discussed. The aerodynamic model is first validated in isolation us-

ing prescribed deformations obtained from measured airloads analysis. The airloads predicted using lifting-line are consistently compared to those obtained using a CFD analysis. The mechanism of the stall in UTTAS pull-up maneuver is studied systematically and understood. The following conclusions are drawn based on this study.

1. The advancing blade stall observed during the peak load factor regime of the maneuver (revolutions $12 - 20$) is a transonic twist stall of steady nature. It is excited by the 5/rev component of blade elastic twist. In the first quadrant, even though the airfoils in the outboard region of blade are operating at low to moderate angles of attack, they are very close to the static stall limit due to high Mach number. The 5/rev component of elastic twist is triggered by two retreating stalls from the previous revolution which are spaced by approximately $1/5th$ rotor revolution. It increases the angle of attack beyond the static stall limit, in the first quadrant, thereby causing shock induced flow separation resulting in stall.

2. CFD predict all three stalls with prescribed deformations. The predicted pitching moment using CFD with prescribed deformation does not capture third stall with desired accuracy. Third stall in the pull-up maneuver is similar to second stall of dynamic stall flight which is known to be sensitive to wake and turbulence modeling. The Baldwin Lomax turbulence model used within the CFD analysis seems to be inadequate for accurate prediction of dynamic stall.

3. In addition to 5/rev elastic twist, the magnitude and extent of the advancing

blade stall sequence is also dictated by the collective angle. For example, a 10% error in collective angle can result in under-prediction of first stall peak by up to 30%.

4. With accurate deformations, lifting-line model is capable of predicting all three stall events observed during the UTTAS pull-up maneuver, but the stall magnitudes are always under-predicted when compared to those obtained using CFD as well as flight test. While, use of CFD significantly improves the magnitude and phasing of the two stalls on the retreating blade, its accurate prediction continues to be a challenge.

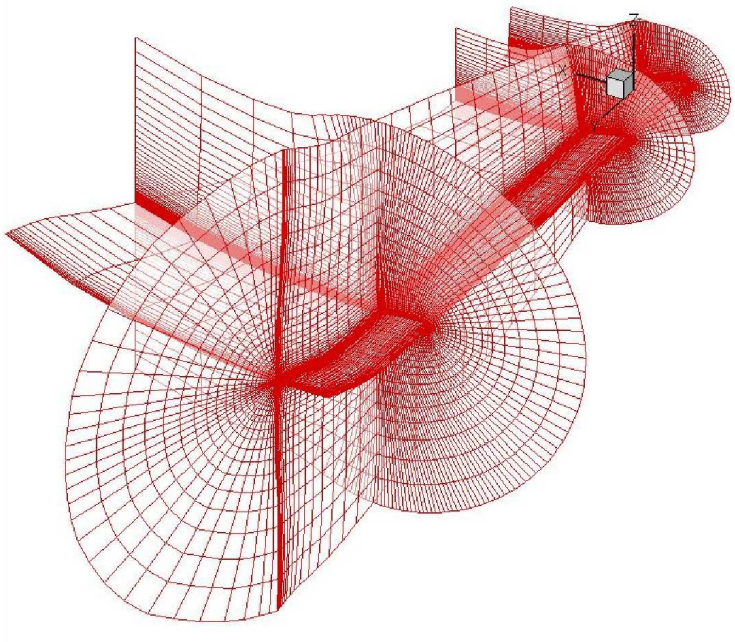

(a) C-O body-fitted mesh

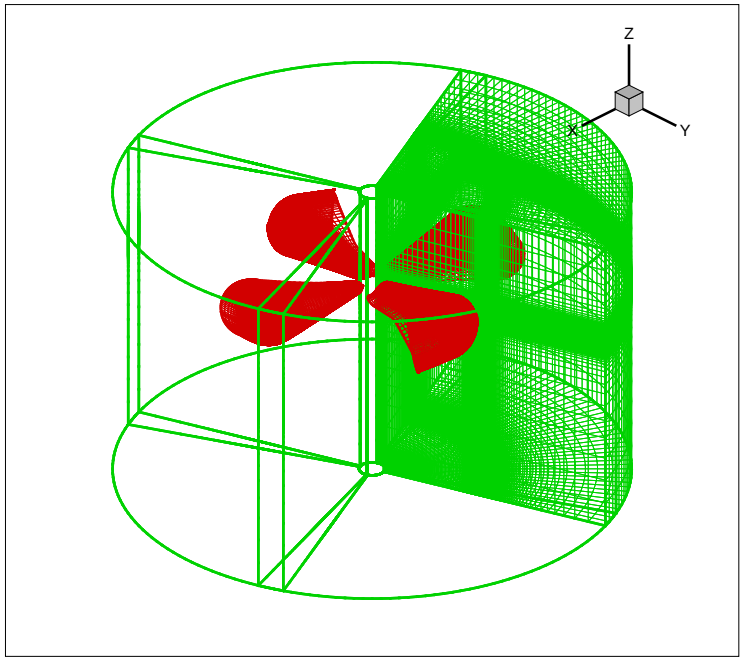

(b) Computational domain with eight mesh system

Figure 3.1: Body fitted blade meshes and the cylindrical off-body meshes used in the OVERTURNS solver.

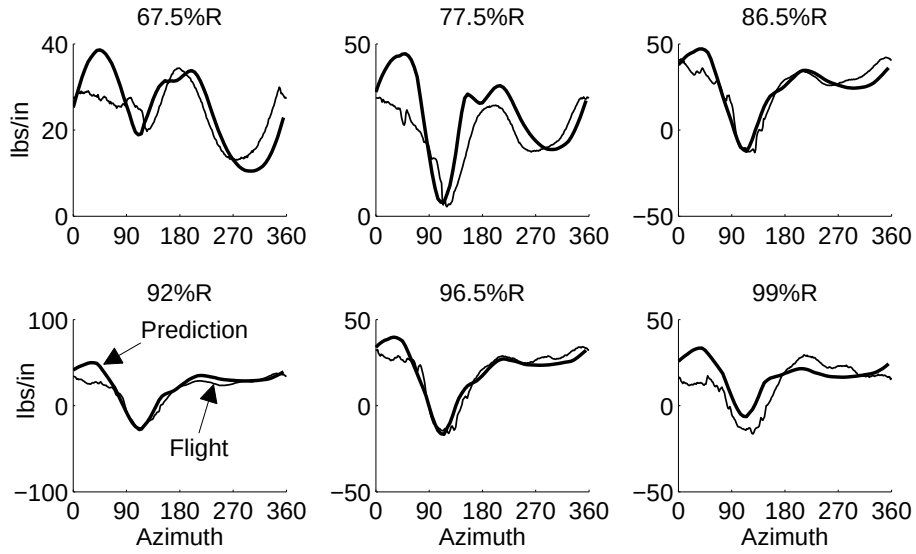

(a) Normal Force

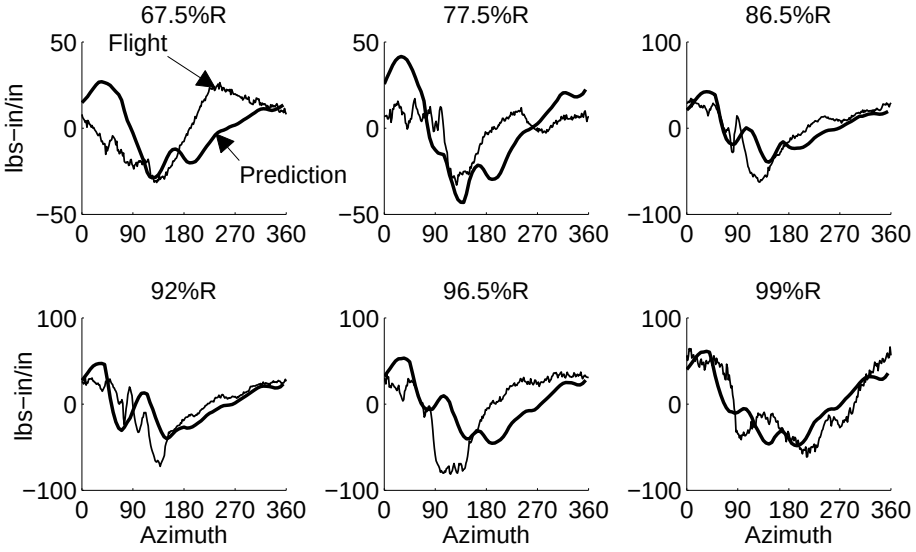

(b) Pitching Moment

Figure 3.2: **Measured and predicted normal force and pitching moment for rev 1; predictions with lifting–line analysis and prescribed deformations obtained using measured airloads.**

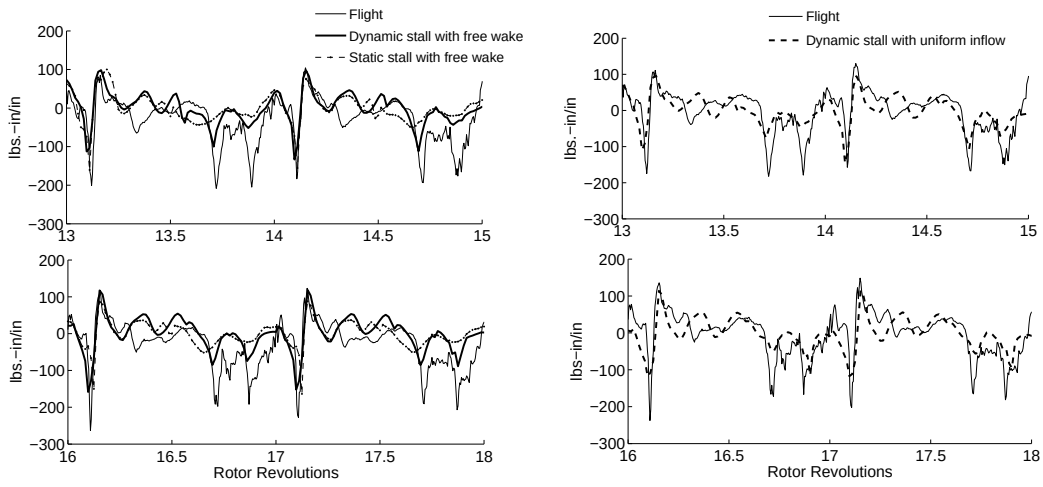

(a) Dynamic stall and static stall with free wake

(b) Dynamic stall with uniform inflow

Figure 3.3: **Measured and predicted pitching moment at** 86.5%**R; predictions with lifting–line analysis and prescribed deformations obtained using measured airloads.**

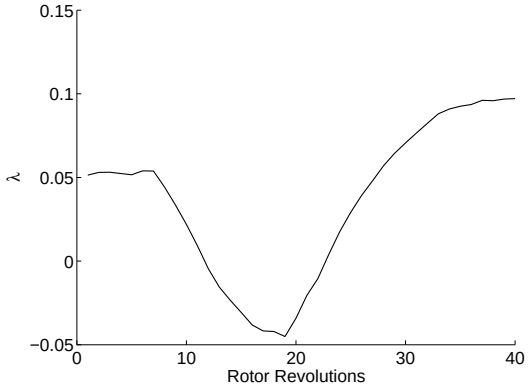

Figure 3.4: **Quasi-steady inflow calculated using measured rotor thrust and shaft angle.**

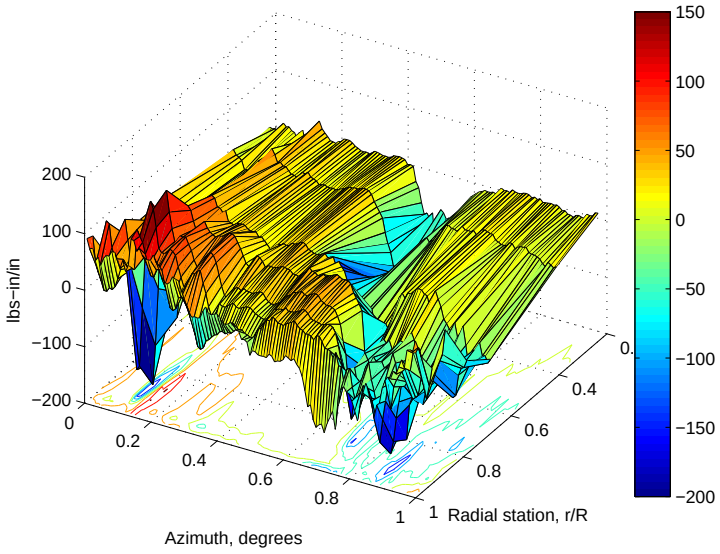

(a) Flight test

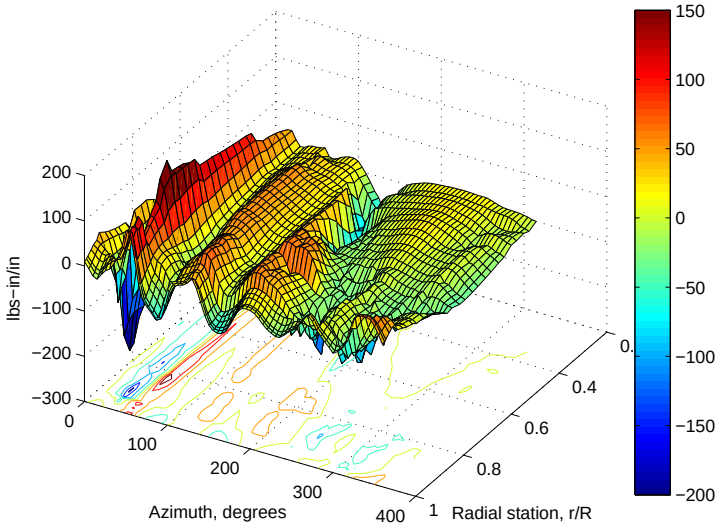

(b) Lifting-line using prescribed deformation

Figure 3.5: **Measured and predicted pitching moment for revolution 18; predictions with lifting–line analysis and prescribed deformations obtained using measured airloads.**

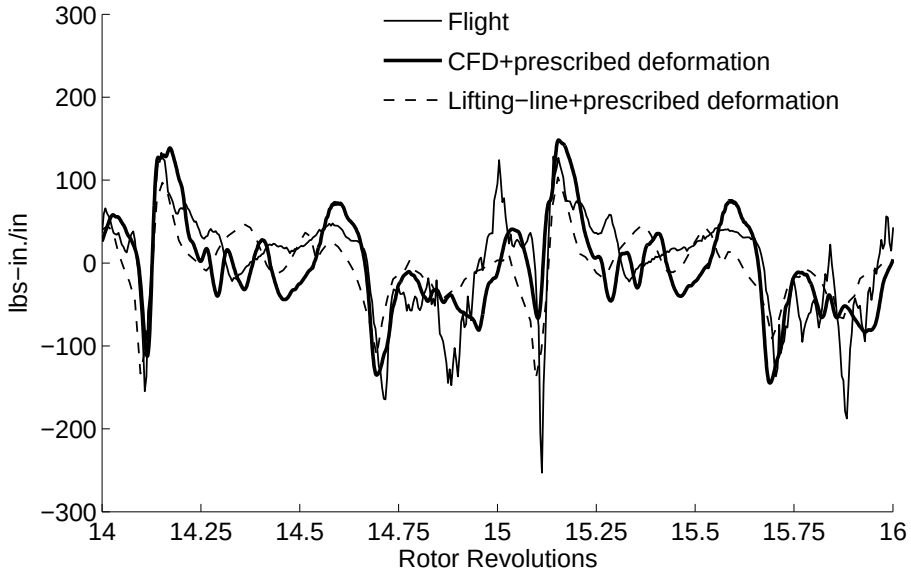

(a)

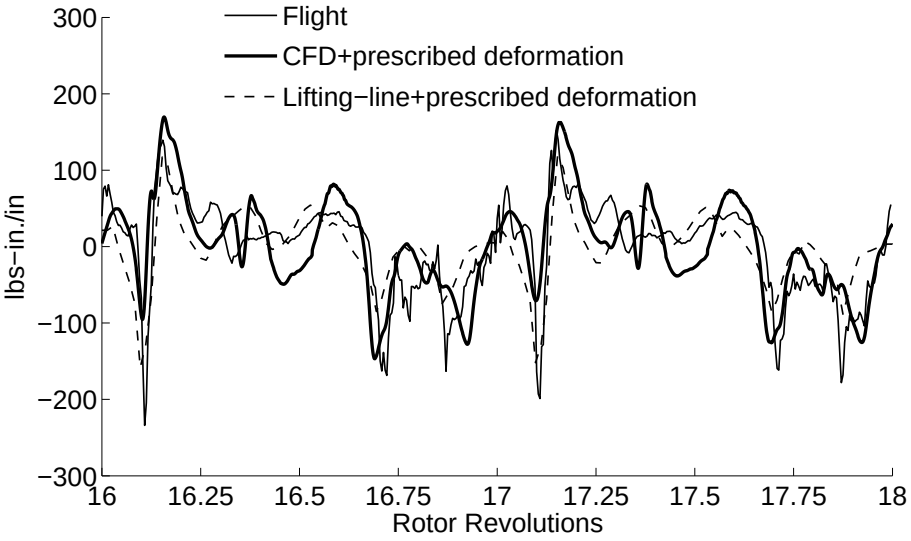

(b)

Figure 3.6: **Measured and predicted pitching moment at** 86.5%**R; predictions with CFD, lifting-line analysis and prescribed deformations obtained using measured airloads.**

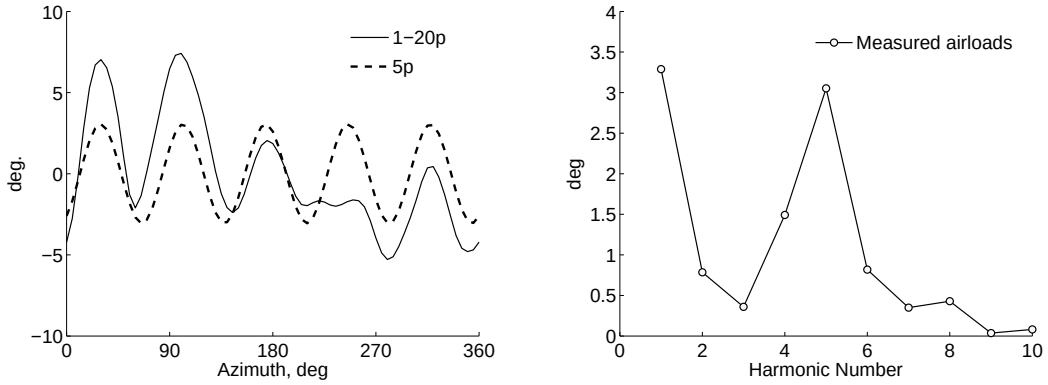

(a) Waveform, contribution of 5/rev harmonic (b) Harmonics

Figure 3.7: **Predicted tip elastic twist deformation for rev 14 ; prediction using measured airloads analysis.**

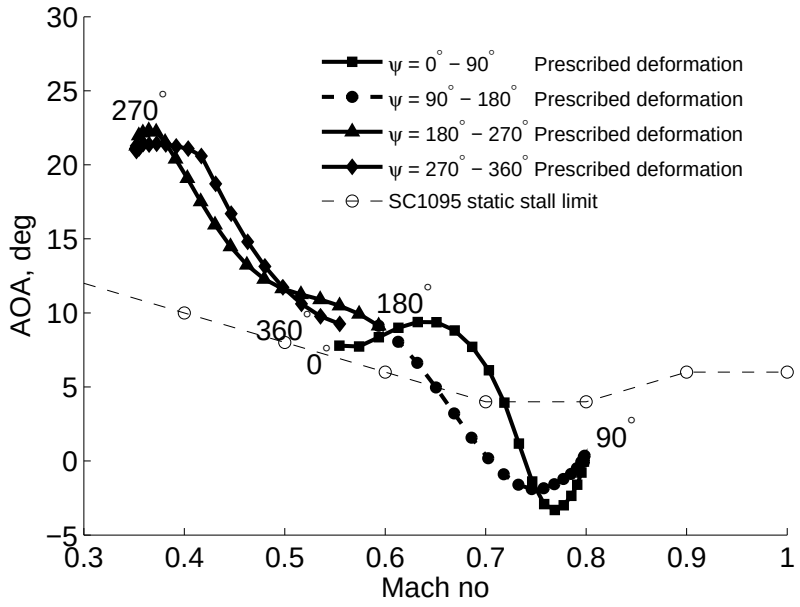

Figure 3.8: **Angle of attack vs. Mach number at** 86.5%**R for rev 14 using prescribed deformations obtained using measured airloads.**

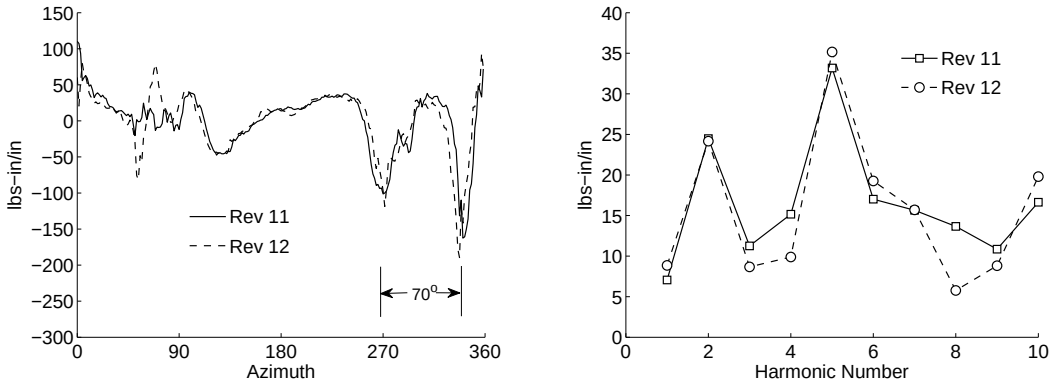

(a) Pitching moment (b) Harmonics of pitching moment

Figure 3.9: **Flight test pitching moment for revs 11 and 12.**

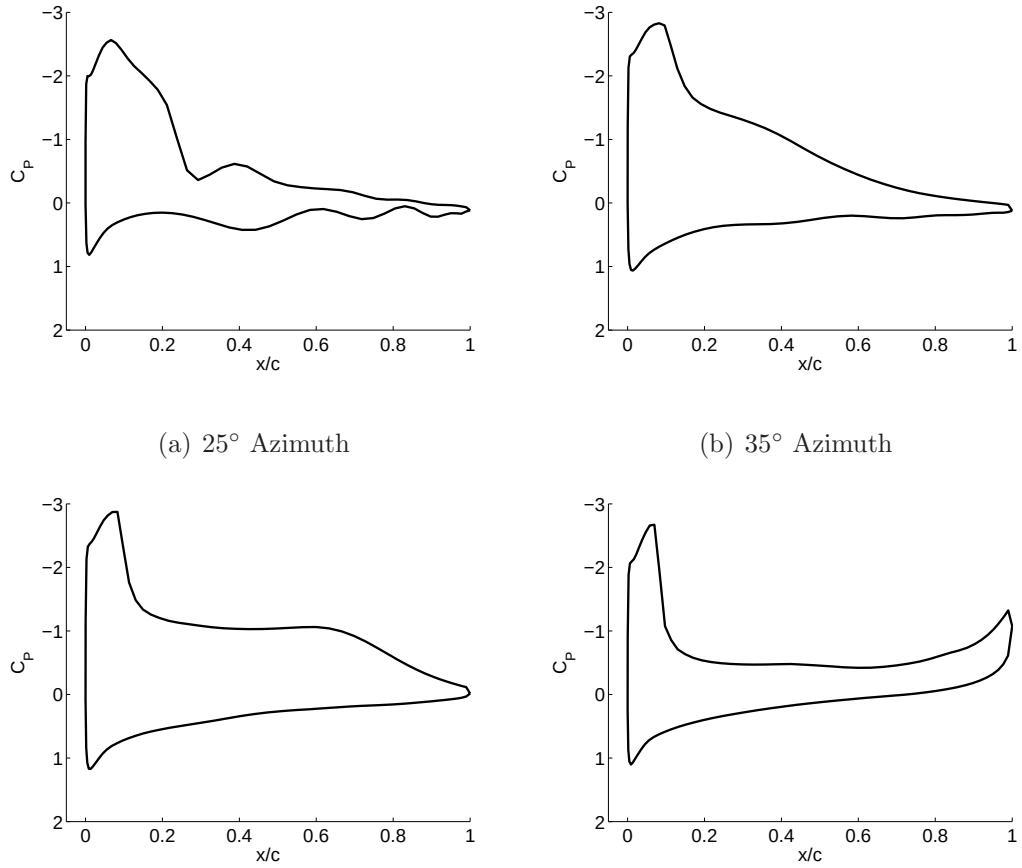

(a) 25° Azimuth (b) 35° Azimuth

(c) 40° Azimuth (d) 45° Azimuth

Figure 3.10: **Pressure coefficient (C_P) plotted at $86.5\%R$ for revolution 14 obtained using calculated deformations obtained using measured airloads.**

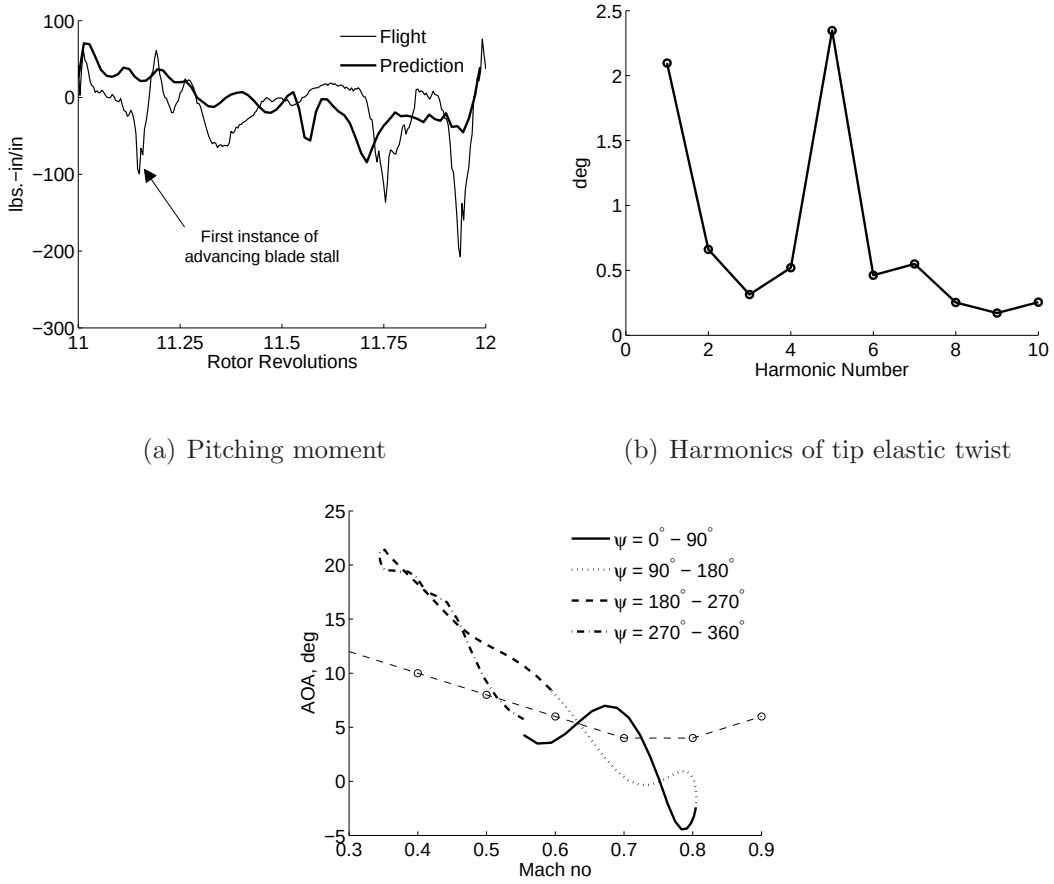

(a) Pitching moment

(b) Harmonics of tip elastic twist

(c) Airfoil operating envelope

Figure 3.11: **Pitching moment, elastic twist and airfoil operating envelope for rev 12 with prescribed deformations obtained using measured airloads.**

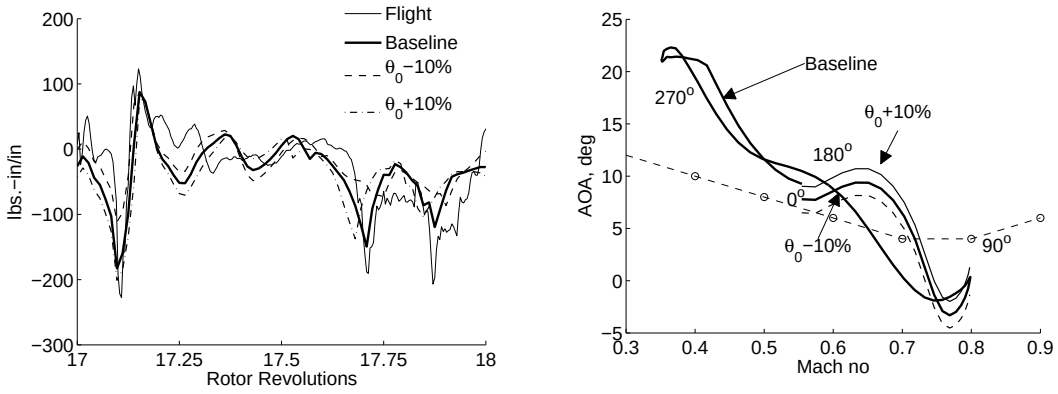

(a) Pitching moment (b) Airfoil operating envelope

Figure 3.12: **Effect of collective angle perturbation on predicted pitching-moment at 86.5%R for rev 18 using prescribed deformations obtained using measured airloads.**

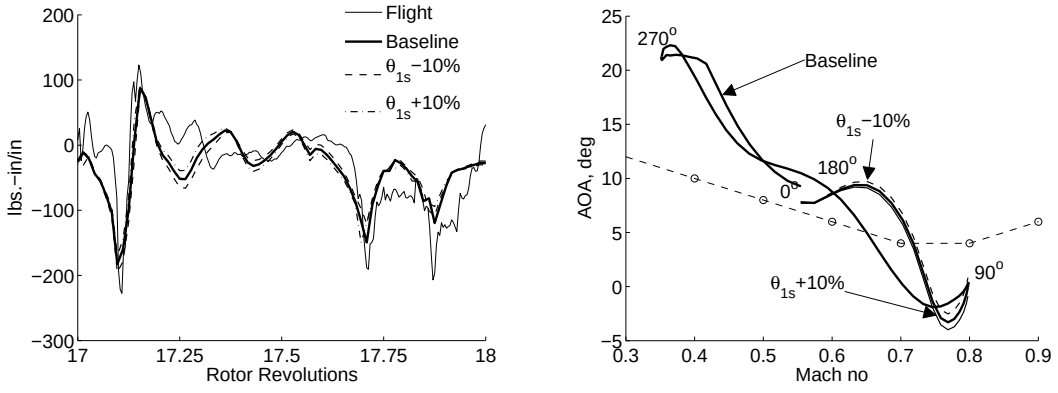

(a) Pitching moment (b) Airfoil operating envelope

Figure 3.13: **Effect of longitudinal cyclic angle perturbation on predicted pitching-moment at 86.5%R for rev 18 using prescribed deformations obtained using measured airloads.**

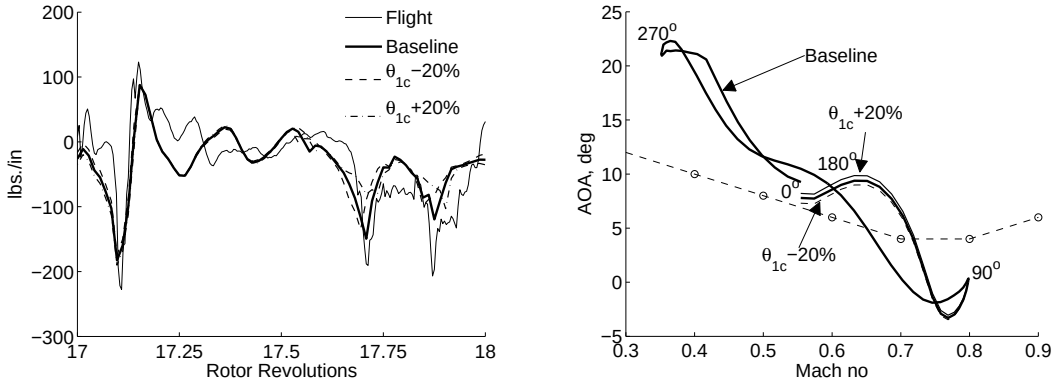

(a) Pitching moment

(b) Airfoil operating envelope

Figure 3.14: **Effect of lateral cyclic angle perturbation on predicted pitching-moment at 86.5%R for rev 18 using prescribed deformations obtained using measured airloads.**

Chapter 4

CSD/Lifting-line Aerodynamics Coupled Analysis

4.1 Introduction

In this chapter, the lifting-line aerodynamic model is coupled to the multibody structural model to study the impact of free wake, dynamic stall, and control pitch angles on predicted airloads, blade loads, pitch-link loads, and swashplate servo loads. While chapters 2 and 3 aimed at isolating the effect of structural dynamics and aerodynamics, this chapter focuses on: (1) isolating the effects of free wake inflow, dynamic stall, and rotor pitch control angles, separately, on the prediction of maneuver loads, and (2) to examine the prediction accuracy of airloads, blade loads, and swashplate servo loads using an unsteady lifting-line aerodynamic model.

An inverse solution procedure to determine the trim variables (pitch control angles, vehicle attitude angles, and yaw control) in order to fly a prescribed trajectory is quite involved and not yet available. In steady level flight, the trajectory is simple, and the aircraft Euler equations reduce to six equilibrium equations from which the trim variables are easily determined. The complexity of the solution procedure has been the primary hurdle for a first principles prediction of maneuver loads. Today, extensive flight test data from the U. S. Army/NASA Airloads

Program (Refs. [1, 2]) has opened opportunity to bypass this complexity. The measured values of rotor controls, aircraft attitudes, and flight trajectory can now all be prescribed from flight test data in order to focus solely on the loads mechanisms.

4.2 Methodology

The solution procedure for the coupled analysis for maneuver, like the analysis with measured airloads, starts with a periodic solution for the first revolution which corresponds to steady flight condition. The steady periodic solution is obtained by marching in time with the calculated trim angles for rev. 1 of the maneuver, by letting the analysis run for 6 revolutions. At least $5 - 6$ revolutions are needed for the lightly damped lag-mode to stabilize. Once the dynamic response settles into periodicity, then, the maneuver is initiated.

The maneuver is initiated from the level flight condition by smoothly merging the control angles. The velocity ratio, shaft angles, attitudes, and rates are subsequently prescribed using the test conditions. During the maneuver, the structural dynamic and the aerodynamic models are advanced in time after exchanging deformations and airloads at every time step. The procedure is same as a CFD/CSD tight coupling, except that instead of CFD a lifting-line model is being used. No sub-iterations are employed to ensure strict time accuracy, i.e. deflections at a given azimuth are calculated based on airloads from the previous azimuth. The calculated deflections are then used to advance the airloads to the current azimuth. The deflections, however, are not updated based on current azimuth airloads. Note that

this procedure is also referred to as loose coupling by the fixed wing CFD/CSD researchers (Ref. [192]).

4.2.1 Inputs to Analysis

The level flight at the beginning of the maneuver is simulated using calculated rotor control angles using conventional trim analysis. After which the measured control angles are corrected using the already calculated trim angles. The trim analysis was calculated using a moment trim targeting thrust and hub moments of 17300 lb, 6059 ft-lb roll left, and 4182 ft-lb pitch down, respectively – corresponding to high speed level flight Counter 8534. The trim angles thus obtained are then used to adjust the control angles obtained from the flight test. In this approach the entire control time history for the maneuver is corrected to match the initial trim angles as described in chapter 3. The time history of control angles used for UMARC2/lifting-line analysis are shown in Fig. 4.1. The flight test data used for the analysis of the UTTAS pull-up maneuver includes translational speed ($\mu\Omega R$), aerodynamic angle of attack (α) and side-slip angle (β), linear accelerations of helicopter CG ($\ddot{u}, \ddot{v}, \ddot{w}$) and vehicle angular rates ($p, q, r, \dot{p}, \dot{q}, \dot{r}$). All measurements are assumed to be referenced to the conventional helicopter non-rotating hub fixed frame. Orientation and location of hub with respect to the helicopter CG is assumed to be fixed. It should be noted that the measured data for the accelerations and rates have high frequency noise which has to be filtered before it is used in the analysis. This is achieved by taking moving average of the raw data. Entire data set is pre-interpolated using

splines for the entire maneuver for the desired time discretization for consistency.

A possible discrepancy was noted by Ref. [158] regarding the parity between measured fuselage angle of attack and pitch angle. For the steady level flight condition, the fuselage angle of attack and pitch angle are expected to be identical for all practical purposes, as observed for C8534 flight which is very similar to the initial steady phase of the C11029 pull-up maneuver. The measured angle of attack seems to be approximately 3.0° larger than the measured pitch angle, implying that either the vehicle was in a steady climb, or that there is an error in either angle of attack or pitch angle measurements. Comparison of the data set with the C8534 data revealed that the angle of attack measurement data suffered with a steady offset of 3.0°, which was then applied to correct the angle of attack data before using it in the analysis.

4.3 Prediction Using Lifting-Line Coupled Analysis

In this section, the multibody rotor structural model is tightly coupled with the transient lifting-line aerodynamic model to predict airloads, blade loads, pitch-link loads and the swashplate servo loads. The baseline results use the full-up aerodynamic model including free wake and dynamic stall.

4.3.1 Blade Root Deflections

The predicted blade pitch angle is compared with the measured values in Fig. 4.2. There is a difference between the two because of the control angle correction

is applied at the beginning of the analysis in order to start from a trimmed level flight condition as mentioned earlier. Figure 4.3 shows the predicted flap angles. Unlike the mechanical airloads case, here, predictions are quite different from test data. The same trend is observed in CFD/CSD analysis as well, which is discussed in chapter 5. The reasons for the deviation may be attributed to the uncertainty associated with measuring small angles accurately.

4.3.2 Blade Airloads

The rotor hub force was not directly measured during the UH-60A Airloads Program and hence has to be computed indirectly, by using either the load factor measurements or by integrating the sectional normal force. The load factor data is multiplied with the vehicle weight to obtain the vertical hub force for the present analysis. The predicted hub force is shown in Fig. 4.4. The predicted vertical hub force shows fair agreement with the flight test data at the beginning of the maneuver when the load factor is 1. As the load factor begins to increase when the helicopter starts to pull-up, there is a significant difference between prediction and flight test measurement (around 6000 lb). This may be due to the contributions from the fuselage and the horizontal tail, and has been clarified in Ref. [157]. Towards the end of the maneuver (revolution 30 onwards), there is an under-prediction of thrust which seems to be stemming from the under-prediction of mean lift. CFD/CSD analysis does not suffer with this deficiency and the reason for this is discussed in chapter 5.

Figure 4.5 shows the sectional normal forces at 86.5%R predicted by the coupled lifting-line analysis. The prediction is able to predict the mean and peak-to-peak of the stall airloads during the course of the maneuver, however the predicted high frequency stall loads are not satisfactory. This is because, accurate prediction of lift stall requires precise prediction of vortex strength accumulation and movement across the chord length. The pitching moment stalls depend primarily on the vortex shedding and therefore are relatively easier to predict. Figure 4.6 shows the sectional chord forces, which are even more difficult to predict, at the same radial station. Similar to normal force, the stall spikes are not present in the predicted chord forces. The lower frequencies are well predicted for normal forces as a consequence of which the peak loads are close to test results. The lower frequencies are over-predicted for chord forces leading to higher peak loads.

The quarter chord pitching moments are shown at two radial stations, 77.5%R (Figs. 4.7 and 4.8) and 86.5%R (Figs. 4.9 and 4.10). The maneuver starts from high speed flight condition, therefore, the pitching moment for the first four revolutions is very similar to that of flight 8534. As we get further into the maneuver (between revolution 10 and 20) the test data begins to show three pitching moment stall cycles in each revolution. Two distinct stall cycles on the retreating side sets in starting from 9th revolution. An additional stall cycle appears on the advancing side between 12^{th} to 20^{th} rev. This occurs under transonic flow conditions. The predicted pitching moments are plotted after removing the steady values. It is observed from Figs. 4.7 and 4.8 that the analysis is able to predict two distinct stall cycles on the retreating side during the course of the maneuver. The stall on

the advancing side, which is a transonic stall, is not predicted by the analysis. This stall, though a dynamic phenomenon, is significantly different from the conventional dynamic stall as discussed in chapter 3. It is also observed that the predicted stall spikes are not as sharp as test data and weaken towards the tip. For example, the predicted pitching moments at 86.5%R as shown in Figs. 4.9 and 4.9 are worse than the predictions at 77.5%R. This is because the net angle of attack which is used to calculate the airloads is sum of the applied control pitch angle and the blade elastic twist. The contribution of the blade elastic twist to the total angle of attack grows as we move outboards along the blade span. Therefore, any error in the blade elastic twist prediction has more significant effect on the airloads on the outboard sections.

4.3.3 Blade Structural Loads

The predicted flap bending moment at 50%R is shown in Fig. 4.11. The peak-to-peak moments are under-predicted by approximately 30% at the beginning of the maneuver, but the trends along the maneuver are similar to that of the test data. Figure 4.12 shows the lag bending moment at 50%R. Consistent with chord force predictions, the trends are less satisfactory compared to flap bending moments.

Figure 4.13 shows the predicted torsion moments at 30%R. Torsion moment is critical for accurate prediction of pitch-link load, which in turn drives the servo loads in fixed frame. Accurate prediction of the torsion moment is a challenge due to the complicated nature of the pitching moment for this particular flight. Although, the pitch-link load shows similar trend as the torsion moment (Fig. 4.14), the peak-

to-peak magnitude correlation with flight test is worse as seen in Fig. 4.15 which summarizes predicted structural loads. This may be due to the fact that the pitch link load is a net effect of torsional deformation of the blade, the reaction due to pitch spring and pitch damper and hence, depends on the accuracy of measured control angles. The effect of control angle perturbation is discussed later in section on fundamental understanding.

4.3.4 Swashplate Servo Loads

The baseline analysis is carried out with swashplate mass equal to zero. This is equivalent to the evaluation of servo loads through static force balance between the pitch-link and servos. The half peak-to-peak values are compared with test data in Fig. 4.16. The swashplate dynamics has a significant effect on the servo loads prediction, as evident from the results obtained for a swashplate mass of 75 kg. For example, the half peak-to-peak forward servo load witnesses a 100% increase in the predicted magnitude with swashplate mass. However, no feedback effect on the blade loads are observed, as discussed later.

4.4 Fundamental Understanding

The lifting-line coupled analysis is used to separate out the effect of wake and dynamic stall on the maneuver loads prediction. To accomplish this, the following three cases are considered: (1) uniform inflow and quasi-steady airloads using static airfoil properties, (2) free wake and quasi-steady airloads, and (3) free wake and

dynamic stall. The last case is the baseline case. In addition, because the control angles are prescribed from test data, a trim angle sensitivity study is carried out by perturbing the control angles by 10% of their baseline values.

4.4.1 Effect of Free Wake Model

The rotor wake cuts through the rotor disk on two occasions. The side and top views of the wake geometry at different stages of the maneuver is shown in the Figs. 4.17 and 4.18. At the end of revolution 6, the advance ratio, μ is 0.358, and the aircraft angle of attack, α is -4.09° (+ve nose–up), the rotor wake is blown straight downstream (Figs. 4.17(a), and 4.17(b)). As the aircraft angle approaches towards 0°, the wake gets closer to the rotor disk (Fig. 4.17(c)), the side-slip angle is very small and hence the rotor wake is fairly straight as seen in the top view (Figs. 4.17(d)). As observed in Figs. 4.17(e), and 4.17(f), the rotor wake is above the rotor disk and is moving to the starboard side by the end of revolution 14 ($\alpha = +9.75^\circ$, and $\beta = -4.35^\circ$). At this point the helicopter is pulling a load factor of 2.08–g. The load factor is mainted above 2–g, between revolution number 14–18, after which the load factor starts to decrease. During this period the wake remains above the rotor plane for most of time (Fig. 4.18(a)). The rotor wake is again seen (Fig. 4.18(c)) in the disk plane at the end of the revolution 24 ($\alpha = +2.72^\circ$), when the wake starts to cut from top to bottom towards the end of revolution 24. By revolution 28 the rotor wake has descended below rotor as shown in Fig. 4.18(e) ($\alpha = -6.51^\circ$, and $\beta = -13.74^\circ$).

The inflow predicted using the free wake model is compared consistently with uniform inflow calculated using flight test thrust and the effective shaft angle with respect to on-coming flow in Fig. 4.19(a). The wake passage is clearly visible near revolution numbers 10 and 24. A choice of 2 or 4 free turns for the wake does not impact the inflow calculation as there is no wake bundling phenomena near the disk. This is expected as at relatively high speeds, the rotor wake gets quickly blown away. However the wake passage has no effect on the airloads Fig. 4.19(b). It is shown later that the sectional angles of attack already operate under deep stall during these revolutions and the wake induced angle of attack variation has little effect on the airloads. The airloads are determined entirely by the post stall airfoil property tables. It is observed from the present analysis that in general the free wake does not affect any of the predicted airloads and structural loads.

4.4.2 Effect of Dynamic Stall

The pull-up maneuver is characterized by three stall cycles, one on the advancing side and two on the retreating side. The capability of lifting–line models is now examined in predicting these stall cycles. Figure 4.20(a), shows the predicted and measured pitching moment at $77.5\%R$ highlights the importance of dynamic stall modeling. Both the waveform and magnitude of prediction require the dynamic stall model. The peak-to-peak pitching moment prediction is improved by more than 50% during revolutions 16–20.

However, the effect on structural loads is less dramatic. Predicted peak-to-

peak torsional moment at 30%R using dynamic stall model show improvement by 10% to 20%, with respect to those obtained without it (Fig. 4.20(b)) during revolution number 16–20. Similar trends are exhibited by the pitch-link load (Fig. 4.20(c) and 4.20(d). It can be observed that the use of dynamic stall model is causing a significant impact on the peak-to-peak loads during the high load factor regime, e.g. during revolution 14,when the load factor is more than 2.0g, an improvment of 24% is observed for peak-to-peak pitch-link load and for revolution 15 the gain is 23%. The gain in structural loads is less significant because the peak-to-peak loads are determined primarily by 1/rev, while the stall loads are mostly 4, and 5/rev.

The rotor stall maps showing moment stalls for revolutions 14, 16 and 18 are shown alongside stall maps from the flight test in Fig. 4.21. The flight test stall maps reveal three stall cycles in the outboard region of the rotor disk, a stall on the advancing side near 50° azimuth, followed by two stall cycles on the retreating side. The predicted stall maps also show three moment stall cycles. The first stall occurring near the 180° blade azimuth is starting from the blade inboard stations (55%R). The other two moment stalls are occurring in the retreating side similar to the flight test. To understand the mechanism of these stalls we need to look at the angle of attack at the onset of moment stall. Figure 4.22 shows the angle of attack variation at 77.5%R. The operating envelope (Fig 4.23(a)) for SC 1095 R8 airfoil at 77.5%R at rev. 16 reveals that when the blade reaches the 180° azimuth, and attains an angle of attack of 10°, the local Mach number of 0.54 is sufficient to take the blade over static stall limits which triggers the dynamic stall model, and thus the first stall cycle is predicted near 180°. The remaining two stall cycles occur in a

similar manner, with the angle of attack remaining deep inside the static stall region. The contribution of the leading edge vortex to quarter chord pitching moment from the three stall events for the revolutions 14–18 is shown in Fig. 4.23(b). It appears that the contribution is not large enough compared to measurements. This under-prediction leads to a reduced nose down torsion deformation which in turn causes the first stall to occur earlier in azimuth. Figures 4.23(c) and 4.23(d) show the airfoil operating envelopes, at 86.5%R and 77.5%R respectively, using all the three aerodynamic analyses. It shows that all analyses predicts the blade to be operating under deep stall condition. This is the reason inflow variation has little or no effect on the loads prediction using present analysis.

4.4.3 Sensitivity to Control Pitch Angles

Because the present flight condition is a prescribed maneuver, and because it is initiated from trim angles calculated for steady flight conditions, it is important to understand the sensitivity of the analysis to pitch control angles. The effect of perturbing the collective and lateral cyclic angles, by 10% of the baseline value, on the predicted peak-to-peak torsion moment at 30%R is shown in Fig. 4.24. A variation in collective angle seems to have most significant impact on the overall dynamics of the rotor, as depicted by the predicted peak-to-peak torsion moment. Increasing the collective angle by 10% is causing an increase in predicted torsion moment from the baseline (Fig. 4.24(a)), while a reduction by 10% is resulting in significant underprediction. This is due to the sensitivity of predicted pitching

moment to the angle of attack which is primarily governed by the control angles. The longitudinal and later cyclic perturbation doesn't have a significant effect on the overall dynamics as shown in Figs. 4.24(b) and 4.24(c). These observations are similar to those made in chapter 3 for the predicted airloads using calculated deformations.

4.4.4 Effect of Swashplate Dynamics

A swashplate mass of 75 kg (165 lb), based on the discussion in chapter 2, is used to study the effect of swashplate dynamics on rotor and servo loads. The predicted servo loads, obtained using coupled blade-swashplate dynamics model, waveform and peak-to-peak values are shown in Fig. 4.16 and peak-to-peak values show fair correlation with the test data. Figure. 4.25 shows predicted pitching moment at $77.5\%R$, torsion moment at $30\%R$, and the pitch-link load. The swashplate dynamics does not seem to affect the rotor loads. But, the swashplate dynamics does have a strong influence on the servo loads which are predominantly 4/rev and 8/rev (20% of 4/rev). It should be noted that, even though the maneuver being studied is an unsteady flight, the revolutions $1-7$, $14-18$, and $26-40$ are relatively steady, and thus the harmonic analysis, though approximate, is valid for establishing trends. Figure 4.26 shows the predicted trends for 4/rev and 8/rev servo loads. It can be observed that in the absense of any swashplate dynamics (swashplate mass 0 kg), the predicted servo loads are dominated by 4/rev and this 4/rev in fixed frame comes from the 3, 4 and 5/rev pitch-link loads in rotating frame. It should

be noted that even though the peak-to-peak pitch-link load is under-predicted, the swashplate loads show better correlation with flight test, because the analysis is able to predict the 3/rev pitch-link load accurately as shown in Fig. 4.27. Further, when the swashplate mass is included in the analysis, the 4/rev prediction improves by 20%–40%, but the 8/rev servo loads which are under-predicted in the absense of swashplate dynamics, are now over predicted. The over-prediction occurs because the swashplate fundamental frequency for a mass of 75 kg lies close to 8/rev (9.48/rev).

4.5 Concluding Observations

The airloads, blade loads, pitch-link loads, and swashplate servo loads of the UH-60A helicopter were predicted and analyzed in a 2.12-g pull-up maneuver. The rotor control angles and the flight dynamic parameters (flight path and velocities, attitude angles and rates) were prescribed from flight test measurements (Counter 11029 of UH-60A Airloads Program). A multibody finite element structural model – including a swashplate servo model – was coupled in time to an unsteady lifting-line aerodynamic model. The coupling in time was a standard time marching procedure (tight coupling in rotorcraft nomenclature) without any sub-iterations. This chapter focused on isolating the effects of free wake, dynamic stall, and rotor control angles, separately, on the loads mechanism of the maneuver. The purpose of using the lifting-line aerodynamic model was to isolate the effects of free wake and dynamic stall modeling and to examine the accuracy level of the lifting-line aerodynamic

model in predicting the structural loads for a severe flight condition. Because the maneuver is prescribed, not simulated from first principles, the sensitivity of the predicted loads to prescribed control angles are also studied. Based on this the following key conclusions are drawn:

1. The pull-up maneuver appears almost entirely to be a stall dominated maneuver. The dynamic stall model, not the free wake, provides the most significant improvement to predicted rotor loads. Almost up to 75% of a typical airfoil operating envelope (outboard of 67.5% R) during the 10-25 revs. occur beyond the static stall boundary. Thus, the sectional airload properties are governed predominantly by stall phenomenon.

2. Similar to flight test – where three distinct stall regions are reported – the analysis also predicts three stall cycles. However, only the two retreating blade cycles are predicted near the correct regions of the rotor disk. The advancing blade transonic stall cycle is not predicted at all. Instead, the third cycle is predicted on the retreating side, together with the first two. In the analysis all these cycles occur due to multiple leading edge vortex shedding phenomena governed entirely by the semi-empirical time constants.

3. The rotor wake passes through the rotor disk approximately during the 10th and 24th revolution. The present analysis does not predict any significant perturbation in the airfoil operating envelopes due to the wake during these revolutions. In general, between uniform inflow and free wake, there is 2–4° perturbation in sectional angles of attack which occurs in the stalled regions

with minor impact on the sectional airloads.

4. The predicted peak-to-peak structural loads are unsatisfactory in general. During the peak load factor of the maneuver, 10–22 revs (above $1.75g$), the flap bending moments are closer to the test data (10–20% underprediction), followed by chord bending (25% overprediction), then torsion moment (30% underprediction), and finally pitch-link load (50% underprediction). In addition, some of the key loads show inconsistent trends. For example, the flap bending moment in the initial part of the maneuver – which is a steady level flight – is underpredicted by 30% while the torsion moment is overpredicted by 30%.

5. The chord bending moment error is primarily due to the absence of the nonlinear damper force in the coupled analysis. In case of measured airloads, including damper force, the predictions are similar to flight test values. The error in torsion moment and pitch link load stems entirely from the error in stall airloads.

6. The swashplate servo loads are determined by the 3, 4, and 5/rev pitch-link loads and the dynamics of the swashplate. The later appears to be an important contributor during the maneuver – unlike in the case of level flight. However, the servo loads, during the maneuver are dominated primarily by 4/rev loading similar to the level flight. Their peak magnitudes, are however magnified 3 times (forward link) to 5 times (aft link) compared to level flight. The analysis predicts this trend correctly – primarily due to the accuracy of

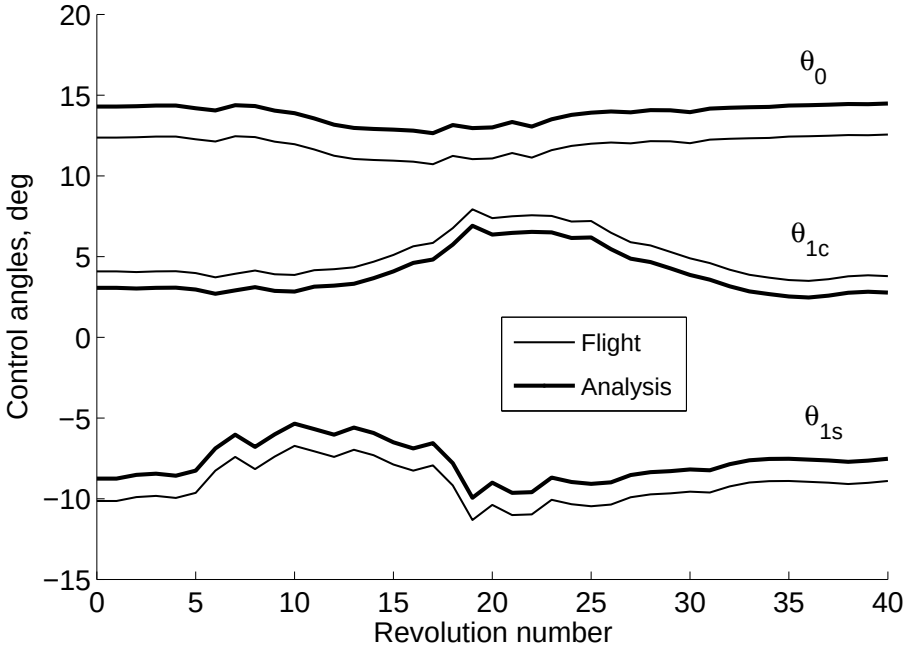

Figure 4.1: **Prescribed control angles (angles are adjusted to match the initial trim); flight C11029**

3/rev pitch-link load prediction. The analysis also show a significant impact of swashplate dynamics on the 8/rev loads.

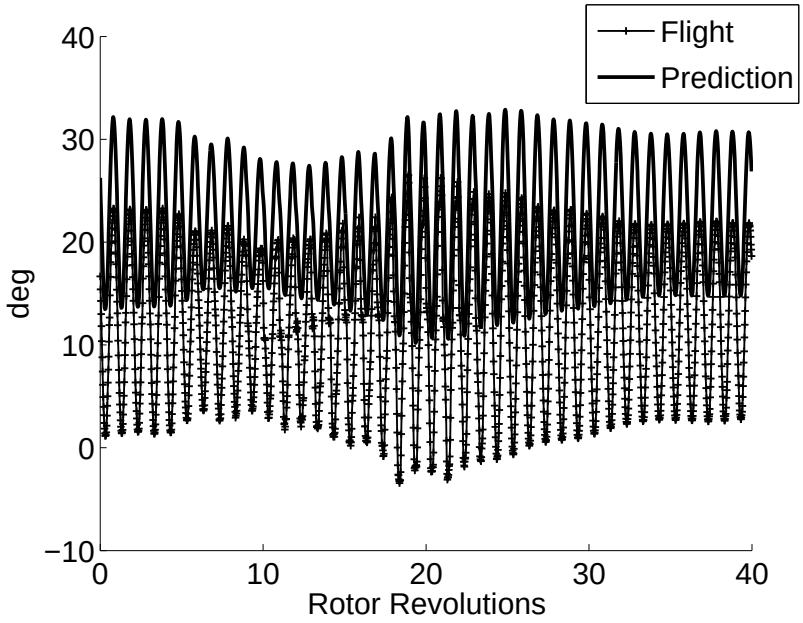

(a) Time history

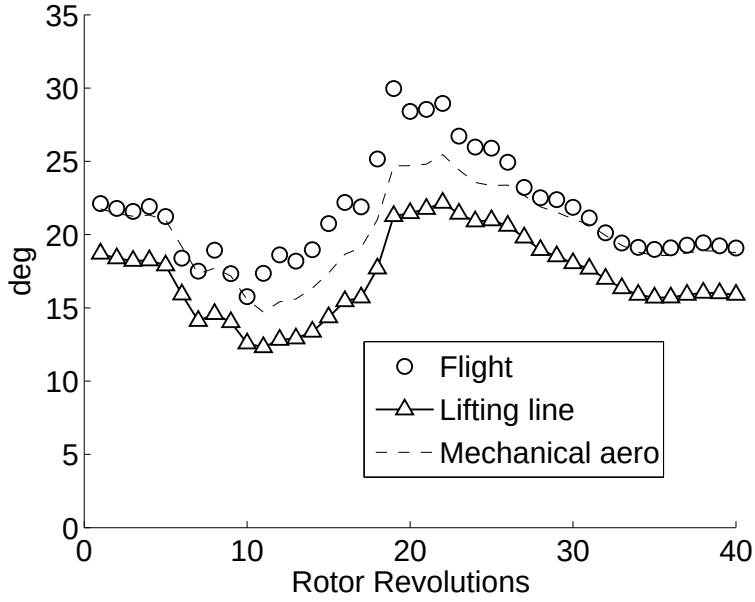

(b) Peak-to-peak

Figure 4.2: **Measured (blade #3) and predicted pitch angle at root; predictions using dynamic stall model; flight C11029**

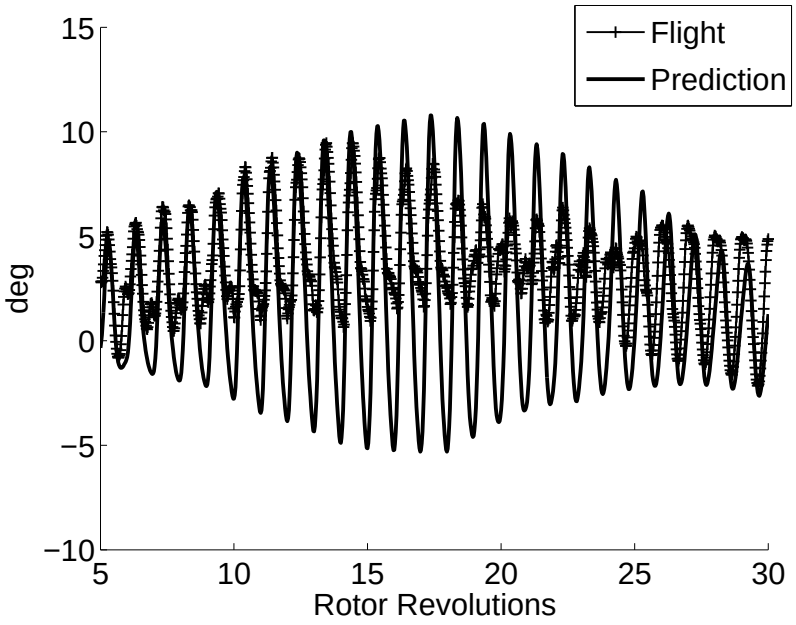

(a) Time history

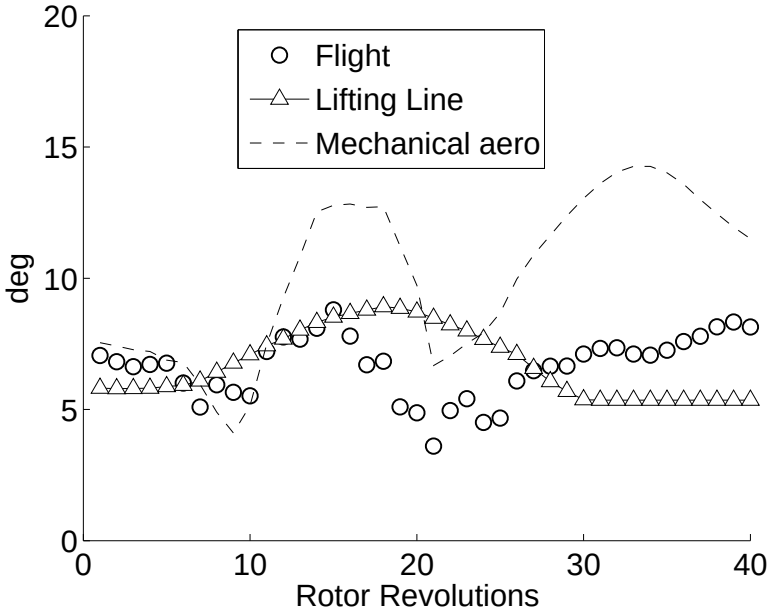

(b) Peak-to-peak

Figure 4.3: **Measured (blade #1) and predicted flap angle at root; predictions using dynamics stall model for flight C11029; time history shown for only 25 revolutions for clarity**

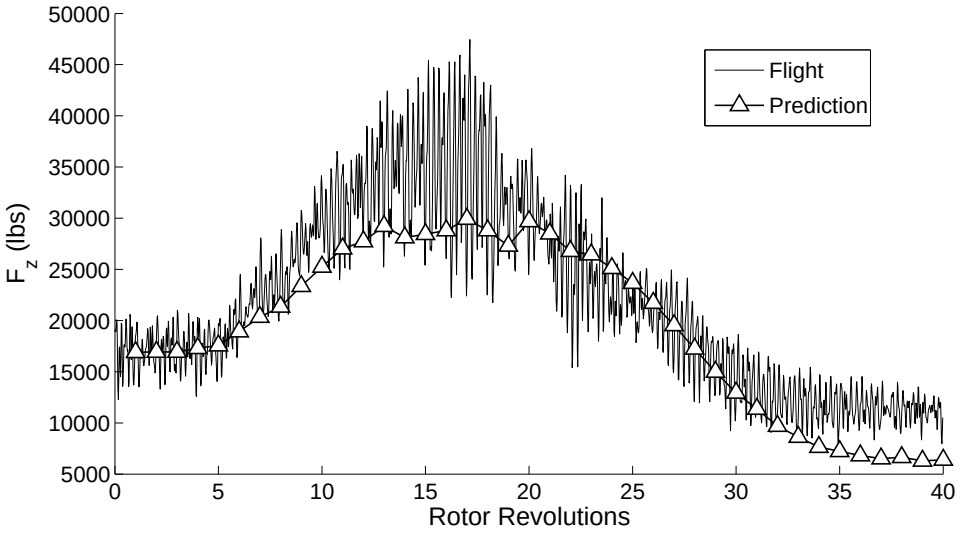

Figure 4.4: **Measured and predicted vertical hub force using dynamic stall model for flight C11029; flight data obtained from measured load factor**

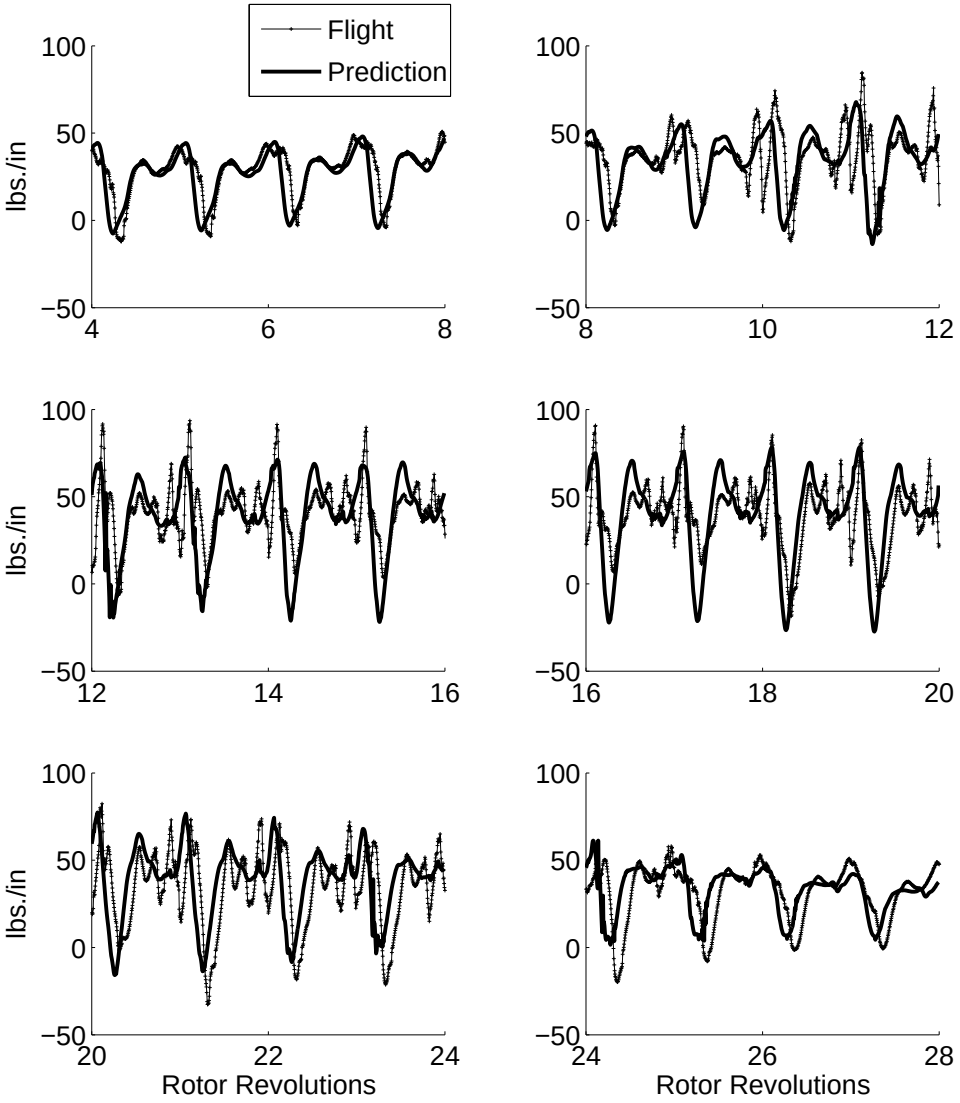

Figure 4.5: **Measured and predicted normal force at 86.5%R; predictions using dynamic stall model**

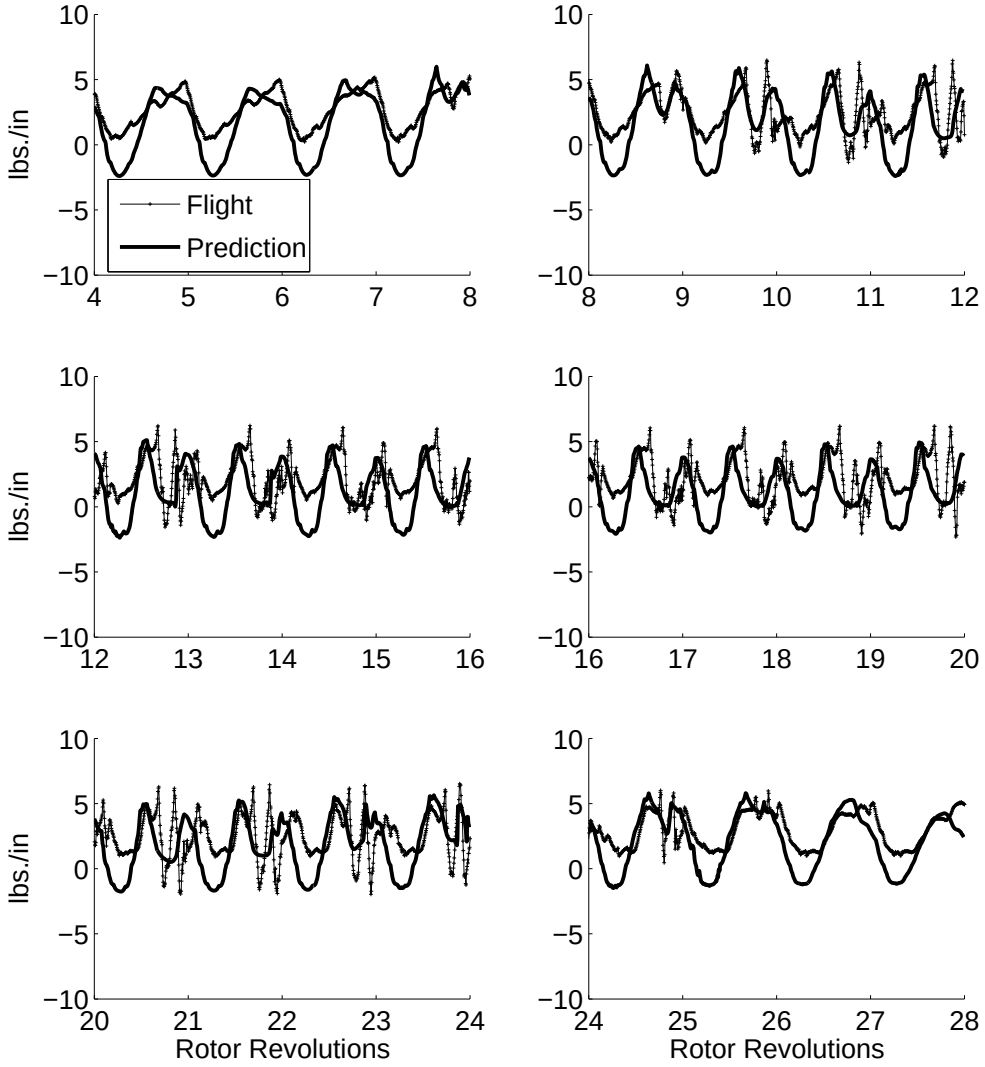

Figure 4.6: **Measured and predicted chord force at 86.5%R; predictions using dynamic stall model**

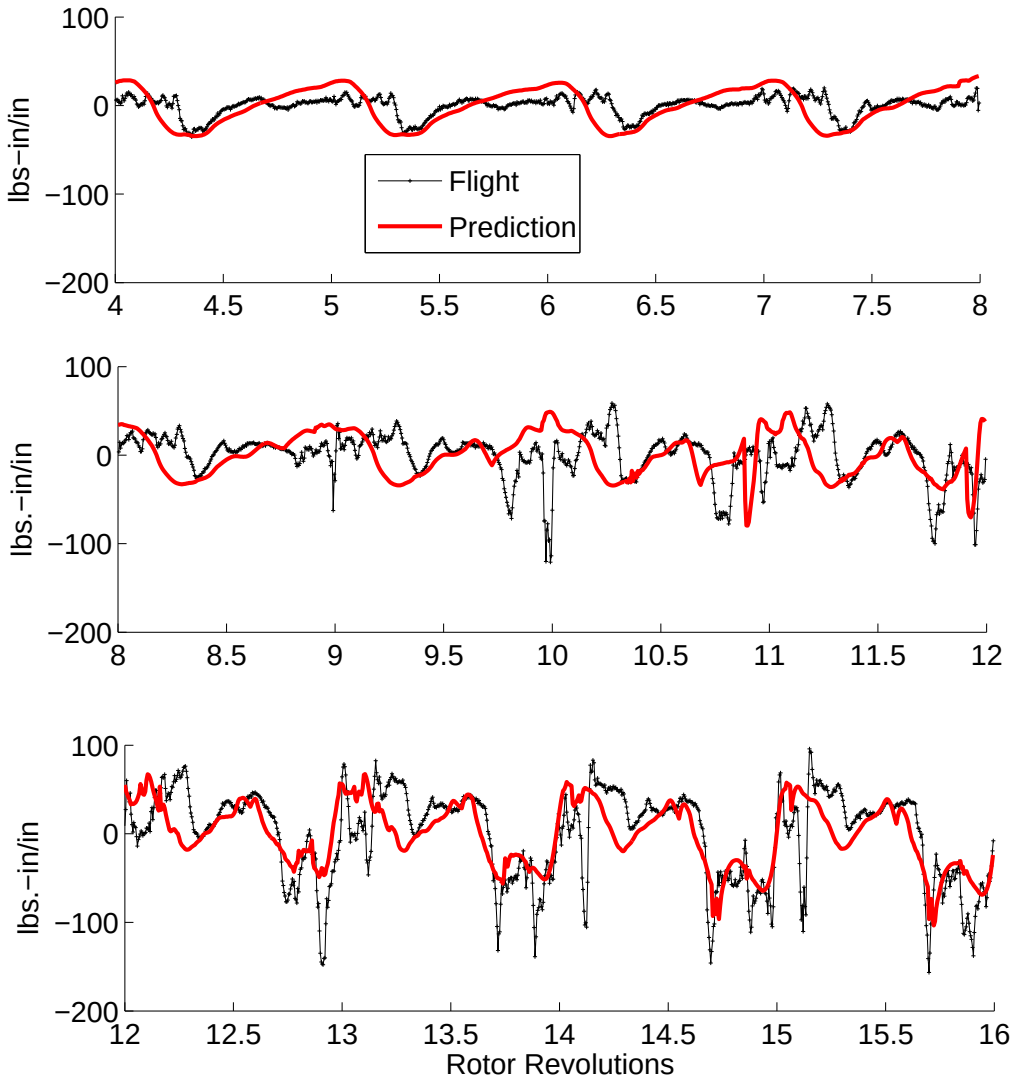

Figure 4.7: **Measured and predicted pitching moment at 77.5%R for revolutions 4-16; predictions using dynamic stall model; mean removed**

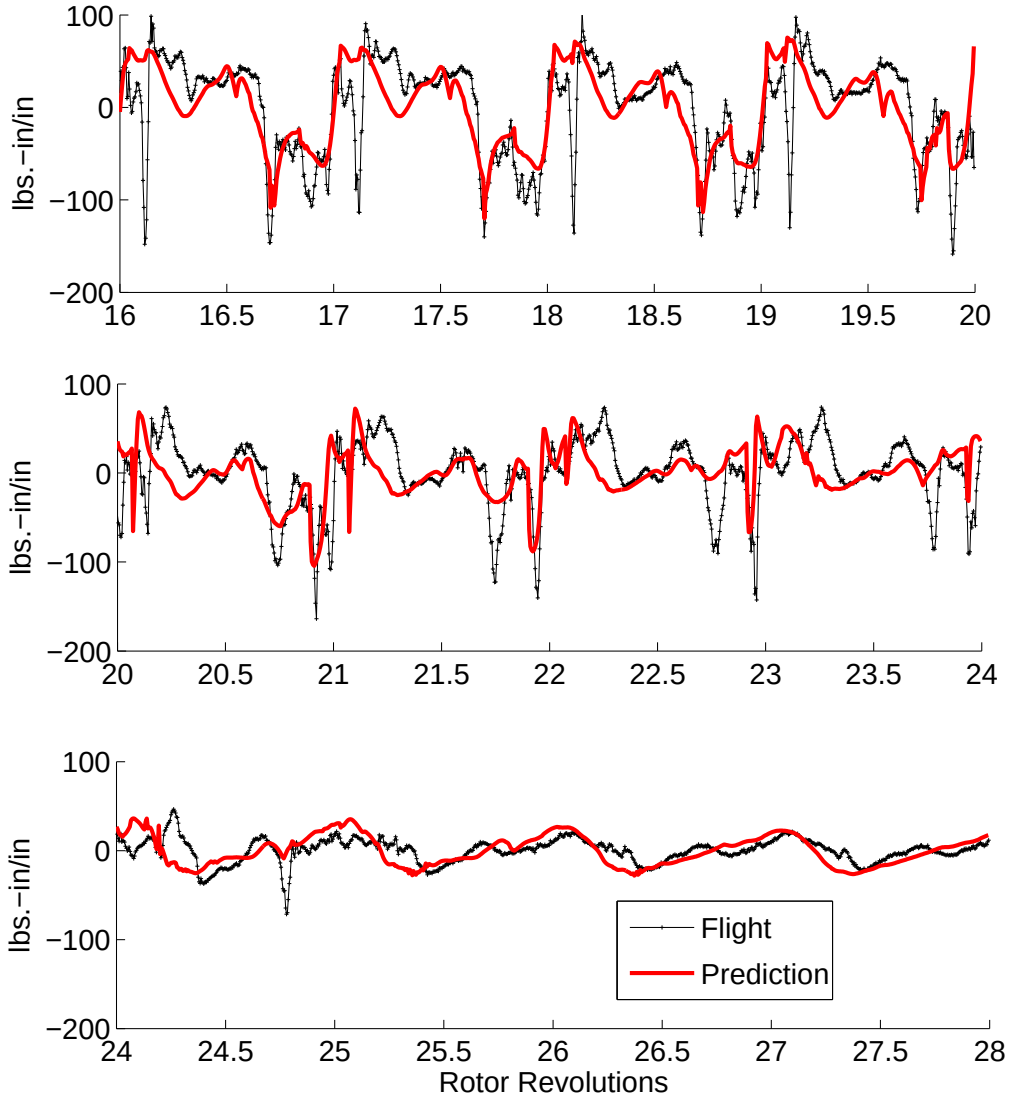

Figure 4.8: **Measured and predicted pitching moment at 77.5%R for revolutions 16-28; predictions using dynamic stall model; mean removed**

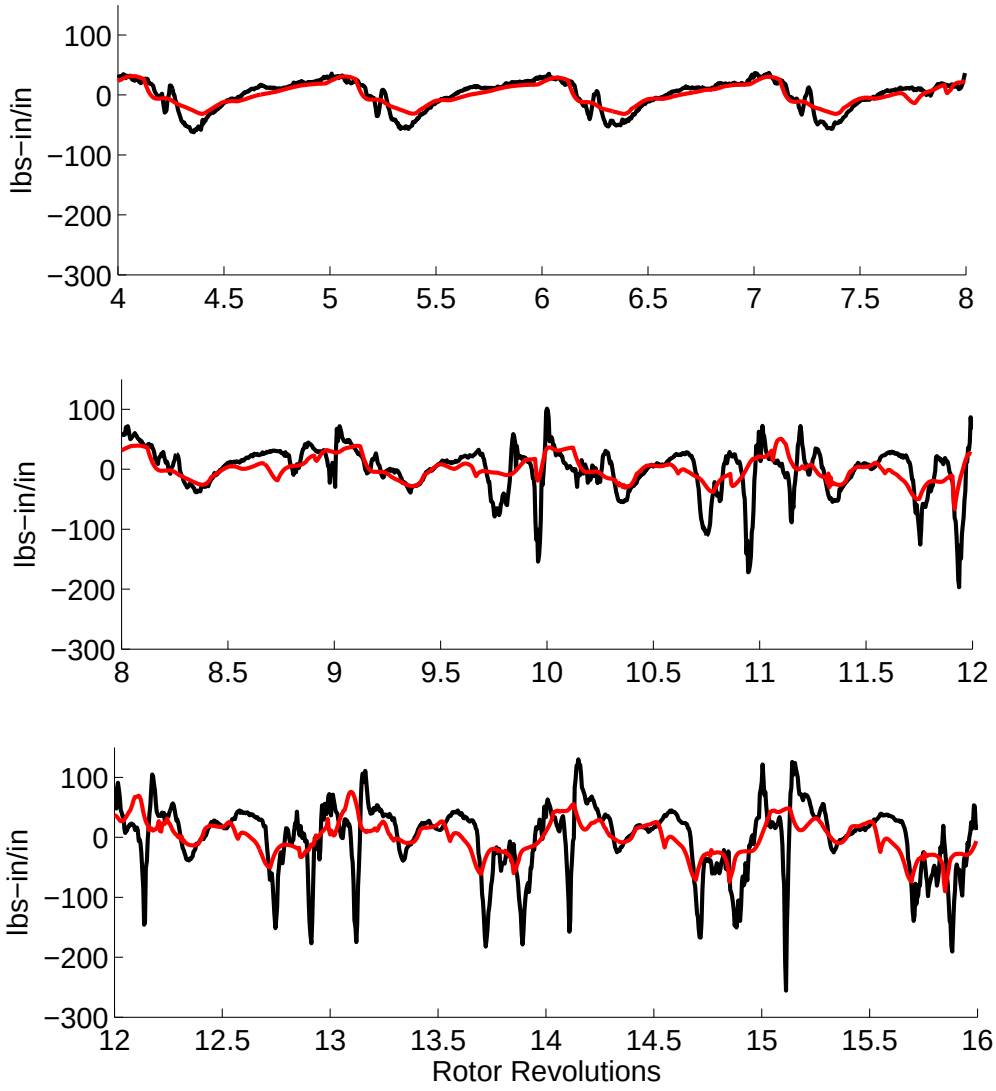

Figure 4.9: **Measured and predicted pitching moment at 86.5%R; predictions using dynamic stall model; mean removed**

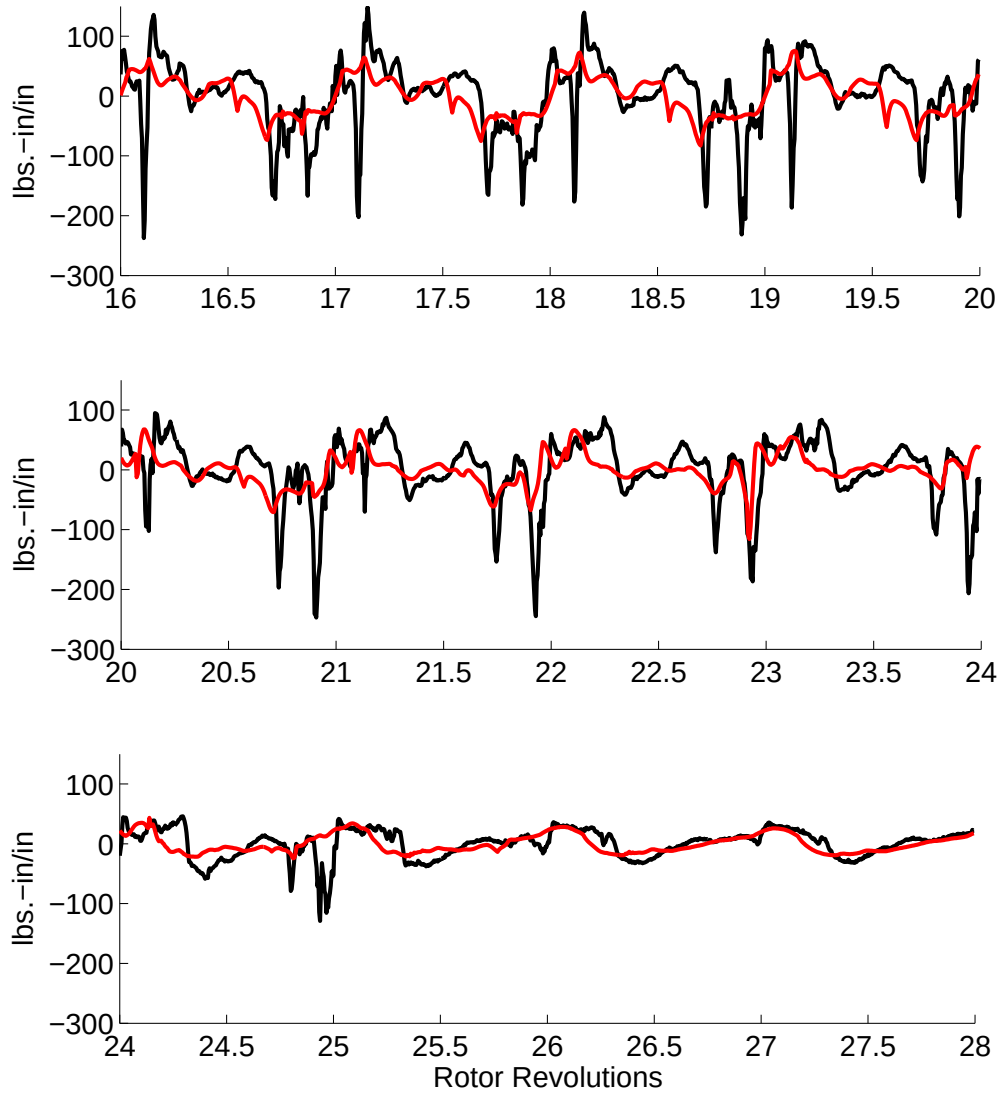

Figure 4.10: **Measured and predicted pitching moment at 86.5%R; predictions using dynamic stall model; mean removed**

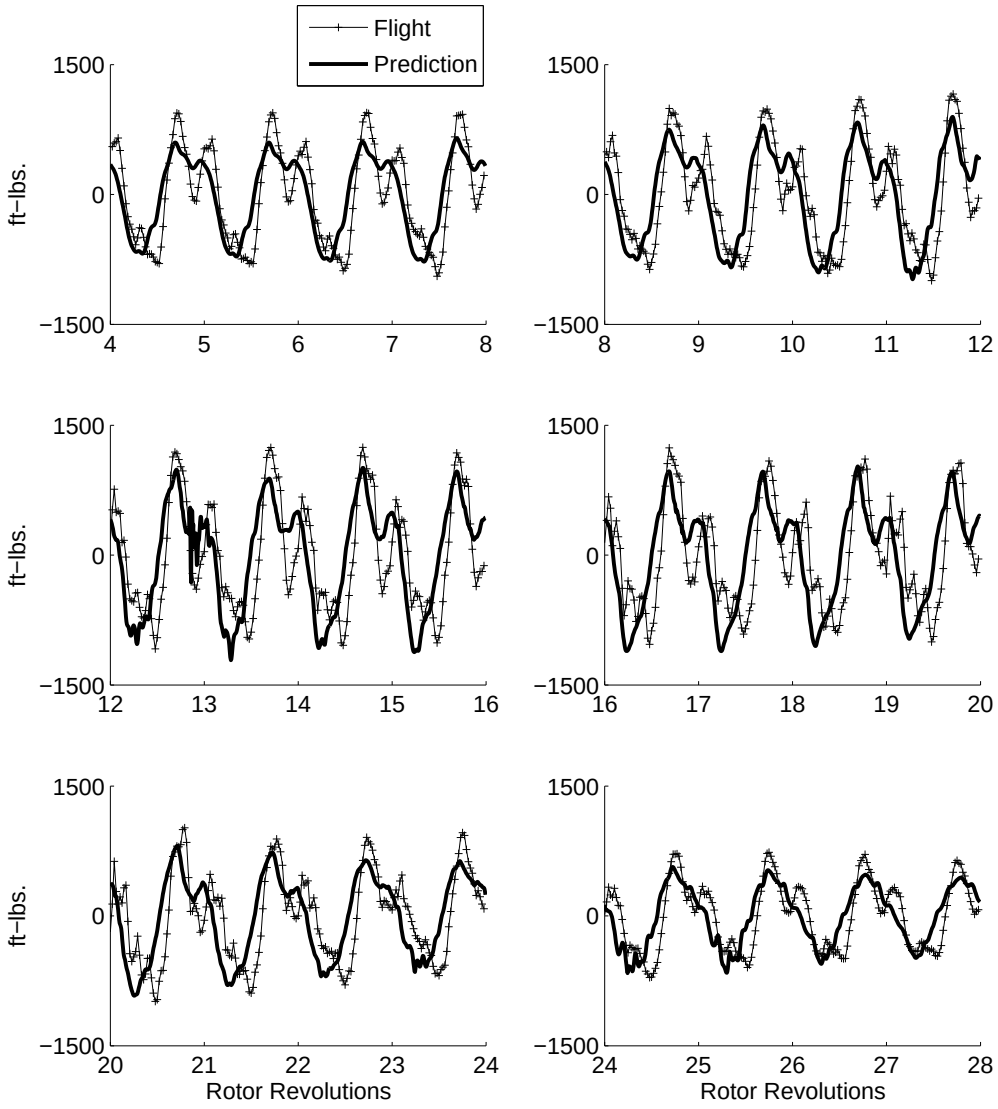

Figure 4.11: **Measured and predicted flap bending moment at 50%R; predictions using dynamic stall model; mean removed**

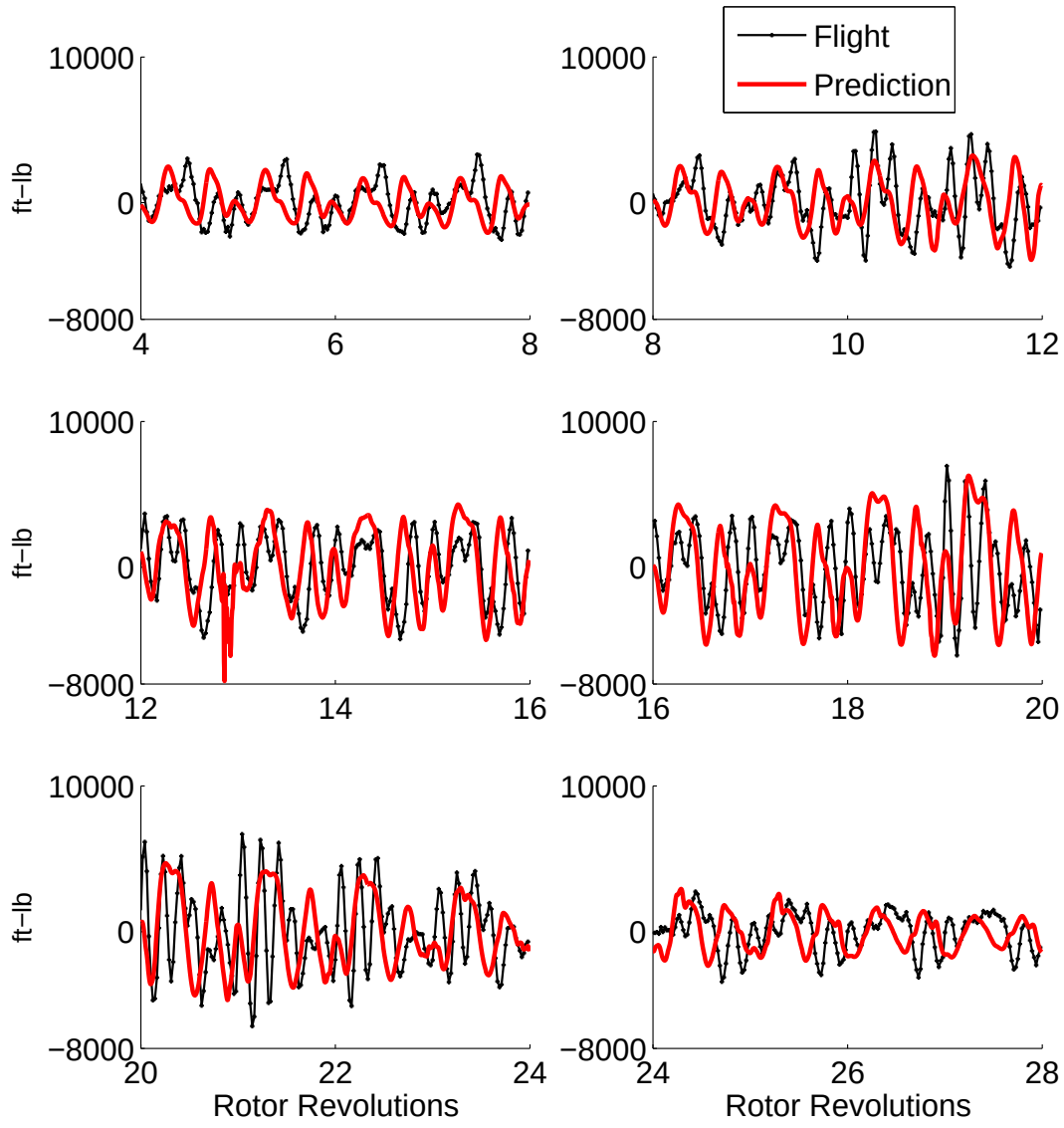

Figure 4.12: **Measured and predicted chord bending moment at 50%R; predictions using dynamic stall model; mean removed**

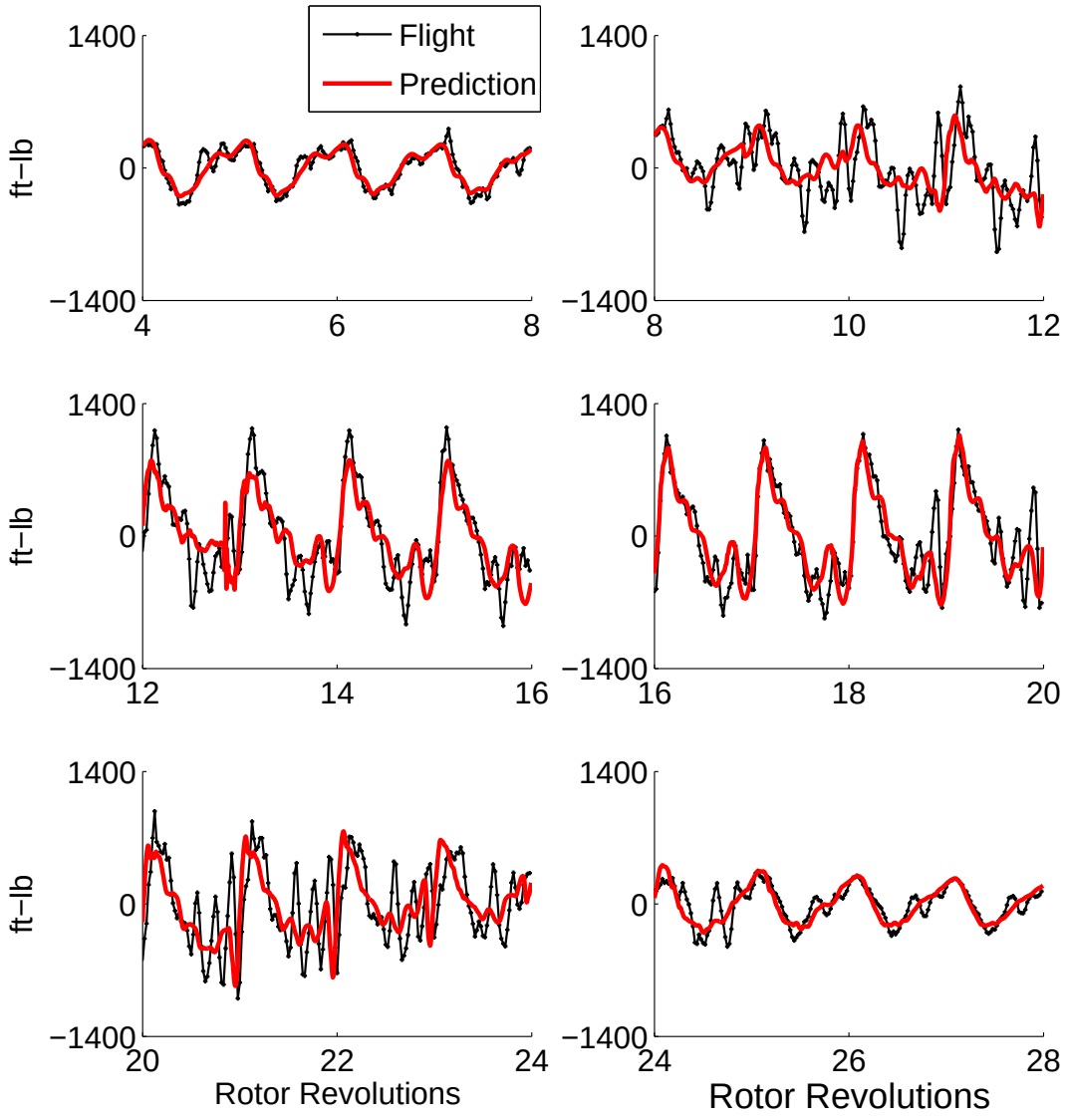

Figure 4.13: **Measured and predicted torsion moment at 30%R; predictions using dynamic stall model; mean removed**

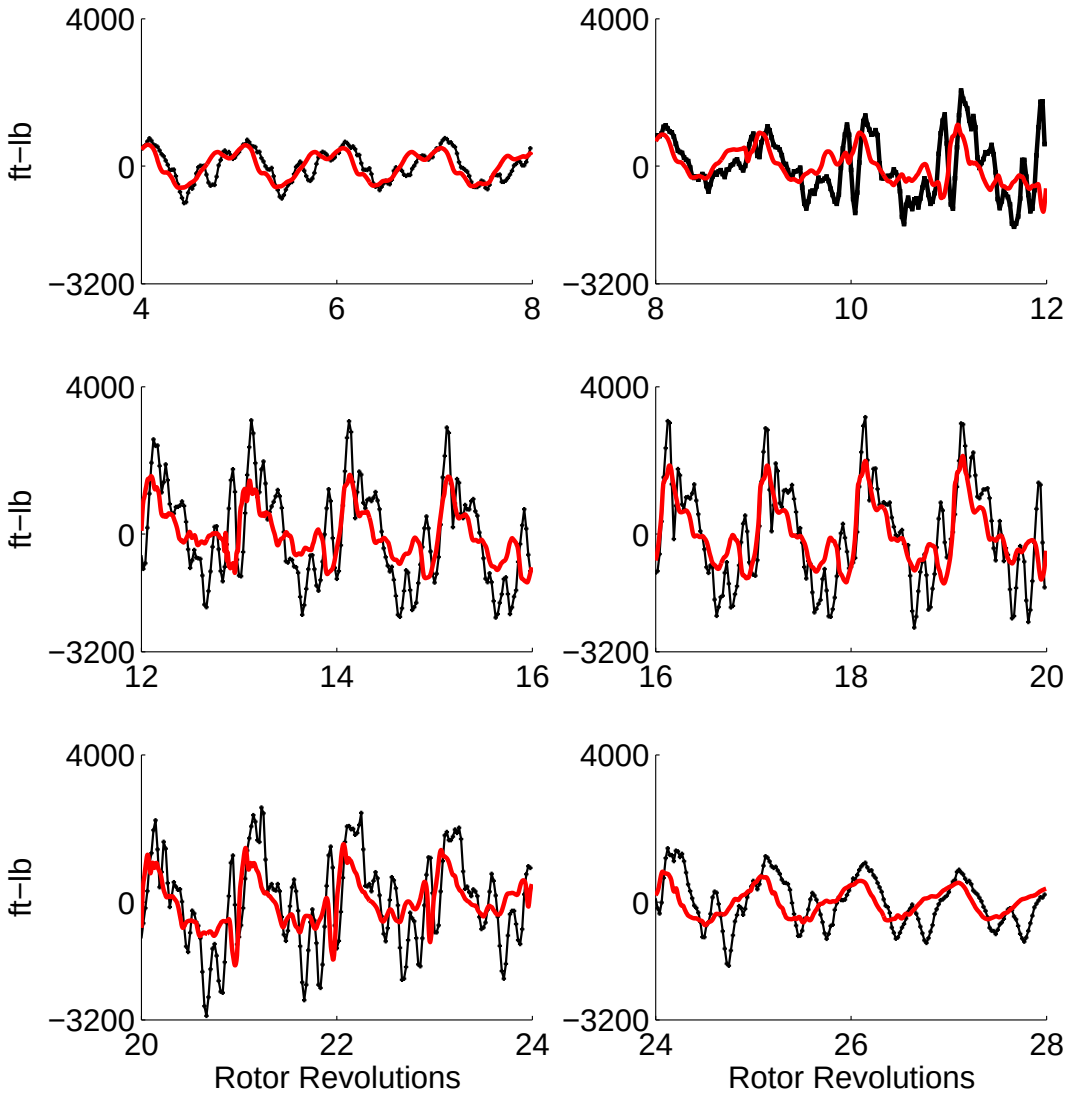

Figure 4.14: **Measured and predicted pitch-link load; predictions using dynamic stall; mean removed**

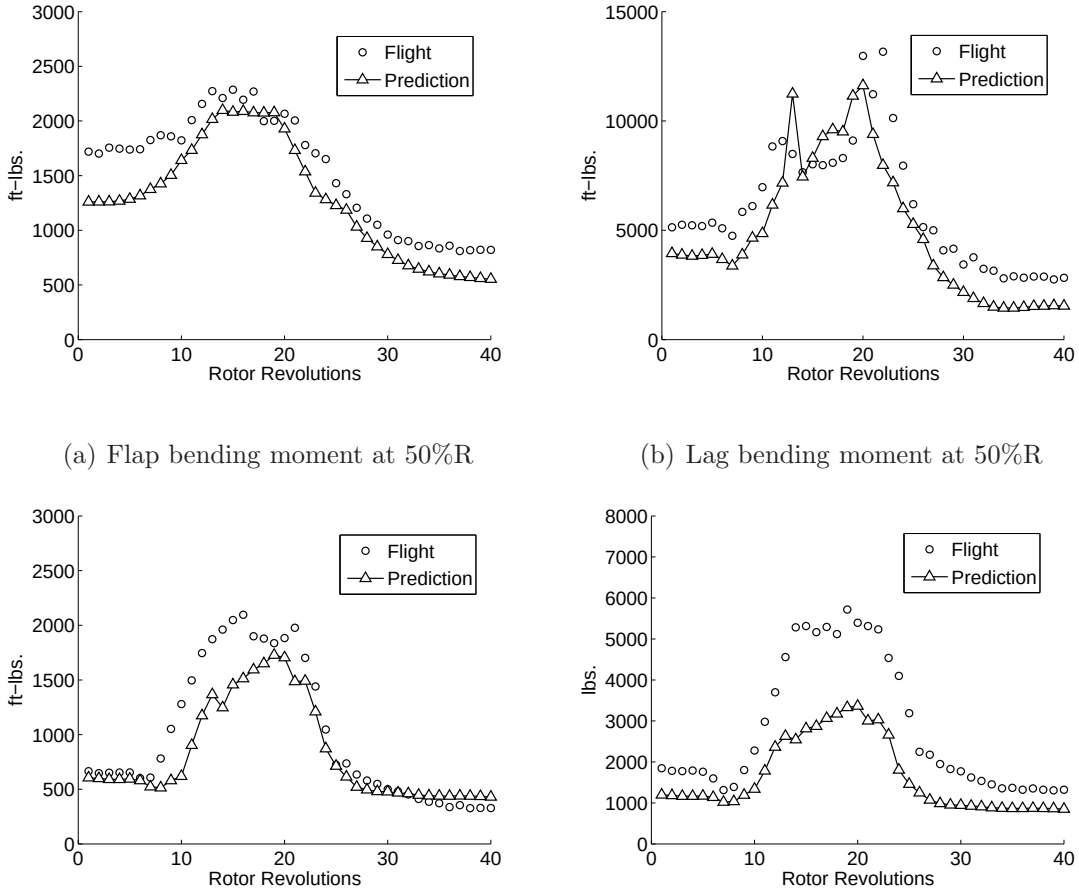

(a) Flap bending moment at 50%R

(b) Lag bending moment at 50%R

(c) Torsion moment at 30%R

(d) Pitch-link load

Figure 4.15: **Measured and predicted peak-to-peak structural loads; predictions using full aerodynamic model with free wake and dynamic stall for flight C11029**

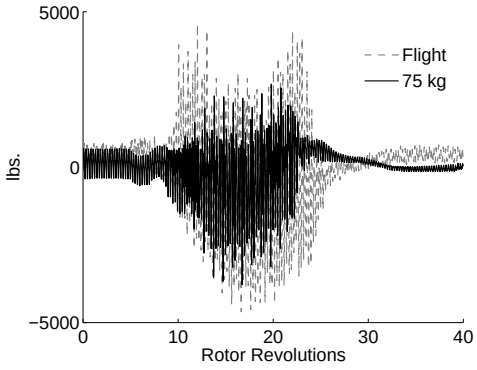

(a) Forward servo link load

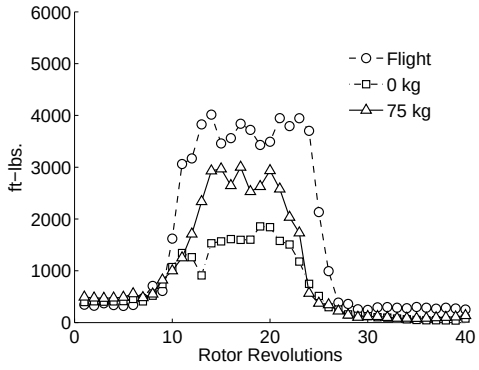

(b) Half peak-to-peak forward link load

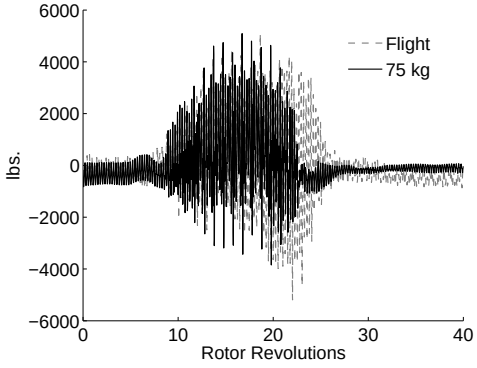

(c) Lateral servo link load

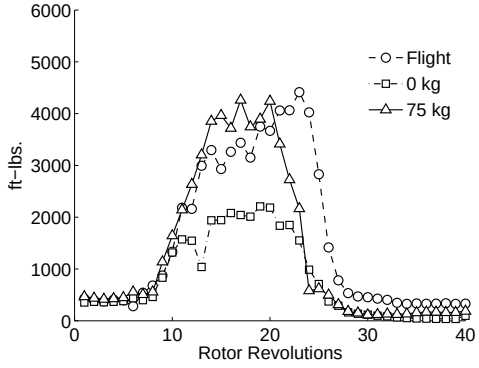

(d) Half peak-to-peak lateral link load

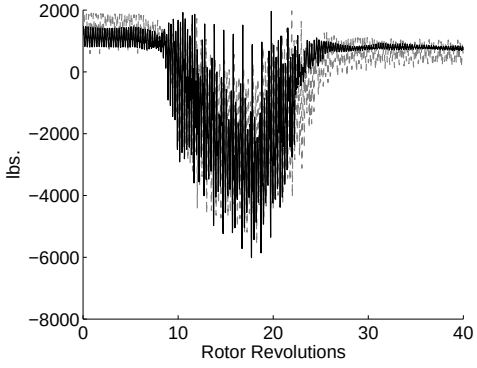

(e) Aft servo link load

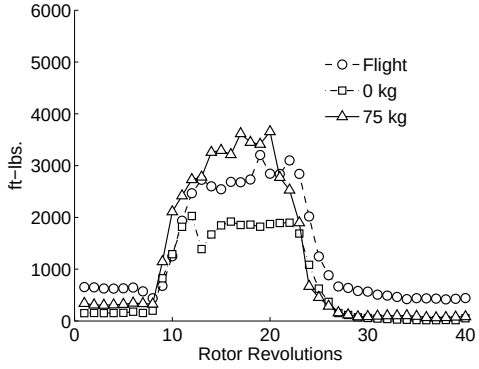

(f) Half peak-to-peak aft link load

Figure 4.16: **Measured and predicted servo loads (mean removed); predictions using dynamic stall model with swashplate mass of** 0 **kg and** 75 **kg; forward link (servo) is located at** $123°56'$ **azimuth, lateral link is at** $213°56'$ **and aft link is at** $303°56'$ **azimuth**

(a) Side view at the end of rev. 6

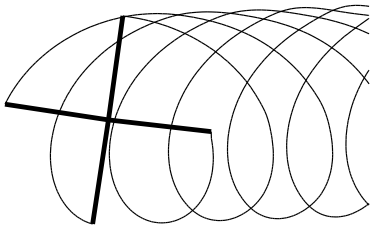

(b) Top view at the end of rev. 6

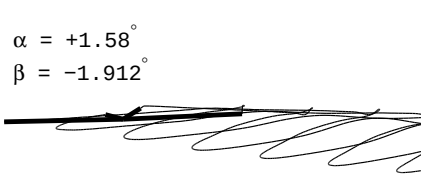

(c) Side view at the end of rev. 10

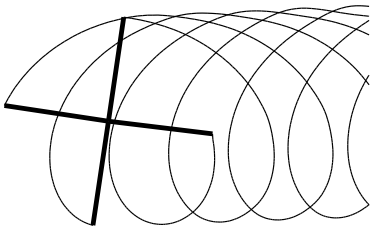

(d) Top view at the end of rev. 10

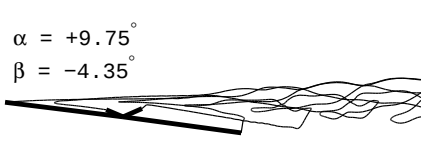

(e) Side view at the end of rev. 14

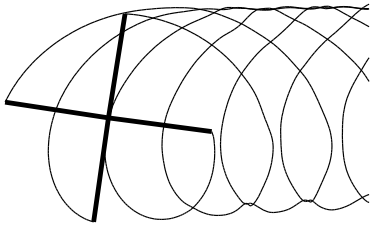

(f) Top view at the end of rev. 14

Figure 4.17: **Instantaneous rotor wake geometries during the maneuver; using 2 wake turns, α is aircraft angle of attack, β is aircraft side-slip angle**

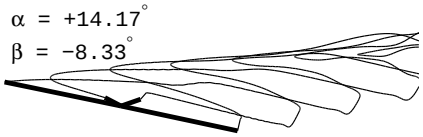

(a) Side view at the end of rev. 18

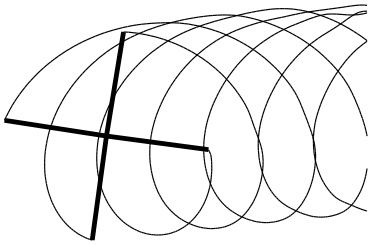

(b) Top view at the end of rev. 18

(c) Side view at the end of rev. 24

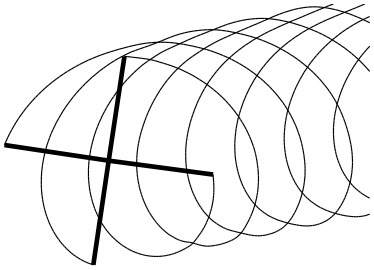

(d) Top view at the end of rev. 24

(e) Side view at the end of rev. 28

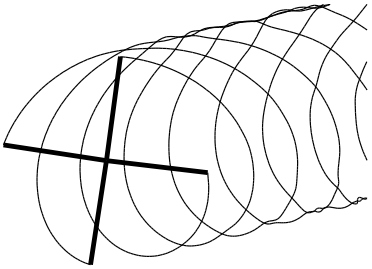

(f) Top view at the end of rev. 28

Figure 4.18: **Instantaneous rotor wake geometries during the maneuver; using 2 wake turns, α is aircraft angle of attack, β is aircraft side-slip angle**

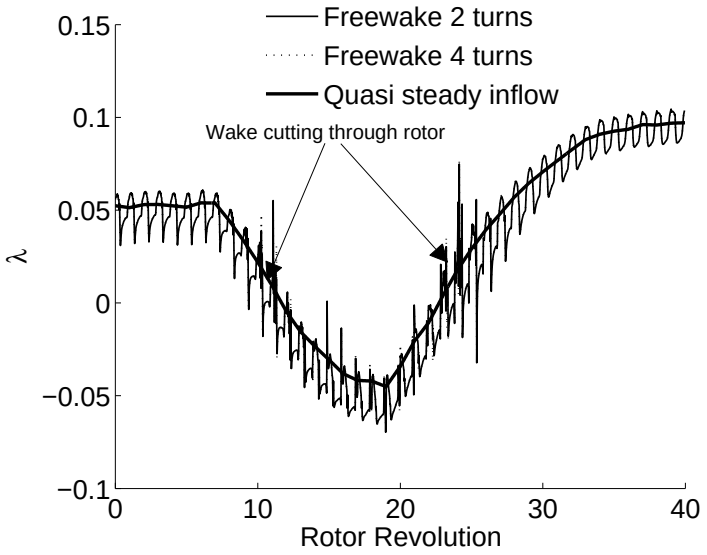

(a) Predicted inflow at 86.5%R

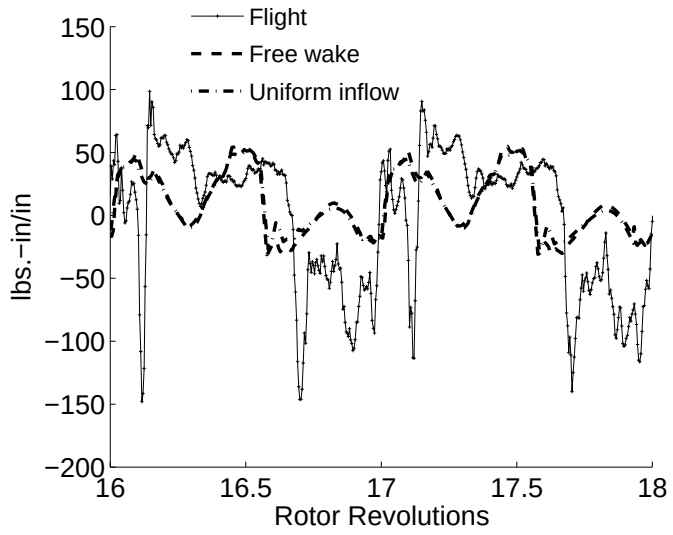

(b) Pitching moment at 77.5%R

Figure 4.19: **Predicted inflow and effect of free wake model on predicted pitching moment; prediction using static stall model**

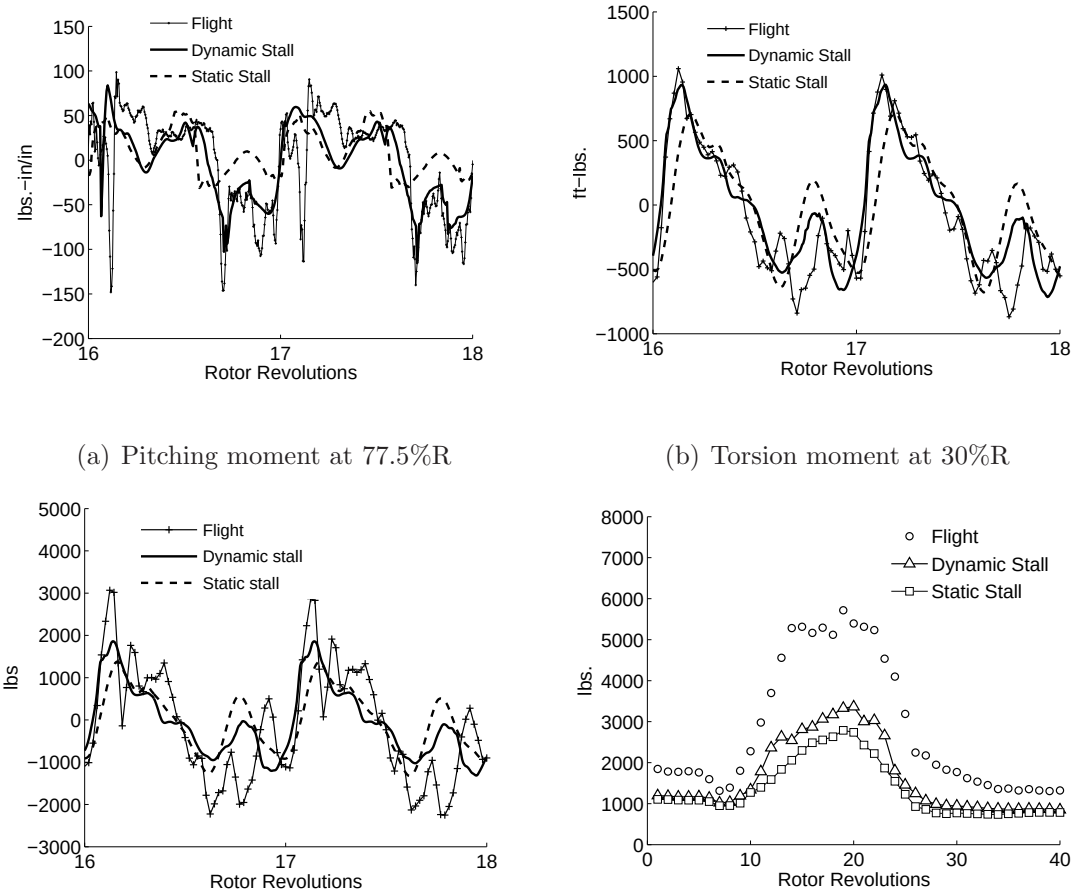

(a) Pitching moment at 77.5%R

(b) Torsion moment at 30%R

(c) Pitch-link load

(d) Peak-to-peak pitch-link load

Figure 4.20: **Comparison of predicted blade loads using dynamic stall and static stall aerodynamic models**

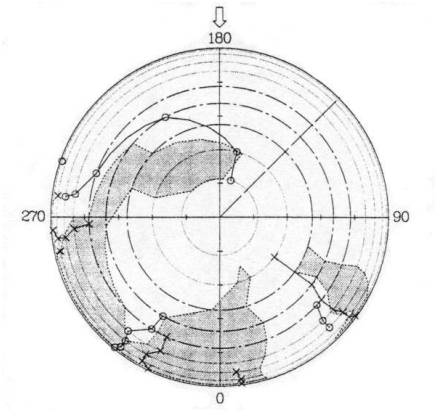

(a) Flight stall map rev 14

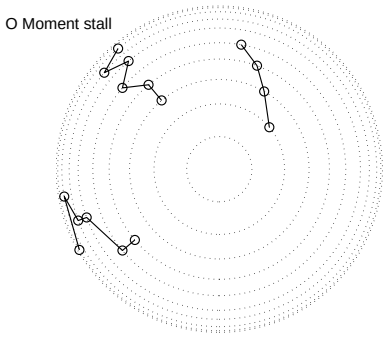

(b) Predicted stall map rev 14

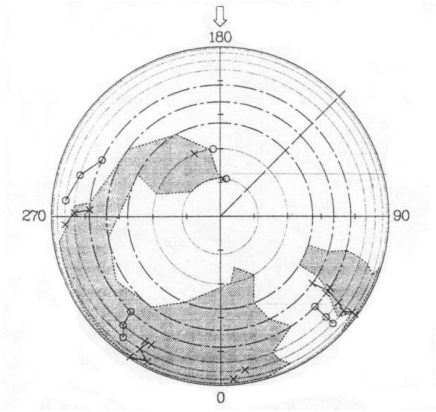

(c) Flight stall map rev 16

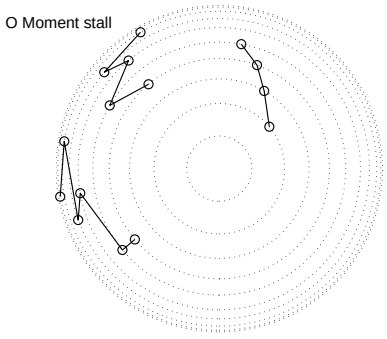

(d) Predicted stall map rev 16

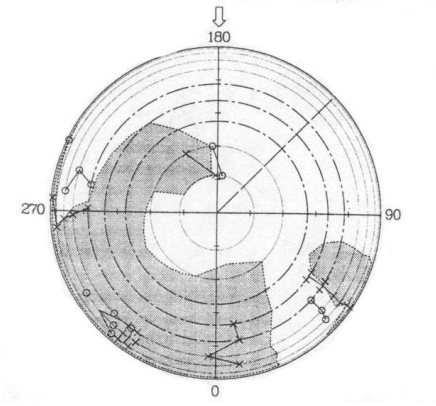

(e) Flight stall map rev 18

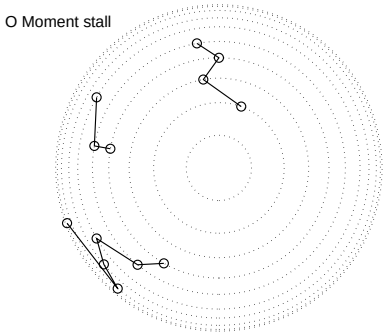

(f) Predicted stall map rev 18

Figure 4.21: **Measured and predicted rotor stall map; predictions using dynamic stall model; flight test data from Ref. [10]**

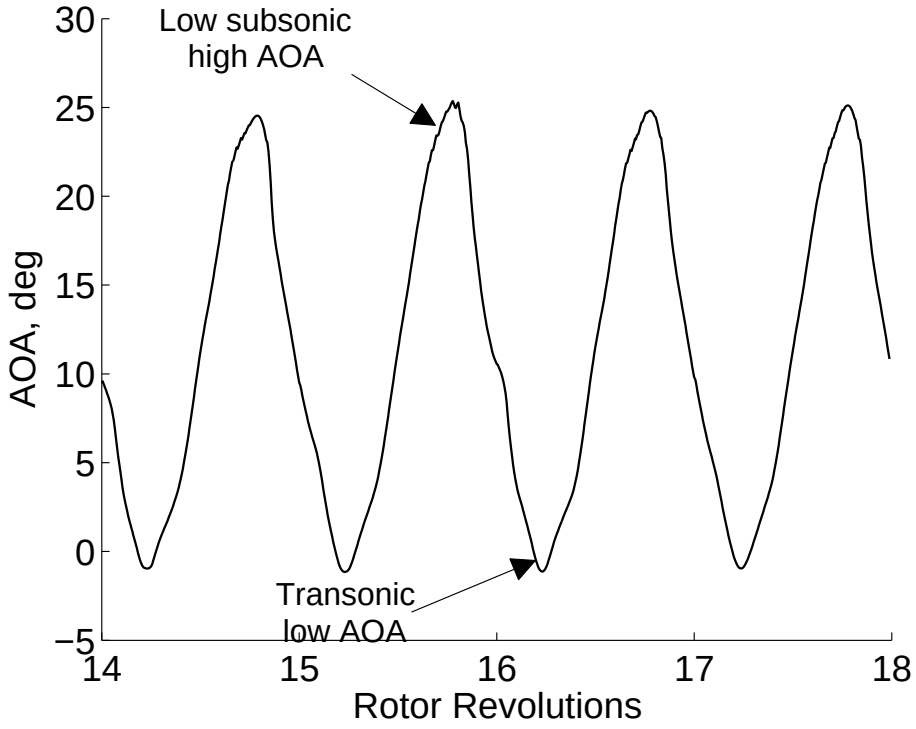

Figure 4.22: **Predicted angle of attack at $77.5\%R$; predictions using dynamic stall model**

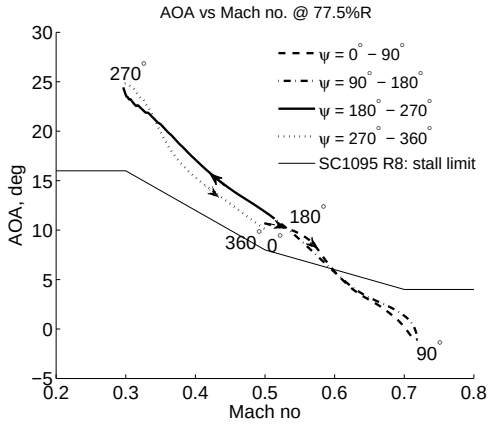

(a) Angle of attack at 77.5%R

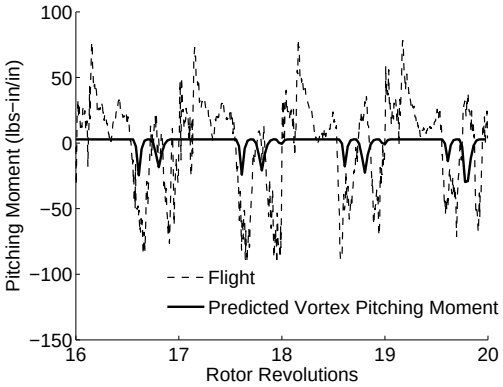

(b) Vortex induced 1/4-chord pitching moment

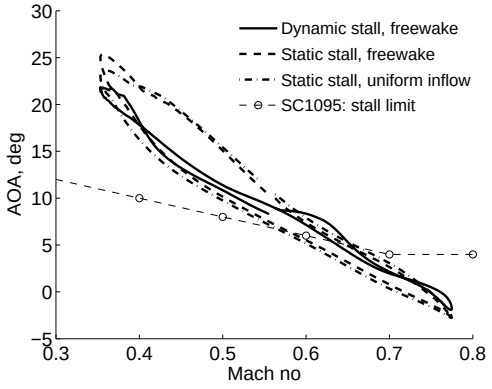

(c) Angle of attack at 86.5%R

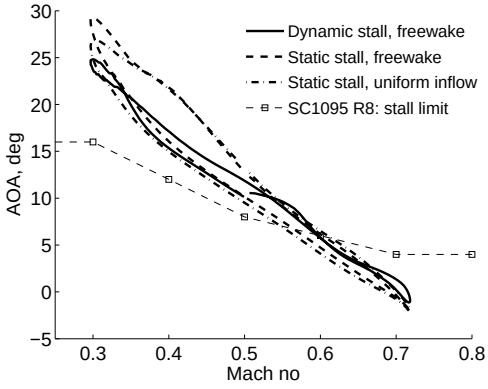

(d) Angle of attack at 77.5%R

Figure 4.23: **Leading edge vortex contribution to** 1/4**-chord pitching moment at** $77.5\%R$ **and predicted airfoil operating envelopes during revolution** 17

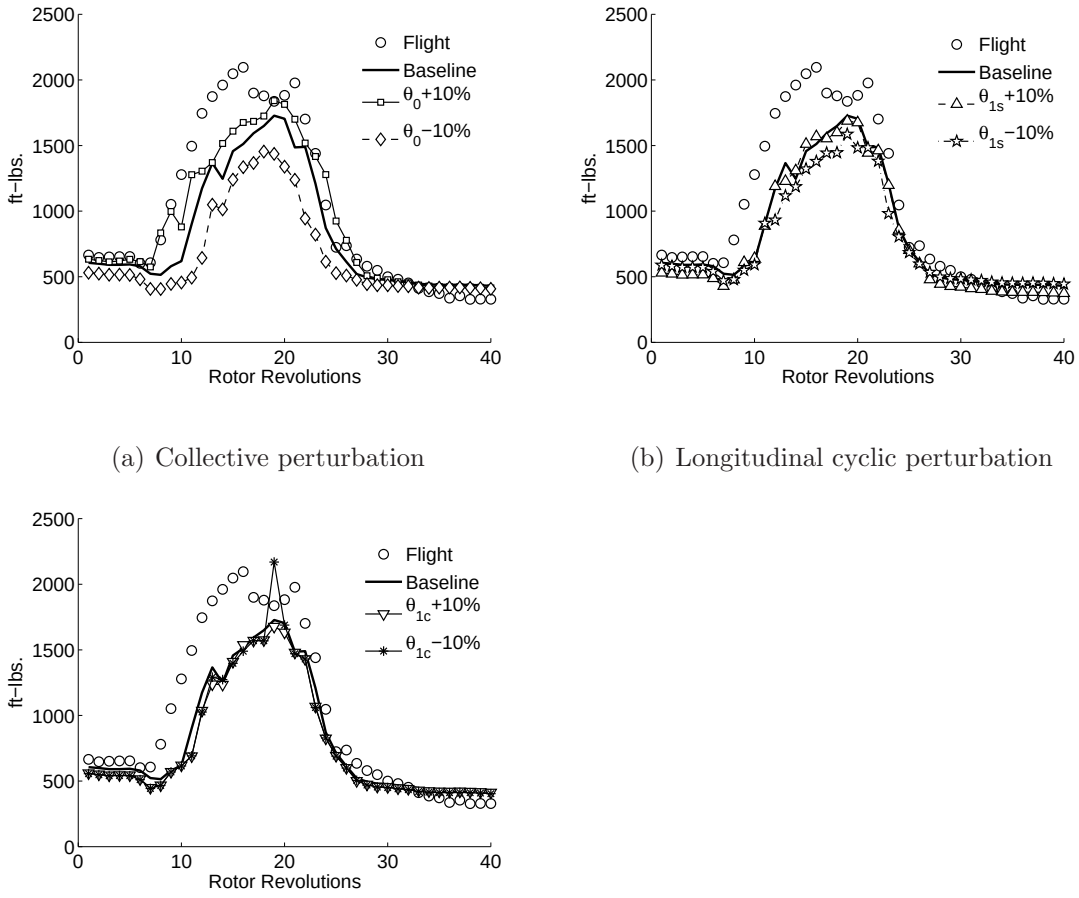

(a) Collective perturbation

(b) Longitudinal cyclic perturbation

(c) Lateral cyclic perturbation

Figure 4.24: **Effect of initial trim angle on the predicted torsion moment at 30%R; predictions using dynamic stall model**

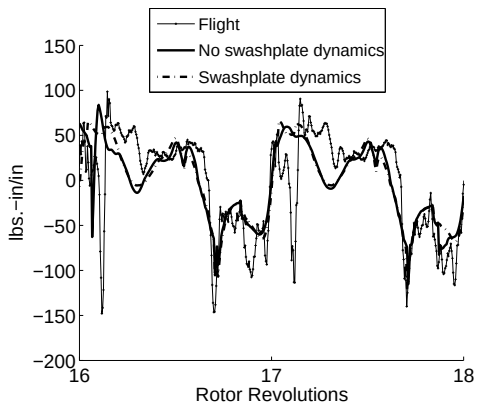

(a) Pitching moment at 77.5%R

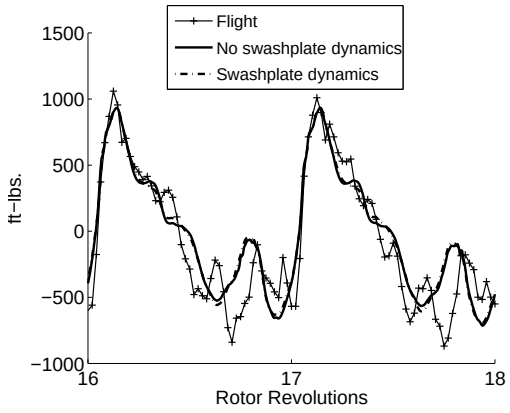

(b) Torsion moment at 30%R

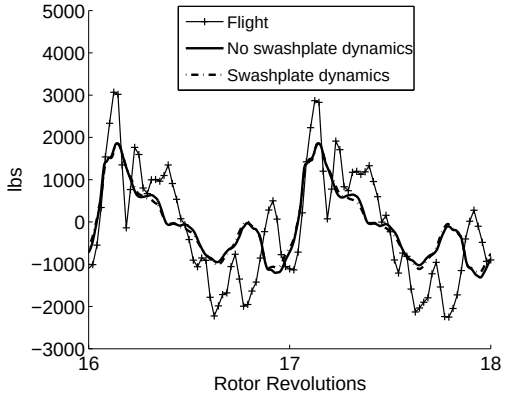

(c) Pitch-link load

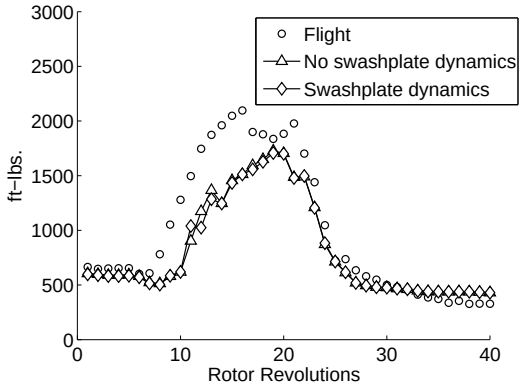

(d) Peak-to-peak torsion moment at 30%R

Figure 4.25: **Effect of swashplate dynamics on blade loads; predictions using dynamic stall model; swashplate mass** 75 **kg**

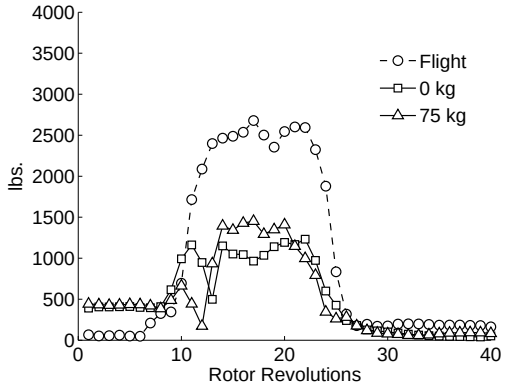

(a) Forward link 4/rev

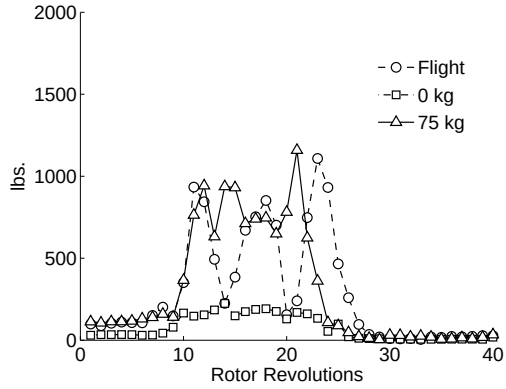

(b) Forward link 8/rev

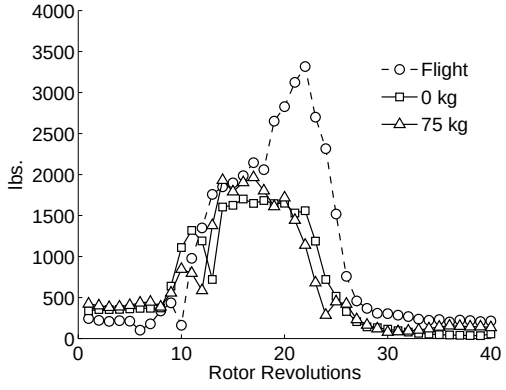

(c) Lateral link 4/rev

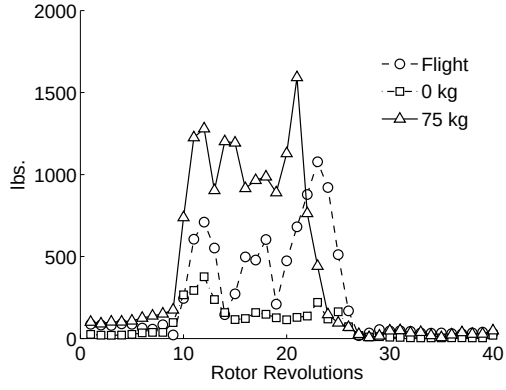

(d) Lateral link 8/rev

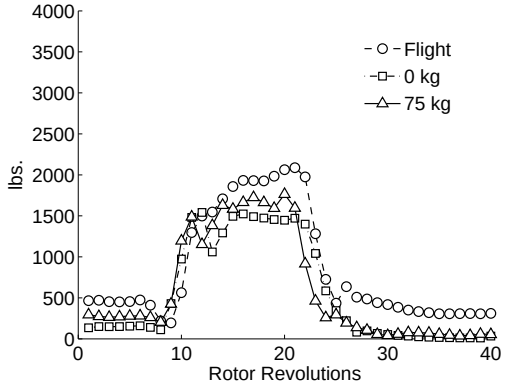

(e) Aft link 4/rev

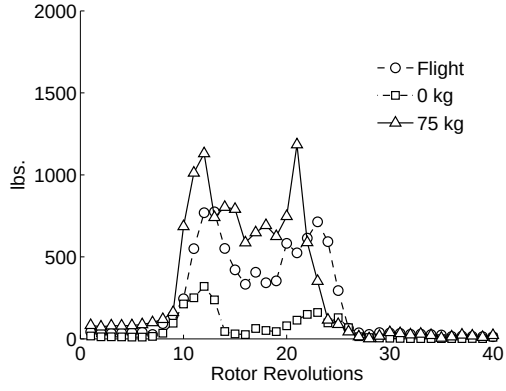

(f) Aft link 8/rev

Figure 4.26: **Measured and predicted 4/rev and 8/rev servo loads; predictions using dynamic stall model**

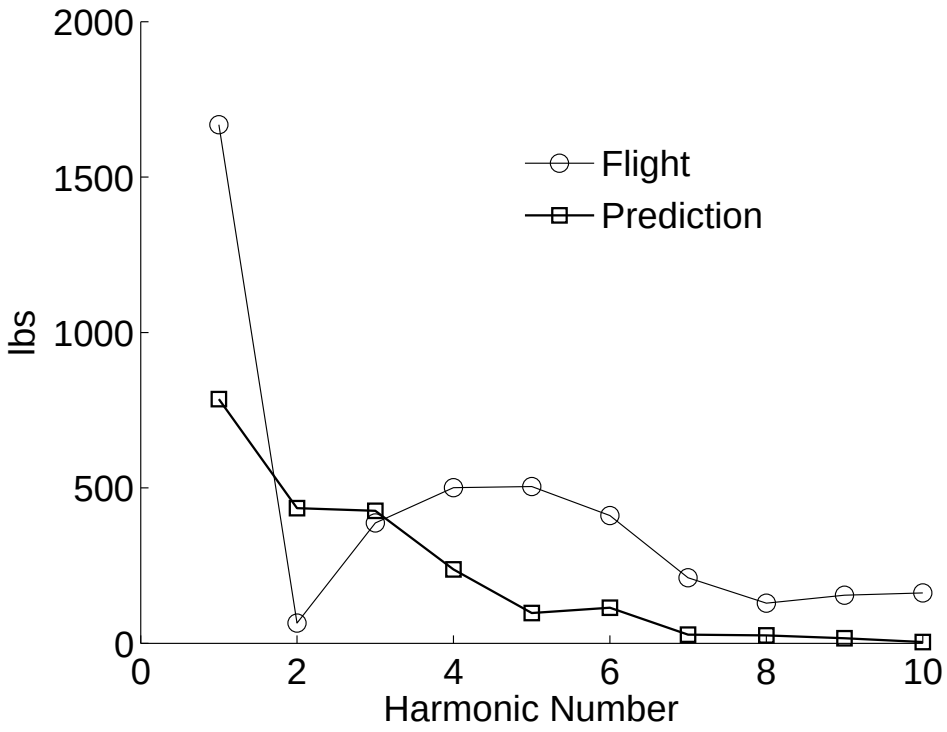

Figure 4.27: **Measured and predicted pitch-link load harmonics for revolution 15**

Chapter 5

CSD/Reynolds Averaged Navier Stokes Coupled Analysis

5.1 Introduction

This chapter describes the coupling of the structural model with the OVERTURNS Reynolds Averaged Navier Stokes (RANS) CFD analysis for prediction of the rotor loads. Chapter 3 discussed airloads predicted by the RANS model using calculated deformations, obtained from measured airloads, for the maneuver. It was observed that, with accurate set of deformations, CFD was capable of resolving the key aerodynamic mechanisms observed during the pull-up maneuver. It was also concluded that the two of the three stall cycles (second retreating stall and advancing blade stall) were elastic twist dominated phenomenon and require accurate pitching moment prediction. Chapter 4 established that for the UTTAS pull-up maneuver, lifting-line model was incapable of accurately predicting the pitching moment stalls, responsible for the high blade loads and control loads. Therefore, it was not able to excite the blade elastic twist reaction necessary to trigger the advancing blade stall. The goal of the CFD/CSD coupling is to improve the pitching-moment prediction using high-fidelity model and compare it consistently with the results obtained using the low fidelity lifting-line analysis. In addition two different coupling methods

(Conventional Serial Staggered and Time Accurate) for coupling structural model with the CFD analysis is discussed.

5.2 Fixed Wing vs. Rotary Wing Solution Procedures

Before getting in to the details of CFD/CSD coupling, it is important to identify the differences between the approaches used for Rotary wing analysis when compared with their Fixed Wing counterparts. The key difference arises due to the loading environment that the rotary wing vehicles are subjected to, which differs markedly from that of fixed-wing aircraft.

CFD/CSD coupled solution for rotorcraft is carried out using domain partitioning approach, this simplifies the solution process by using domain-specific solvers that solve the fluid and structural governing equations separately using the most efficient solution strategy for the specific domain. The partitioned domains interact at the fluid-structure interface to provide the fully-coupled aeroelastic response of the rotor. But, the first principles solution of rotorcraft aeroelastic problems require more than just CFD and CSD. A continuous prediction of aircraft operating state and control angles is also required. This is referred to as Vehicle Flight Dynamics (VFD). This requirement is imposed because unlike fixed wing the dynamic loads, flutter (flap-lag) and air resonance characteristics are non-linearly coupled to the vehicle dynamics via the control angles applied at the blade root. The optimal control problem of determining the control angles needed to execute a helicopter maneuver, whether for a prescribed trajectory or for a prescribed mean loading schedule,

is beyond the state-of-the-art, even with lower order free wake based lifting-line aerodynamic models.

5.2.1 Level Flight with Trim

The rotary wing aeroelasticity is inherently non-linear due to a combination of centrifugal and Coriolis forces arising from the blade rotation, due to which even the steady flight analysis involves complicated dynamic loadings. The fixed-wing analysis for steady flight on the other hand is less complicated as the loads are essentially static in nature. Even for a complicated flutter critical transonic regime, for a fixed wing fighter aircraft, where unsteady shock motions of three different types determine the nature of energy exchange between the fluid and the structure, a linear structural model combined with high-fidelity RANS CFD approach is shown to be adequate for the analysis [193]. This is unlike the helicopter blades, for which the flap-lag flutter is determined by aeroelastic non-linearities coupled to vehicle operating state, making the analysis more involved.

For steady flight conditions the vehicle flight dynamics requirement simplifies to the solution of a six degrees-of-freedom (DOF) equilibrium state for level flight and eight DOF equilibirum for most general steady maneuvers (for example, a coordinated helical turn). Calculation of vehicle flight dynamics (also referred as 'coupled trim') is the first step for any aeroelastic analysis, both in level flight and in maneuvers. The trim for CFD/CSD coupled analysis can be obtained using a *loose coupling* methodology following the innovative *delta* method proposed by Tung

et al. [122] in 1986, which has remained the most efficient approach and has paved way for current advances in rotorcraft CFD/CSD. This method is also termed as 'loose coupling', and it should not be confused with the CFD/CSD loose coupling in fixed wings. Unlike the loose coupling in fixed wing, strict time accuracy can be enforced for the *delta* method.

5.2.2 Transient Flight with Prescribed Controls

The 'loose coupling' is very efficient way for analyzing steady flight, but it cannot be used for transient analysis and use of 'tight coupling' is a must. A partitioned aeroelastic coupling method is comprised of two components, (1) spatial (fluid-structure interface), and (2) temporal (time accuracy). The fluid-structure interface which comprises of transfer of fluid pressure and stresses to blade airloads and then interpolation of blade deformations to grid motions. The spatial component remains the same for all coupling methodologies, be it loose coupling or tight coupling. The difference lies in the solution procedure of the temporal equations. Apart from the classical loose coupling procedure, the fluid-structure coupling can be carried out in the following two ways: (1) conventional serial staggered (CSS), in which the CFD airloads and the blade loads are exchanged once every time step, and (2) time-accurate (TA), in which data exchange takes place at every sub-iteration level ensuring strong coupling. The CSS approach is the conventional procedure of solving the fluid structure equation in time marching manner with the data exchange happening at each time step and is identical to the approach used for coupling the

structural model with the lifting-line analysis as described in chapter 4. It is similar to the 'loose coupling' in fixed wing sense as the strict time accuracy is not enforced. All the baseline CFD/CSD results shown in this chapter have been obtained using CSS method with a time step of 0.25° azimuth.

For the analysis of unsteady maneuver, the analysis procedure can be simplified, if the rotor control angles and vehicle dynamics are known, either from flight test or from an isolated lower order inverse flight simulation. Then, the CFD/CSD analysis can be carried out in an uncoupled fashion from the vehicle flight dynamics making it a straight-forward, partitioned, and resulting numerical-integration procedure can be similar to those encountered in fixed wing analysis.

However, prescribed controls maneuver analysis must start from a level flight trim condition. For the present study, 'loose coupled' trim analysis was carried out using traditional steady UMARC coupled with the CFD solver to obtain blade control pitch settings for the steady flight condition, see Ref. [194] for more details. The steady, periodic flight condition is used as the initial solution from which the maneuver is initiated. This makes the analysis of maneuver conceptually simpler as the time history of control angles and vehicle dynamics, either obtained from flight test or lower order predictions, can be applied as delta corrections to the trim angles obtained using the 'loose coupling', thereby uncoupling the vehicle flight dynamics from the CFD/CSD simulation.

5.2.2.1 Time Accurate Solution Procedure

Time accurate coupling or strong coupling is achieved by using the Modified Newton Raphson (MNR) method coupled to the Newmark Algorithm, and is a tight coupling procedure as per the fixed-wing definition. The governing differential equation can be rewritten in the following form

$$M\ddot{\mathbf{x}}^{(i)}_{t+\Delta t} + C\dot{\mathbf{x}}^{(i)}_{t+\Delta t} + K\Delta\mathbf{x}_t = F_t^{i+1} - Q_r^{(i)} \tag{5.1}$$

where, notations have their usual meaning and F_t is the external loads vector and Q_r is the internal force vector which is given by

$$Q_r^{(i)} = K\mathbf{x}_t + F_{NL}^{(i)} \tag{5.2}$$

where F_{NL} is the sum of non-linear structural forces. As discussed in chapter 2, the integration formula that depends on two parameters β and γ is given by

$$\mathbf{x}_{t+\Delta t} = \mathbf{x}_t + \Delta t\dot{\mathbf{x}}_t + \frac{\Delta t^2}{2}[(1-2\beta)\ddot{\mathbf{x}}_t + 2\beta\ddot{\mathbf{x}}_{t+\Delta t}] \tag{5.3}$$

$$\dot{\mathbf{x}}_{t+\Delta t} = \dot{\mathbf{x}}_t + \Delta t[(1-\gamma)\ddot{\mathbf{x}}_t + \gamma\ddot{\mathbf{x}}_{t+\Delta t}] \tag{5.4}$$

These equations can be rewritten in the following form

$$\left.\begin{aligned} \ddot{\mathbf{x}}_{t+\Delta t} &= \tfrac{1}{\beta\Delta t^2}[\mathbf{x}_{t+\Delta t} - \mathbf{x}_t] - \tfrac{1}{\beta\Delta t}\dot{\mathbf{x}}_t + \left(1 - \tfrac{1}{2\beta}\right)\ddot{\mathbf{x}}_t \\ \dot{\mathbf{x}}_{t+\Delta t} &= \tfrac{\gamma}{\beta\Delta t}[\mathbf{x}_{t+\Delta t} - \mathbf{x}_t] + \left(1 - \tfrac{\gamma}{\beta}\right)\dot{\mathbf{x}}_t + \left(1 - \tfrac{\gamma}{2\beta}\right)\ddot{\mathbf{x}}_t \end{aligned}\right\} \tag{5.5}$$

Substituting Eq. 5.5 in Eq. 5.1 gives the following

$$\hat{K}_t\Delta\mathbf{x}^{(i+1)} = \Delta\hat{F}^{(i+1)}_{t+\Delta t} \tag{5.6}$$

where

$$\left.\begin{aligned} \hat{K}_t &= \tfrac{1}{\beta\Delta t^2}M + \tfrac{\gamma}{\beta\Delta t}C_t + K_t \\ \Delta\hat{F}^{(i+1)}_{t+\Delta t} &= F^{(i)}_{t+\Delta t} + M\left\{\tfrac{1}{\beta\Delta t}\dot{\mathbf{x}}_t + \left(\tfrac{1}{2\beta}-1\right)\ddot{\mathbf{x}}_t\right\} - Q^{(i)}_r \\ &+ C_t\left\{\tfrac{1}{\beta\Delta t}[\mathbf{x}_t - \mathbf{x}^{(i)}_{t+\Delta t}] + \left(\tfrac{\gamma}{\beta}-1\right)\dot{\mathbf{x}}_t + \left(\tfrac{\gamma}{2\beta}-1\right)\ddot{\mathbf{x}}_t\right\} \end{aligned}\right\} \tag{5.7}$$

The above Modified Newton Raphson method coupled to Newmark Formulation is in predictor-corrector form (Ref. [195]). The procedure can be started by predicting the structural motions at t_{n+1} or at time $t+\Delta t$. The initial guess for this prediction is the motion at t_n which is used to start the sub-iteration.

At time, t=0 prediction for $i=1$ is given by $\begin{cases} \mathbf{x}^{(1)}_{t+\Delta t} = \mathbf{x}_t \\ \Delta\mathbf{x}^1 = 0 \\ F^{(1)}_{t+\Delta t} = F_t \end{cases}$

The prediction for (i+1)-th sub-iteration is evaluated using information from i-th sub-iteration step by using Eq. 5.6. After that the structural motions are transferred to the CFD grid and a single sub-iteration is executed for the CFD. The loads predicted by CFD are then applied on the CSD and a single sub-iteration step is executed for the CSD using the latest airloads guess at t_{n+1}. Now the guess for solution at t_{n+1} is corrected using

$$\mathbf{x}^{(i+1)}_{t+\Delta t} = \mathbf{x}^{(i)}_{t+\Delta t} + \Delta\mathbf{x}^{(i+1)} \tag{5.8}$$

The predictor-corrector sequence is repeated several times till convergence is attained. Typically 7–8 sub-iteration steps are needed for convergence.

For both CSS as well as TA approaches, the maneuver is initiated from the level flight condition by smoothly merging the control angles as per the incremental procedure similar to that used for lifting-line analysis discussed in chapter 4.

5.3 Results and Discussion

The UTTAS pull-up maneuver is initiated from a steady, level flight condition with an advance ratio $\mu = 0.357$, and a blade loading coefficient $C_T/\sigma = 0.0793$. The steady state solution is obtained from a coupled UMARC/OVERTURNS simulation using a delta coupling methodology. The solution is then marched in time and the instantaneous values of the blade control pitch settings, the transient velocities, the vehicle attitude and attitude rates are prescribed as inputs to the CSD and the CFD solvers. Note that rather than specifying the actual control pitch settings obtained from the flight test data, shown in Tab. 5.1, the time histories are corrected using a constant offset such that the values correspond to the trim solution predicted by the UMARC/OVERTURNS analysis at time $t = 0$. The OVERTURNS solver was coupled with the UMARC2 structural solver, to analyze the transient maneuver. Both lifting line analysis and OVERTURNS were coupled with UMARC2 to analyze the differences in the aerodynamic models. In this chapter, the full lifting line model including the time-accurate free-vortex wake model and the dynamic stall model described in chapters 3 and 4 is used to compare the lower-order model with the high-fidelity CFD solver.

5.3.1 Blade Root Deflection

Figure 5.1 shows the time history and peak-to-peak magnitude of the predicted blade flap angle. Investigation of the time history reveals that for the initial part of the maneuver (revolution number 0-6) the blade flap angle is predominantly 1/rev,

with significant 2/rev only in the later part of the maneuver – see Fig. 5.1(b). The predictions show good correlation with the magnitude as well as the waveform of the measured root flap angle during the steady flight regime of the maneuver. The waveform of predicted flap angle shows trend similar to the flight test data during the entire course of the maneuver. However, after revolution number 7 (Fig. 5.1(c)), the magnitude of the flap angle is over-predicted, with a maximum over-prediction by a factor of 2 observed during rev 14, which also corresponds to a high load factor of $2.08g$. This trend of predicted root flap angle has been observed for the analyses carried out using lifting-line aerodynamics as well as measured airloads.

5.3.2 Blade Airloads

The study of C11029 maneuver can be divided into three different phases. The initial 5 revolutions are steady, with the pitch and roll angles remaining nearly constant, and would be referred as the steady flight regime. The unsteady phase starts around revolution 6, with helicopter attaining high pitch rate and linear acceleration with tip-path-plane tilting backwards. The vehicle load factor crosses $2.0g$ towards the beginning of revolution 13, and remains above $2.0g$ till revolution 18 and would be called the maneuvering flight regime. After which the vehicle tries to attain back its original steady level flight attitude which constitutes the third and final phase.

5.3.2.1 Steady Flight Regime

This section compares the airloads predicted during the steady phase of the maneuver. The airloads at all the eight flight test radial-stations are compared. Figures 5.2, and 5.3 show the time histories of the normal force and pitching moment predicted by two different simulations: (1) coupled UMARC2 with lifting-line analysis (shown in red), and (2) coupled UMARC2/OVERTURNS analysis (shown in blue). The analysis with lifting line aerodynamics was performed at a time-step of 2.0°, while the CFD/CSD analysis was performed at a time-step of 0.25°. The lifting line analysis is unable to resolve the phasing of the negative lift peak adequately. This is primarily due to the inaccurate elastic twist, which in turn is due to the inaccurate pitching moment prediction by the lifting-line analysis. It can be observed that the lifting-line analysis is unable to accurately predict the large positive to negative moment oscillation on the advancing side near the tip. This behavior is a result of the effect of 3D relief on unsteady formation and collapse of shocks on the advancing blade [165], a 3D phenomenon, which is not properly accounted for in the lifting-line model. The inadequacy of the lifting-line model in this region is well documented in literature [129]. CFD/CSD coupled analysis on the other hand is able to accurately predict the 3D unsteady transonic pitching moment.

5.3.2.2 Maneuvering Flight Regime

Figures 5.4 and 5.5 show the time history of normal force at 86.5% radial station, predicted using the CFD/CSD coupled analysis. The high-fidelity analysis

is able to predict the higher harmonic stall loads, which are primarily 4, and 5/rev during the maneuvering flight regime, which are missed by the lifting-line model.

The prediction of pitching moment is shown at two stations 77.5%R and 86.5%R. Figures 5.6 and 5.7 compare the predictions using CFD/CSD with those obtained using lifting-line analysis at 77.5%R spanwise station. The prediction using lifting-line analysis shows 'relatively' improved correlation with the flight test data at this station than compared to the lifting-line prediction at 86.5%R which are shown in . While, the lifting-line analysis is able to capture the trends of the waveform correctly, the stall magnitude is under-predicted all through the maneuver. At the 86.5%R station shown in Figs. 5.8 and 5.9 CFD/CSD results are consistently able to predict the two retreating stall cycles. The pull-up maneuver is characterized by three stall cycles occurring across the rotor disk, with first stall cycle occurring on the advancing side, followed by two dynamic stall events on the retreating side, as shown by the dark blue regions in the flight test contour plot for the non-dimensional pitching moment for the revolution 14 (Fig. 5.10(c)). While the CFD/CSD analysis is showing fair correlation for the peak magnitude of the stall loads, the lifting-line model is under-predicting it significantly at most times. The airloads time histories, particularly the pitching moments, clearly indicate the dynamic stall phenomenon as the dominant aerodynamic characteristic of the UT-TAS maneuver. To gain further insight into the severity and the extent of this stall across the rotor disk the variations of the pitching moments across the rotor disk at the peak of the maneuver, Fig. 5.10(c), is compared with the conditions observed in the steady flight conditions, Fig. 5.10(a). The pitching moment variations during

steady flight conditions are benign and show no steep gradients across the rotor disk. During this phase, the CFD/CSD analysis shows good correlation with the flight test data. In contrast, the pitching moment contours for rev. 14 of the flight test data show steep gradients in the first and fourth quadrants indicating moment stall near the blade tips. While the flight test data appears to indicate that the stall is restricted to the outermost regions of the retreating side, the CFD/CSD analyses predict a much more widespread region of moment variations. This could be because of the low spanwise resolution of the flight test data (only nine radial stations across span). The third stall event seen as a pronounced down-up gradient in the first quadrant is missed by both the computational analyses.

The predicted chord force at 86.5% radial station is shown in Fig. 5.11. In general, the prediction shows good correlation with the flight test data, but the peak-to-peak magnitude is over-predicted, this could stem from the fact that the lag-dynamics of UH-60A rotor is significantly influenced by the non-linear lag damper, which is not included in the present structural model.

5.3.2.3 Attitude Recovery Phase — The Lift Deficiency Problem

It is important to note that a deficiency in the predicted mean normal forces during the attitude recovery phase of the maneuver, has been reported by several researchers [160,163]. A similar discrepancy is also observed in the linearized aerodynamic analysis conducted using the coupled UMARC2/lifting-line analysis discussed in chapter 4, but not in the coupled CFD/CSD analysis (Fig. 5.12). The reason for

this may be attributed to the fact that the lifting-line analysis always under-predicts the pitching moment stall magnitude by a significant margin, thereby introducing errors in the steady elastic twist response which accumulates over the period of time to cause a net deficiency in the angle of attack resulting in reduced mean lift towards the end of the maneuver.

5.3.2.4 Conventional Serial Staggered vs. Time Accurate Coupling

It is observed that the Conventional Serial Staggered (CSS) CFD/CSD analysis is able to predict only the two stall events observed on the retreating side of the blade, and is unable to resolve the advancing blade stall. Therefore, the effect of time accurate coupling over the airloads prediction is studied. As noted earlier, time accurate coupling also referred to as CSD/CSD strong coupling is carried out by exchanging the airloads and deformations between the structure and fluid solvers at every sub-iteration level.

Figures. 5.13 and 5.14 compare the predicted normal force and pitching moment at $86.5\%R$ radial station respectively for the two methods. The results obtained using time accurate coupling shows better correlation for the normal force negative lift peak, and is able to resolve some of the higher frequencies in greater detail. However, the pitching moment predictions using time accurate coupling reveals no new physical phenomenon, as the predictions continue to miss the advancing blade stall. The reason for which is explained in the next sub-section.

5.3.2.5 Advancing Blade Stall

The objective is to understand the inability to predict advancing blade stall. From the study of measured airloads problem, followed by isolated calculation of airloads using prescribed deformations in chapter 3, it was concluded that with accurate airloads, the structural dynamic model is capable of predicting accurate deformations, which in turn predicts all three stalls. The advancing blade stall is first observed in flight test from revolution 12. Therefore, deformations and airloads from coupled CFD/CSD analysis for revolutions 12 and 13 are studied carefully to understand the reason for this inability of the analysis to capture advancing blade stall.

Figure 5.15(a) shows the predicted pitching moment for revolution 12 using CFD/CSD coupled analysis as well as CFD with prescribed deformation. The blade deformations corresponding to coupled CFD/CSD analysis shows similar 5/rev harmonics as shown in Fig. 5.15(b). Therefore, the reason for first stall being missed can be either an under-prediction of 5/rev elastic twist or the lower angle of attack set by blade control settings as noted for prediction using lifting-line analysis discussed earlier in this text. The later seems to be the case.

At the beginning of revolution 13, CFD pitching moment prediction using prescribed deformations shows sign of advancing blade stall, but is significantly under-predicted (Fig. 5.16(a)). Similar to rev 12, it may be related to inaccuracies in the applied control angles. Note that the third stall prediction is unsatisfactory, and due to this, 5/rev elastic twist for the coupled CFD/CSD analysis is severely under-

predicted (Fig. 5.16(b)). This under-prediction signifies that coupled CFD/CSD analysis would not predict advancing blade stall in next rev and 5/rev elastic twist under-prediction would never be recovered. Therefore, prediction of advancing blade appears to be tied to accurate prediction of two retreating stalls. The second stall being determined by control angle is relatively easier to predict, but third stall is known to be sensitive to turbulence modeling and grid size and its accurate prediction would require further investigation.

5.3.3 Blade Structural Loads

Predictions of the structural bending moments during the steady phase are shown in Fig. 5.17. The flap bending moment is almost entirely determined by the predicted lift. While, the predictions using the CFD/CSD simulation, shows good agreement with the flight test, the results from the lifting-line model show poor correlation, with a peak-to-peak under-prediction of 26%. In the absence of non-linear lag damper model, both the predictions for the lag bending moments are less satisfactory, as it is dominated by the lag damper force. The predicted torsion moment using UMARC2/OVERTURNS analysis is showing good correlation with the flight test, the predictions using the lifting-line analysis also shows peak-to-peak correlation with an under-prediction of only 10%, however the waveform is less satisfactory on the retreating side.

As with the steady flight results, the predicted flap bending moment using the CFD/CSD analysis shows good correlation with the flight test (Figs. 5.18 and 5.19).

There is an over-prediction in the peak-to-peak magnitude of the lag bending moment after revolution 7 as shown in Figs. 5.20 and 5.21. Further, the waveform shows poor correlation with the flight test towards the later part of the maneuver. The torsion moment time history is shown in Figs. 5.22 and 5.23. The predicted waveform is similar to the flight test data, but there is an over-prediction of 40%–60% in the peak-to-peak magnitude during the maneuver regime. This discrepancy is a result of over-prediction of the 5 and 6/rev torsional moment (Fig. 5.24), which is driven by the over-prediction of dynamic stall peaks at the inboard blade locations. The predicted pitch-link load shows similar trend (Fig. 5.25). The peak-to-peak magnitude of the structural loads predicted using the CFD/CSD and the lifting-line analyses is summarized in the Fig. 5.26. In general CFD/CSD analysis is able to show better prediction for all the structural loads when compared with the lifting-line model. In particular, the peak-to-peak magnitude of the predicted pitch-link load is under-predicted by 50% during rev 14 using the lifting-line analysis, while the CFD/CSD analysis over-predicts it only by 15%. The over-prediction of peak pitch-link loads, during the revolutions 9–13 is due to premature stall onset in the CFD/CSD analysis.

5.4 Concluding Observations

The UH-60A UTTAS pull-up maneuver was re-analyzed using a Python-based CFD/CSD simulation framework. Similar to lifting-line analysis the rotor control angles and the flight dynamic parameters (flight path and velocities, attitude angles

and rates) were prescribed from flight test measurements. This study allowed the identification of the strengths and weaknesses of the traditional lifting-line analysis when compared to the high-fidelity CFD/CSD simulation. The trim solution for CFD/CSD analysis was obtained using a *loosely coupled* UMARC/OVERTURNS simulation. The key conclusions from this study are summarized here:

1. The pull-up maneuver is characterized by the three distinct stall events as the rotor experiences load factors greater than $1.75g$ during the maneuver. The two dynamic stall events on the retreating side are predicted by the CFD/CSD analysis. The lifting-line analysis is unable to predict the high-frequency stall loads during the maneuver, especially the peak magnitude of pitching moment is under-predicted significantly.

2. CFD/CSD coupled analysis is unable to predict first quadrant stall due to less accurate prediction of 5/rev elastic twist arising from the under-prediction of the two retreating blade stalls from previous revolution. The prediction of second retreating blade stall is extremely challenging and its accurate prediction is essential for the prediction of the advancing blade stall.

3. The blade root flap angle over-prediction by the CFD/CSD analysis, is unclear and the trend is common to other analyses noted in chapters 2 and 4. The source of this discrepancy may possibly be related to the inaccuracies associated with the measurement of very small angles during the flight test.

4. The predictions of the structural loads do not show the same level of correlation as the airloads when compared with flight test data. Even though the

flap bending moment prediction looks satisfactory, the inability to predict the structural loads accurately is a problem even with steady flight analysis and is not an issue specific to the analysis of maneuvering flight.

	Collective $\theta_{\mathbf{0}}$	**Longitudinal cyclic** $\theta_{\mathbf{1s}}$	**Lateral cyclic** $\theta_{\mathbf{1c}}$
Flight test	12.32	−9.78	4.68
UMARC standalone (targeted)	14.29	−8.76	3.06
UMARC/OVERTURNS	15.41	−9.13	4.29

Table 5.1: **Trim solutions predicted by different simulations for the initial steady phase of the UTTAS pull-up maneuver.**

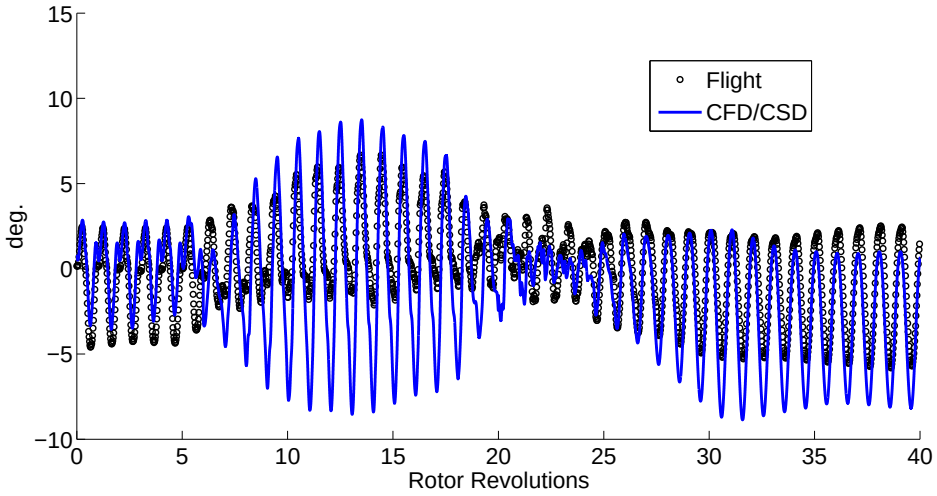

(a) Time history

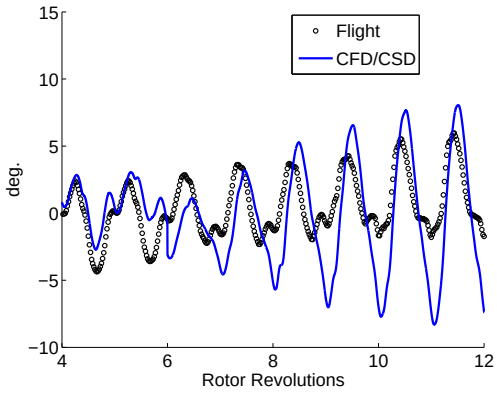

(b) Time history (zoomed)

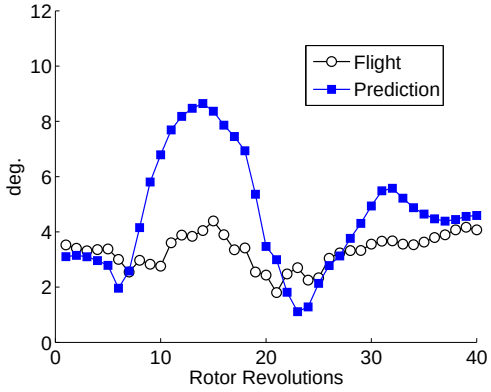

(c) Half peak-to-peak

Figure 5.1: **Root flap angle predicted by UMARC2 coupled with OVERTURNS**

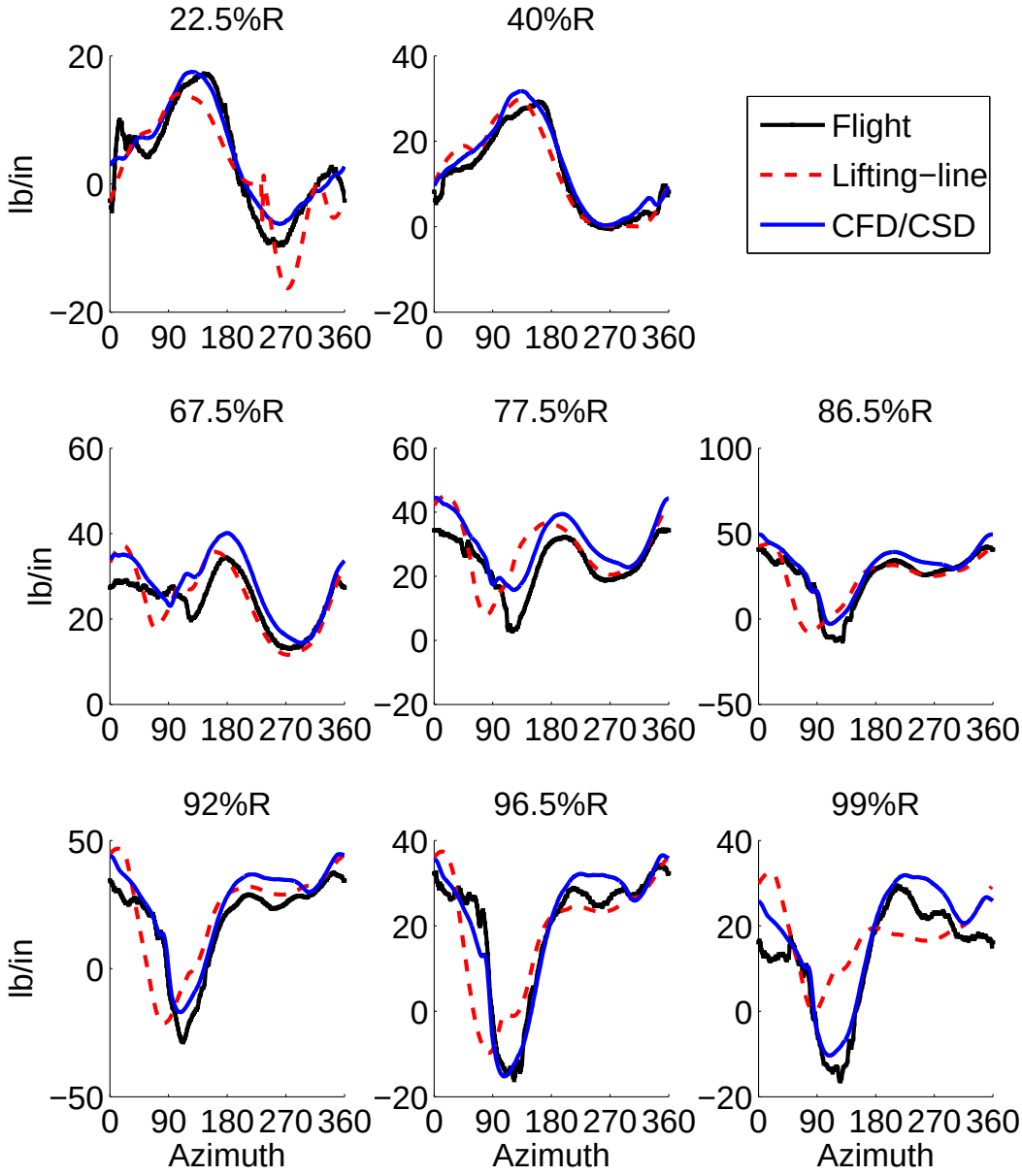

Figure 5.2: **Predictions of the normal force for steady flight regime (Rev 1) predicted by coupled lifting-line analysis and CFD/CSD**

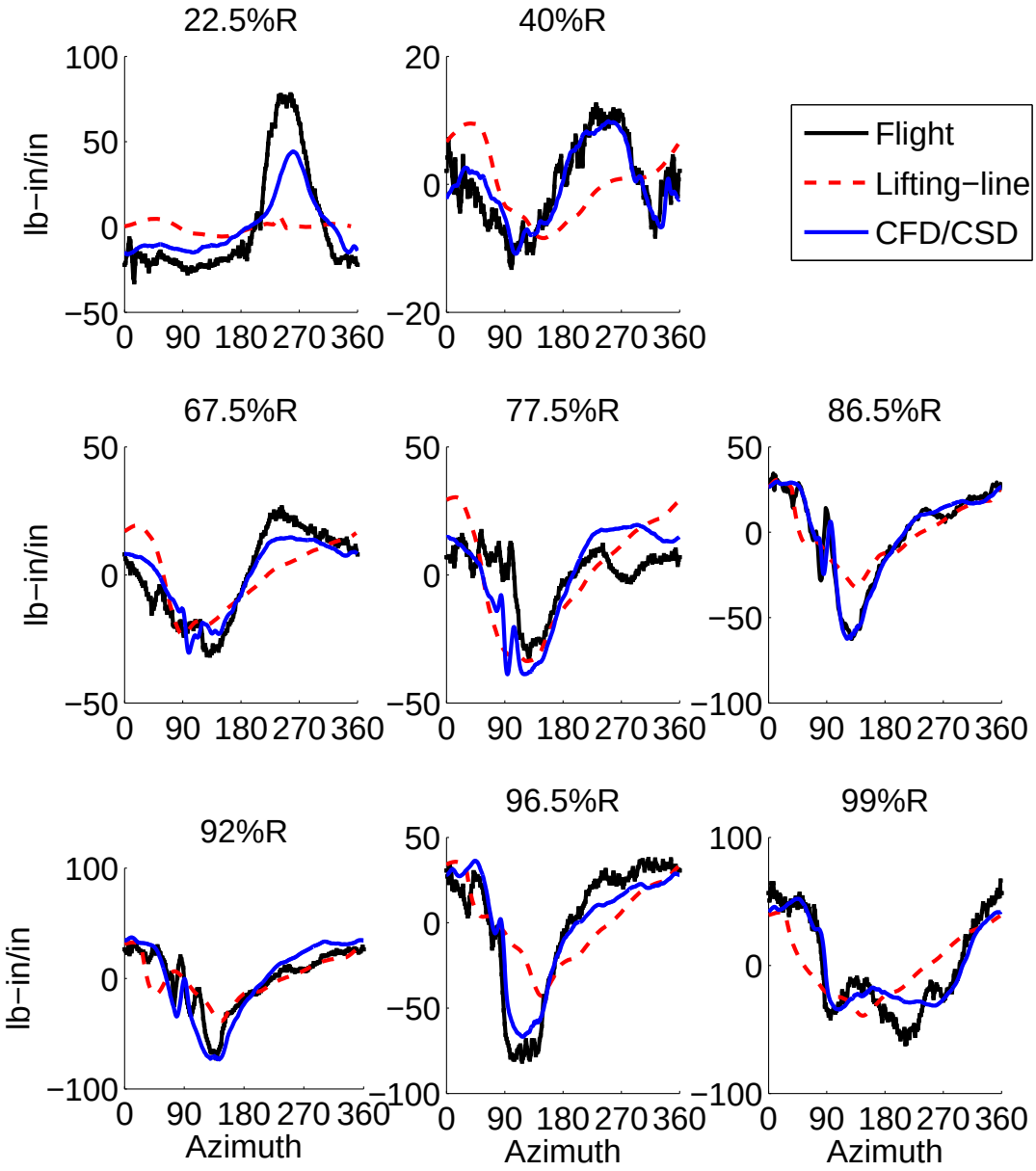

Figure 5.3: **Predictions of the pitching moment (mean removed) for steady flight regime (Rev 1) predicted using coupled lifting-line analysis and CFD/CSD**

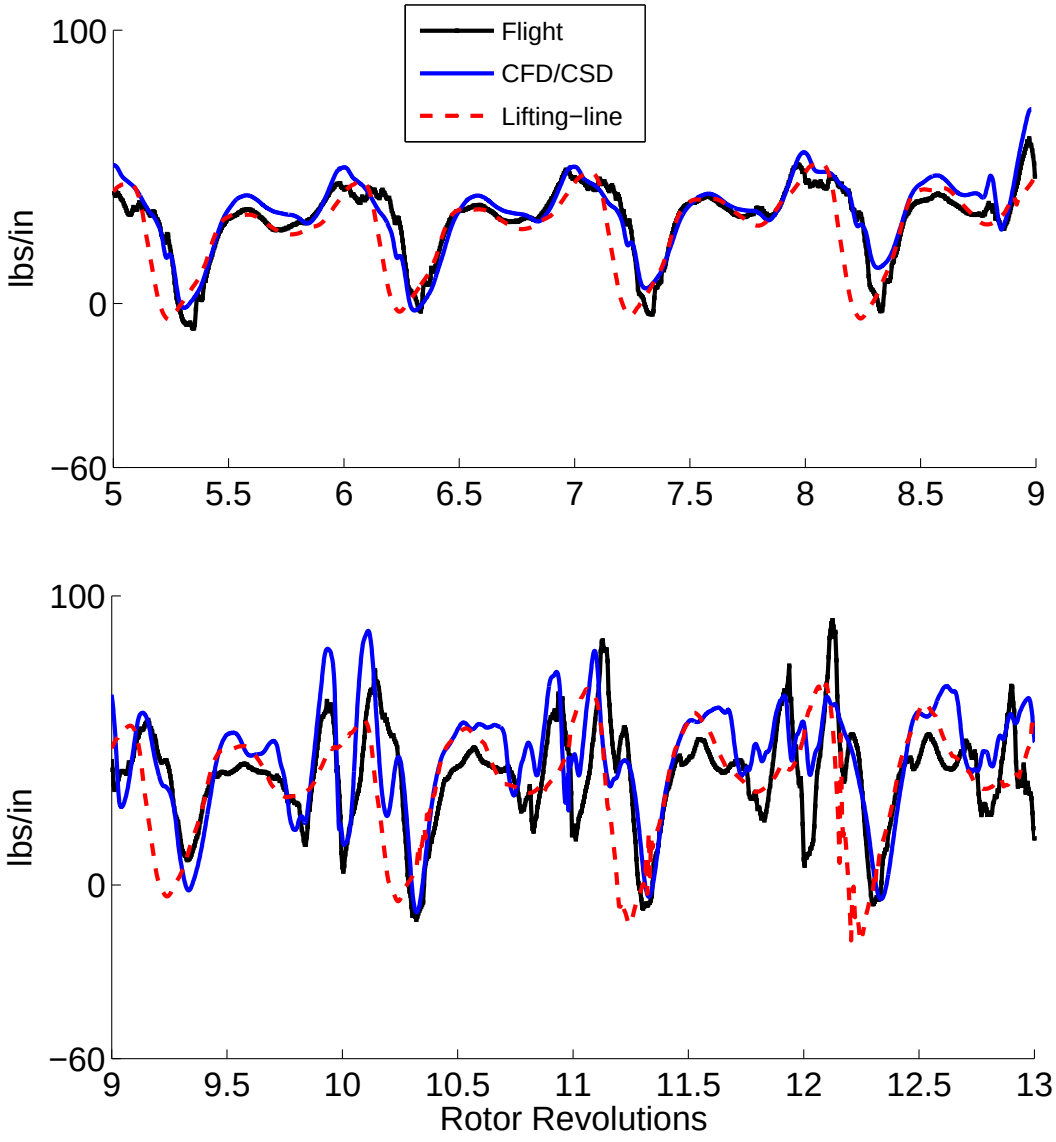

Figure 5.4: **Predicted normal force time history for the UTTAS pull up maneuver; predictions using coupled lifting-line and CFD/CSD at** $86.5\%R$

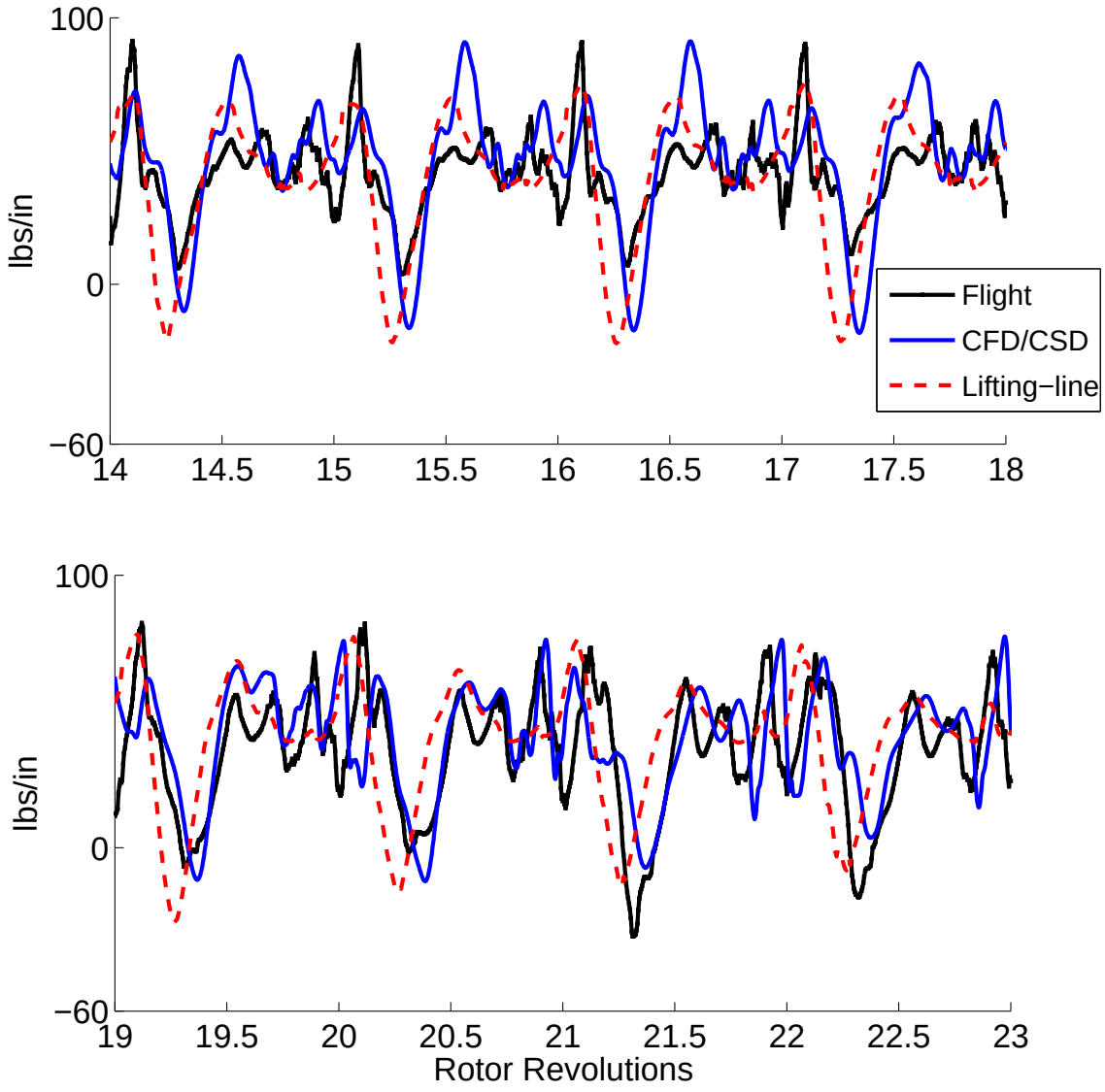

Figure 5.5: **Predicted normal force time history for the UTTAS pull up maneuver; predictions using coupled lifting-line and CFD/CSD at** $86.5\%R$

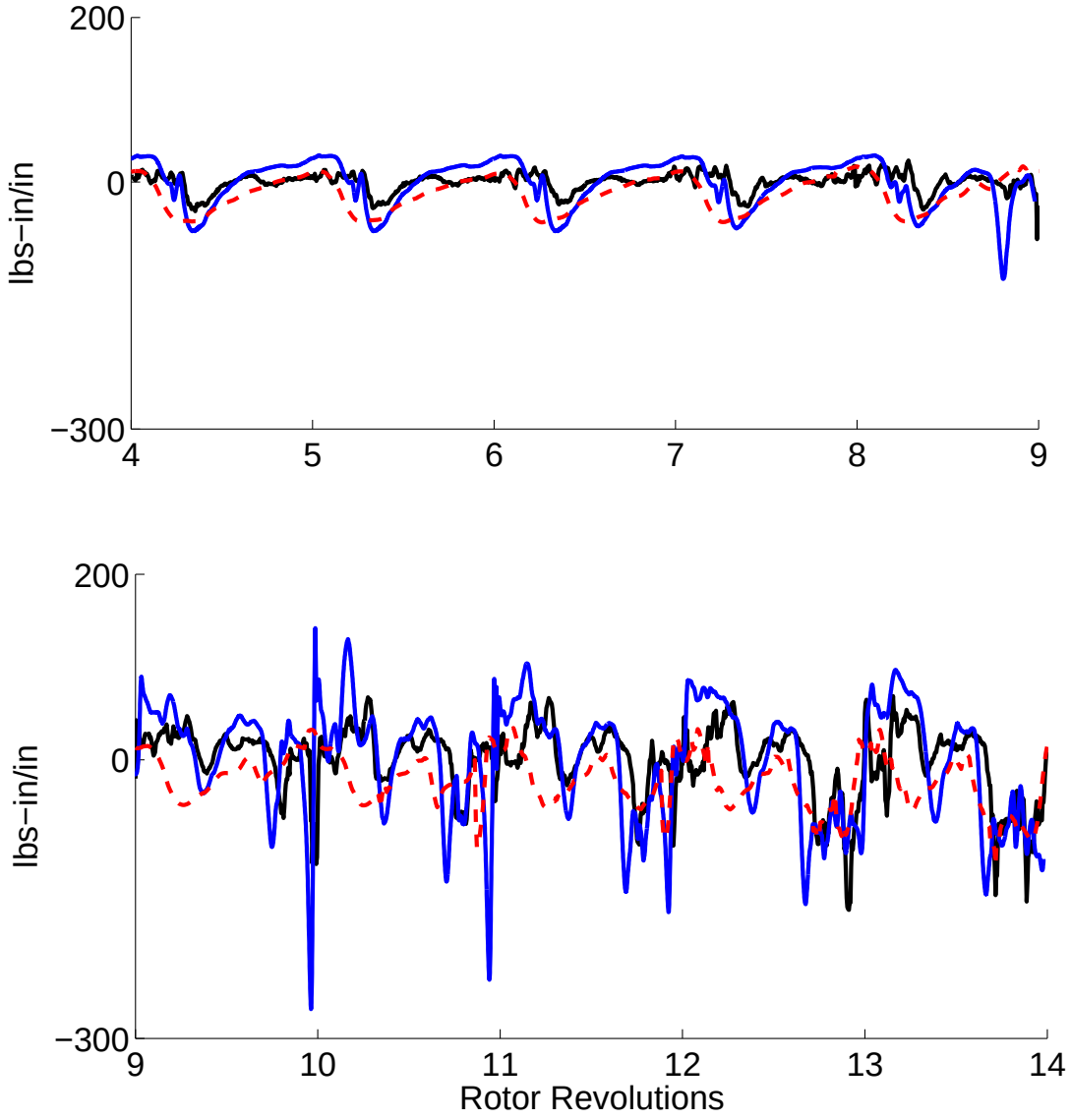

Figure 5.6: **Predicted pitching moment (mean removed) for the UTTAS pull up maneuver; predictions using coupled lifting-line analysis and CFD/CSD at** $77.5\%R$

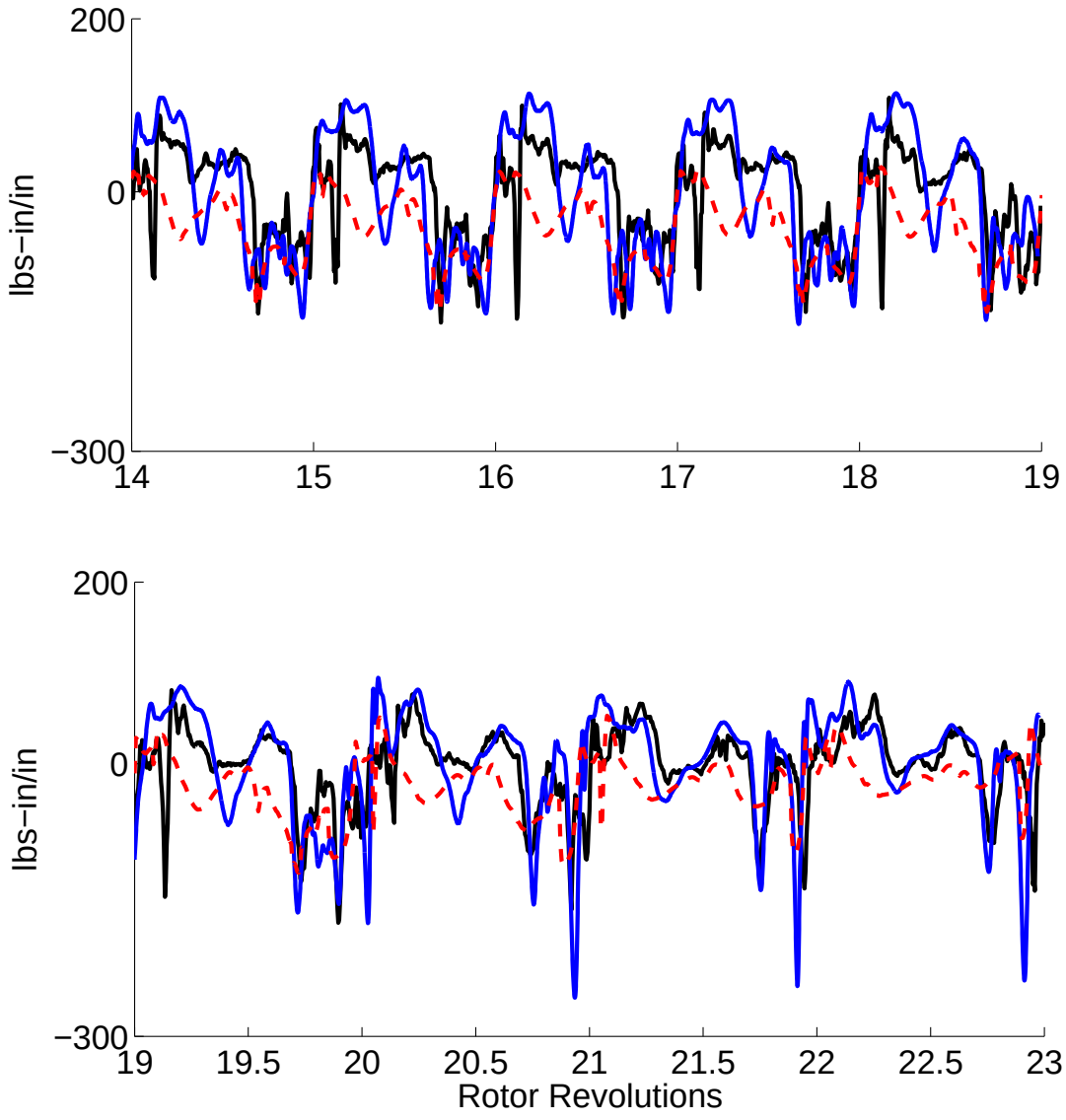

Figure 5.7: **Predicted pitching moment (mean removed) for the UTTAS pull up maneuver; predictions using coupled lifting-line analysis and CFD/CSD at** $77.5\%R$

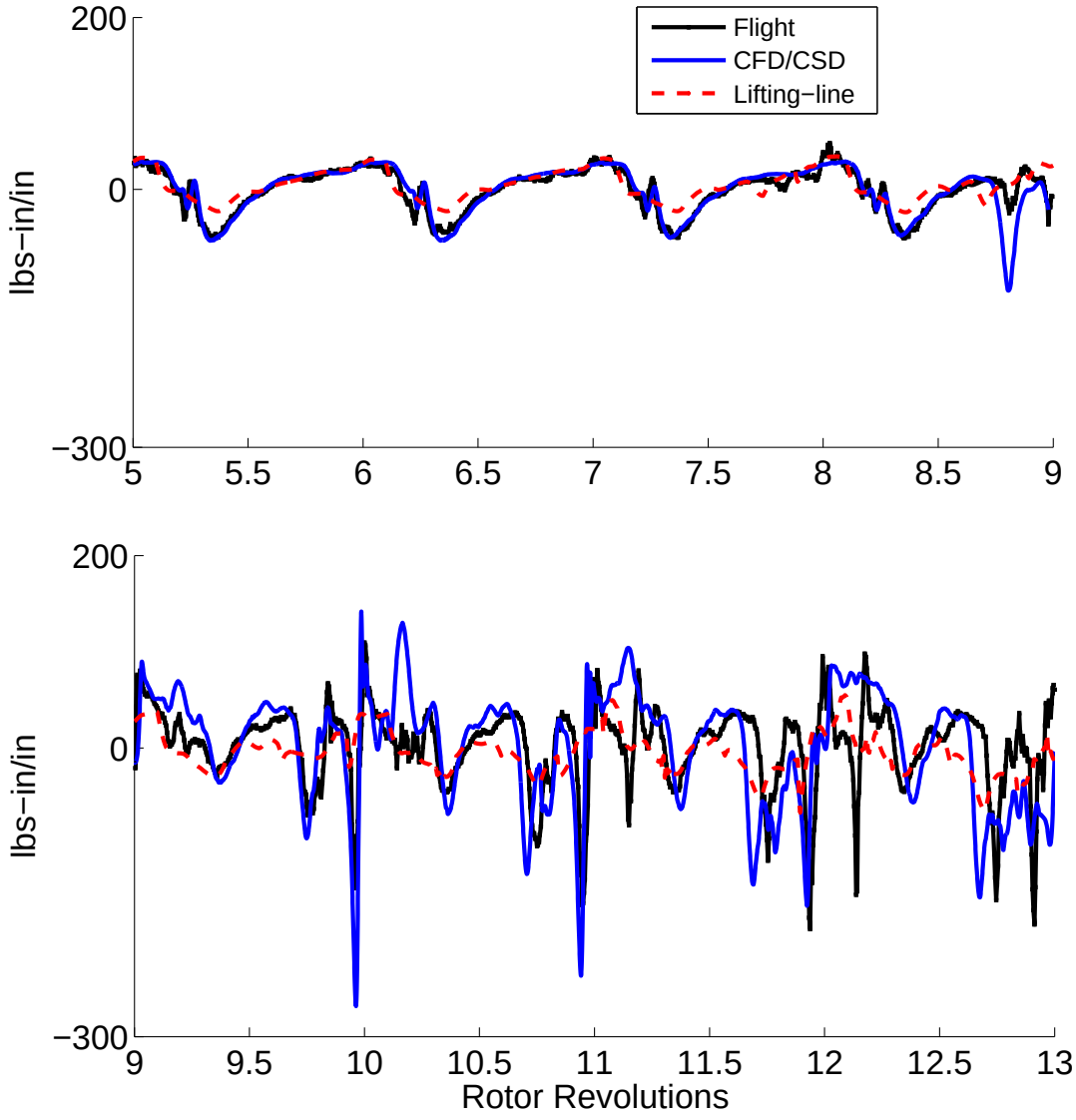

Figure 5.8: **Predicted pitching moment (mean removed) for the UTTAS pull up maneuver; predictions using coupled lifting-line analysis and CFD/CSD at** $86.5\%R$

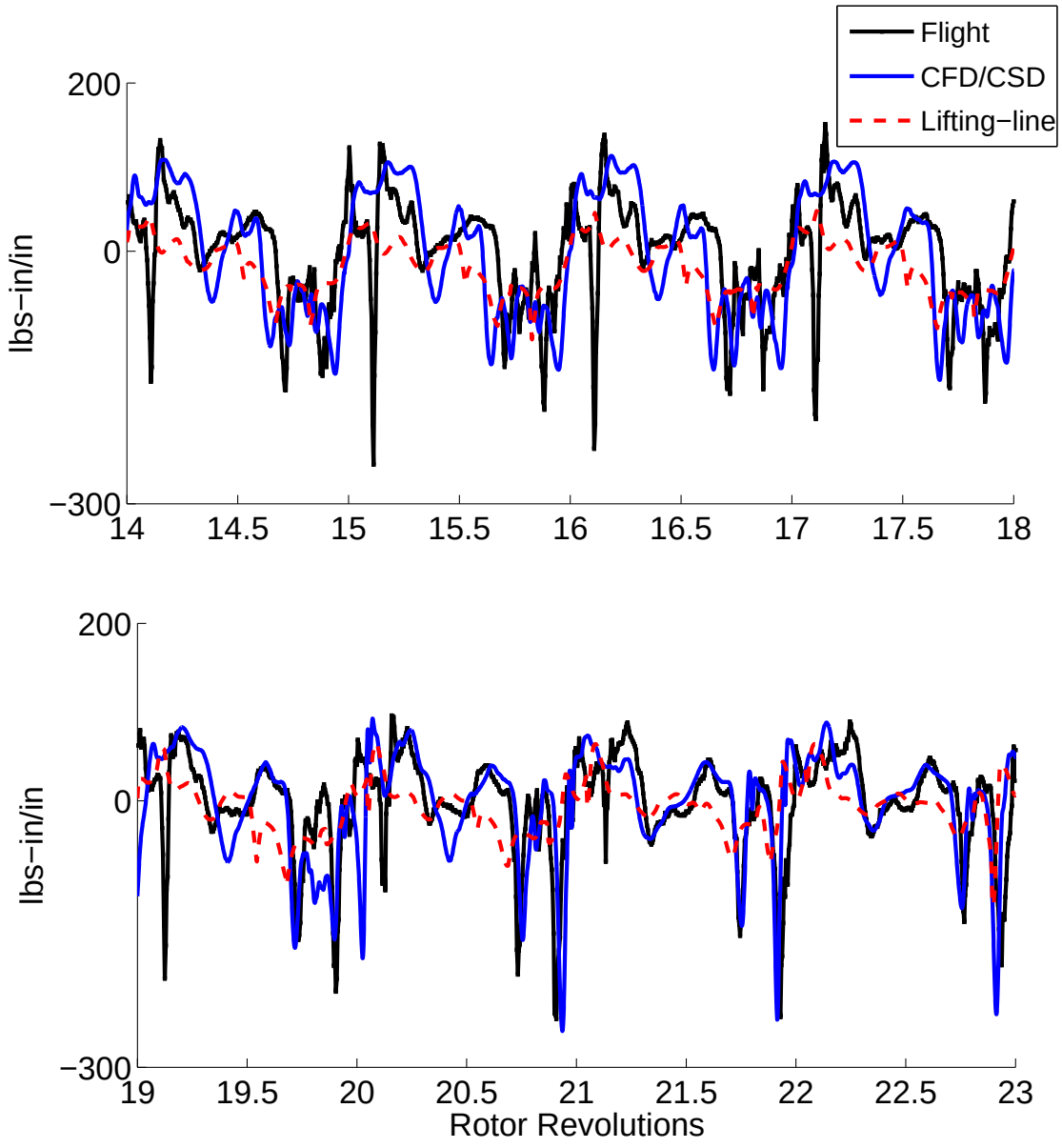

Figure 5.9: **Predicted pitching moment (mean removed) for the UTTAS pull up maneuver; predictions using coupled lifting-line analysis and CFD/CSD at** $86.5\%R$

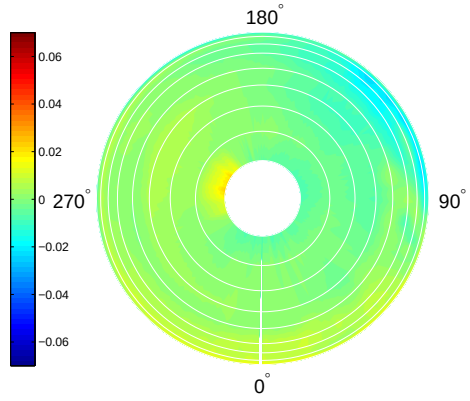

(a) Flight test rev. 4

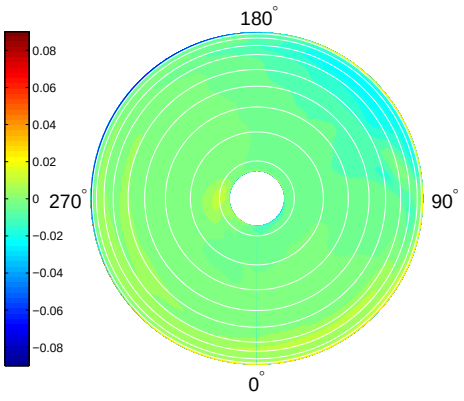

(b) UMARC2/OVERTURNS rev. 4

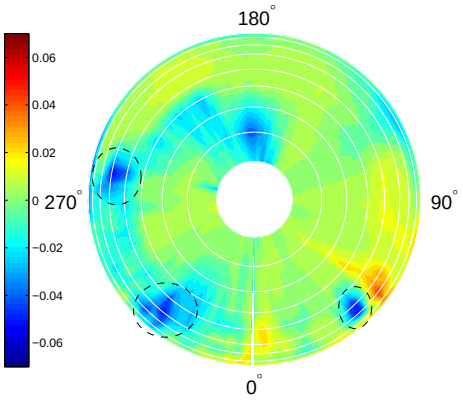

(c) Flight test rev. 14

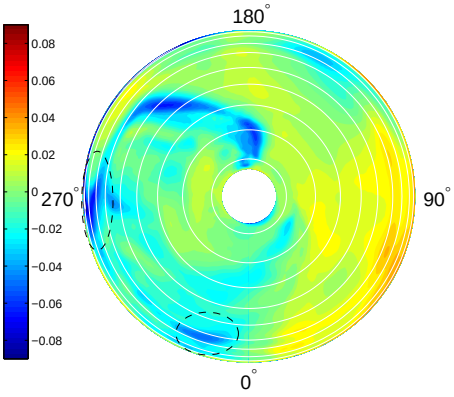

(d) UMARC2/OVERTURNS rev. 14

Figure 5.10: **Contour plots of the non-dimensional aerodynamic pitching moments (mean removed) during revs. 4 and 14 of the UTTAS pull-up maneuver predicted by UMARC2 coupled with OVERTURNS**

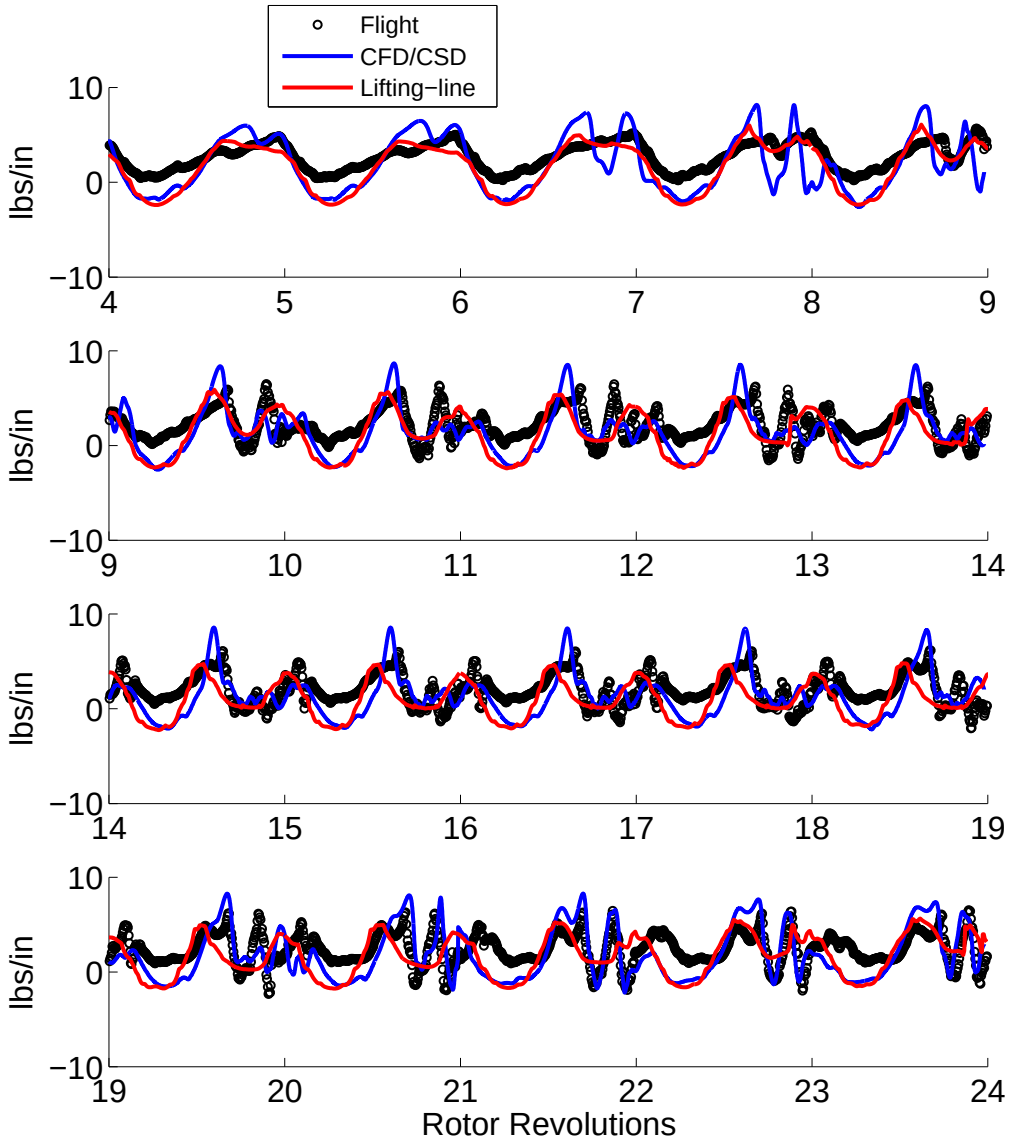

Figure 5.11: **Predicted chord force time history for the UTTAS pull up maneuver; predictions using lifting-line analysis and CFD/CSD at** $86.5\%R$

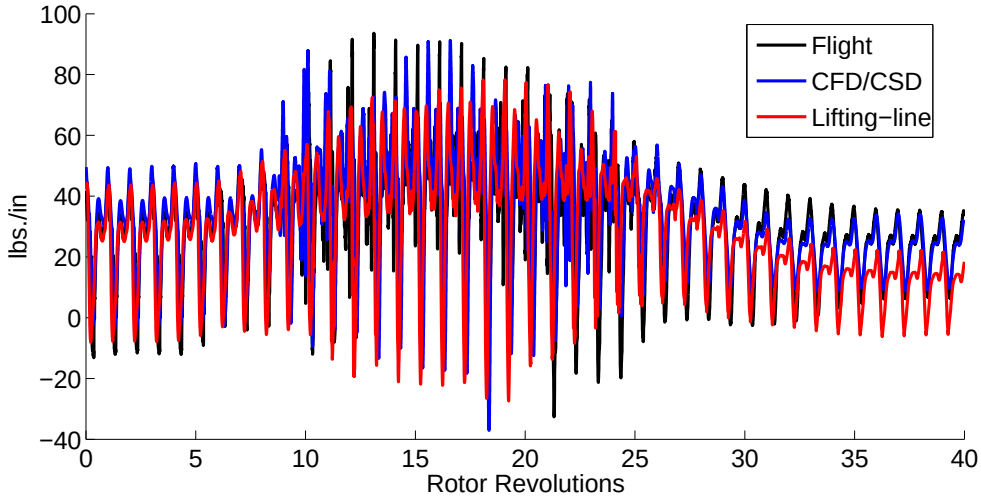

(a) Normal force

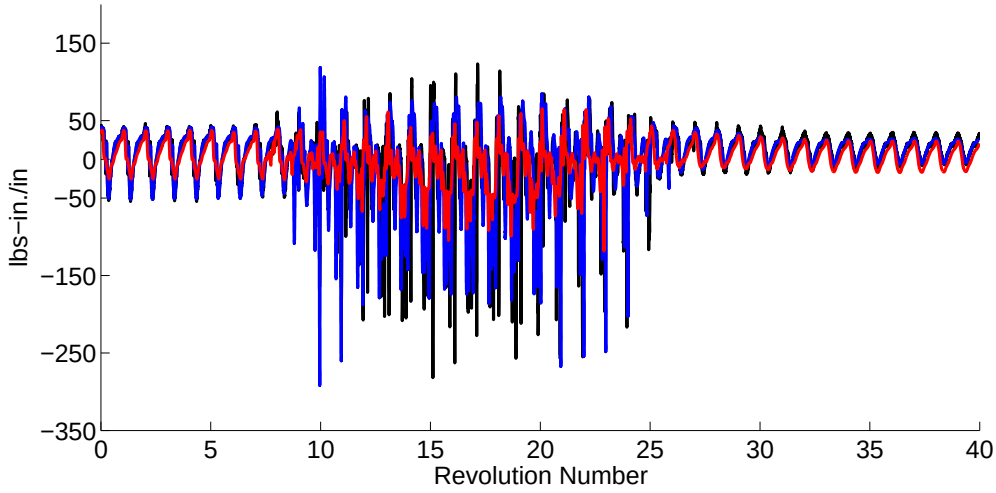

(b) Pitching moment

Figure 5.12: **Comparison of the CFD/CSD and coupled lifting-line simulations showing the lift deficiency problem at** $86.5\%R$

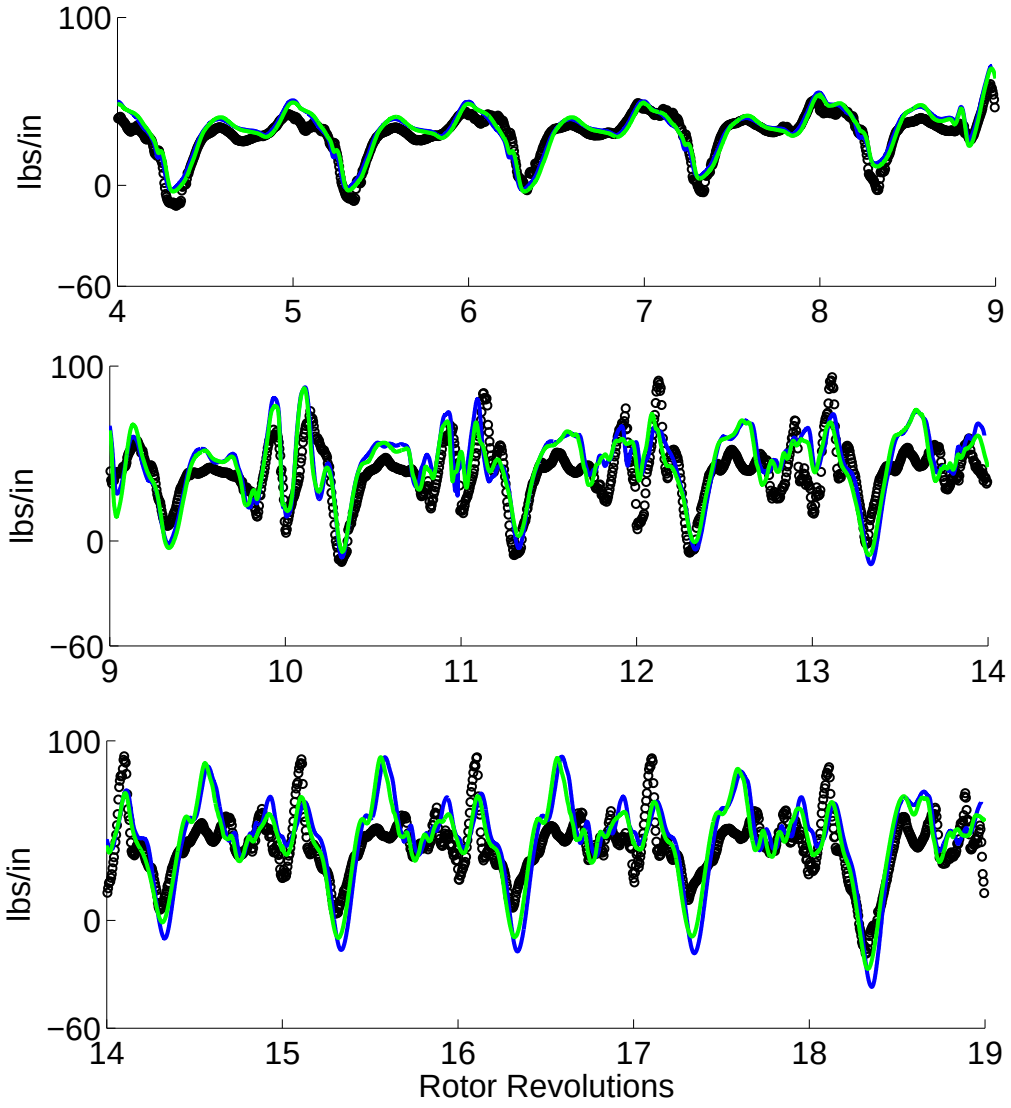

Figure 5.13: **Predicted normal force time history for the UTTAS pull up maneuver using CSS and time accurate approaches at** $86.5\%R$

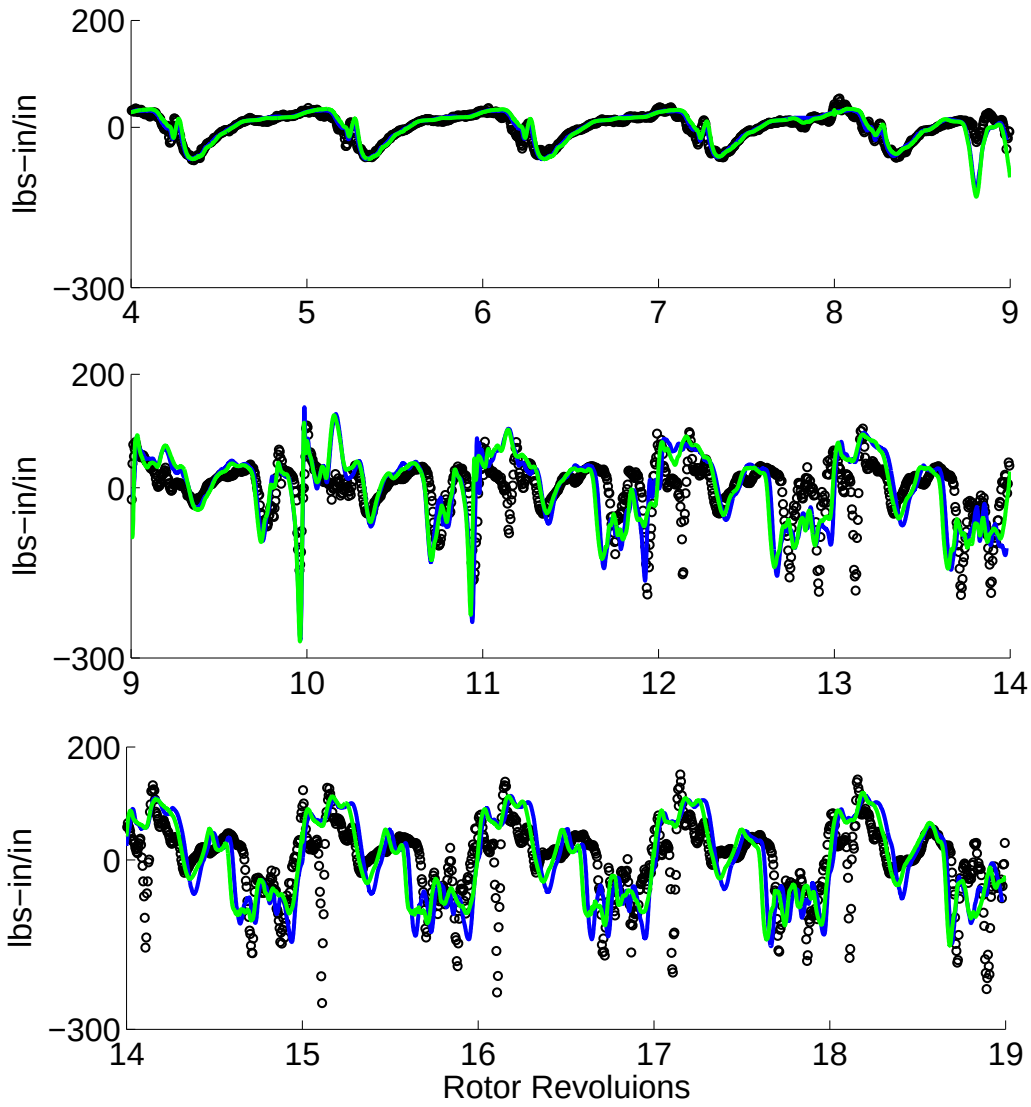

Figure 5.14: **Predicted pitching moment time history for the UTTAS pull up maneuver using CSS and time accurate approaches at** $86.5\%R$

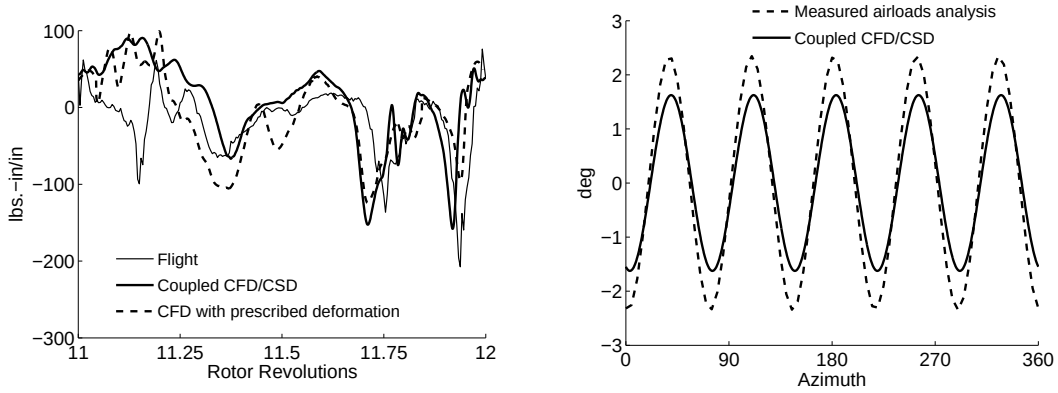

(a) Pitching moment at 86.5%R (b) 5/rev elastic twist at blade tip

Figure 5.15: **Comparison of pitching moment and 5/rev elastic twist for rev 12 using coupled CFD/CSD and CFD with prescribed deformations obtained using measured airloads.**

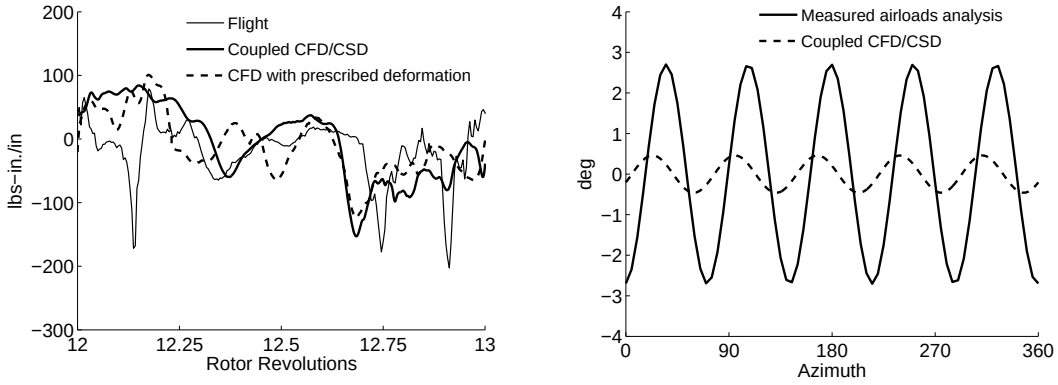

(a) Pitching moment at 86.5%R (b) 5/rev elastic twist at blade tip

Figure 5.16: **Comparison of pitching moment and elastic twist for rev 13 using coupled CFD/CSD and CFD with prescribed deformations obtained using measured airloads.**

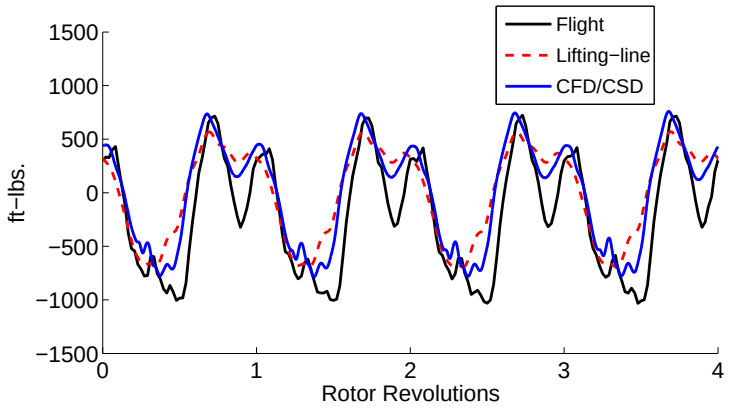

(a) Flap bending moment at 50%R

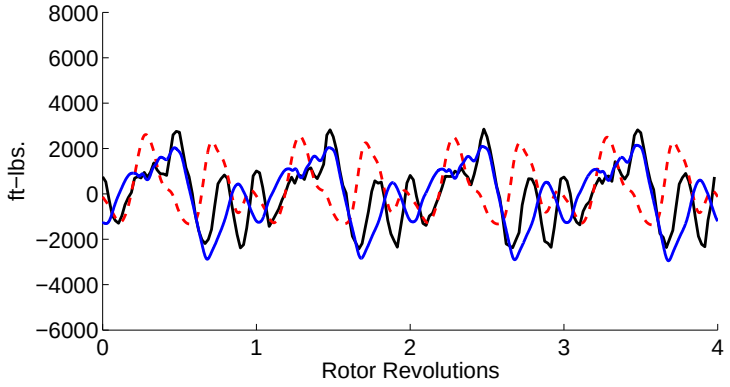

(b) Lag bending moment at 50%R

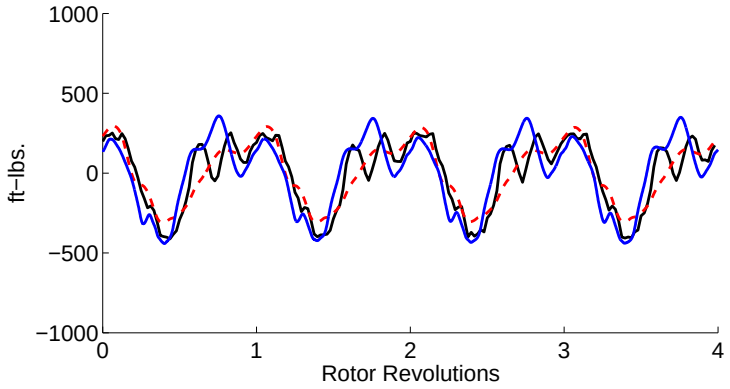

(c) Torsion moments at 30%R

Figure 5.17: **Predicted flap, lag and torsional moment (mean removed) time histories (mean removed), for the steady flight regime using coupled lifting-line and CFD/CSD**

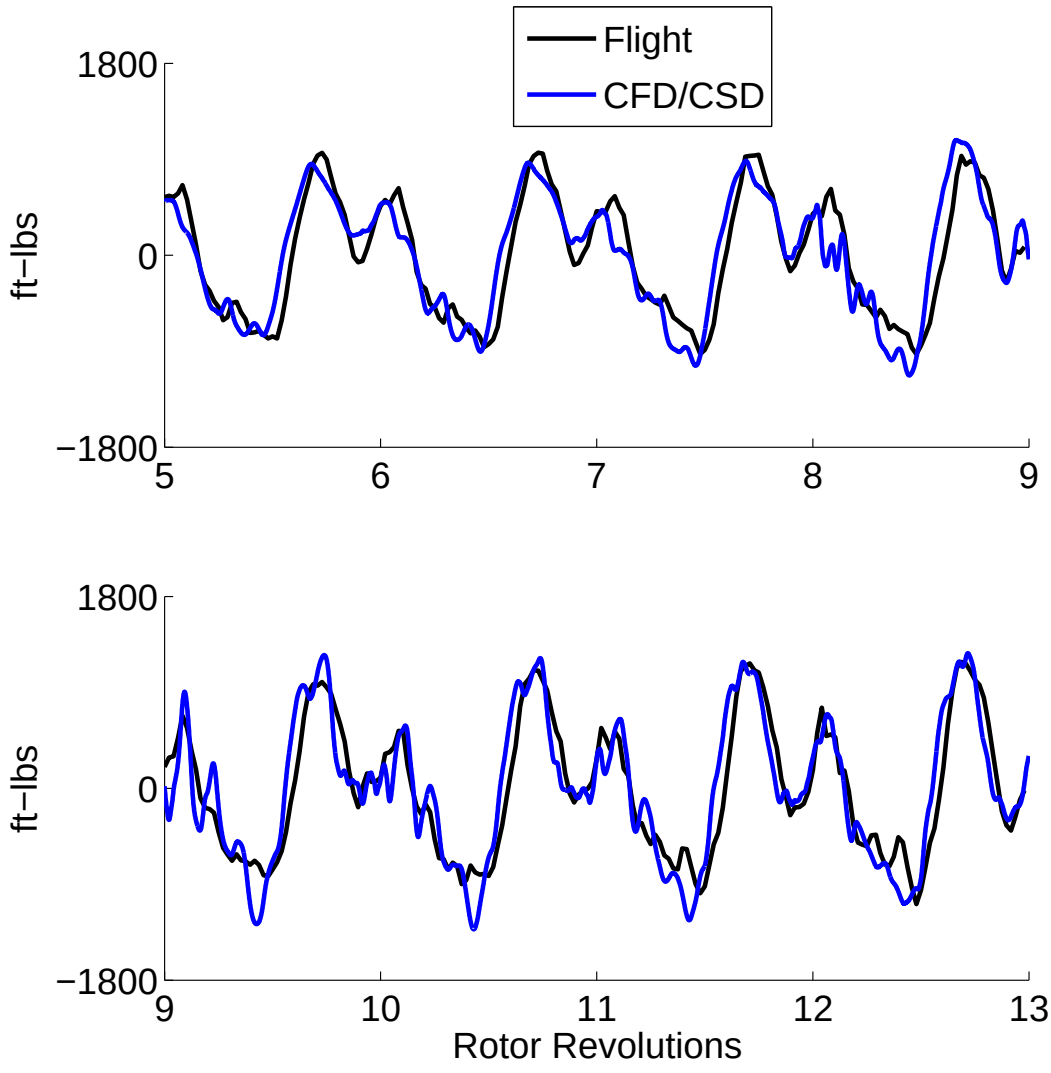

Figure 5.18: **Predicted sectional flap bending moment (mean removed) time histories for the UTTAS pull up maneuver using CFD/CSD at** $50\%R$

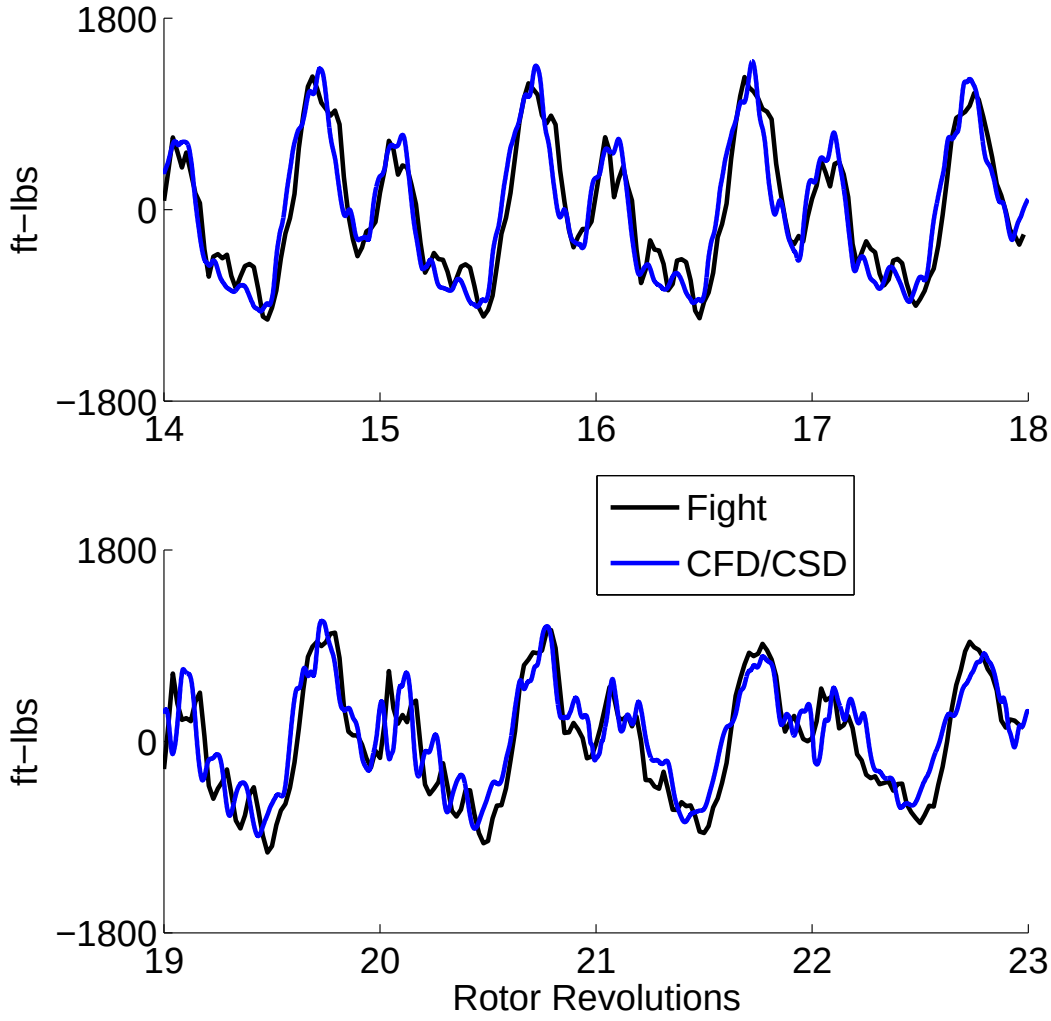

Figure 5.19: **Predicted sectional flap bending moment (mean removed) time histories for the UTTAS pull up maneuver using CFD/CSD at** $50\%R$

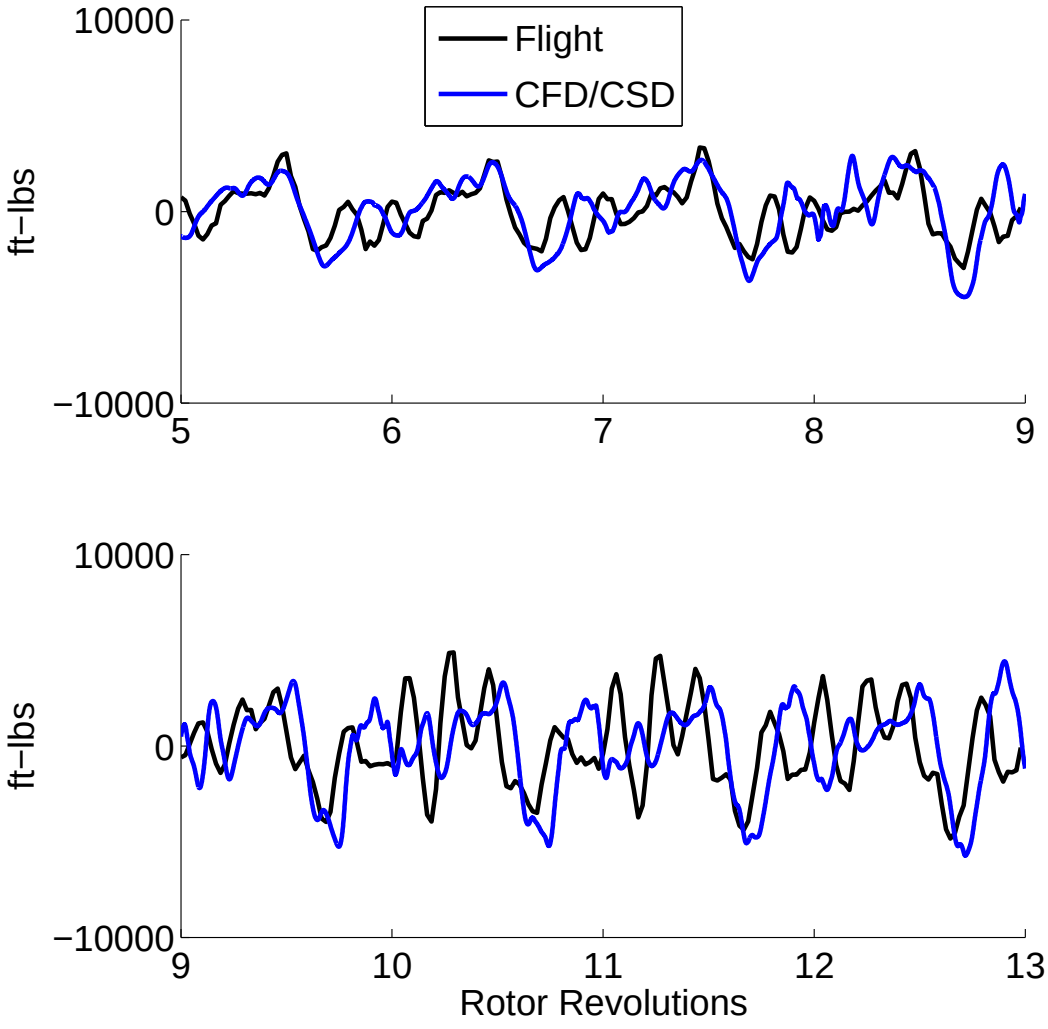

Figure 5.20: **Predicted sectional lag bending moment (mean removed) time histories for the UTTAS pull up maneuver using CFD/CSD at** $50\%R$

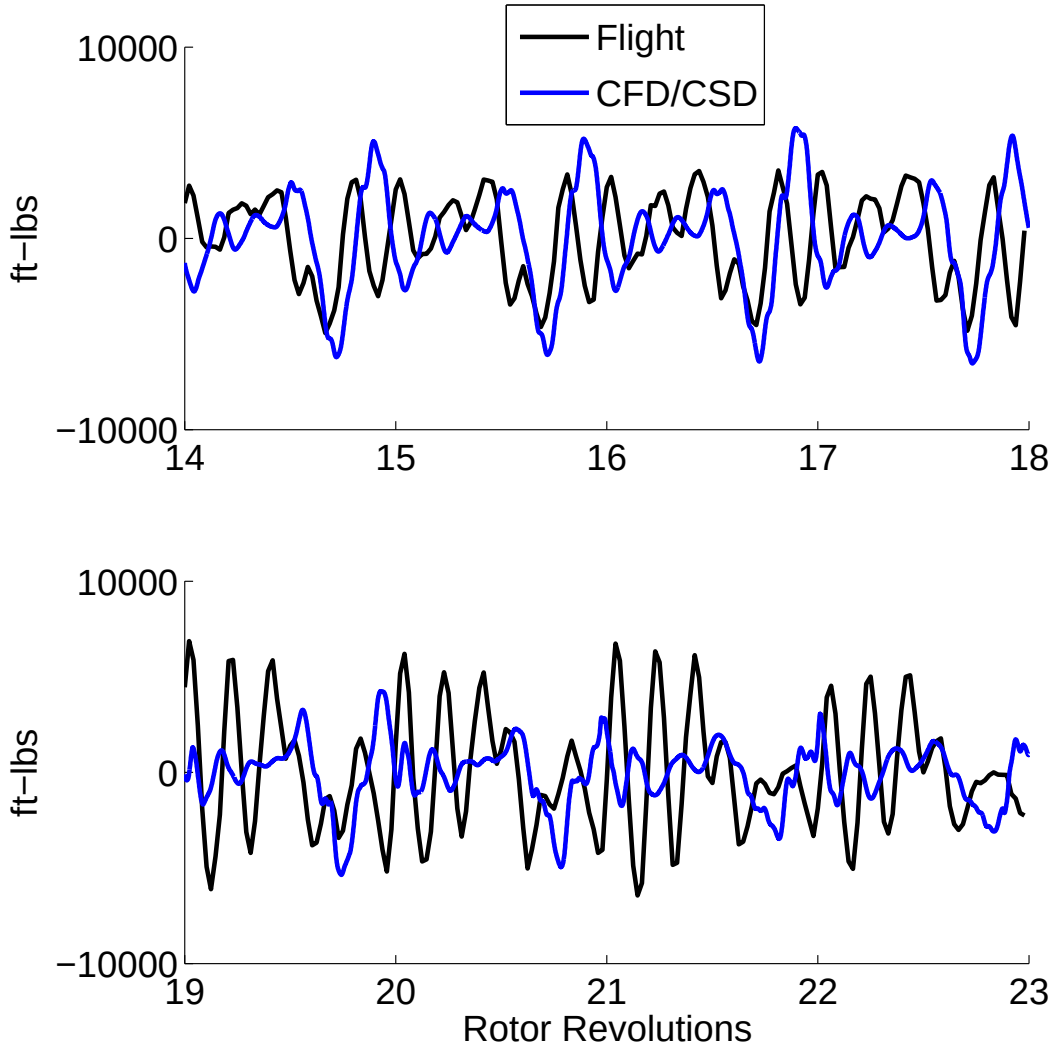

Figure 5.21: **Predicted sectional lag bending moment (mean removed) time histories for the UTTAS pull up maneuver using CFD/CSD at** $50\%R$

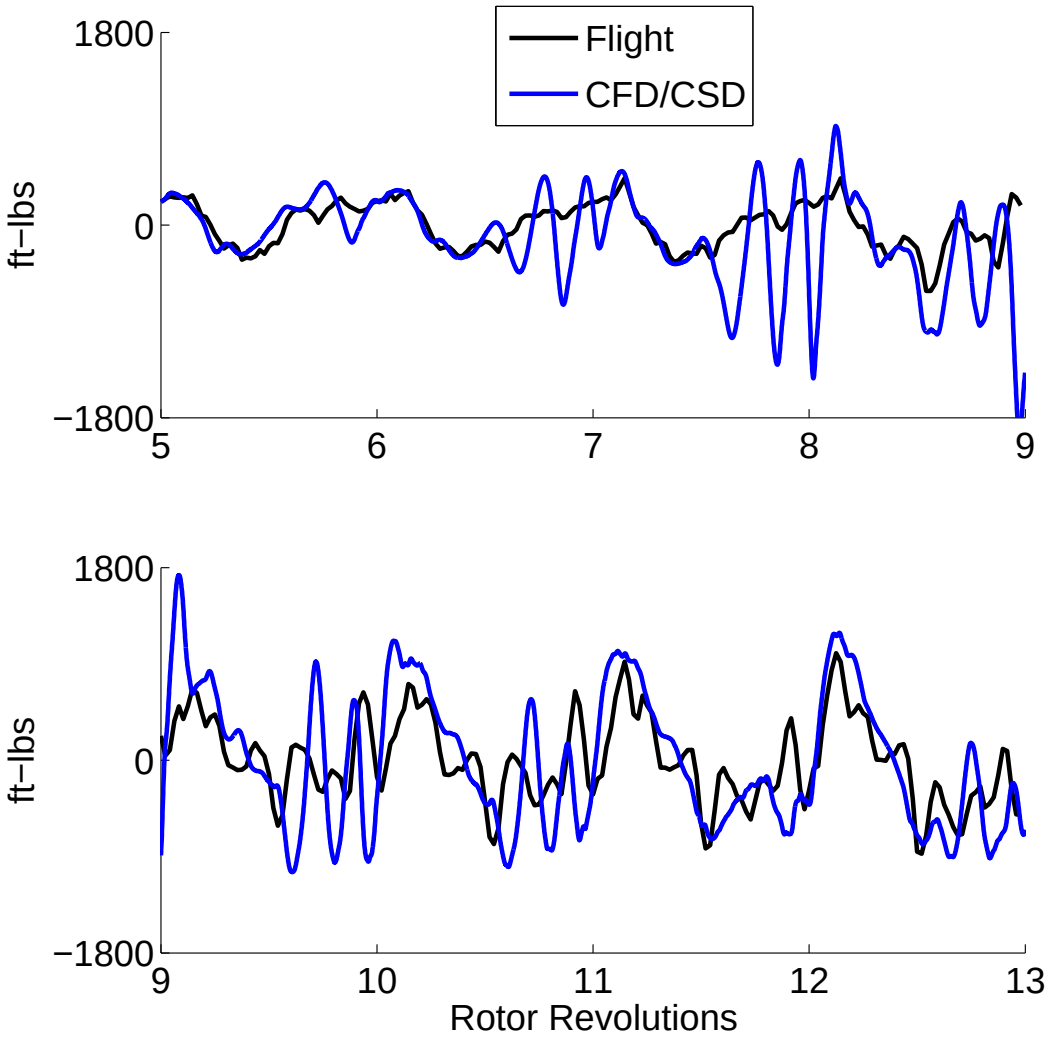

Figure 5.22: **Predicted sectional torsional moment (mean removed) time histories for the UTTAS pull up maneuver using CFD/CSD at** $30\%R$

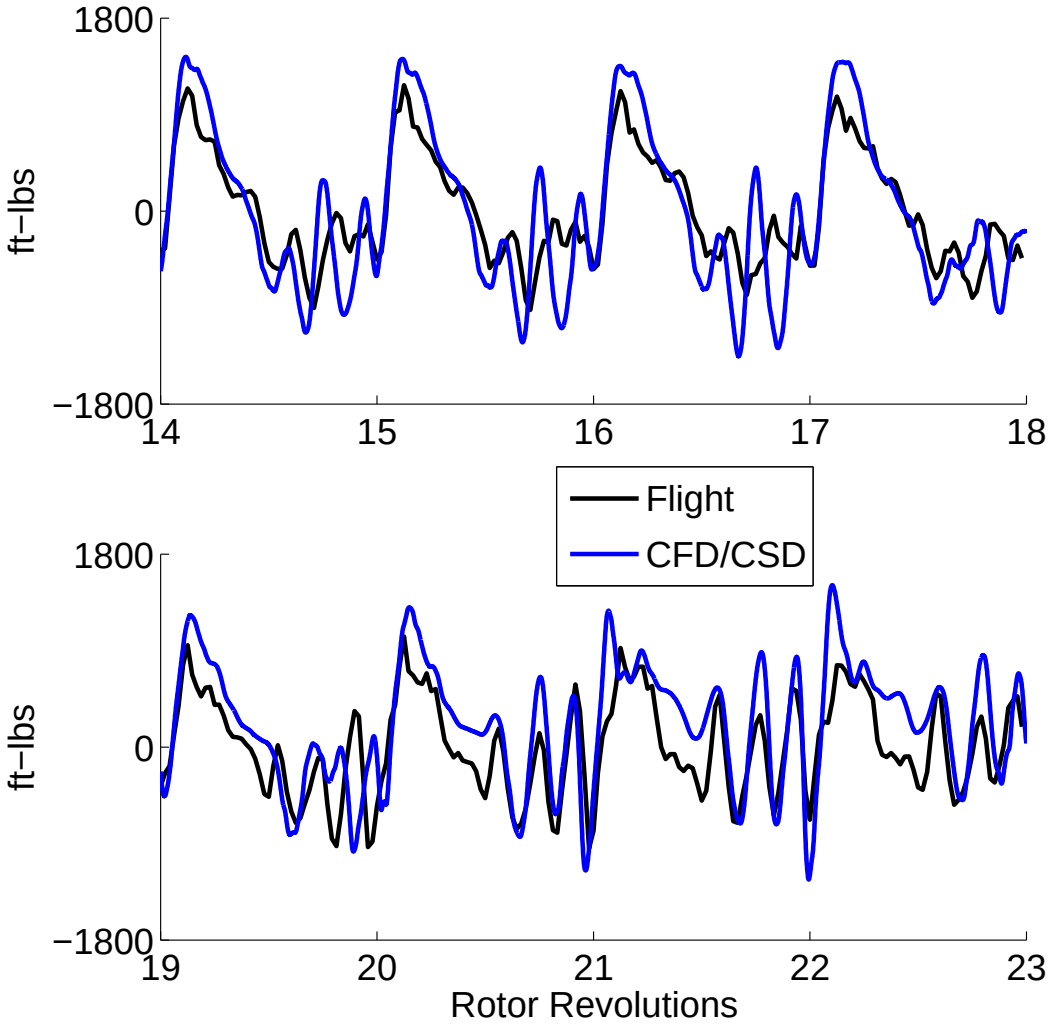

Figure 5.23: **Predicted sectional torsional moment (mean removed) time histories for the UTTAS pull up maneuver using CFD/CSD at** $30\%R$

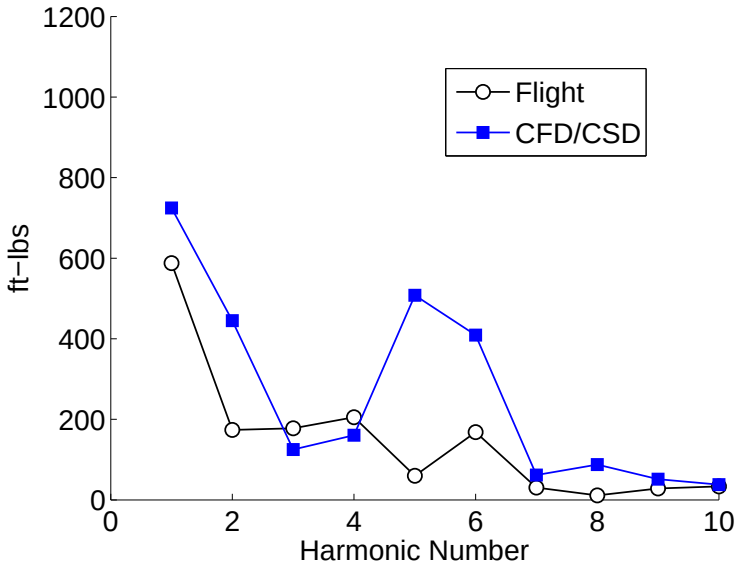

Figure 5.24: **Torsional moment harmonics at 30%R for the rev 14; prediction using CFD/CSD**

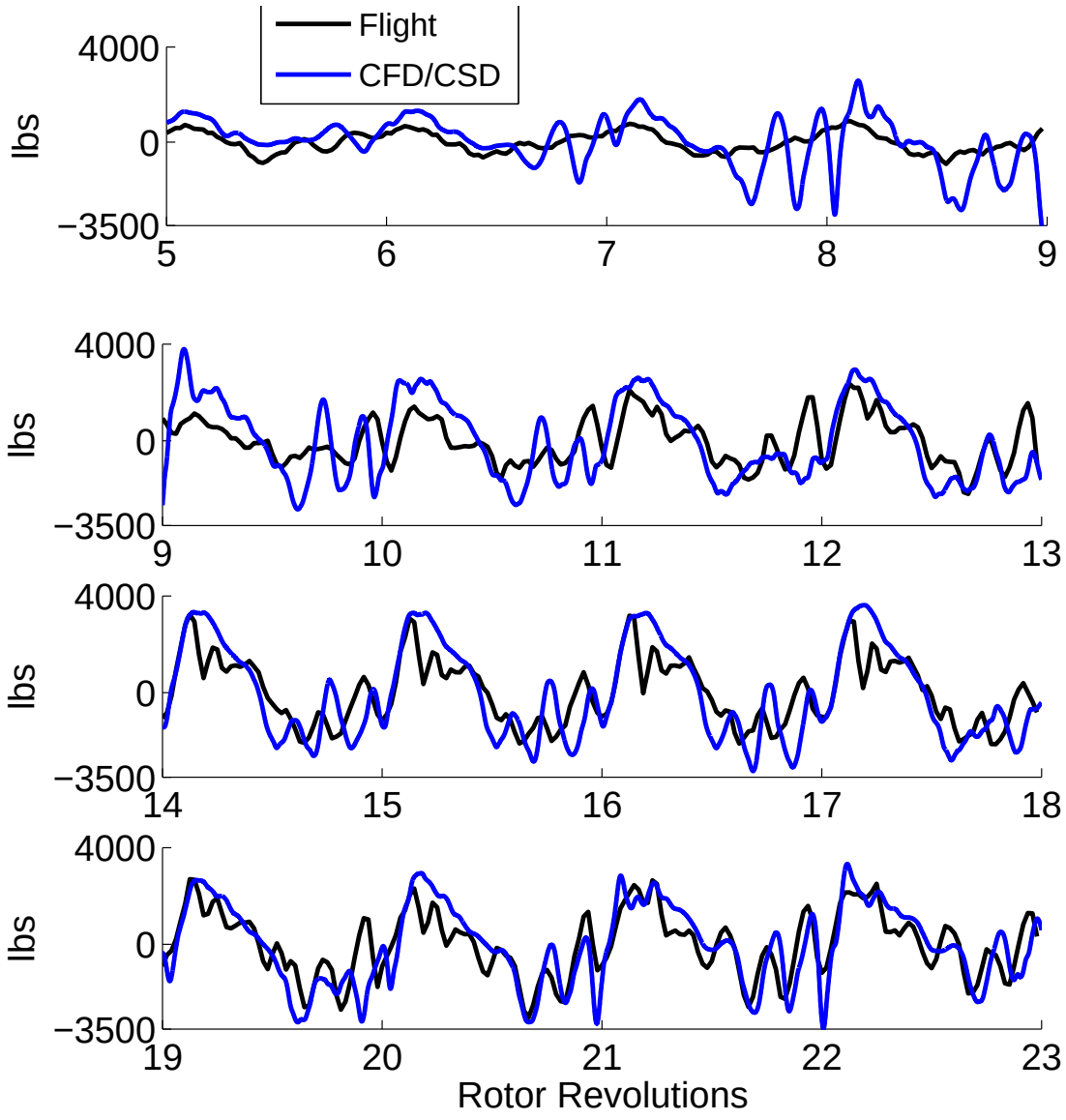

Figure 5.25: **Predicted pitch-link load (mean removed) time histories for the UTTAS pull up maneuver using CFD/CSD**

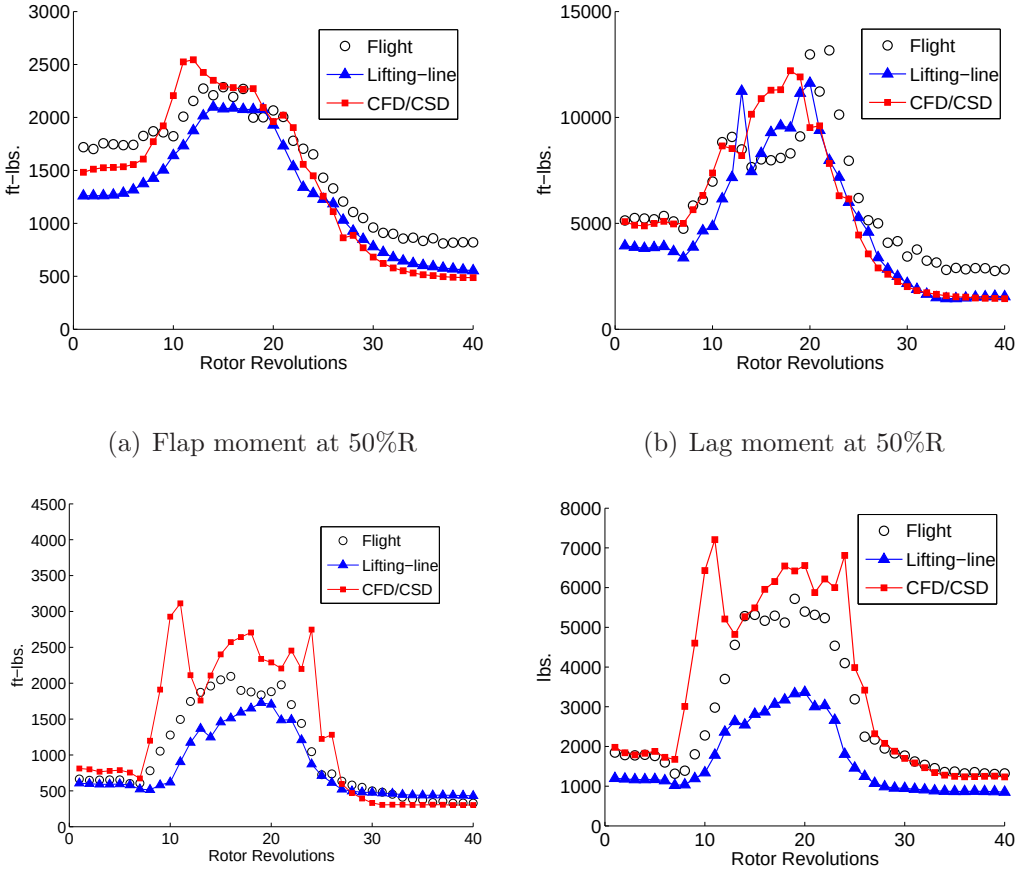

(a) Flap moment at 50%R

(b) Lag moment at 50%R

(c) Torsion moment at 30%R

(d) Pitch-link load

Figure 5.26: **Summary of structural loads predicted using coupled lifting-line analysis and CFD/CSD**

Chapter 6

Conclusions

6.1 Concluding Remarks

Summary of the key conclusions of this research is presented in this chapter. The focus of this research work was the development of refined analysis, followed by prediction and validation with flight test and finally, the fundamental understanding of the loads mechanisms in a prescribed unsteady maneuver. The UTTAS pull-up maneuver from the UH-60A flight test database was chosen for the validation of the predictions. The UTTAS pull-up maneuver designated by counter C11029 is a high speed (139 kts) 2.1g maneuver, and is the second most severe maneuver from the structural loads point of view. In the first step, the physics of aerodynamics and structural dynamics was separated by studying the prediction capability of structural model in isolation using the flight test airloads data. After the validation of structural loads, the calculated blade deformations were used to predict the airloads. The freezing of the response allows for consistent comparison of aerodynamic models and is also used to study the effect of perturbations in control angles. The airloads sensitivity study for control angles is necessary for the study of prescribed maneuver, due to the uncertainties associated with the measured control angles. After the validation of structural loads, the calculated blade deformations were used to

predict the airloads and all three stall cycles, typical to this flight, were predicted. The mechanism of the advancing blade was hypothesized as the 5/rev elastic twist, triggered by the two dynamic stall cycles from the previous revolution on the retreating side of the blade. The structural model was then coupled with lifting-line model to isolate the effect of wake, dynamic stall and swashplate dynamics. Finally the structural model was coupled to CFD for identification of limitations of the lifting-line model and improvements in loads prediction provided by CFD analysis.

The conclusions from each section of this thesis are summarized at the end of each chapter. The key conclusions are also listed below.

1. The advancing blade stall observed during the peak load factor regime of the maneuver (revolutions $12 - 20$) is a transonic twist stall of steady nature. Study conducted using lifting-line analysis with calculated deformations from measured airloads revealed that the blade stall in first quadrant was insensitive to wake or dynamic stall. Harmonic analysis of elastic twist pinned its source to be the 5/rev elastic torsion excitation. The role of the 5/rev elastic twist is to increase the angle of attack beyond static stall limit for the airfoils in the outboard region. Although, these airfoils are operating at low to moderate angles of attack, they are very close to the static stall limit due to high Mach number. The 5/rev component of elastic twist necessary for prediction of advancing blade stall is generated by two retreating stalls from the previous revolution which are spaced by approximately $1/5th$ rotor revolution. The study with CFD revealed that the flow separation causing the stall in the first

quadrant is caused by a strong shock sitting near mid-chord position.

2. In addition to 5/rev elastic twist, the magnitude and extent of the advancing blade stall is also sensitive to the collective angle. For example, a 10% error in collective angle was observed to induce an under-prediction of first stall peak magnitude by up to 30%.

3. The structural model is able to predict the correct trends for the structural loads using the measured airloads data, but the root flap angle shows significant over-prediction in the later part of the maneuver. This discrepancy is not resolved, even when the structural model is coupled to lifting-line or CFD model, and might be related to uncertainties associated with the flight test data.

4. Even though the wake cuts through the rotor disk on two occasions (10th and 24th revolution) during the maneuver, it appears almost entirely to be dominated by stall. The dynamic stall model, provides the most significant improvement to predicted rotor loads, and the free wake does not appear to be important for prediction of these loads. Almost up to 75% of a typical airfoil operating envelope (outboard of 67.5% R) during the 10-25 revs. occur beyond the static stall boundary. Thus, the sectional airloads are governed predominantly by stall phenomenon, and the 2–4° perturbation in sectional angles of attack in already stalled region only has a minor impact on the sectional airloads.

5. The predicted peak-to-peak structural loads using lifting-line analysis are less satisfactory in general. During the peak load factor of the maneuver, 10–22 revs (above $1.75g$), the flap bending moments are closest to test data (10–20% underprediction), followed by chord bending (25% overprediction), then torsion moment (30% underprediction), and finally pitch-link load (50% underprediction). These errors stem from the aerodynamics and not the structural dynamics. The error in airloads which shows up in the underprediction of structural loads is due to the significant underprediction of pitching moments, as lifting-line analysis is unable to predict transonic shock in the pitching moment at the beginning of the maneuver and also under predicts the intensity of dynamic stall cycles with desired accuracy, during the high load-factor regime.

6. The swashplate servo loads are an important design parameter in the overall helicopter design and their accurate prediction is desired. The swashplate servo loads in the fixed frame are determined by the 3, 4, and 5/rev pitch-link loads in the rotating frame and the dynamics of the swashplate. The servo loads, during the maneuver are dominated primarily by 4/rev loading similar to the level flight, but the swashplate dynamics seems to play a more significant role than that observed in steady flight. The peak loads observed during the maneuver, are magnified by three times (forward link) to five times (aft link) compared to level flight. The analysis predicts this trend correctly – primarily due to the accuracy of 3/rev pitch-link load prediction. The analysis also show a significant impact of swashplate dynamics on the 8/rev loads.

7. The two dynamic stall events on the retreating side are predicted by the CFD/CSD analysis. But the analysis is unable to predict first quadrant stall due to less accurate prediction of 5/rev elastic twist arising from the under-prediction of the two retreating blade stalls from previous revolution. The prediction of second retreating blade stall is extremely challenging and its accurate prediction is essential for the prediction of the advancing blade stall. The lifting-line model is unable to predict the high-frequency stall loads during the maneuver, especially the peak magnitude of pitching moment is under-predicted significantly.

8. The predictions of the structural loads do not show the same level of correlation as the airloads when compared with flight test data. The lower frequencies of the structural loads are resolved well when accurate airloads data (flight test airloads) is used for predicting the structural loads. However, the accurate prediction of higher harmonics (4/rev and higher) are much harder to predict. The errors stem from the structural modeling. The detailed modeling of boundary condition and inclusion of periodic variation of control system stiffness doesn't seem to have any impact on these loads prediction. The inability to predict the structural loads accurately using beam element based models is a problem even with steady flight analysis and is not an issue specific to the analysis of maneuvering flight and needs further investigation.

In this study the maneuver was studied in a prescribed manner and the flight dynamics and controls time history available from the flight test was used to decouple

the flight dynamics to focus solely on the loads mechanisms. This was an unavoidable simplification due to the challenges associated with the first principle solution to the problem of blade aeromechanics coupled to flight dynamics. The findings of this work should be used as a stepping stone for the fully coupled analysis of the maneuver to verify the findings of this work. For this to become a reality, the validity of state-of-art flight dynamics inverse simulation techniques would have to be tested under deep-stall conditions. Further, the computational penalty associated with coupling conventional Jacobian based inverse simulation approaches to a CFD/CSD simulation, has to be addressed to make the solution procedure computationally practical.

6.2 Future Work

This section suggests the future directions for the research. In the present work a prescribed unsteady pull-up maneuver was studied and the mechanisms responsible for high loads were identified. It was concluded that the dynamic stall, and not the rotor-wake interaction, was the standout phenomenon dominating the blade loads. The study was conducted using the prescribed control angles obtained from the flight test. The dynamic stall events encountered during this flight were observed to be sensitive on the control angles used during the solution which stresses out the importance of a inverse flight dynamics simulation for accurate estimation of the control angles for the analysis of the maneuver. Further to attain greater confidence in the tools developed for this analysis, other maneuvers should be analyzed. Until

a practical inverse flight simulation module is integrated in the CFD/CSD analysis, steady maneuvers should be studied to get greater insight on the limitations of the current structural and aerodynamic models. Key recommendation for future research directions related to this work are summarized below.

1. This study should be expanded to other steady and unsteady maneuvers. Flight test data is available for several other maneuvers and therefore analyzing other flights in a prescribed manner appears to be the natural course of action.

2. An inverse flight dynamic simulation capable of being interfaced with the current CFD/CSD simulations, without the computational penalty, is the next most important component of analysis necessary for accurate prediction of maneuver loads.

3. The prediction of dynamic stall is not satisfactory at all times, the study using the calculated blade deformations obtained from the measured airloads analysis, indicated that the error stems from the aerodynamics and not the structural dynamics. The RANS closure in the present CFD analysis was achieved using the Baldwin-Lomax turbulence model. The prediction of dynamic stall is known to be sensitive to turbulence modeling. The effect of turbulence modeling should be investigated using other turbulence models like Spalart-Almaras and K-epsilon models. The sensitivity to grid refinements should also be addressed.

4. During an unsteady maneuver, the interaction between the rotor and the fuse-

lage may be of more significance than the steady flight and the rotor-fuselage structural as well as aerodynamic interaction may be another thrust area that should be addressed.

5. Greater computational efficiency may be achieved by parallelizing the structural algorithms and free wake calculations and must be examined.

6. This study focused on a fully articulated rotor and should be carried out for other rotor configurations, such as hingeless and bearingless rotors.

Appendix A

Simple Beam Bending Problem

A.1 General Formulation

A simple rotating beam bending problem is considered to illustrate the methodology used for modeling the rotor blades. The coordinate system defined for the problem is shown in Fig. A.1. $X,\ Y$ represents the coordinate system of the frame of reference rotating with a constant angular speed Ω, and $x_E,\ y_E$ represents the coordinate system of the element frame of reference. The unit vectors (basis) associated with these frames are $\hat{i},\ \hat{j}$ and $\hat{i}_E,\ \hat{j}_E$ respectively. The element frame remains attached to the root of the element and rotates with it. Let P denote a point on the beam which moves to its new position P' when the beam deforms. The position vector, $\mathbf{r}_P$, of the point P' in the inertial frame measured in inertial basis would be given by

$$\mathbf{r}_P = \mathbf{R} + A\mathbf{u} \tag{A.1}$$

where, $\mathbf{R}$ is the position of the origin of the element frame (attached to element root) in inertial frame measured in inertial basis, $\mathbf{u}$ is the position of P' in element frame measured in element basis, A is the rotation matrix that rotates the element frame to inertial frame. In the element frame, the location of point P' can be written

as

$$\mathbf{u} = \bar{u}_0 + \bar{u}_e = \bar{u}_0 + H\mathbf{q}_f \tag{A.2}$$

where $\bar{u}_0$ is the undeformed location of point P, $\bar{u}_e$ is the deformation, H is the shape function used to interpolate deformation within the element, and $\mathbf{q}_f$ is the vector of elastic nodal coordinates. For example, for a two noded beam element

$$u_0 = \begin{Bmatrix} x_0 \\ y_0 \end{Bmatrix} \text{ and } u_e = \begin{bmatrix} 0 & 0 & 0 & 0 \\ H_1 & H_2 & H_3 & H_4 \end{bmatrix} \begin{Bmatrix} w_1 \\ w_1' \\ w_2 \\ w_2' \end{Bmatrix} \text{ and}$$

$$H_1 = 2s^3 - 3s^2 + 1$$

$$H_2 = l(s^3 - 2s^2 + s)$$

$$H_3 = -2s^3 + 3s^2$$

$$H_4 = l(s^3 - s^2)$$

If at the deformed position of the beam the attached $x_E y_E$ coordinate is oriented at an angle θ with respect to the XY coordinate then the transformation matrix A is given by

$$A = \begin{bmatrix} \cos\theta & \sin\theta \\ -\sin\theta & \cos\theta \end{bmatrix} \tag{A.3}$$

The velocity of the point P at its new location P' is given by

$$\mathbf{v} = \dot{\mathbf{r}}_P = \dot{\mathbf{R}} + \dot{A}\mathbf{u} + A\dot{\mathbf{u}} \tag{A.4}$$

For simplification, lets assume that the position of the root of the beam does not

change relative to the inertial frame, i.e. $\dot{\mathbf{R}} = 0$. Therefore, we have

$$\dot{\mathbf{r}}_P = \dot{A}\mathbf{u} + A\dot{\mathbf{u}} \tag{A.5}$$

where

$$\dot{A} = \begin{bmatrix} -\dot{\theta}\sin\theta & \dot{\theta}\cos\theta \\ -\dot{\theta}\cos\theta & -\dot{\theta}\sin\theta \end{bmatrix} = -\begin{bmatrix} 0 & -\dot{\theta} \\ \dot{\theta} & 0 \end{bmatrix}\begin{bmatrix} \cos\theta & \sin\theta \\ -\sin\theta & \cos\theta \end{bmatrix} = -\tilde{\dot{\theta}}A \tag{A.6}$$

and

$$\tilde{\dot{\theta}} = \dot{\theta}\begin{bmatrix} 0 & -1 \\ 1 & 0 \end{bmatrix} = \dot{\theta}\tilde{\mathbf{I}} \tag{A.7}$$

$$\dot{\mathbf{u}} = \dot{\bar{u}}_e = H\dot{\mathbf{q}}_f \tag{A.8}$$

Using Eqs. A.6 and A.8 in Eq. A.5, we get

$$\dot{\mathbf{r}}_P = -\dot{\theta}\tilde{I}A\mathbf{u} + AH\dot{\mathbf{q}}_f \tag{A.9}$$

Similarly, the acceleration can be written as

$$\mathbf{a} = \ddot{\mathbf{r}}_P = -\ddot{\theta}\tilde{\mathbf{I}}A\mathbf{u} - \dot{\theta}\tilde{\mathbf{I}}\dot{A}\mathbf{u} - \dot{\theta}\tilde{\mathbf{I}}A\dot{\mathbf{u}} + \dot{A}H\dot{\mathbf{q}}_f + AH\ddot{\mathbf{q}}_f \tag{A.10}$$

which on simplification and using the fact that

$$\tilde{\mathbf{I}}\,\tilde{\mathbf{I}} = -\mathbf{I} \tag{A.11}$$

gives

$$\mathbf{a} = -\ddot{\theta}\tilde{\mathbf{I}}A\mathbf{u} - \dot{\theta}^2 A\mathbf{u} - 2\dot{\theta}\tilde{\mathbf{I}}AH\dot{\mathbf{q}}_f + AH\ddot{\mathbf{q}}_f \tag{A.12}$$

The net inertial force can be estimated using the Kane's equation given by

$$\{f^*\} = -\sum_{i=1}^{N}\int_0^l m\{\mathbf{a}\}\frac{\partial\{\mathbf{v}\}}{\partial\dot{p}_i}dl \tag{A.13}$$

where, p_i is the i-th generalized coordinate. Using expressions for $\mathbf{a}$ and $\mathbf{v}$ in Eq. A.13 we get

$$\{f^*\} = -\int_0^l m(\mathbf{u}^T A^T \tilde{\mathbf{I}}^T + H^T A^T)\{-\ddot{\theta}\tilde{\mathbf{I}} A\mathbf{u} - \dot{\theta}^2 A\mathbf{u} - 2\dot{\theta}\tilde{\mathbf{I}} AH\dot{\mathbf{q}}_f + AH\ddot{\mathbf{q}}_f\}dl \quad \text{(A.14)}$$

which can be written in the form

$$\{f^*\} = -\int_0^l m \left(\begin{bmatrix} \mathbf{u}^T\mathbf{u} & \mathbf{u}^T\tilde{\mathbf{I}}^T H \\ H^T\tilde{\mathbf{I}}\mathbf{u} & H^T H \end{bmatrix} \begin{Bmatrix} \ddot{\theta} \\ \ddot{\mathbf{q}}_f \end{Bmatrix} + \begin{bmatrix} -\dot{\theta}\mathbf{u}^T\tilde{\mathbf{I}}\mathbf{u} & 2\dot{\theta}\mathbf{u}^T H \\ -2\dot{\theta}H^T\mathbf{u} & 2\dot{\theta}H^T\tilde{\mathbf{I}} \end{bmatrix} \begin{Bmatrix} \dot{\theta} \\ \dot{\mathbf{q}}_f \end{Bmatrix} + \dot{\theta}^2 H^T\mathbf{u} \right) dl \quad \text{(A.15)}$$

This equation gives the symmetric element mass matrix, M, and the non-linear damping matrix, C, given by

$$M = -\int_0^l m \begin{bmatrix} \mathbf{u}^T\mathbf{u} & \mathbf{u}^T\tilde{\mathbf{I}}^T H \\ H^T\tilde{\mathbf{I}}\mathbf{u} & H^T H \end{bmatrix} dl \quad \text{(A.16)}$$

and

$$C = -\int_0^l m \begin{bmatrix} -\dot{\theta}\mathbf{u}^T\tilde{\mathbf{I}}\mathbf{u} & 2\dot{\theta}\mathbf{u}^T H \\ -2\dot{\theta}H^T\mathbf{u} & 2\dot{\theta}H^T\tilde{\mathbf{I}} \end{bmatrix} dl \quad \text{(A.17)}$$

Mass matrix is of the form

$$M = \begin{bmatrix} M_{\theta\theta} & M_{\theta f} \\ M_{f\theta} & M_{ff} \end{bmatrix} \quad \text{(A.18)}$$

The generalized elastic forces can be obtained by differentiating the net strain energy with respect to the generalized coordinates to get

$$K = \begin{bmatrix} 0 & 0 \\ 0 & K_{ff} \end{bmatrix} \quad \text{(A.19)}$$

The total strain energy for a rotating beam element is given by

$$U = \frac{1}{2}\int_0^l EIw''^2 dl + \frac{1}{2}\int_0^l F_A(x)w'^2 dl \quad \text{(A.20)}$$

where, F_A is the centrifugal force acting at a distance x from the center of rotation. Substituting for w'' and w' in the Eq. A.20 gives

$$U = \mathbf{q}_f^T(\frac{1}{2}\int_0^l EIH''^T H'' dl + \frac{1}{2}\int_0^l F_A(x)H'^T H' dl)\mathbf{q}_f \tag{A.21}$$

thus, the stiffness matrix is given by

$$K_{ff} = \int_0^l EIH''^T H'' dl + \int_0^l F_A(x)H'^T H' dl \tag{A.22}$$

The generalized external forces can be given by

$$f_{ext} = \begin{Bmatrix} 0 \\ f_{ff} \end{Bmatrix} = \int_0^l \begin{Bmatrix} 0 \\ H^T f_e \end{Bmatrix} dl \tag{A.23}$$

in the Eq. 2.22 to obtain the governing differential equation of the form

$$M\ddot{\mathbf{x}} + C\dot{\mathbf{x}} + K\mathbf{x} = f(t, x, \dot{x}..) \tag{A.24}$$

which can be solved using methods described in Chapter 2.

A.2 Two Element Rotating Beam

The problem being attempted is a simple rotating beam with a root spring modeled using two elements. This section describes the procedure to solve such a problem using the approach described above.

The equation of motion for each element is established with respect to the local element frame of reference and is solved to calculate deformation in the local element basis, from which it is then transformed to the global reference frame. In this approach, the motion of the end of the parent element (adjacent element in the

direction of beam root) is assigned to the frame of the current element from which it is transferred to each finite element node using Eqs. A.1, A.5 etc.

Likewise, the forces and moments of the child element are multiplied by the shape function at the end node. The resulting forces and moments are summed with element inertial, structural, and external (aerodynamics) forces and moments and the sum of the forces and moments are passed to the parent element.

Boundary conditions are applied at the element level. For example, for the two element rotating pinned beam, the first element has all its degrees of freedom, except the deformation at the pinned station, retained. This is illustrated below for stiffness matrix which is of the form

$$K = \begin{bmatrix} 0 & 0 & 0 & 0 & 0 \\ 0 & K_{11} & K_{12} & K_{13} & K_{14} \\ 0 & K_{21} & K_{22} & K_{23} & K_{24} \\ 0 & K_{31} & K_{32} & K_{33} & K_{34} \\ 0 & K_{41} & K_{42} & K_{43} & K_{44} \end{bmatrix} \tag{A.25}$$

To apply a hinge or pinned boundary condition, the second row and column, which corresponds to the deformation at the hinge location is removed. Similarly, the presence of a torsional spring is incorporated by its adding the appropriate stiffness to the K_{22} element of the stiffness matrix. The second element is rigidly attached to the end of the first element, therefore, the nodal rotational degree of freedom θ is no longer an unknown and instead specified as a prescribed quantity. The deformation and slope at the root node of the second element must be same as that at the end node of first element, therefore the degrees of freedom corresponding

to the deformation and slope at the root node of the second element are removed during the solution process by removing the corresponding rows and columns from the mass, stiffness, damping matrices and the force vector, which is second and third rows and columns for the matrix shown above.

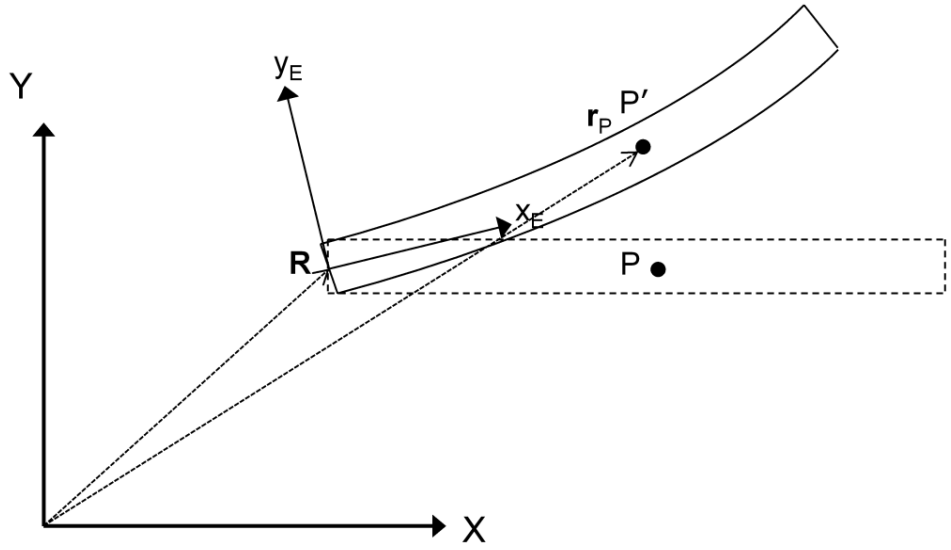

Figure A.1: **Coordinate systems for a 1D beam with only flap degree of freedom**

Bibliography

[1] Kufeld, R. M., Balough, D. L., Cross, J. L., Studebaker, K. F., Jennison, C. D., and Bousman, W. G., "Flight Testing of the UH-60A Airloads Aircraft," American Helicopter Society 50^{th} *Annual Forum* Proceedings, Washington, D. C., May 1994.

[2] Bousman, W. G. and Kufeld, R. M., "UH-60A Airloads Catalogue". NASA/TM-2005-212827, AFDD/TR-05-003, August 2005.

[3] Kee, R. M., "Main Rotor BladeDesign and Development," *Journal of American Helicopter Society*, Vol. 4, (4), 1959, pp. 29–39.

[4] Chrichlow, W. J., Buzzetti, C.J., and Fairchild, J., "The Fatigue and Fall.Safe Program for the Certification of the Lockheed Model 286 Rigid Rotor Helicopter,", Paper presented at the 5th I.C.A.F. Symposium entitled, "Aircraft Fatigue - Design, Operational and Economic Aspects", Melbourne, Australia, 24 May, 1967.

[5] de Jonge, J.B., "Loads and Damage Tolerance for Helicopters", National Aerospace Laboratory NLR, NLR TR 86018L, 14 February 1986.

[6] Groth, W. P., Chuga, G. M. and Nelson, V. S., "Modern Techniques of Conducting a Flight Loads Survey Based on Experience Gained on the Black Hawk

Helicopter," *Journal of American Helicopter Society*, Vol. 26, (2), April 1981, pp. 3–50.

[7] Beno, E. A., "Analysis of Helicopter Maneuver-Loads and Rotor Loads Flight Test Data," NASA CR-2225, March 1973.

[8] Kufeld, R. M., "High Load Conditions Measured on a UH-60A in Maneuvering Flight," *Journal of the American Helicopter Society*, Vol. 43, (3), July 1998, pp. 202–211.

[9] McHugh, F,J., "What are the Lift and Propulsive Force Limits at High Speed for the Conventional Rotor?," American Helicopter Society 34th Annual Forum, Washington, D.C., May 1978.

[10] Bousman, W. G., "A Qualitative Examination of Dynamic Stall from Flight Test Data," *Journal of the American Helicopter Society*, Vol. 43, (4), October 1998, pp. 279–295.

[11] Washuta, K. W. and Stocker, B. P., "Air-to-Air Combat Test (AACT II) Maneuvering Flight Loads for UH-60A and AUH-76 Helicopters," US-AAVSCOM TR-86-D-1, April 1986.

[12] Datta, A., Nixon, M. and Chopra, I., "Review of Rotor Loads Prediction with the Emergence of Rotorcraft CFD," *Journal of the American Helicopter Society*, Vol. 52, (4), October 2007, pp. 287–217.

[13] Parkus, H., "The Disturbed Flapping Motion of Helicopter Rotor Blades," *Journal of the Aeronautical Sciences*, Vol. 15, (2), February 1948, pp. 103–106.

[14] Flax, A. H., "The Bending of Rotor Blades," *Journal of the Aeronautical Sciences*, Vol. 14, (1), January 1947, pp. 42–50.

[15] Johnson, W. C. and Mayne, R., "Effect of Second-Harmonic Flapping on the Stresses of a Hinged Rotor Blade," Goodyear Aircraft Report No. R-107-4, Part 111, 1946

[16] DiPrima, R. C. and Handelman, G. H., "Vibrations of Twisted Beams," Quarterly of Applied Mathematics, Vol. XII, (3), October 1954, pp. 241–259.

[17] Shulman, Y., "Stability of a Flexible Helicopter Rotor Blade in Forward Flight," *Journal of the Aeronautical Sciences'*, Vol. 23, (7), July 1956, pp. 663–670.

[18] Houbolt, J. C. and Brooks, G. W., "Differential Equations of Motion for Combined Flapwise Bending, Chordwise Rending, and Torsion of Twisted Nonuniform Rotor Blades," NACA Report 1346, October 1958.

[19] Hodges, D. H., and Dowell, E. H., "Nonlinear Equations of Motion for the Elastic Bending and Torsion of Twisted Nonuniform Rotor Blades," NASA TN D-7818, December 1974.

[20] Ormiston, R. A., Hodges, D. H., and Peters, D. A., "On the Nonlinear Deformation Geometry of Euler-Bernoulli Beams," NASA Technical Paper 1566,

1980.

[21] Kaza, K. R. V. and Kvaternik, R. G., "Nonlinear Aeroelastic Equations for Combined Flapwise Bending, Chordwise Bending, Torsion, and Extension of Twisted Nonuniform Rotor Blades in Forward Flight," NASA TM 74059, August 1977.

[22] Rosen, A. and Friedmann, P. P., "Nonlinear Equations of Equilibrium for Elastic Helicopter or Wind Turbine Blades Undergoing Moderate Deformations," NASA CR-159478, 1978.

[23] Johnson, W., "Aeroelastic Analysis for Rotorcraft in Flight or in a Wind Tunnel," NASA TN D-8515, 1977.

[24] Crespo da Silva, M. R. M., "Flap-Lag-Torsional Dynamic Modelling of Rotor Blades in Hover and in Forward Flight, 1ncluding the Effects of Cubic Nonlinearities," NASA CR-166194, July 1981.

[25] Hodges, D. H., "Nonlinear Equations for Dynamics of Pretwisted Beams Undergoing Small Strains and Large Rotations," NASA X-2770, May 1973. Technical Paper 2470, May 1985.

[26] Simo, J. C., "A Finite Strain Beam Formulation. The Three- Dimensional Dynamic Problem. Part I," *Computer Methods in Applied Mechanics and Engineering*, Vol. 49, 1985, pp. 55–70.

[27] Hodges, D. H., "A Mixed Variational Formulation Based on Exact Intrinsic Equations for Dynamics of Moving Beams," *International Journal of Solids and Structures*, Vol. 26, (11), 1990, pp. 1253–1233.

[28] Simo, J. C. and Vu-Quoc, L., "On the Dynamics in Space of Rods Undergoing Large Motions - A Geometrically Exact Approach," *Computer Methods in Applied Mechanics and Engineering*, Vol. 66, 1988, pp. 125–161.

[29] Jelenic, G., and Crisfield, M. A., "Geometrically exact 3D beam theory: Implementation of a strain-invariant finite element for statics and dynamics," Computer Methods in Applied Mechanics and Engineering, Vol. 171, (1-2), March 1999, pp. 141171.

[30] Hodges, D. H., "Geometrically exact, intrinsic theory for dynamics of curved and twisted anisotropic beams," *AIAA Journal*, Vol. 41, (6), June 2003, pp. 1131–1137; also "Erratum: Geometrically exact, intrinsic theory for dynamics of curved and twisted anisotropic beams," *AIAA Journal*, Vol. 42, (7), July 2004, pp. 1500–1500.

[31] Bauchau, O. A., and Kang, N. K., "A Multibody Formulation for Helicopter Structural Dynamic Analysis," *Journal of the American Helicopter Society*, Vol. 38, (2), April 1993, pp. 3–14.

[32] Johnson, W., "Rotorcraft Dynamics Models for a Comprehensive Analysis," 54^{th} *Annual Forum*, American Helicopter Society, Washington D.C., May 20-

22, 1998.

[33] Saberi, H., Khoshlahjeh, M., Ormiston, R.A. and Rutkowski, M. J., "Overview of RCAS and Application to Advanced Rotorcraft Problems," 4^{th} *Decennial Specialists' Conference on Aeromechanics*, American Helicopter Society, San Francisco, CA, January 2004.

[34] Argyris, J.H., Kelsey, S., and Kaneel, H., "Matrix Methods for Structural Analysis: A Precis of Recent Developments", MacMillan, New York, 1964.

[35] Belytschko, T. and Hsieh, B. J., "Non-linear Transient Finite Element Analysis with Convected Co-ordinates," *International Journal of Numerical Methods in Engieering*, Vol. 7, 1973, pp. 255–271.

[36] Shabana, A. A., and Wehage, R. A., "Variable Degree of Freedom Component Mode Analysis of Inertia Variant Flexible Mechanical Systems," *J. Mech., Trans., & Autom. Design*, Vol. 105, 1983, pp. 371–378.

[37] Oden, T.D., "Finite Elements of Nonlinear Continua", McGraw-Hill, New York, 1972.

[38] Bathe, K.J., Ramm, E., and Wilson, E. L., "Finite Element Formulations for Large Deformation Dynamic Analysis," *International Journal of Numerical Methods in Engineering*, Vol 9, 1975, pp. 353–386.

[39] Downer, J. D., Park, K. C., and Chiou, J. C., "A Computational Procedure for Multibody Systems Including Flexible Beam Dynamics," Paper No. AIAA-90-1237-CP, AIAA Dynamics Specialists Conference, Long Beach, California, April 1990.

[40] Shabana, A. A., Bauchau, O. A., and Hulbert, G., "Integration of Large Deformation Finite Element and Multibody System Algorithms," *Journal of Computational and Nonlinear Dynamics*, Vol. 2, (4), October 2007, pp. 351–359.

[41] Shabana, A. A., "Flexible Multibody Dynamics: Review of Past and Recent Developments," Multibody System Dynamics, Vol. 1, (2), June 1997, pp. 189–222.

[42] Wasfy, T. M., and Noor, A. K., "Computational Strategies for Flexible Multibody Systems,", *Applied Mechanice Review*, November 2003, Vol. 56, (6), pp. 553–614.

[43] Hodges, D. H., Hopkins, A. S., Kunz, D. L., and Hinnant, H. E., "Introduction to GRASP-General Rotorcraft Aeromechanical Stability Program-A Modern Approach to Rotorcraft Modeling," *Journal of the American Helicopter Society*, Vol. 32, (2), April 1987, pp.78–90.

[44] Ghiringhelli, G. L., Masarati, P., and Mantegazza, P., "Analysis of an Actively Twisted Rotor by Multibody Global Modeling," *Composite Structures*, Vol 52, (1), April 2001, pp. 113–122.

[45] Thompson, B. S., and Barr, A. D. S., "A Variational Principle for the Elastodynamic Motion of Planar Linkages," *ASME Journal of Engineering for Industry*, November 1976, pp. 1306 –1312.

[46] Song, J. O. and Haug, E. J., "Dynamic Analysis of Planar Flexible Mechanisms," *Computer Methods in Applied Mechanice and Engineering*, Vol 24, (3), 1980, pp. 359–381.

[47] Bauchau, O. A. and Laulusa, A., "Review of Contemporary Approaches for Constraint Enforcement of Multibody Systems," *Journal of Computational & Nonlinear Dynamics*, Vol. 3, (1), pp 011005 1–8, 2008.

[48] Laulusa, A. and Bauchau O. A., "Review of Classical Approaches for Constraint Enforcement in Multibody Systems," *Journal of Computational & Nonlinear Dynamics*, Vol. 3, (1), pp. 011004 1–8 2008.

[49] Datta, A., and Johnson, W., "A Multibody Formulation For Three Dimensional Brick Finite Element Based Parallel and Scalable Rotor Dynamic Analysis," Presented at the American Helicopter Society 66^{th} Annual Forum, Phoenix, Az, May 11–13, 2010.

[50] Gessow, A., "Understanding and Predicting Helicopter Behavior: Then and Now," Journal of American Helicopter Society, Vol. 31, (1), 1986, pp. 3–28.

[51] Coleman, R. P., Feingold, A. M., and Stempin, C. W., "Evaluation of the

Induced-velocity Field of an Idealized Helicopter Rotor ," NACA-ARR-L5E10; NACA-WR-L-126, 1945.

[52] Castles, W. Jr., De Leeuw, J. H., "The Normal Component of the Induced Velocity in the Vicinity of a Lifting Rotor and Some Examples of its Application," NACA-TN-2912, 1953.

[53] Piziali, R. A., and DuWaldt, F., "Computation of Rotary Wing Harmonic Airloads and Comparison with Experimental Results," American Helicopter Society 18th Annual National Forum, Washington DC, 1962.

[54] Piziali, R. A., "A Method for Predicting the Aerodynamic Loads and Dynamic Response of Rotor Blades," *Journal of Sound and Vibration*, Vol. 4, (3), 1966, pp. 445–489.

[55] Landgrebe, A. J., "An Analytical Method for Predicting Rotor Wake Geometry," *Journal of the American Helicopter Society*, Vol. 14, (4), October 1969, pp. 20–32.

[56] Landgrebe, A. J., "The Wake Geometry of a Hovering Rotor and its influence on Rotor Performance," *Journal of the American Helicopter Society*, Vol. 17, (4), October 1972, pp. 2–15.

[57] Scully, M. P., "A Method of Computing Helicopter Vortex Wake Distortion," MIT, ASRL TR 138-1, June 1967.

[58] Crimi, P., "Theoretical Prediction of the Flow in the Wake of a Helicopter Rotor," Cornell Aeronautical Laboratory Report BB-1994-5-1, Buffalo NY, September 1965.

[59] Scully, M. P., "Computation of Helicopter Rotor Wake Geometry and Its Influence on Rotor Harmonic Airloads," MIT, ASRL TR 178-1, March 1975.

[60] Egolf, T. A., Landgrebe, A. J., "Helicopter Rotor Wake Geometry and its influence in Forward Flight, Vol. 1 - Generalized Wake Geometry and Wake Effects in Rotor Airloads and Performance," NASA CR-3726, October 1983.

[61] Beddoes, T. S., "A Wake Model for High Resolution Airloads," Proceedings of the 2nd International Conference on Basic Rotorcraft Research, Traingle Park, NC, 1985.

[62] Wachspress, D. A., Quackenbush, T. R., Boschitsch, A. H., "First-Principles Free-Vortex Wake Analysis For Helicopters and Tiltrotors," Presented at the American Helicopter Society, 59th Annual Forum, Phoenix, AZ, May 6–8, 2003.

[63] Johnson, W., "A General Free Wake Geometry Calculation For Wings and Rotors," Presented at the American Helicopter Society 51st Annual Forum, Fort Worth, Texas, May 9–11, 1995.

[64] Bagai, A., Leishman, J. G., "The Maryland Free-Wake Analysis - Theory, Implementation and Users Manual," University of Maryland, Department of

Aerospace Engineering, Technical Report Prepared for NASA Langley Research Center, Aeroacousitics Branch, Fluid Mechanics and Acoustics Division, Contract No. 015-2685, December 1995.

[65] Johnson, W., "Influence of Wake Models on Calculated Tiltrotor Aerodynamics," American Helicopter Society Aerodynamics, Acoustics, and Test and Evaluation Technical Specialist Meeting Proceedings, San Francisco, CA, January 2002.

[66] Clark, D. R. and Leiper, A. C., "The Free Wake Analysis - A Method for Prediction of Helicopter Rotor Hovering Performance," Journal of the American Helicopter Society, Vol. 15, (1), January 1970, pp. 3-11.

[67] Sadler, S. G., "A Method for Predicting Helicopter Wake Geometry, Wake Induced Inflow and Wake Effects on Blade Airloads," American Helicopter Society 27th Annual National Forum, Washington DC, May 1971.

[68] Gray, R. B., "An Aerodynamic Analysis of a Single-bladed Rotor in Hovering and Low-speed Forward Flight as Determined from Smoke Studies of the Vorticity Distribution in the Wake.", Princeton University Aerospace Engineering Department, Report No.356, September 1956.

[69] Egolf, T. A., "Rotor Wake Modeling for High Speed Applications," American Helicopter Society 44th Annual National Forum,Washington D.C., June 16-18 1988.

[70] Baron, A., and Boffadosi, M., "Unsteady Free Wake Analysis of Closely Interfering Helicopter Rotors," 19th European Rotorcraft Forum, Cernobbio, Italy, September 14-16, 1993.

[71] Bhagwat, M. J., and Leishman, J. G., "Stability, Consistency and Convergence of Numerical Algorithms for Time-Marching Free-Vortex Wake Analyses," *Journal of American Helicopter Society*, Vol. 46, (1), January 2001, pp. 59–71.

[72] Bhagwat, M. J., Leishman, J. G., "Rotor Aerodynamics During Maneuvering Flight Using a Time-Accurate Free-Vortex Wake," *Journal of American Helicopter Society*, Vol. 48, (3), July 2003.

[73] Ananthan, S., and Leishman, J. G., "Predictions of Transient Rotor Wake Aerodynamics in Response to Time-Dependant Blade Pitch Inputs," *Journal of Aircraft*, Vol. 41, (5), 2004, pp. 1025–1041.

[74] Ananthan, S., and Leishman, J. G., "Helicopter Wake Dynamics During Tactical Maneuvers," Proceedings of the 60th Annual Forum of the American Helicopter Society International, Baltimore, MD, June 7–10, 2004.

[75] Leishman, J. G., "Challenges in Modeling the Unsteady Aerodynamics of Wind Turbines,", *Wind Energy*, Vol. 5, (2), April 2002, pp. 85–132.

[76] Bisplinghoff, R.L., Ashley H., and Halfman, R.L., "Aeroelasticity," Addison-

Wesley Publishing Co., Reading, MA, 1955.

[77] McCroskey, W. J., "The Phenomenon of Dynamic Stall," NASA 81264, 1981.

[78] Carta, F. O., "An Analysis of the Stall Flutter Instability of Helicopter Rotor Blades," Journal of the American Helicopter Society, Vol. 12, (4), 1967, pp. 1–18.

[79] Bielawa, R. L., "Synthesized Unsteady Airfoil Data with Applications to Stall Flutter Calculations," 31st Annual Forum of the American Helicopter Society, Washington DC, May 13–15, 1975

[80] Gross, D. W., and Harris, F. D., "Prediction of In-Flight Stalled Airloads from Oscillating Airfoil Data," 25th Annual Forum of the American Helicopter Society, Washington DC, May 14–16, 1969.

[81] Gormont, R. E., "A Mathematical Model of Unsteady Aerodynamics and Radial Flow for Application to Helicopter Rotors," USAAVLABS TR 72–67, 1973.

[82] Beddoes, T. S., "A Synthesis of Unsteady Aerodynamic Ef- fects Including Stall Hysteresis," Vertica, Vol. 1, 1976, pp. 113–123.

[83] Beddoes, T. S., "Onset of Leading Edge Separation Effects under Dynamic Conditions and Low Mach Number," 34th Annual Forum of the American Helicopter Society, Washington DC, May 15–17, 1978.

[84] Gangwani, S. T., "Synthesized Airfoil Data Method for Prediction of Dynamic Stall and Unsteady Airloads," Vertica, Vol. 8, (2), 1984, pp. 93–118.

[85] Johnson, W., "The Response and Airloading of Helicopter Rotor Blades Due to Dynamic Stall," ASRL TR 130-1, May 1970.

[86] Ham,N. D., and Garelick, M. S., "Dynamic Stall Considerations in Helicopter Rotors," *Journal of American Helicopter Society*, Vol. 13, April 1968, pp. 49–56.

[87] Tran, C. T., and Petot, D., "Semi-Empirical Model for the Dynamic Stall of Airfoils in View of the Application to the Calculation of the Responses of a Helicopter Blade in Forward Flight," Vertica, Vol. 5, (1), 1981, pp. 35–53.

[88] McAlister, K. W., Lambert, O., and Petot, D., "Application of the ONERA Model of Dynamic Stall," NASA Technical Paper 2399, AVSCOM Technical Report 84-A-3, 1984.

[89] Petot, D., "Differential Equation Modeling of Dynamic Stall," *La Recherche Aerospatiale*, No. 1989-5 (Corrections dated October 1990).

[90] Truong, V. K., "A 2-D Dynamic Stall Model Based on a Hopf Bifurcation," 19th European Rotorcraft Forum, Marseiles, France, September, 1998.

[91] Leishman, J. G., and Beddoes, T. S., "A Semi-Empirical Model for Dynamic Stall," *Journal of the American Helicopter Society*, Vol. 34, (3), July 1989, pp. 3–17.

[92] Leishman, J. G., and Beddoes, T. S., "A Semi-Empirical Model for Dynamic Stall," *Journal of the American Helicopter Society*, Vol. 34, (3), July 1989, pp. 3–17.

[93] Beddoes, T. S., "Representation of Airfoil Behaviours," Vertica Vol. 7, No. 2,1983, pp. 183–197.

[94] Johnson, W., "Recent Developments in Rotary-Wing Aerodynamic Theory," AIAA Journal, Vol. 24, No. 8, August 1986, pp. 1219–1245.

[95] Dwyer, H. A., and McCroskey, W. J., "Crossflow and Unsteady Boundary-Layer Effects on Rotating Blades," *AIAA Journal*, Vol. 9, (8), 1971, pp. 1498–1505.

[96] St. Hillaire, A. O., Carta, F. O., Fink, M. R., and Jepson, W. D., "The Influence of Sweep on the Aerodynamic Loading of a NACA 0012 Airfoil," Vol. 1, NASA CR 3092, 1979.

[97] St. Hillaire, A. O., and Carta, F. O., "Analysis of Unswept and Swept Wing Chordwise Pressure Data from an Oscillating NACA 0012 Airfoil Experiment," Vol. 1, NASA CR 3567, 1983.

[98] Desopper, A., "Study of Unsteady Transonic Flow on Rotor Blade with Different Tip Shapes," Vertica, Vol. 9, (3), July 1985.

[99] Desopper, A., Lafon, P., Ceroni, P., and Phillipe, J. J., "10 Years of Rotor Flow Studies at ONERA - State of the Art and Future Studies," 42nd Annual Forum

of the American Helicopter Society, Washington D.C., June 1986.

[100] Philippe, J. J., Vuillet, A., "Aerodynamic Designs of Advanced Rotors with New Tip Shapes," 39th Annual Forum of the American Helicopter Society, St. Louis, Missouri, May 1983.

[101] Tarzanin, F. J., Vlaminck, R. R., "Investigation of the Effects of Blade Sweep on Rotor Vibratory Loads," NASA CR-166526, Oct. 1983.

[102] Leishman, J. G., "Modeling Sweep Effects on Dynamic Stall," *Journal of the American Helicopter Society*, Vol. 34, (3), 1989, pp. 18–29.

[103] Caradonna, F. X., and Isom, M. P., "Subsonic and Transonic Potential Flow over Helicopter Rotor Blades," *AIAA Journal*, Vol. 10, (12), Dec. 1972, pp. 1606–1612.

[104] Caradonna, F. X., Isom, M. P., "Numerical Calculation of Unsteady Transonic Potential Flow over Helicopter Rotor Blades," *AIAA Journal*, Vol. 14, (4), April 1976, pp.482–488.

[105] Caradonna, F. X., and Phillippe, J. J., "Flow Over a Helicopter Blade Tip in the Transonic Regime," Vertica, Vol. 2, (1), April 1978, pp. 43–60.

[106] Caradonna, F. X., Desopper, A., and Tung, C., "Finite Difference Modeling of Rotor Flows Including Wake Effects," *Journal of the American Helicopter Society*, Vol. 29, (2), April, 1984, pp.26–33.

[107] Phillippe, J. J., and Chattot, J. J., "Experimental and Theoritical Studies on Helicopter Blade Tips at ONERA," 6th European Rotorcraft Forum, Bristol, England, Paper 46, September 1980, pp. 16–19.

[108] Arieli, R. and Tauber, M. E., "Computation of Subsonic and Transonic Flow about Lifting Rotor Blades," *AIAA Journal*, Vol. 24, (5), May 1986, pp.722–727.

[109] Chang, I. C. and Tung, C., "Numerical Solution of the Full-Potential Equation for Rotors and Oblique Wings using a New Wake Model," Paper AIAA 85-0268, Aerospace Sciences Meeting, 23rd, Reno, January 14–17, 1985.

[110] Egolf, T. A. and Sparks, S. P., "Rotor Analysis With Wake Influence Using an Inner-Outer Domain Technique," *Journal of the American Helicopter Society*, Vol. 32, (3), July 1987, pp. 15–24.

[111] Sankar, L. N., and Prichard, D., "Solution of Transonic Flow past rotor blades using the Conservative Full Potential Equation," AIAA 85-5012, Applied Aerodynamics Conference, 3rd, Colorado Springs, CO, October 14–16, 1985.

[112] Strawn, R. C., and Caradonna, F. X., "Conservative full potential model for unsteady transonic rotor flows," *AIAA Journal*, Vol. 25, (2), February 1987, pp. 193–198.

[113] Jameson, A., Caughey D. A., "Numerical Calculation of the Transonic Flow

Past a Swept Wing," ERDA Research and Development, Mathematics and Computing, June 1977.

[114] Bridgeman, J. O., Steger, J. L., and Caradonna, F. X., "A Conservative Finite-Difference Algorithm for the Unsteady Transonic Potential Equation in Generalized Coordinates," Paper AIAA 82-1388, Atmospheric Flight Mechanics Conference, 9th, San Diego, CA, August 9–11, 1982.

[115] Steinhoff, J., and Ramachandran, K., "Free Wake Analysis of Compressible rotor flows," *AIAA Journal*, Vol. 28, (3), 1990, pp. 426–431.

[116] Pulliam, T. H. and Steger, J. L., "Implicit Finite-Difference Simulations of Three-Dimensional Compressible Flow," *AIAA Journal*, Vol. 18, (2), February 1980, pp. 159–167.

[117] Wake, B. E., and Sankar, N. L, "Solution of Navier-Stokes Equations for the flow over a rotor blade," *Journal of the American Helicopter Society*, Vol. 34, (2), April 1989, pp. 13–23.

[118] Srinivasan, G. R., and McCroskey, W. J., "Navier-Stokes Calculations of Hovering Rotor Flowfields," *Journal of Aircraft*, Vol. 25, (10), October 1988, pp. 865–874.

[119] Agarwal, R. K., and Deese, J. E., "Navier-Stokes Calculations of Hovering Rotor Flowfields," AIAA Paper 88-0106, Aerospace Sciences Meeting, 26th,

Reno, NV, January 11–14, 1988.

[120] Wake, B. E. and Baeder, J. D., "Evaluation of a Navier-Stokes Analysis Method for Hover Performance Prediction," Journal of the American Helicopter Society, Vol. 38, (1), January 1996, pp. 1–11.

[121] Farhat, C., Pierson, K., and Degand, C., "Multidisciplinary Simulation of the Maneuvering of an Aircraft," *Engineering with Computers*, Vol. 17, (1), 2001, pp. 16–27.

[122] Tung, C., Caradonna, F. X., and Johnson, W., "Conservative Full Potential Model for Unsteady Transonic Rotor Flows," *AIAA Journal*, Vol. 25, (2), 1987, pp. 193–198.

[123] Altmikus, A. R. M., Wagner, S., Beaumier, P., and Servera, G., "A Comparison : Weak versus Strong Modular Coupling for Trimmed Aeroelastic Rotor Simulation," American Helicopter Society 58th Annual Forum, Montreal, Quebec, June 2002.

[124] Bauchau, O., A. and Ahmad, J., U., "Advanced CFD and CSD Methods for Multidisciplinary Applications of Rotorcraft Problems," AIAA 6th Symposium on Multidisciplinary Analysis and Optimization, Seattle, WA, September 1996.

[125] Pomin, H. and Wagner, S., "Navier-Stokes Analysis of Helicopter Rotor Aerodynamics in Hover and Forward Flight," AIAA 2001-0998, Reno, NV January

2001.

[126] Datta, A.and Sitaraman, J., Baeder, J., and Chopra, I., "Analysis Refinements for Prediction of Rotor Vibratory Loads in High-Speed Forward Flight," 60th Annual Forum of the American Helicopter Society International, Alexandria, VA, June 2004.

[127] Datta, A., Sitaraman, J., Chopra, I., and Baeder, J., "CFD/CSD Prediction of Rotor Vibratory Loads in High-Speed Flight," *AIAA Journal of Aircraft*, Vol. 43, (6), 2006, pp. 1698 – 1709.

[128] Sitaraman, J., Datta, A., Baeder, J., and Chopra, I., "Coupled CFD/CSD Prediction for Rotor Aerodynamic and Structural Dynamic Loads for Three Critical Flight Conditions," Proceedings of the 31st European Rotorcraft Forum, Firenze, Italy, 2005.

[129] Sitaraman, J., Datta, A.and Baeder, J. D., and Chopra, I., "Fundamental Understanding and Prediction of Rotor Vibratory Loads in High-Speed Forward Flight," 29th European Rotorcraft Forum, September 2003.

[130] Potsdam, M., Yeo, H., and Johnson, W., "Rotor Airloads Prediction Using Loose Aerodynamic/Structural Coupling," American Helicopter Society 60th Annual Forum and Technology Display, Baltimore, MD, June 7–10 2004, later published in, Journal of Aircraft, Vol. 43, (3), May-June, 2006, pp. 732–742.

[131] Johnson, W, "A Comprehensive Analytical Model of Rotorcraft Aerodynamics and Dynamics, Part I : Analysis Development," NASA TM-81182, June 1980.

[132] Thomson, D., and Bradley, R., "Inverse Simulation as a Tool for Flight Dynamics Research – Principles and applications", *Progress in Aerospace Sciences*, Vol. 42, 2006, pp. 174–210.

[133] Etkin, Dynamics of flight, Stability and Control, 1st ed. Inverse problems, 1959. pp. 341–52 [chapter 11].

[134] Wood, T. L., Ford, D.G., and Brigman, G. H., "Maneuver Evaluation Program," USAAMRDL-TR-74-32, 1974.

[135] Haverdings, H., "A Control Model for Maneuvering Flight for Application to a Computer-flight-testing Program," Vertica 1983, 7, (3), pp. 259–69.

[136] Haverdings, H., "Improved Pilot Model for Application to a Computer-flight-testing-program for Helicopters," Proceedings of the 9th European rotorcraft forum, Paper no. 66, Stresa, Italy, September 1983.

[137] Thomson, D. G., and Bradley, R., "Recent Developments in the Calculation of Inverse Solutions of the Helicopter Equations of Motion," Proceedings of the UK simulation Council Triennial Conference, September 1987.

[138] Thomson, D. G., and Bradley, R., "Development and Verification of an Algorithm for Helicopter Inverse Simulation," Vertica, Vol. 14, (2), 1990, pp.

185–200.

[139] Hess, R.A., Gao, C., and Wang, S.H., "Generalized Technique for Inverse Simulation Applied to Aircraft Maneuvers," *Journal of Guidance, Control, and Dynamics*, Vol. 14, (5), September–October 1991, pp. 920–926.

[140] Hess, R. A., Gao, C., "A Generalized Algorithm for Inverse Simulation Applied to Helicopter Maneuvering Flight," *Journal of the American Helicopter Society*, Vol. 38, (3), October 1993, pp. 3–15.

[141] Rutherford, S., and Thomson, D. G., "Improved Methodology for Inverse Simulation," The Aeronautical Journal, Vol. 100, (993), March 1996, pp. 79–86.

[142] Lin, K. C., "Comment on Generalized Technique for Inverse Simulation Applied to Aircraft Maneuvers," *Journal of Guidance, Control, and Dynamics*, Vol.16, (6), 1993, pp. 1196–1205.

[143] de Matteis, G., de Socio, L. M., and Leonessa, A., "Solution of Aircraft Inverse Problems by Local Optimization," *Journal of Guidance, Control, and Dynamics*, Vol. 18, No. 3, May-June 1995, pp. 567–571.

[144] Celi, R., "Optimization-based inverse simulation of a Helicopter Slalom Maneuver," Proceedings of the 25th European Rotorcraft Forum, Rome, Italy, 1999.

[145] Avanzini, G., and de Matteis G., "Two-timescale Inverse Simulation of a Helicopter Model," *Journal of Guidance, Control, and Dynamics*, Vol. 24, (2), 2001, pp. 330–339.

[146] Bottasso, C. L., Croce, A., Leonello, D., and Riviello, L., "Optimization of Critical Trajectories for Rotorcraft Vehicles,", *Journal of the American Helicopter Society*, Vol. 50, (2), 2005, pp. 165–177.

[147] Bousman, W. G., "Putting the Aero Back into Aeroelasticity," 48$^{\text{th}}$ Annual ARO Worshop on Aeroelasticity of Rotorcraft Systems, Pennsylvania State University, University Park, PA, October 1999.

[148] Hooper, W. E., "The Vibratory Airloading of Helicopter Rotors," Vertica, Vol. 8, 1984.

[149] Bousman, W. G., "The Response of Helicopter Rotors to Vibratory Airloads," *Journal American Helicopter Society*, Vol. 35, (4), October 1990, pp. 53–62.

[150] Lorber, P. F., "Aerodynamic Results of Pressure-Instrumented Model Rotor Test at the DNW," *Journal of the American Helicopter Society*, Vol. 36, (4), October 1991, pp. 66–76.

[151] Torok, M. S. and Goodman, R. K., "Analysis of Rotor Blade Dynamics Using Experimental UH-60A Airloads Obtained at the DNW," *Journal of the American Helicopter Society*, Vol. 39, (1), January 1994, pp. 63–69.

[152] Torok, M. S. and Berezin, C. R., "Aerodynamic and Wake Methodology Evaluation Using Model UH-60A Experimental Data," *Journal of the American Helicopter Society*, Vol. 39, (2), April 1994, pp. 21–29.

[153] Bousman, W. G., and Kufeld, R. M., "UH-60A Airloads Catalog," NASA TM 2005-212827, August 2005.

[154] Kufeld, R. M., Cross, J. L., and Bousman, W. G., "A Survey of Rotor Loads Distribution in Maneuvering Flight," American Helicopter Society Aeromechanics Specialists Conference, San Francisco, CA, Jan. 19–21 1994.

[155] Schillings, J. J., Roberts, B. J., Wood, T. L., and Wernicke, K. G., "Maneuver Performance Comparison Between the XV-15 and an Advanced Tiltrotor Design," JAHS, v35, (2), May 1990, pp. 4–14.

[156] Sopher, R and Duh, J. E., "Prediction of Control System Loads in Level Flight and Manveuvers," Proceedings of the 50$^{\text{th}}$ Annual Forum of the American Helicopter Society, Washington D. C., May 11–13, 1994.

[157] Bhagwat, M. J., Ormiston, R. A., Saberi, H. A., and Xin, H., "Application of CFD/CSD Coupling for Analysis of Rotorcraft Airloads and Blade Loads in Maneuvering Flight," Proceedings of the 63$^{\text{rd}}$ Annual Forum of the American Helicopter Society, Virginia Beach, VA, May 1–3 2007.

[158] Bhagwat, M. J., and Ormiston, R. A., "Examination of Rotor Aerodynamics

in Steady and Maneuvering Flight using CFD and Conventional Methods," American Helicopter Society Specialist's Conference on Aeromechanics, San Francisco, CA, January 23–25, 2008.

[159] Abhishek, A., Datta, A., and Chopra, I., "Comprehensive Analysis, Prediction, and Validation of UH-60A Blade Loads in Unsteady Maneuvering Flight," American Helicopter Society 63rd Annual Forum Proceedings, Virginia Beach, VA, May 1–3, 2007.

[160] Yeo, H., "Investigation of Rotor Airloads and Structural Loads in Maneuvering Flight," American Helicopter Society 64$^{\text{th}}$ Annual Forum and Technology Display, Montréal, Canada, April 29–May 1 2008.

[161] Abhishek, A., Datta, A., Ananthan, S., and Chopra, I., "Prediction and Analysis of Main Rotor Loads in a Prescribed Pull-Up Maneuver," *Journal of Aircraft*, Vol. 47, (4), July–August 2010, pp. 1197–1215.

[162] Abhishek, A., Silbaugh, B., Ananthan, S., Baeder, J., and Chopra, I., "Coupled CFD/CSD Analysis of A Prescribed Pull-up Maneuver," 3$^{\text{rd}}$ International Basic Research Conference on Rotorcraft Technology, Nanjing, China, Oct. 14–16, 2009.

[163] Sitaraman, J., and Roget, B., "Prediction of Helicopter Maneuver Loads Using A Coupled CFD/CSD Analysis," The 26$^{\text{th}}$ Congress of International Council of the Aeronautical Sciences, September 14–19, 2008.

[164] Thomas, S., Shreyas, A., and Baeder, J., "Wake coupling CFD-CSD Analysis of helicopter rotors in steady and maneuvering flight conditions," American Helicopter Society Aeromechanics Specialists Conference, San Francisco, January 2010.

[165] Silbaugh, B., and Baeder, J., "Coupled CFD/CSD Analysis of a Maneuvering Rotor Using Staggered & Time-Accurate Coupling Schemes," AHS Specialist's Conference on Aeromechanics, San Francisco, CA, January, 23–25 2008.

[166] Abhishek, A., Ananthan, S., Baeder, J., and Chopra, I., "Prediction and Fundamental Understanding of Stall Loads in UH-60A Pull-up Maneuver," American Helicopter Society 66$^{\text{th}}$ Annual Forum and Technology Display, Phoenix, Arizona, May 11–13 2010.

[167] Reissner, E., "On One-Dimensional Large-Displacement Finite-Strain Beam Theory," *Studies in Applied Mathematics*, Vol. 52, (2), April 1973, pp. 87–95.

[168] Datta, A., "Fundamental Understanding, Prediction and Validation of Rotor Vibratory Loads in Steady-Level Flight," Ph.D. Dissertation, Dept. of Aerospace Engineering, University of Maryland, College Park, MD, 2004.

[169] Sweers, J.E., "In-flight Measurements and Correlation with Theory of Blade Airloads and Responses on the XH-51A Compound Helicopter Rotor. Vol. 3. Theoretical Prediction of Airloads and Structural Loads and Correlation with

Flight Test Measurements," USAAVLABS Technical Report 68-22c, Lockheed-California Company, Burbank, CA, May 1968

[170] Esculier, J. and Bousman, G., "Calculated and Measured Blade Structural Response on a Full-Scale Rotor," *Journal of the American Helicopter Society*, Vol. 33, (1), January 1988, pp. 3–16.

[171] Torok, M.,S. and Goodman, R. K., "Analysis of Rotor Blade Dynamics Using Model Scale UH-60A Airloads," *Journal of the American Helicopter Society*, Vol. 39, (1), January 1994, pp. 63–69.

[172] Kufeld, R.M., and Bousman, W.G., "UH-60A Airloads Program Azimuth Reference Correction," *Journal of American Helicopter Society*, Vol. 50, (2), April 2005, pp. 211-213.

[173] Kane, T.R., and Levinson, D.A., Dynamics, Theory and Application, Mc.Graw-Hill, New York 1985.

[174] Hilber, H.M., Hughes, T.J.R., and Taylor, R.L., "Improved numerical dissipation for time integration algorithms in structural dynamics," *Earthquake Eng. and Struct. Dynamics*, 1977, pp. 283–292.

[175] Newmark, N.M., "A method of computation for structural dynamics," *Journal of the Engineering Mechanics Division*, ASCE, 1959, pp. 67–94.

[176] Gere, J.M., and Timoshenko, S.P., "Mechanics of Materials," *Deflections of Beams*, $3^{rd}ed.$, PWS-KENT, Boston, 1990, pp. 514-517.

[177] Dowell, E.H., Traybar, J., and Hodges, D.H., "An Experimental-Theoretical Correlation Study of Non-Linear Bending and Torsion Deformations of a Cantilever Beam," *Journal of Sound and Vibration*, Vol. 50, (4), February 1977, pp. 533–544.

[178] Dowell, E.H., and Traybar, J., "An Experimental Study of the Nonlinear Stiffness of a Rotor Blade Undergoing Flap, Lag, and Twist Deformations," NASA CR 137968, January 1975; and NASA CR 137969, December 1975.

[179] Hopkins, S.A.,and Ormiston, R.A., "An Examination of Selected Problems in Rotor Blade Structural Mechanics and Dynamics," *Journal of the American Helicopter Society*, Vol. 51(1), Jan 2006, pp 104–119.

[180] Kufeld, R. M., and Johnson, W., "The Effects of Control System Stiffness Models on the Dynamic Stall Behavior of a Helicopter," *Journal of the American Helicopter Society*, Vol. 45, (4), October 2000, pp. 263–269.

[181] Datta, A., and Chopra, I., "Validation of Structural and Aerodynamic Modeling Using UH-60A Airloads Program Data," *Journal of the American Helicopter Society*, Vol. 51, (1), January 2006, pp. 43–58.

[182] Ormiston, R. A., "An Investigation of the Mechanical Airloads Problem for

Evaluating Rotor Blade Structural Dynamics Analysis," 4^{th} *Decennial Specialist's Conference on Aeromechanics*, American Helicopter Society, San Francisco, CA, January 21-23, 2004.

[183] Datta, A., and Chopra, I., "Prediction of UH-60A Main Rotor Structural Loads Using CFD/Comprehensive Analysis Coupling," *Journal of the American Helicopter Society*, Vol. 53, (4), October, 2008, pp. 351–365.

[184] Shanley, J.P., "Application of the Comprehensive Analytical Model of Rotorcraft Aerodynamics and Dynamics to the UH-60A Aircraft," SER-72126, February 1986.

[185] Stepniewski, W.Z., and Shinn, R.A., "A Comparative Study of Soviet vs. Western Helicopters. Part 2: Evaluation of Weight, Maintainability and Design Aspects of Major Components," NASA CR 3580, March 1983.

[186] Weissinger, J., "The Lift Distribution of Swept-Back Wings," National Advisory Committee for Aeronautics, Technical Memorandum No. 1120, 1947.

[187] Sitaraman, J. and Baeder, J., "Field Velocity Approach and Geometric Conservation Law For Unsteady Flow Simulations," *AIAA journal*, vol. 44, (9), pp. 2084-2094.

[188] Duraisamy, K. and Baeder, J., "High Resolution Wake Capturing Methodology for Hovering Rotors," , *Journal of the American Helicopter Society*, Vol.

52, (2), April 2007, pp. 110 – 122.

[189] Yoon, S., and Jameson, A., "Lower-Upper Symmetric-Gauss-Seidel Method for Euler and Navier-Stokes equations," *AIAA Journal*, Vol. 26, 1988.

[190] Pulliam, T., "Time Accuracy and the use of Implicit Methods," AIAA-93-3360, 11^{th} AIAA Computational Fluid Dynamics Conf., Orlando, FL, July 1993.

[191] Datta, A., and Chopra, I., "Prediction of UH-60A Dynamic Stall Loads in High Altitude Level Flight using CFD/CSD Coupling," Proceedings of the 61^{st} Annual Forum of the American Helicopter Society International, Grapevine, Texas, June 1–3 2005.

[192] Guruswamy, G. P., and Yang, T. Y., "Aeroelastic Time-Response Analysis of Thin Airfoils by Transonic Code LTRAN2." *Computers and Fluids*, Vol. 9, (4), pp. 409–425, December, 1980.

[193] Datta, A., and Johnson, W., "An Assessment of the State-of-the-art in Multidisciplinary Aeromechanical Analyses," AHS Specialist's Conference on Aeromechanics, San Francisco, CA, January, 23–25 2008.

[194] Ananthan, S., Sitaraman, J., Baeder, J. D., Hahn, S., and Iaccarino, G., "Hybrid Unsteady Simulation of Helicopters: HUSH," 26^{th} AIAA Applied Aerodynamics Conference, AIAA-2008-7339, Honolulu, HI, August 18–21 2008.

[195] Ahmadian, M. T., Borhan, H. and Esmailzadeh, E., "Dynamic Analysis of Geometrically Nonlinear and Electrostatically Actuated Micro-beams," *Communications in Nonlinear Science and Numerical Simulation*, Vol. 14(2009), pp. 1627-1645.